Investigations on The Synthesis, Structure and Properties of Some Metal-Organic Compounds of Hydroxyl Functionalized Aromatic Carboxylates

A THESIS

Submitted by

SAYANI HUI

for the award of the degree

DOCTOR OF PHILOSOPHY (SCIENCE)

Department of Chemistry
Jadavpur University
Kolkata-700032, India
November, 2024

যাদবপুর বিশ্ববিদ্যালয়
কলকাতা-৭০০ ০৩২, ভারত

*JADAVPUR UNIVERSITY
KOLKATA-700032, INDIA

FACULTY OF SCIENCE : DEPARTMENT OF CHEMISTRY : INORGANIC SECTION

CERTIFICATE FROM THE SUPERVISOR

This is to certify that the thesis entitled **"Investigations on The Synthesis, Structure and Properties of Some Metal-organic Compounds of Hydroxyl Functionalized Aromatic Carboxylates"** Submitted by Smt. Sayani Hui who got her name registered on 18.03.2021 (Index No: 3/21/chem./27) for the award of Ph. D. (Science) Degree of Jadavpur University, is absolutely based upon her own work under the supervision of Dr. Partha Mahata and that neither this thesis nor any part of it has been submitted for either any degree / diploma or any other academic award anywhere before.

Date: 22/11/2024

Partha Mahata
(Dr. Partha Mahata)
Department of Chemistry
(Inorganic Chemistry Section)
Jadavpur University
Kolkata- 700032
India

Dr. Partha Mahata
Assistant Professor
Department of Chemistry
Jadavpur University
Kolkata-700 032

Dedicated to my Parents
and husband

DECLARATION

I hereby declare that the research work embodied in the present thesis entitled **"Investigations on The Synthesis, Structure and Properties of Some Metal-organic Compounds of Hydroxyl Functionalized Aromatic Carboxylates"** being submitted to Jadavpur University, Kolkata, has been carried out at the Jadavpur University under the supervision of Dr. Partha Mahata, Assistant Professor, Jadavpur University. This work is original and has not been submitted in part or in full, for any degree whatsoever.

……………………………………

(Sayani Hui)

Signature of Scholar with date

Preface

The research embodied in the present thesis entitled "**Investigations on The Synthesis, Structure and Properties of Some Metal-organic Compounds of Hydroxyl Functionalized Aromatic Carboxylates**" deals with the synthesis of the Metal-organic Compounds with some commercially available hydroxyl functionalized aromatic carboxylic acid followed by their structure elucidation and characterization and their various applications in material sciences.

Investigations described in this thesis have been carried out by the author in the Jadavpur University, Jadavpur, Kolkata-700032, India during the time of July, 2018 to October, 2024 under the supervision of Dr. Partha Mahata. The entire work has been described and summarized within the five chapters of this thesis.

Chapter 1 is the general introduction which provides the comprehensive literature survey on the hydroxyl functionalized aromatic carboxylates and the Metal-organic Compounds formed with this ligand. This chapter highlights the structure of various types of Metal-organic Compounds, synthetic methods and characterization techniques used for the work. At the end of the chapter, their application in different fields of material science have been described briefly.

In **Chapter 2**, the synthesis, structure and photoluminescence-based detection of pH using metal-organic compound are presented. For this purpose, we have successfully synthesized a 10% Tb doped Y based MOF, $[Y_{1.8}Tb_{0.2}(CAM)_3(H_2O)_4].2H_2O$, **1**, (CAM= Chelidamate) for the visible detection of pH in range of 7 to 9 where the self-quenching is minimized through the increase of distance between emitting centres. Luminescence response of compound **1** in the biologically important pH range 5-9 based on the free hydroxyl groups suggest its usefulness for real life application and human health.

In **Chapter 3**, we have successfully synthesized a new Eu- based metal-organic material (MOM), $[Eu(CAM)_2(H_2O)]\cdot 0.5H_2Pip\cdot H_2O$**, 2** (pip= Piperazine) via hydrothermal technique for the visible detection of amino acids. It exhibits luminescence turn-on behavior in the basic pH region (11-13) in an aqueous medium. Moreover, Luminescence turn-off was observed in the presence of the two amino acids namely, arginine and histidine and the quenching efficiency was 80.52% and 61.56%

for Arg and His respectively due to the molecular level interaction between the compound and amino acids.

In **Chapter 4**, we have synthesized a 3d-4d heterobimetallic metal- organic framework, $[YMn_{1.5}(C_7N_1H_3O_5)_3(H_2O)_6] \cdot 11H_2O$, **3**, ($C_7N_1H_3O_5$ = chelidamate) hydrothermally by using Y(III), Mn(II) and chelidamic acid for the luminescence turn-on based selective detection of phosphate anion in water medium. In this case the selectivity of phosphate detection was performed in presence of different anions for the compound.

In **Chapter 5**, we have successfully prepared a porous Cu- based metal-organic framework, $[Cu(C_{23}H_{14}O_6)(C_{10}H_8N_2)_2] \cdot H_2O \cdot DMSO$, **4, (**$C_{23}H_{16}O_6$= pamoate and $C_{10}H_8N_2$ = 4,4'- bipyridine**)** by layer diffusion technique by using Cu(II), pamoic acid and 4, 4'- bipyridine for selective staining of the cellular nucleus through fluorescence imaging and selective sorption of methylene blue dye.

Each chapter (**chapter 2** to **5**) begins with a short 'Introduction' followed by 'Experimental Section', 'Results and discussion' and 'Conclusion'. For convenience, 'References' are given at the end of each chapter. List of publications and list of poster presentation has been appended at the end of the thesis.

Acknowledgements

In the odyssey of my doctoral research work, many people were instrumental in shaping my academic career. Here is a small tribute to all those personalities.

First and foremost, I would like to extend my heartfelt gratitude to my supervisor ***Dr. Partha Mahata***, Assistant Professor, Department of Chemistry, Jadavpur University for providing me the opportunity to join in his research group. I am thankful to him for his valuable suggestions, cheerful enthusiasm and constant guidance throughout the progression of my research. He provides me with enough academic liberty to conduct research work that enable me to explore the fascinating field of metal-organic compounds.

I am thankful to Head of the Department, Section-in-charge, Inorganic Chemistry section and all the faculty members of our department, Jadavpur University.

I am also indebted to Prof. Sudip Kumar Mondal, Siksha-Bhavana, Visva-Bharati University and Dr. Samit Guha, Asst. Professor, Jadavpur university for their constructive feedback that greatly enriched the quality of works.

I am also thankful to Prof. Ayan Datta, IACS for his thoughtful suggestions that enhanced the depth of the works.

It is my pleasure to acknowledge all my lab members, Mrs. Priyanka Manna, Mr. Chhatan Das, Mr. Sourav Sarkar and dear brother Mr. Akash Kumar Chandra for their immense help in my lab work throughout my PhD journey. Specially Akash helps me lot to draw some important schematic presentation for the dissertation.

I am thankful to RUSA and Govt. of West Bengal for financial support during my doctoral research tenure.

I do not have words to express my thanks to two internet giants Google and Wikipedia, as I cannot dream of compiling my research work without them.

I take this platform to acknowledge all my teachers from school to university. Their teaching and encouragement motivated me for pursuing higher studies in scientific research. Thoughtful suggestions of Prof. Pranab Sarkar and Prof. Nabakumar Bera are deeply acknowledged in this regard.

I am very much thankful to former and present M.Sc. project students of our lab, Chandan, Isha, Saheli, Prantik, Sayan, Rajibul, Siddhanta, Kankan and Suman for their kind cooperation.

I convey my acknowledge to the neighboring lab members and specially Mrs. Mohafuza Khatun. She always helps me in my ups and downs throughout this journey in both academic and non-academic matters.

I would also like to thank Viswa-Bharati lab mates, Mr. Debal Kanti Singha, Mr. Prakash Majee, Ms. Pooja Daga, Mr. Debmalya Ghosh, Mr. Sahil Azam and Mr. Subhajit Dutta.

Now, it is time to mention the names of the most important persons in my life, my parents, my husband and my dear sister. Maa, Baba, your unconditional love and prayers make me whatever I am today. My best friend and husband, Sachin, your love, care and unconditional supports never left me alone in my hard days throughout this journey. My little sister, Shnaoli, your selfless love makes the path easier for me. I want to thank my in-laws for their support and love.

Finally, I want to thank everyone who helped me to finish my thesis and apologies for not naming everyone.

Jadavpur University ……………………………………….
Department of Chemistry Sayani Hui
Kolkata-700032, India
Date:

Abstract

Index No: 3/21/chem./27

Thesis title: "Investigations on The Synthesis, Structure and Properties of Some Metal-organic Compounds of Hydroxyl Functionalized Aromatic Carboxylates"

The main focus of the research work is to synthesize Metal-organic Compounds, characterize them through various techniques and to study their various applications in many fields of material chemistry. In order to attain this goal, a variety of metal ions (Transition metals as well as Lanthanide metals), carboxylate-based ligands and neutral basic ligands have been used and synthesized the desire Metal-organic Compounds through both the hydrothermal and Layer diffusion technique. By employing single- crystal structure determination strategy, we have determined the structure of the all compounds. The structural architecture has been designed in such a way that the compounds can show luminescence sensing, cell imaging and dye adsorption process.

In **first work**, we have successfully synthesized two isomorphous two-dimensional metal-organic compounds and We have determined the structure of the synthesized compound by using single crystal X-ray diffraction. Compound **1** is well characterized by PXRD, TGA, IR and UV- vis spectroscopy. The luminescence properties of this compound were utilized for the sensing of pH and it has been observed that the emission intensity increases by 4.7 times from pH 5 to pH 9 along with sudden jump at pH> 7.5, which is the physiological pH of human blood. Further, we have designed another Eu- based metal-organic material (MOM) *via* hydrothermal technique in **second work**. The coordination geometry around Eu^{3+} is bicapped trigonal prismatic in the compound **2**. The compound shows pH-responsive behavior in the basic region. The luminescence properties of this compound were utilized for the sensing of arginine and histidine and it has been observed that the emission intensity is quenched and the quenching efficiency was 80.52% and 61.56% for Arg and His. There is a strong interaction between the amino acid and Eu center. In **third work**, we have demonstrated a 3d-4d heterobimetallic metal- organic framework, synthesized through hydrothermal technique by using Y(III), Mn(II) and chelidamic

acid. The luminescence property of compound **3** is utilized for the highly selective and sensitive sensing of phosphate in aqueous media through luminescence turn- on and 4.09 times turn- on of the initial luminescence intensity is observed. The observed limit of detection (LOD) was 0.321 μM (30.49 ppb) for phosphate (PO_4^{3-}) and the observed luminescence enhancement coefficient, K_{SV} value was supreme to those of all other metal- organic frameworks reported previously. The hydroxyl groups decorated acidic pocket is the important part of the compound for molecular level interactions with the anions specially phosphate. Time resolved luminescence studies confirm the turn-on behavior in presence of phosphate anions through preferential molecular level interactions by reducing non-radiative decay pathways.

The work narrated in the **4th** work of the thesis includes the selective dye adsorption behavior of the compound **4** and selective staining of cellular nucleus through fluorescence imaging. Fluorescence microscopic experiments using human epithelioid cervix carcinoma HeLa cell line were carried out and it clearly showed that our compound selectively stained the cellular nucleus. For the sorption studies, it has been confirmed that the compound has high affinity towards methylene blue (MB) dye and it can sorb 88% of the dye. The pseudo second order kinetics fits well to the resulting data. The sorption isotherm was explained through the Langmuir adsorption isotherm. The compound can also separate the selective dye from a solution of mixture of dyes. The possible mechanism of the dye sorption behavior was discussed in terms of size and charge of dye molecules with respect to molecular level interactions between the framework and the dye molecules.

Partha Mahata
22/11/24
....

Dr. Partha Mahata

(Signature of the Supervisor date with official seal)

Contents

Table of Contents

Chapter || 1 *Introduction and literature survey*

Chapter || 2 *pH Response of a Hydroxyl-Functionalized Luminescent Metal-Organic Framework based Phosphor*

Chapter || 3 *A Supramolecular Assembly of Anionic Metal-Organic Complex and Cationic Amine: Selective Recognition Behavior Towards Arginine and Histidine*

Chapter || 4 *Highly Selective Luminescence Turn - On Based Sensing of Phosphate in Presence of Other Interfering Anions Using a Heterobimetallic (3d- 4d) MOF with Acidic Pocket*

Chapter || 5 *A Two-Dimensional Cu-Based MOF for Staining of Cellular Nucleus through Fluorescence Imaging and Selective Sorption of Dye Molecules in Aqueous Medium*

Abbreviations

MOC = Metal-organic Compound

MOF = Metal-organic Framework

MOM = Metal-organic Material

DMF = Dimethylformamide

DEF = Diethylformamide

Pyz = pyrazine

BDC = 1,4-benzenedicarboxylic acid

CAM = Chelidamic acid

PAM = Pamoic acid

Bpe = 1,2-bis(4-pyridyl) ethane

dib = 1,4-di(1H-imidazol-1-yl) benzene

Phen = 1,10-phenanthroline

Bpi = 1-([1,1’-biphenyl]-4-yl)-1H-imidazole

PTFE = Polytetrafluroethylene

RT = Room Temperature

PXRD = Powder X-ray Diffraction

SEM = Scanning Electron Microscopy

EDAX/ EDX = Energy Dispersive X-ray analysis

TGA = Thermogravimetric Analysis

IR = Infrared Spectroscopy

FTIR = Fourier Transform-Infra red

BET = Brunauer-Emmett-Teller

UV-vis = Ultraviolet/visible spectroscopy

TCSPC = Time-Correlated Single Photon Counting measurement

LOD = Limit of detection

SV = Stern-Volmer equation

LMCT = Ligand to Metal charge transfer

MLCT = Metal to Ligand charge transfer

MB = Methylene blue

MO = Methyl orange

RhB = Rhodamine B

OG = Orange G

CV = Crystal violet

AO = Acridine orange

CR = Congo red

MV = Methyl violet

DAPI = 4’, 6-di-amidino-2-phenylindole

HCT- 15 = Human colon cancer cell

CCDC = Cambridge Crystallographic Data Center

H_2Pip = diprotonated piperazine

Arg = L- Arginine

His = L- Histidine

Cti = L- Cystine

Cys = L-Cysteine

Met = L-Methionine

Leu = L-Leucine

Ala = L-Alanine

DMEM = Dulbecco’s Modified Eagle Medium

MTT = (3-(4,5-dimethylthiazolyl-2)-2,5-diphenyltetrazolium bromide)

Chapter: 1

Introduction and Literature Survey

1.1 INTRODUCTION

The term, “metal-organic compound” has made itself a broad area in modern coordination chemistry that includes both supramolecular coordination complexes and metal-organic frameworks.[1] The former is a discrete system that comprises metal moieties and multidentate organic ligands. In contrast, the latter is an open framework structure with an infinite network and voids consisting of meal ions or clusters bridged through organic linkers by coordination bonds (see Figure 1.1). Alfred Werner, the father of coordination chemistry, proposed a theory in 1893 to explain the bonding in metal complexes and with this breakthrough invention, the journey of coordination chemistry began.[2] From then on, a substantial increase in coordination chemistry was observed by studying the different properties of novel metal-organic complexes, organometallic complexes, and inorganic polymers.

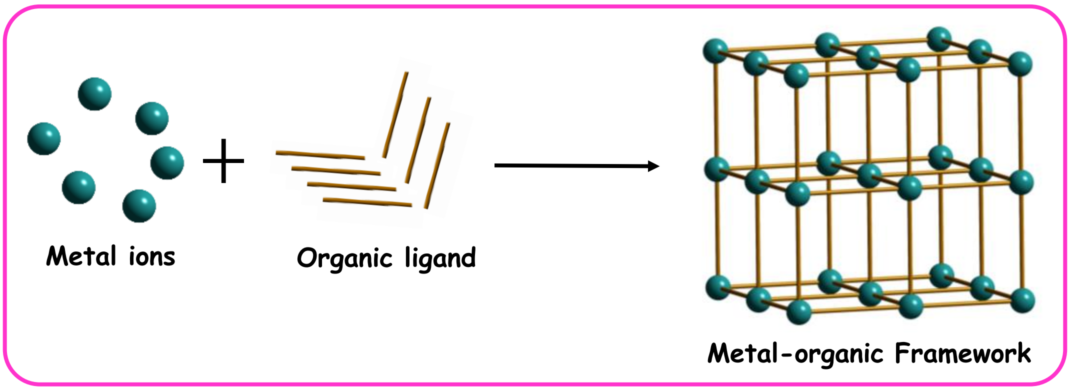

Fig. 1.1 A Schematic representation of a metal-organic framework formed using metal ions and organic ligands.

In 1967, J.C. Bailar first applied the term, coordination polymer.[3] Coordination polymer is nothing but a repeating unit of coordination complexes in one, two, or three dimensions and is comprised of metal and ligands. In 1897, Hofmann and Kuspert for the first time reported the synthesis of a porous coordination polymer (Hofmann’s clathrate).[4] It is synthesized by the addition of $Ni(CN)_2$ into the solution of ammonia and benzene. It has a similar structural element to the Prussian blue and an extended structure bridged by cyanide ligand. After this discovery, scientists planned to synthesize an extended porous 3D network. In 1949, Powell and Rayner discovered Prussian blue, the mixed valent Fe (II) and Fe (III) network structure, the first synthetic coordination polymer, but these types of compounds are too weak to retain their porosity.[5] Then in the meantime, zeolites were invented but it has poor water stability.[6]

Zeolites are crystalline aluminosilicates, which are also porous materials. Although most of the zeolites have pore sizes less than 2 nm, there found a very few natural or synthetic zeolites with large pore sizes.

So, in the late twentieth century, chemists started to discover alternatives to zeolites. Then, various coordination networks were discovered by various scientists, namely, Saito, Robson, Fujita, Zaworotko, and Yaghi from 1959 to 1995 respectively.[7-11] Saito and coworkers discovered the first coordination network with the cationic framework and anions are placed in the pore, having diamondoid topology. Prof. R. Robson and coworkers reported the second coordination polymer, synthesized by using Cu and 2,5-dimethyl-N, N-dicyanoquinonediimine anionic salt. He also discovered a third coordination polymer, synthesized by Cu and 4,4',4",4"' tetracyanotetraphenylmethane. Prof. Fujita and coworkers invented a fourth coordination polymer by using $Cd(NO_3)_2$ and 4,4' bipyridine in a 1:2 ratio in an ethanol medium. The fifth coordination polymer was discovered by Prof. Zaworotko and coworkers. They synthesized SIF-6 by using a Zn metal node and 4,4' bipyridine. The sixth coordination polymer was discovered by Prof. Yaghi and coworkers by using $Cu(NO_3)_2$ and 4,4' bipyridine having the diamond topology. But all these networks were not so stable and frameworks were collapsed due to their charged framework.

Then, for the first time, Prof. Yaghi introduced the "Metal-organic framework" in 1995 but it was a 2D layer structure.[12] He used carboxylate-based organic ligands because metal-carboxylates are more easily crystallizable than metal-oxides. Prof. Yaghi and coworkers reported MOF-1, produced by using copper as a metal node, and 1,3,5-benzene tricarboxylic acid as an organic ligand in pyridine solvent to generate a neutral framework. In 1998- 1999, he reported 3D framework with permanent porosity.[13, 14] MOF-2 was prepared by using zinc acetate, and 1,4-benzenedicarboxylic acid in DMF medium. It has permanent porosity and reversible gas sorption behavior. Then, MOF-5, $[Zn_4O(1,4\text{-bdc})_3(DMF)_8(C_6H_5Cl)]$ (see Figure 1.2) was discovered in 1999 by using Zn(II), 1,4-benzenedicarboxylic acid in DMF or DEF medium at 100°C for 20 hours.[15]

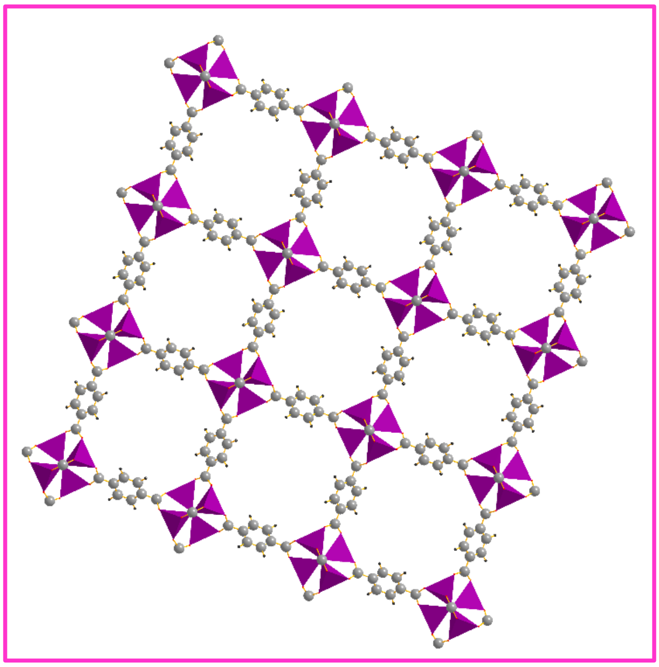

Fig. 1.2 Representation of the MOF-5 framework.

Kitagawa and coworkers reported microporous pyridyl-based MOMs and Yaghi and coworkers reported carboxylate-based porosity.[16] Kitagawa and coworkers discovered pyridyl-based metal-organic material with permanent porosity. These two were milestone discoveries by them.

The term metal-organic framework is suitable for any extended array encompassed of metal centers. Now, in modern MOF chemistry, the only goal of many researchers is to synthesize extremely porous material with a large surface area. Coordination polymers are connected through covalent metal-ligand bonding to form a 1,2 or 3-dimensional framework.[17] Now, there are many similarities between these two important terms, one is MOF and the other is coordination polymer. Coordination polymer can be one-, two- or three-dimensional architecture whereas MOF is a three-dimensional network structure with permanent porosity.

In the year 1960, Pedersen and coworkers reported that small guest molecules can reside in the cavity of the metal-organic compound *via* non-covalent interaction.[18] A variety of coordination complexes can be formed *via* π-π interaction, intramolecular H-bonding, van der Wall forces, and many other weak interactions.

Metal-organic compound chemistry is a broad field due to its versatile applications in many fields like gas storage and separation,[19-27] magnetism,[28-31] catalysis,[32-36] proton conduction,[37-40] energy storage,[41-44] non-linear optics,[45-47] drug delivery,[48-51] supercapacitors,[52-54] sensing,[55-59] live cell imaging[60-62] and dye adsorption.[63-65] Porous materials have drawn much attention due to their large surface area, tunable pore size, various structures, high thermal stability, and many chemical properties.[66-69]

1.2 Metal ions used in Metal-Organic Compounds

For the synthesis of metal-organic compounds, mostly transition metal and lanthanide metals are used. More specifically, these metals are used as acetate, nitrate, sulfate, halide, or phosphate salts. Besides these, very few numbers of alkali or alkaline earth metal-based metal-organic compounds have been reported previously. Furthermore, metal-organic compounds based on metal clusters or secondary building units have also been reported. Generally, metal ion with higher coordination numbers produces three-dimensional structures and with lower coordination number generates one-dimensional or two-dimensional structures.

Recently, mixed metal-organic compounds have drawn much attention due to their many interesting properties.[70, 71] Chen and coworkers reported a mixed metal-organic framework, $[Fe(pyz)Ni(CN)_4]$ for the efficient separation of acetylene and methane.[72] Mortensen *et al.* synthesized four 3d-4f mixed metal-organic framework having similar structures $CuGd_2(BDC)_4$, $CuHo_2(BDC)_4$, $CuEu_2(BDC)_4$, and $CuDy_2(BDC)_4$.[73]

1.3 Organic Linkers Used in Metal-Organic Compounds

There are various kinds of multidentate organic ligands present in literature. These organic linker molecules are used to bridge between metal ions. The two most important types of organic ligands are well known, one is nitrogen donor and the other is oxygen donor ligand. A broad range of heterocyclic nitrogen donor ligands were used in previous literature. Some of them are shown in Figure 1.3. These ligands tend to generate various 1D, 2D, and 3D metal-organic compounds. There is a wide variety of carboxylic acid ligands to produce metal-organic compounds including carboxylate, polycarboxylates, and oxalates. Recently, lots of works reported based on many functional groups substituted aromatic carboxylates. Hydroxyl-functionalized aromatic carboxylates are also very common in this category. In Figure 1.4 some oxygen-donor aromatic carboxylate ligands are shown. Carboxylate ligands coordinate with the metal center in various manners to form different kinds of metal-organic compounds (Figure 1.5).

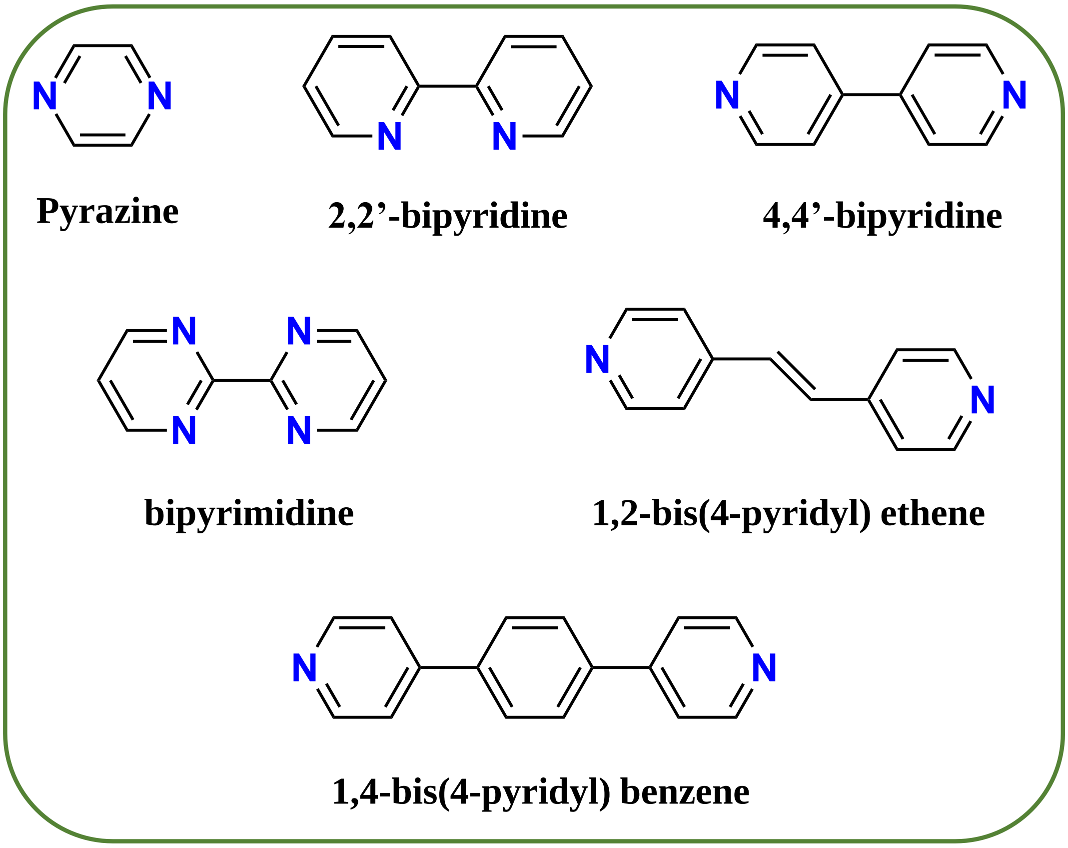

Fig. 1.3 N-donor ligands useful for the preparation of metal-organic compounds.

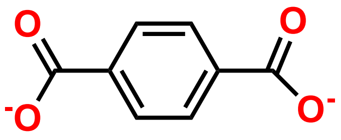

1,4-benzenedicarboxylate

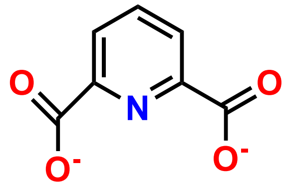

2,6-pyridinedicarboxylate

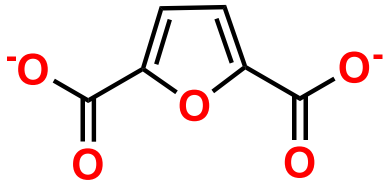

2,5-furandicarboxylate

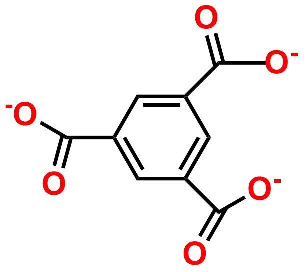

1,3,5-benzenetricarboxylate

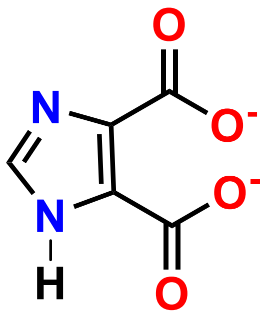

4,5-imidazoledicarboxylate

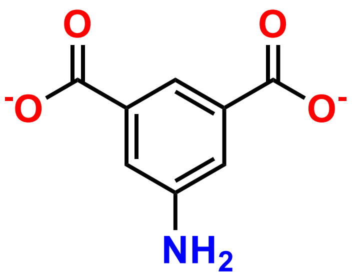

5-aminoisophthalate

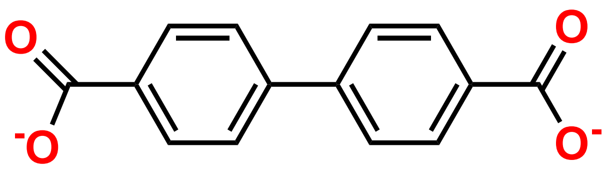

Biphenyl-4,4'-dicarboxylate

Fig. 1.4 O-donor ligands useful for the preparation of metal-organic compounds.

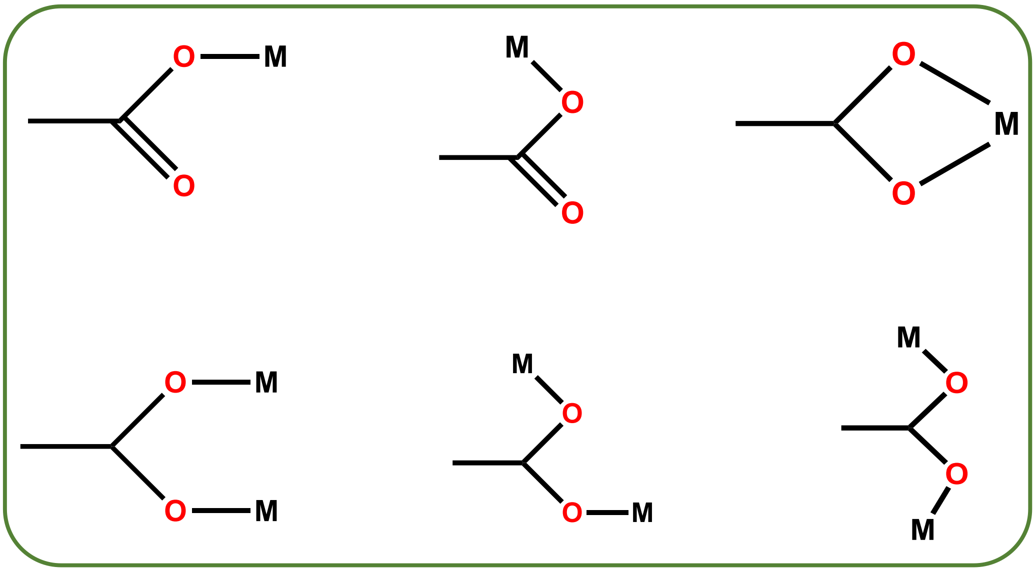

Fig. 1.5 Different modes of carboxylate ions shown in metal-organic compound.

1.3.1 Hydroxyl Functionalized Aromatic carboxylates

Chelidamic acid (CAM), 4-hydroxy-2,6-pyridine dicarboxylic acid has wide used in the field of biochemical field.[74-76] But in the past two decades, it has been a very well-known ligand in coordination chemistry. In 1926, the first work was reported based on CAM.[77] Then after 2002, the crystal structure of this pyridine dicarboxylic acid was determined.[78] Due to the interconversion between the two forms of chelidamic acid i.e. keto and enol form, the hybridization of the N atom can change from sp^2 to sp^3 and vice versa. Therefore, it has lots of use in both medicinal chemistry as well as in coordination chemistry.[79] On the other hand, Pamoic acid i.e. 4,4'-methylenebis (3-hydroxynaphthalene-2-carboxylic acid) is a familiar and cheap laboratory precursor. It has a famous pharmacology background but nowadays it is used as a chemical for industry purposes. The versatility of this ligand is due to: (i) as symmetrical nature, it can act as a bent bridging rod, (ii) the presence of sp^3 carbon makes it more flexible, (iii) the different binding mode of the carboxylate group, (iv) presence of two naphthalene rings allow it for π-π stacking interaction and (v) extended π-conjugation.[80] In this investigation, we have used these two hydroxyl-functionalized carboxylic acids (see Figure 1.6) to synthesize the metal-organic compounds.

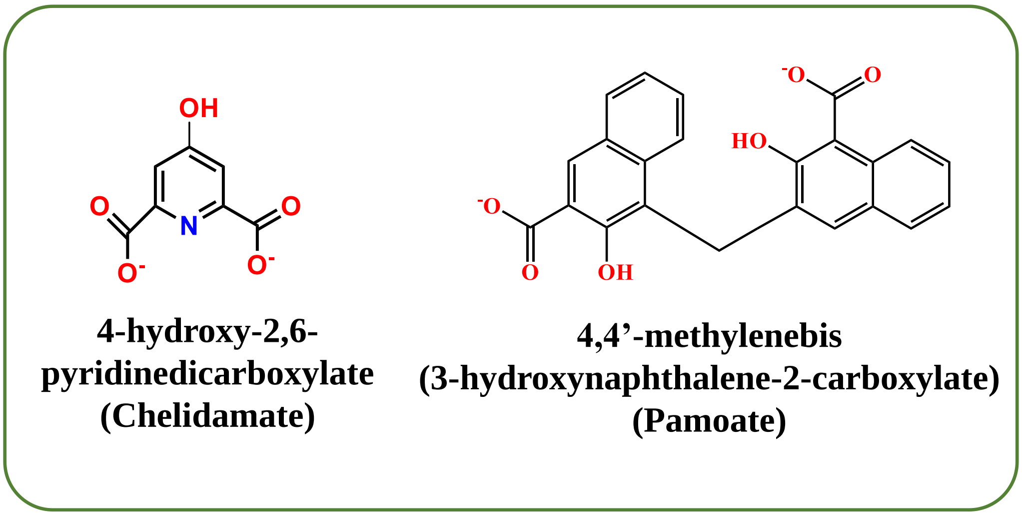

Fig. 1.6 Hydroxyl functionalized aromatic carboxylate used as O-donor ligand.

1.4 Structures of Metal-Organic Compounds

Pyridine rings containing carboxylic acids were very much used in the formation of metal-organic compounds. But this section will concentrate on the use of hydroxyl functionalized pyridine or naphthalene dicarboxylic acid-based metal-organic compounds.

1.4.1 Alkaline earth metal-based metal-organic compounds

Motieiyan *et al.* reported the alkaline earth metal-based metal-organic framework, $[Ba(C_7H_3NO_5)_2(H_2O)_4Ba(H_2O)_3]_n\cdot(2H_2O)_n$, where two independent barium centers are monocapped and bicapped square antiprismatic geometry (see Figure 1.7).[81] This is the first example of an alkaline earth metal-based coordination polymer containing chelidamic acid.

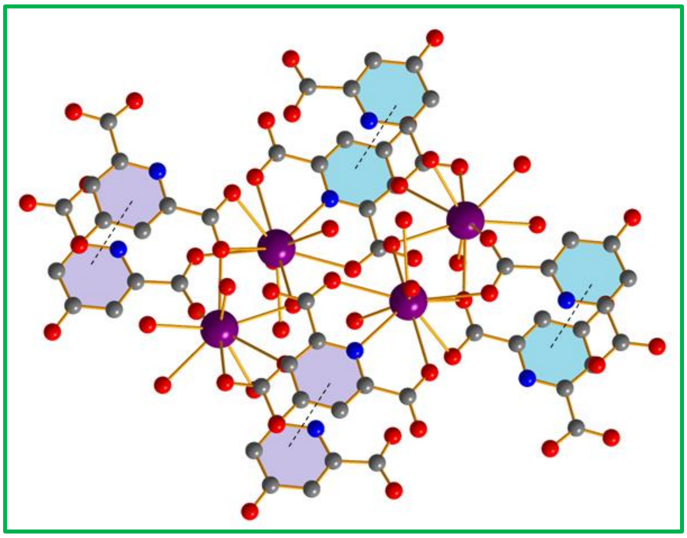

Fig. 1.7 The different coordination environments around Ba centers and π-π stacking interaction.

Koner and coworkers synthesized two metal-organic frameworks, $[Mg(HL)(H_2O)_2]_n$ (**1**) and $[Ca(H_2L)_2]_n$ (**2**), where (H_3L= chelidamic acid) by hydrothermal process. Compound **1** has a 2D structure whereas compound **2** has a 3D structure. Topological analysis of compound 1 revealed that the compound has a 2D net structure with a Schläfli symbol of $\{4^4.6^2\}$ (see Figure 1.8).[82]

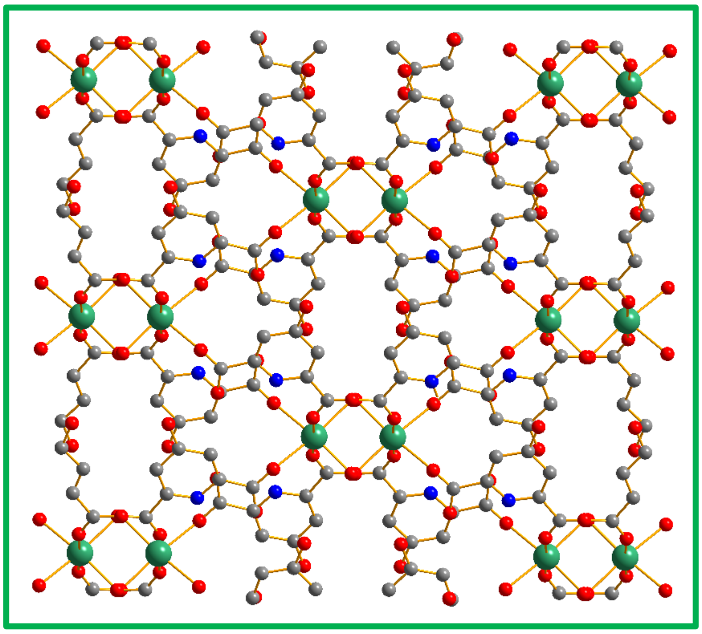

Fig. 1.8 3D framework of $[Ca(H_2L)_2]_n$. Color code: Ca (Green), O (Red), N (Blue) and C (Grey).

1.4.2 Transition metal-based metal-organic compounds

Based on the chelidamic acid, there are various coordination polymers reported. Ghosh *et al.* reported Mn(II) staircase compound, stitched with water cluster to form a three-dimensional MOF, $\{[Mn_2(cda)_2{\cdot}4H_2O]{\cdot}4H_2O\}_n$.[83] This group again reported a Cu-based tubular coordination compound through supramolecular bonding.[84] Two cadmium-based one-dimensional coordination polymers were reported by Chen and coworkers. Both Cd centers have pentagonal bipyramidal geometry.[85] Very recently, Lu *et al.* synthesized a 3D porous metal-organic framework, $(H_3O)[(Mn_4(CAM)_3]{\cdot}H_2O$,1 by hydrothermal technique. The compound has a cage structure (see Figure 1.9). The compound contains a H_3O^+ counterion and by using the metal ion and corresponding ligand, CAM it formed a large cage cavity.[86]

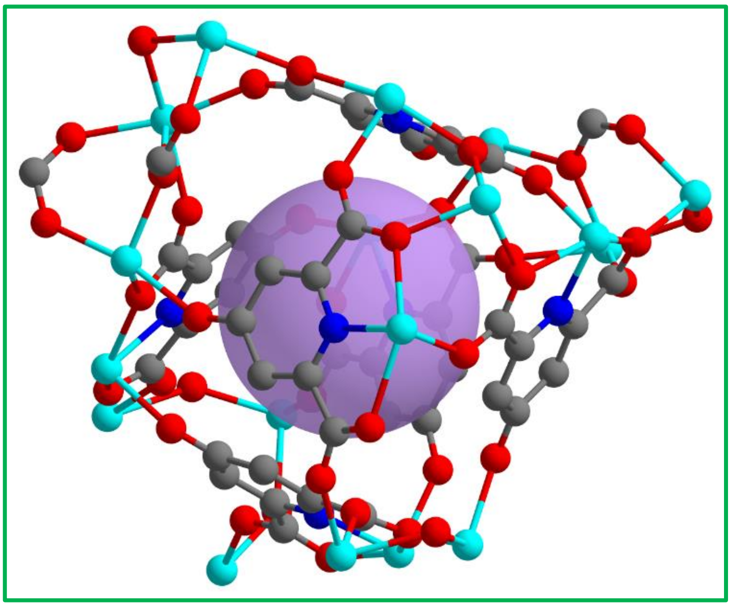

Fig. 1.9 view of $[Mn_{15}]$ coordination cage in the compound. Color code: Mn (Cyan), O (Red), N (Blue), C (Grey) and void space (violet sphere).

Mandal and coworkers synthesized a three-dimensional coordination polymer by using pamoic acid. Topological analysis showed it has five-fold interpenetration with an unimodal 4c net (see Figure 1.10).[87]

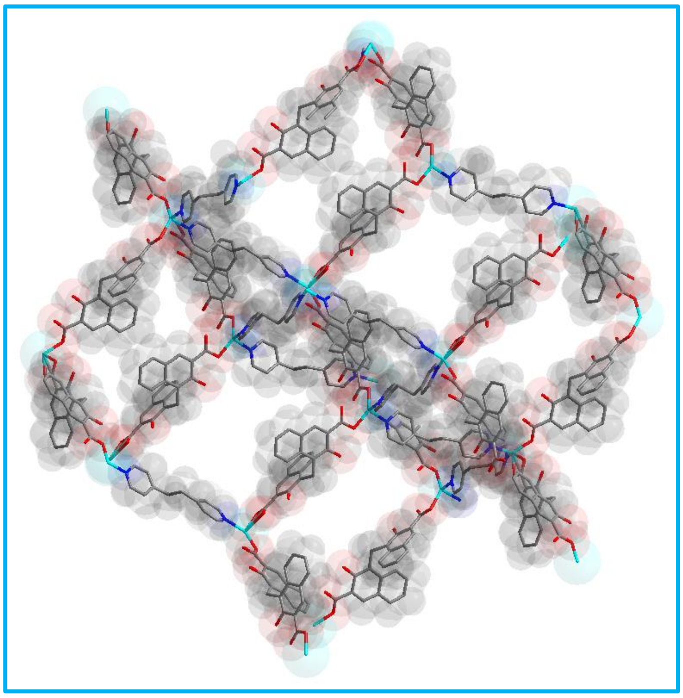

Fig. 1.10 Three-dimensional framework formed by the connectivity among Zn, pamoic acid, and bpe ligand. Color code: Zn (Cyan), O (Red), N (Blue) and C (Grey).

Kaur *et al.* reported a Cd-based metal-organic framework by using 4,4'-bipyridine and pamoic acid by solvothermal technique. Cadmium ions are in distorted pentagonal bipyramidal geometry (see Figure 1.11).[88]

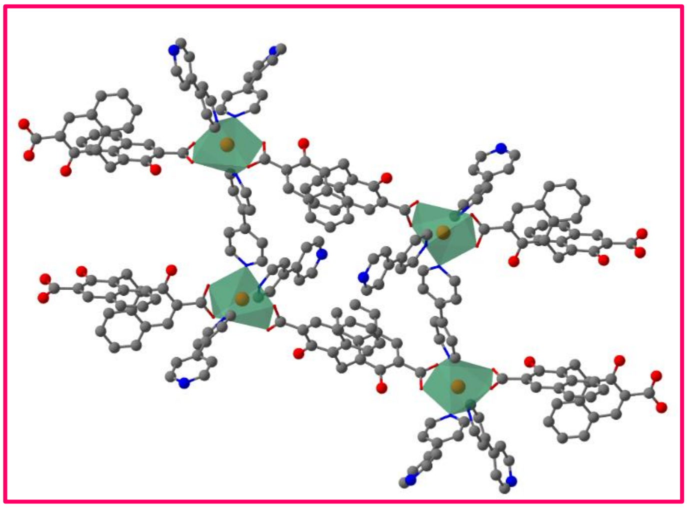

Fig. 1.11 The coordination network of Cd-MOF. Color code: Cd (Green polyhedron), O (Red), N (Blue) and C (Grey).

1.4.3 Lanthanide metal-based metal-organic compounds

Frontera and coworkers synthesized hybrid inorganic-organic assembly from trinuclear lanthanide cluster and keggin type polyoxometalates (see Figure 1.12) having formula $\{Na(H_2O)_3[Ln(HCAM)(H_2O)_3]_3\}^{4+}$, 1 where Ln= La, Ce and Eu.[89]

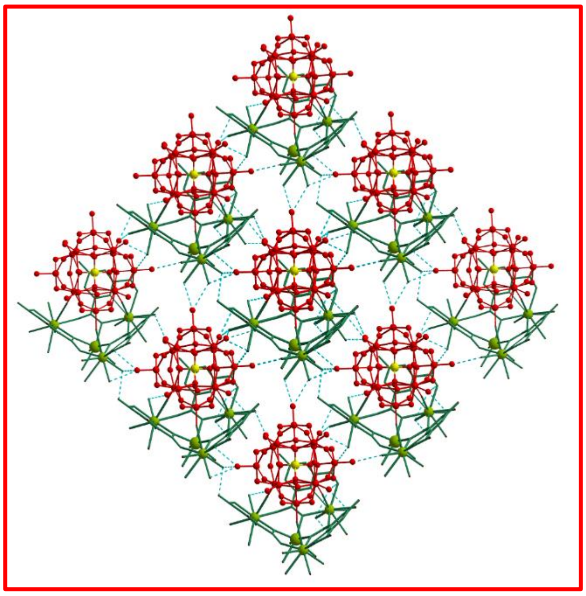

Fig. 1.12 A view of the 3-D supramolecular structure in the compound. Color code: Si (Yellow), Ln (Green), O (Red) and N (Blue).

Xiong *et al.* reported a series of lanthanide-based metal-organic frameworks by using chelidamic acid and 4,4'-bipyridyl ligand.[90] Mani *et al.* synthesized a series of lanthanide-based coordination polymers, $[Ln(C_7H_2NO_5)(H_2O)_3].H_2O$ (Ln = Eu, Gd, Tb, and Dy) by a solvothermal technique using H_2O-DMF in 4:1 ratio.[91] In all the cases lanthanide ions adopted distorted dodecahedron geometry. All the dodecahedron units are connected to form a 2D layer and the two-dimensional layers are connected through H-bonding to get a three-dimensional structure (see Figure 1.13).

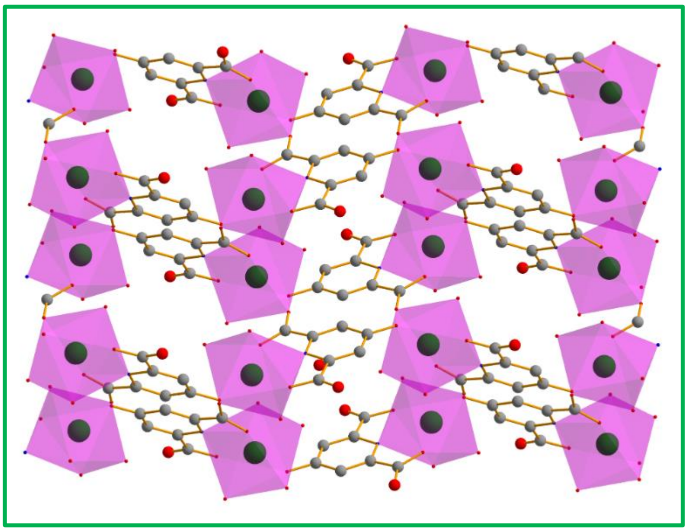

Fig. 1.13 Two-dimensional layer structure of the compound. Color code: Ln (Green), Polyhedron (Magenta)O (Red), N (Blue) and C (Grey).

Shakir and coworkers developed europium-based MOF by using pamoic acid through the solvothermal method. In the structure, there are two DMF molecules and two water molecules (see Figure 1.14).[92]

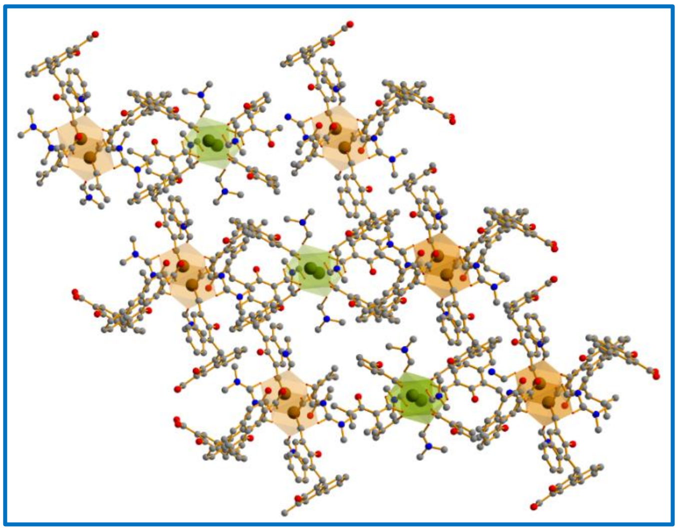

Fig. 1.14 3D representation of the MOF. Color code: Eu (Green & Orange polyhedron), O (Red), N (Blue) and C (Grey).

1.4.4 Mixed metal-based metal-organic compounds

Two 3d-4f (Dy-Mn) coordination polymers were reported with high symmetry (S_6) by Zhao *et al.* The compound has luminescence selectivity towards Mg^{2+}.[93] Huang and coworkers reported a heterobimetallic coordination polymer, $[AgCu_2(C_7H_2NO_5)(C_7H_3NO_5)]_n \cdot 2nH_2O$ with 4^4 topology. The compound showed non-linear optical properties and magnetic properties.[94] Qian *et al.* synthesized a 3d-4f heterobimetallic coordination polymer, $[Tb_2Ni_3(HCAM)_6(H_2O)_{12}]_n$ for the selective recognition of human serum albumin and MnO_4^- anion (see Figure 1.15).[95]

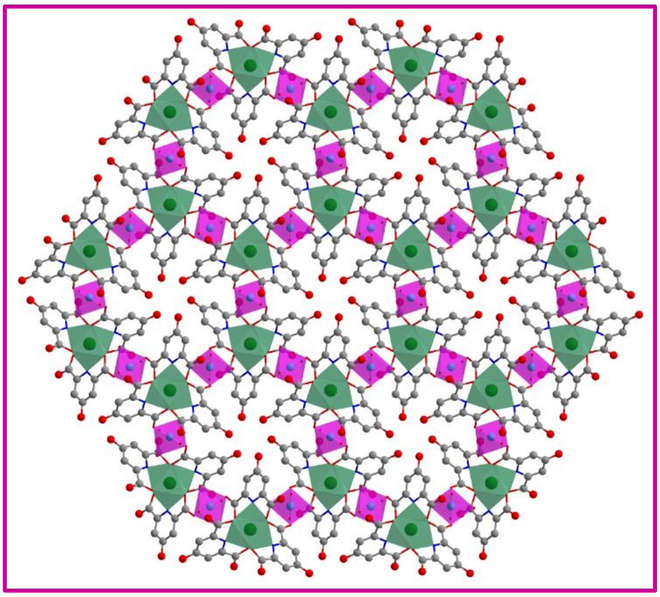

Fig. 1.15 The chelidamate ligands connect with one dimensional zigzag chain to form a hexagonal cycle. Color code: Tb (Green), Ni (Magenta), O (Red), N (Blue) and C (Grey).

Li *et al.* invented a heterometallic MOF, $[(CH_3)_2NH_2][CaEu(CAM)_2(H_2O)_2] \cdot 4H_2O \cdot 4DMF$ (CaEu-CAM) through a hydrothermal synthesis technique.[96] The compound crystallizes in a tetragonal crystal system. Two different channels (see Figure 1.16) are obtained after the formation of a three-dimensional compound.

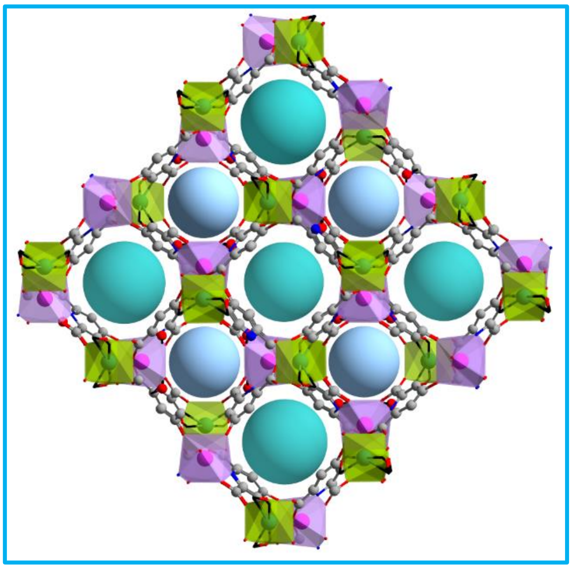

Fig. 1.16 Construction of CaEu-CAM with two different channels. Color code: Eu (Magenta), Ca (Green), O (Red), N (Blue), C (Grey) and Light blue sphere represents void space.

Gao *et al.* developed four iso-reticular heterometallic coordination polymers, $\{[Ln_2(HCAM)_6 M_3(H_2O)_{12}] \cdot nH_2O\}_n$, (where Ln= Ho and Er and M= Mn and Zn) two-dimensional honeycomb type structures (see Figure 1.17).[97]

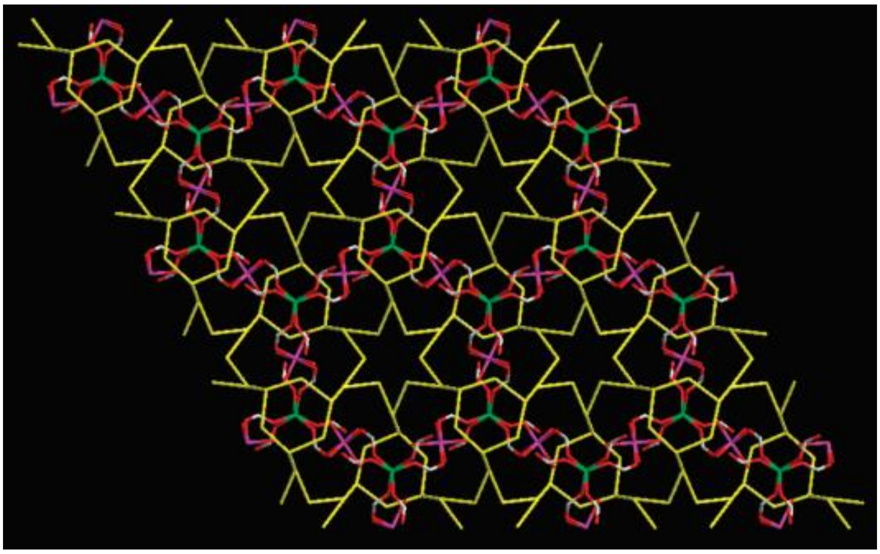

Fig. 1.17 Perspective view showing the interpenetration of the 2D water sheet and 2D coordination layer.[97] Color code: Ho or Er (Green), Mn or Zn (Purple), O (Red), C (White) and water sheet (yellow layer).

1.4.5 Heavy metal-based metal-organic compounds

Yang *et al.* synthesized a series of uranium-organic frameworks having the formula, $UO_2(L_3)(H_2dib)_{0.5}$ (3), $UO_2(L_3)(phen)$ (4), and $UO_2(L_3)_2(Hbpi)_2$ (5). Compound **3** formed a layer structure by combining the UO_7 unit and chelidamate ligand (see Figure 1.18).[98]

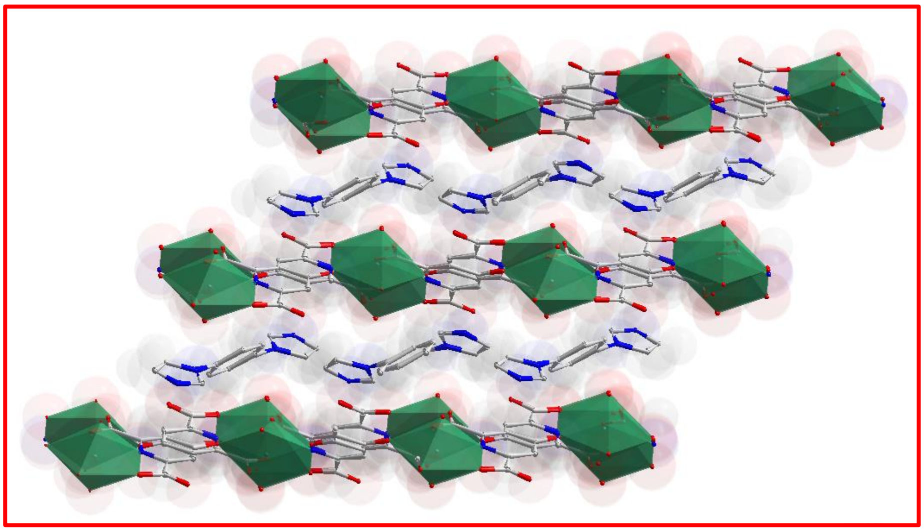

Fig. 1.18 The layered structure of the compound formed by UO_7 units and chelidamate ligand. Color code: U (Green polyhedron), O (Red), N (Blue) and C (Grey). The position of dib molecules in the interlayer space are shown.

1.5 Synthetic Methods for Metal-Organic Compounds

Metal-organic compounds generally appear as a single crystal in the reaction medium and so these compounds require some crystal growth procedures so that one can get a suitable single crystal for the X-ray diffraction studies. Over three decades numerous synthetic procedures have been applied to produce these metal-organic compounds. All these methods depend upon various factors such as temperature, reagents concentration and mole ratio, types of solvents, pH of the reaction medium, duration of the reaction, etc. All these factors are very important for the generation of the crystals and also the purity of the compound. Some of the methods for the synthesis of metal-organic compounds are as solvothermal method, microwave synthesis, sonochemical method, mechanochemical synthesis, and slow layer diffusion technique. We have employed solvothermal and slow-layer diffusion techniques in our studies. These two methods are discussed below.

1.5.1 Solvothermal Synthesis

For the preparation of metal-organic compounds, the "solvothermal *method"* is the most frequently used process because it is a facile technique that can produce substances with miscellaneous morphologies. The term solvothermal is used for whatever the composition of the solvent but hydrothermal synthesis is specific when we use water as a reaction medium. This particular method is suitable for very slightly soluble materials. For the compounds with low solubility and high melting point, a substance is added which is known as a "*mineralizer*". It is very important to choose a perfect solvent for the solvothermal method. The solvents generally used for this method are dimethyl formamide (DMF), dimethyl sulfoxide (DMSO), acetonitrile, methanol, ethanol and so many others. For the preparation of metal-organic compounds by this method, three fundamental things must be followed which are metal ions, the polydentate ligand, and solvent. Usually, the heterogeneous reaction mixture is heated above the boiling point of the particular solvent and the high temperature pressure also reaches much. As a result, a supercritical fluid is generated in which most of the component's dissolve. In solid state chemistry for the discussion of crystal growth technique, Rabenau and Laudise first applied the hydrothermal technique.

There are several advantages in the hydrothermal technique over the other methods which are discussed here. (i) One can exactly regulate the size and shape of the product, (ii) the energy consumption for this process is low, (iii) this method does not use any harmful substances, and (iv) the crystallinity and morphology of the compound are also good. Recently, Zhang and coworkers reviewed the hydrothermal synthesis method for different important material synthesis.[99]

Water, a green solvent is very important for the solvothermal method in terms of dielectric constant. With rising temperature, the dielectric constant of water decreases and increases with rising pressure.

Since high pressure is produced within the reaction vessel, the use of an autoclave is usually necessary. Previously, the autoclave was made of steel with noble metal lining. Then Herdtweck described the use of a new material, Teflon for the reaction vessel. Under pressure Teflon becomes more porous, so PTFE is used. These autoclaves are now also termed as digestion bombs (see Figure 1.19). Speed and Filice also describe the use of quartz glass ampoules.

Fig. 1.19 (a) The external view of the autoclave used for the synthesis described in this thesis with Teflon inserts used as digestion bombs; (b) Different parts of the autoclave.

1.5.2 Slow Layer Diffusion Method

Another effective method for the synthesis of metal-organic compounds is the slow layer diffusion technique. In this technique, two different solvents are used for the layering. One solvent is added to the other one to form a distinguishable layer. Generally, a less dense solvent forms a layer on the top, and highly dense solvent is on the below. In this technique, a capped glass tube or sometimes NMR tubes are used because as the surface area decreases good layer forms. At first metal ions and different ligands are taken into different beakers and with the suitable solvent they form a homogeneous mixture. The metal ion is usually taken in a polar solvent like water and the organic ligands in a non-polar solvent. Then first with the help of a glass syringe the metal solution is placed in the bottom of the glass tube. Then very carefully another solution of organic ligand is layered upon the first layer. Then the glass tube is capped and kept in a stable condition with undisturbed so that crystal growth is not hampered. This process takes several weeks to appear crystals. The crystal appears in the wall of the tube. This process is usually done at room temperature (see Figure 1.20). Sometimes between these two layers, one can use a buffer solution of a 1:1 mixture of two different solvents. By using the buffer solution, the diffusion process is slower and crystallization becomes more favorable. This phenomenon utilizes the surface tension between the two layers to generate new crystals.

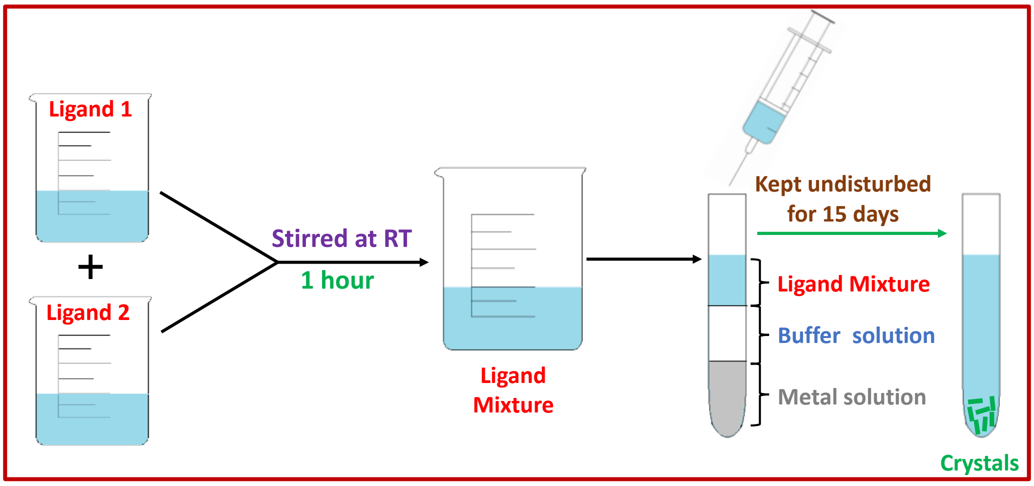

Fig. 1.20 Schematic illustration of synthesis procedure *via* slow layer diffusion method.

1.6 Characterization Techniques

1.6.1 Powder X-ray Diffraction (PXRD)

In the characterization technique, powder X-ray diffraction is a very essential tool to check the purity of the metal-organic compound. After getting the crystal form of the compound it is the first duty to measure the PXRD pattern of the compound. Moreover, many other information we can get from a PXRD pattern. There are two important factors to index the powder pattern the peak position (2θ) and full width half maximum (FWHM). For the structural analysis, precise relative intensities are important. For the fruitful measurement of relative peak intensities, we have to check three parameters: (i) divergence slit, (ii) sample thickness and (iii) proper orientation. There is an assumption for many powder diffraction analyses that in the sample there are several crystallites.

To prove the purity of the metal-organic compounds, the experimentally obtained PXRD pattern is matched with the simulated pattern obtained from the single crystal X-ray diffraction instrument. If the experimental data matches well with the simulated powder X-ray diffraction data, then the metal-organic compound is formed in the pure phase. Any small changes in the peak positions prove that there may be changes in the structure of the compound.

In the thesis all the described compounds' powder X-ray patterns were recorded on Bruker D8 discover instrument using a flat plate sample holder. The X-ray used is monochromatic and based on Cu Kα radiation. All the measurements were done at room temperature. Liquid N_2-cooled solid state detectors are used in this instrument. In most cases, the powder XRD patterns indicate that the product has a pure phase and a new material.

1.6.2 Scanning Electron Microscopy (SEM)

A scanning electron microscope is a type of electron microscope that uses a beam of electrons to scan the surface of metal-organic compounds. The beam of electrons is generated by a tungsten filament or a field emission gun. Both the tomography and morphology of a metal-organic compound can be measured by scanning electron microscope. The scanning electron microscope utilizes the emitted electrons with high energy to determine the size and shape of any specimen. There is an interaction between the emitted electrons and the atoms present in the sample then generates different signals that contain the data about the samples. First, the crystals are powdered well with the help of mortar and pestle, and then either it is directly mounted on the glass slide or sometimes drop cast on a silicon wafer. In the present investigations, the SEM experiment was recorded using a Zeiss Gemini SEM 45 field emission scanning electron microscope.

1.6.3 Determination of Elemental Composition

To know about the chemical composition of a sample researcher carried out the Energy dispersive X-ray analysis. This technique is applied to identify the ratios between the different elements present in the composite. The experiment was carried out using a scanning electron microscope, equipped with a spectrometer. In the present study, the energy dispersive X-ray analysis (EDAX) was carried out on an EDAX, QUANTA 200. Since the organic ligands, which are one of the main building units of the metal-organic compound, contain elements like C, H, N, the determination of these elements must require the CHN analysis. Practically, C, H, and N analyses are carried out using an elemental micro-analysis instrument.

1.6.4 Thermogravimetric Analysis (TGA)

One of the important characterization techniques for the metal-organic compounds that is often used is thermogravimetric analysis (TGA). This technique measures the thermal stability of the compound. The ultimate changes in physical and chemical properties of a material are measured concerning temperature (with constant heating rate) and time. There is a continuous flow of nitrogen gas at a flow of 20 ml min^{-1}. The experiment was performed in the temperature range between 30-800° C with a heating rate of 20° C/min. From the raw data, we have to plot the TGA graph and from the plotted data we have obtained the number of water molecules present in the compound and also the temperature at which the decomposition occurs. The weight loss can occur due to many reasons like the release of lattice water molecules, the removal of coordinated water molecules, and detachment of any other species. In the present investigation, TGA analysis was done by using the Perkin-Elmer instrument STA 6000 and the Perkin-Elmer Diamond instrument (STA 6000).

1.6.5 Infrared Spectroscopy (IR)

The information about the different kinds of functional groups present in the metal-organic compounds can be obtained from the IR studies. It is the technique to measure the interaction of infrared radiation with the substance by absorption, emission, or reflection. This spectroscopic technique gives information about the molecular level vibration. In this technique, the KBr palette is often used for the investigation of the stretching and bending of the compound. The wave number of IR bands depends on the coordination environment present in the compound. Two main drawbacks detected in IR spectroscopic studies are (i) some particular species can lead to broad bands destroying other specific bands that happen in proximity and (ii) two or more functional groups present within a compound can give rise to vibrational bands in the same region of frequencies making their discrepancy almost impossible. The IR spectral studies of the samples were recorded on Nicolet Magna IR 750 series-II FTIR- spectrophotometer in the solid state. IR spectroscopic measurements are also done in the presence of different analytes to check any spectral band change in the main compound. To do this experiment the powdered form of the compound was soaked into the aqueous solution of any analyte for 24 h and dried, then an IR spectroscopy experiment was performed.

1.6.6 Nitrogen Gas Adsorption-Desorption (BET) Experiment

Nowadays this technique is very useful and mandatory to determine the pore size distribution and surface area of a compound. The nitrogen gas adsorption-desorption isotherm can be produced at liquid nitrogen temperature using an adsorption analyzer. The isotherm exhibits a hysteresis loop at a relative pressure p/p_0. The right degassing procedure is very important for this experiment. In this method, it is assumed that a statistical film is formed on the surface of the material. It is a multilayer adsorption of a gas on the surface of the material. This technique is for the adsorption of gas molecules in the solid surface. This method usually requires the types of gas molecules that do not interact with the compound. Generally, nitrogen gas is used for this experiment. After obtaining the raw data, a plot of total gas uptake *vs* p/p_0 has to be done. In the present study, nitrogen gas adsorption-desorption of the sample (BET experiment) was carried out using Autosorb iQ2, Quantachrome Instruments, USA.

1.6.7 UV-visible Spectroscopy (UV-vis)

UV-visible spectroscopy is a method in which interaction between UV light and the metal-organic compound occurs to characterize the sample. When the light is passed through a metal-organic compound, there is a vibration within the molecule so that the resulting spectra are observed. The wavelength at which the maximum absorption occurs by the molecule is called the absorption maximum. This technique uses electromagnetic radiation. Usually, tungsten filament is used for this experiment. The experiment is carried out within the wavelength region 200-800 nm. The detector used in this experiment is usually a photomultiplier tube. The electronic transition arises due to the different transitions in the bonding ligand such as $n \rightarrow \pi^*$ or $\pi \rightarrow \pi^*$ and also ligand to metal charge transfer. For the characterization of different d-d transitions in various transition metal ions and in the case of rare-earth elements the f-f transition in the visible region is useful. To calculate the band gap UV-visible spectroscopy is also useful.

Recently, dye sorption studies have also been done by using metal-organic compounds. Dye sorption in the surface and pore of a metal-organic compound were also studied through the UV-visible spectroscopic studies. In the present study, the UV-visible absorption spectroscopic studies were carried out in the SHIMADZU UV-1900i spectrophotometer and SHIMADZU UV 3101PC spectrophotometer instrument.

1.6.8 Photoluminescence Spectroscopy

For studying the luminescence nature of metal-organic compounds photoluminescence spectroscopy is used. It is a non-destructive optical technique that is used for the identification and characterization of a very minute amount of sample by exciting the sample with ultraviolet light. Since the aromatic organic ligand shows the intra-ligand transitions, most of the metal-organic compounds also possess this type of transition. For the lanthanide-based metal-organic compound ligand sensitized metal-centered luminescence has been detected. For the photoluminescence spectroscopic studies, the excited wavelength is fixed and we get the emission wavelength over a wide region. In the case of excitation spectroscopy, the emission wavelength is fixed and the excitation wavelength is scanned. The luminescence graph is obtained by plotting the luminescence intensity to the wavelength. Through the interaction between the metal-organic compound and the analyte, different parameters may change such as intensity, anisotropy, lifetime, etc. By changing different parameters, we can recognize different analytes.

In a spectrofluorometer, there is a light source which passes through the monochromator. When the sample is getting excited with the excitation wavelength luminescence is emitted in all directions. The detector is placed at a 90° angle to the light source to minimize the risk of the incident light directly on the detector and to eliminate any interruption of the transmitted excited light. Another monochromator is placed before the detector. The detector sends the signal to the desktop, and desktop software alters the signal to the equivalent luminescence intensity and is plotted against the wavelength found from the collecting monochromator. In the present investigation, the luminescence experiment was performed by using a Hitachi F-7100 spectrofluorometer and Horiba Fluoromax- 4 spectrofluorometer.

1.6.9 Time-Correlated Single Photon Counting (TCSPC) Measurements

For the fluorophore molecules luminescence lifetime measurement is an important tool. The lifetime is in the order of nanoseconds, microseconds, and milliseconds. Fluorescence and phosphorescence lifetimes vary from compound to compound. In contrast to steady-state luminescence studies, we can get much clearer information about the photophysical studies from the excited state luminescence spectroscopy. To confirm the molecular level interaction luminescence lifetime study is more accurate.

By fixing the excitation wavelength and emission wavelength, the luminescence lifetime decay profile is obtained. The decay curves were fitted in a mono, bi, or tri-exponential manner. In the case of the quenching phenomenon, from the lifetime values one can decide whether the quenching is static or dynamic. In the present investigation, the time-correlated single photon counting (TCSPC) measurements were done at room temperature in different solvents using the HORIBA Jobin-Yvon instrument in the nanosecond time domain.

1.6.10 Cell Culture and Fluorescence Microscopic Studies

Cell imaging is a microscopic technique with which one can monitor the cell physiology. It is used to detect and analyze macromolecules and organelles. It is used to study the spatial arrangement of biomolecules within the cell. To study living cells over some time live cell imaging uses time-lapse microscopy. In the present investigation, HeLa cells are cultured. Fluorescence microscopy images were captured using a fluorescence microscope equipped with a 60× and 100× oil plan apochromatic objective. Fluorescence microscopic images were captured using an Olympus IX71 inverted fluorescence microscope.

1.6.11 Single Crystal Structure Determination

A perfect single crystal was selected under a microscope and glued cautiously to a thin glass fiber. We have carried out the single crystal XRD experiment using Bruker D8 Quest machine at 293(2) K. The X-ray generator was operated at 1 mA and 50 kV using Mo Kα having λ=0.71073Å radiation. With ω scan width of 0.5º data were acquired. By keeping the sample-to-detector distance constant at 6.03 cm, a total of 408 frames were collected in three different settings of φ (0, 90, 180º) and the detector position (2θ) fixed at -25º. Using an APEX3 program the final data sets were reduced, while for the integration of diffraction profiles a SAINTPLUS[100] The program was used. A SADABS program[101] was employed to carry out the absorption correction (multi-scan). The structure was initially solved by SIR 92,[102] and then we again used the full matrix least-square method (SHELXL-2016[103]), which is present in the WinGx suit of programs (Version 1.63.04a).[104, 105] All the non-hydrogen atoms from Fourier maps are effectively located and at the final cycles, we have refined them with anisotropic displacement parameters. Finally, all the hydrogen atoms are fixed at premeditated positions and comprised in the refinement procedure using the riding model accompanied with isotropic thermal parameters.

1.7 Properties of Metal-organic Compounds

1.7.1 Photoluminescence Property

Photoluminescence is an important property of the metal-organic compound. By absorbing some light, a compound gets excited and stays in the excited state for sometimes and then comes back to the ground state through radiative as well as non-radiative pathways. To get a deeper knowledge of the whole luminescence process we have to know the Jablonski diagram (see Figure 1.21).

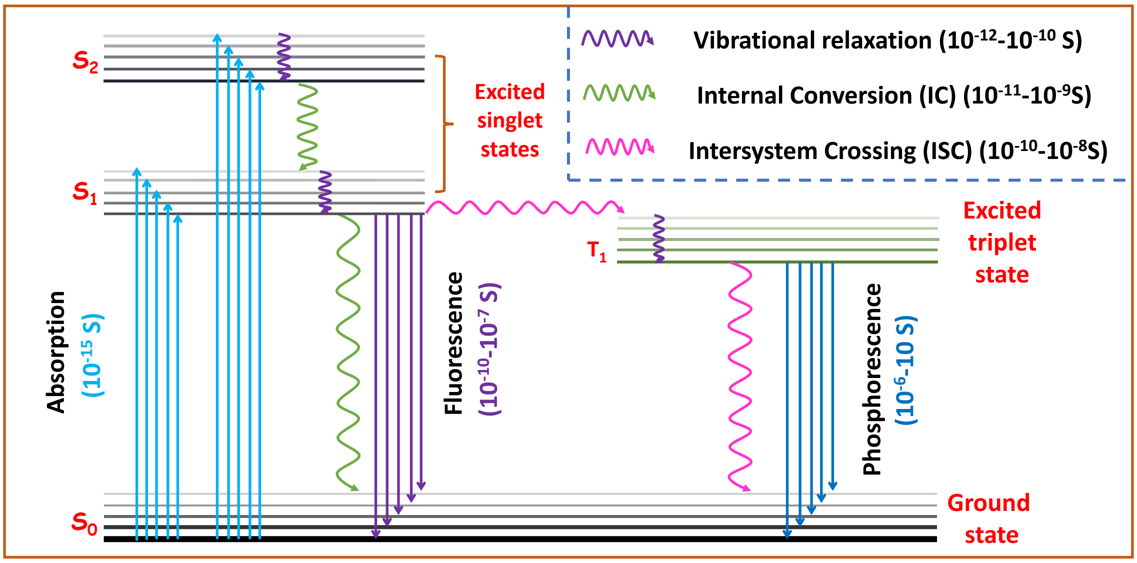

Fig. 1.21 Schematic representation of Jablonski Diagram.

By varying the structure and concentration of the compound, the photoluminescence spectra of the compound change as it is a very sensitive experiment. Since metal-organic compounds contain a variety of metal ions and organic ligands along with pores within them, it has a long range of options to adjust their photoluminescence properties. Photoluminescence spectroscopy is also used to detect whether the process is fluorescence or phosphorescence depend upon the concept of spin state. Due to the inherent structure and property relationship and the biocompatible structural building block, it is of great significance for metal-organic compounds to play a huge role in the field of sensitization. The photoluminescence property of metal-organic compounds mainly lies in the synthetic pathway and their huge usefulness in sensing. The luminescence-based metal-organic compound has versatile applications in various areas such as imaging, lighting, solar light harvesting, and sensing. The main reason behind the luminescence phenomenon shown by the metal-organic compound is due to two important factors: (i) the extended π conjugated system present in the aromatic bridging ligand and (ii) the metal ions or clusters including lanthanides and some transition metals also have strong luminescence. Moreover, the presence of some guest molecules also gives strong emission. In the luminescence phenomenon, there is sometimes a turn-on in luminescence, or sometimes quenching in intensity may occur. Both these phenomena happen due to some molecular-level interaction between the guest analytes and the host framework compound. There are two types of luminescence quenching such as static quenching and dynamic quenching. Dynamic quenching is also known as collisional quenching. Dynamic quenching constant is determined by Stern- Volmer equations,

$$\frac{I_0}{I} = K_D[Q] + 1$$

Where, I_0 and I are the initial and final luminescence intensities respectively, K_D is the stern-volmer quenching constant and [Q] is the molar concentration of the quencher. The time-resolved measurements can separate these two quenching mechanisms. In case of static quenching, life time decay value is constant before and after addition of the analytes but for dynamic quenching life time value is different by the incremental addition of the analyte. Limit of detection (LOD) is another important parameter in sensing. In sensing, LOD is the lowest concentration that can be detected through experiment. The limit of detection (LOD) for the analyte was calculated using the equation, LOD= $3\sigma/m$, where σ = standard deviation of blank determination and m = slope of the linear curve plotted at a lower concentration for LOD measurements. Sensing, by using a metal-organic compound is very effective because of the several interaction sites present in the compound. The luminescence of metal-organic compounds arises due to several reasons: ligand-to-metal charge transfer, ligand-to-ligand charge transfer, metal-to-metal charge transfer, metal-to-ligand charge transfer as well as guest-sensitized emission. In the case of the non-lanthanoid systems, the emission originates from the $\pi^* \rightarrow \pi$ and $\pi^* \rightarrow n$ transitions of aromatic ligands. For rare-earth elements, ligand-sensitized metal-centered emission is generally observed. The lanthanide-based metal-organic compounds show unique emissions because of large stokes shift and very high lifetime values. In the case of lanthanide elements, first, the ligand absorbs energy from the UV-visible range and goes to the excited state of the ligand and then from the excited state *via* intersystem crossing transfers in the excited state of the metal and then we observe metal-centered luminescence (see Figure 1.22).

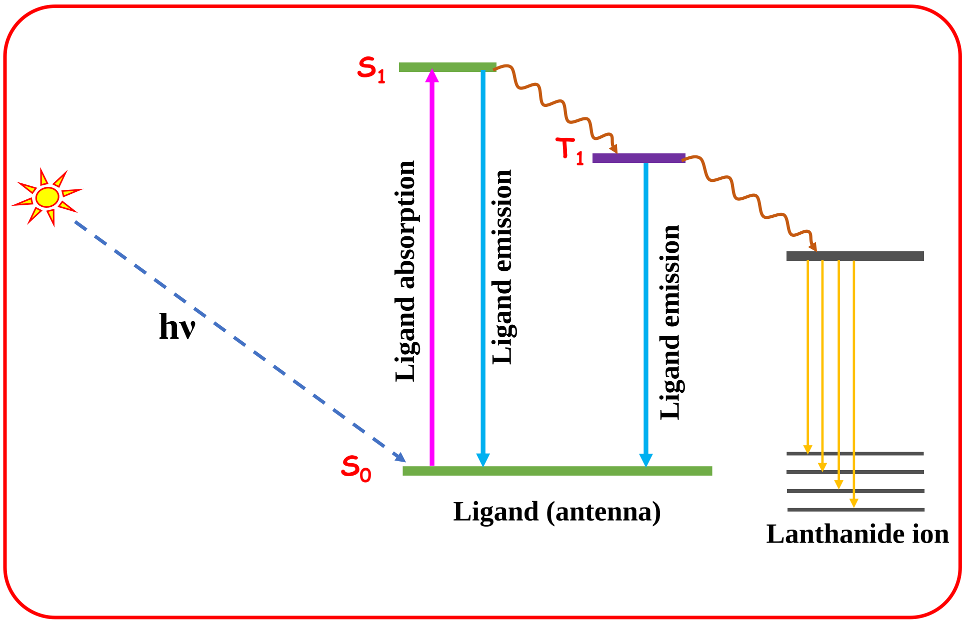

Fig. 1.22 Schematic diagram of excited state processes in lanthanide-organic frameworks.

The effectiveness of lanthanide emission also depends upon the energy level matching between the metal ion and ligand. Several reasons have attracted the sensing mechanism of luminescent metal-organic frameworks such as Förster resonance energy transfer (FRET), photo-induced electron transfer (PET), intramolecular charge transfer (ICT), and excited state intramolecular proton transfer (ESIPT). In the case of lanthanides, there are three types of transitions available such as sharp 4f-4f transition, broad 4f- 5d, and broad charge transfer transition (LMCT and MLCT). Among these transitions, the 4f-4f transitions are Laporte forbidden whereas 4f-5d and charge transfer transitions are Laporte-allowed. The emission bands found for Eu^{3+} ions at around 592, 615, 650, and 693 nm can be assigned to the $^5D_0 \rightarrow {}^7F_1$, $^5D_0 \rightarrow {}^7F_2$, $^5D_0 \rightarrow {}^7F_3$, and $^5D_0 \rightarrow {}^7F_4$ transitions, respectively, and the emission bands found for Tb^{3+} ions at around 491, 545, 585, and 623 nm can be assigned to the $^5D_4 \rightarrow {}^7F_6$, $^5D_4 \rightarrow {}^7F_5$, $^5D_4 \rightarrow {}^7F_4$, and $^5D_4 \rightarrow {}^7F_3$ transitions respectively (see Figure 1.23).

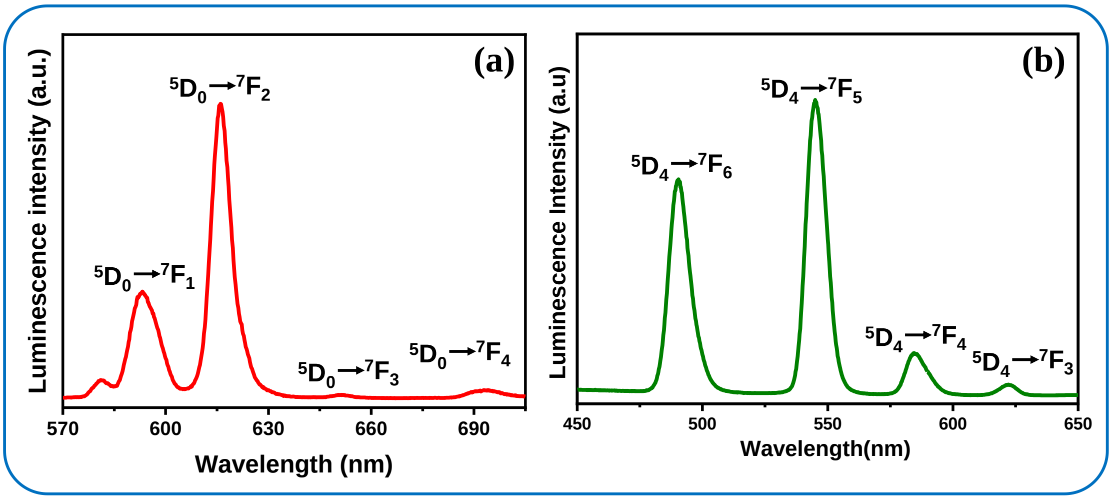

Fig. 1.23 (a) The emission spectra and corresponding emission bands observed in Eu-based MOF. (b) The emission spectra and corresponding emission bands observed in Tb-based MOF.

1.7.2 Dye Sorption

Metal-organic compounds have always been one of the most useful materials in coordination chemistry. In every aspect, it has shown its versatility due to its robust structure and porous open framework. In past decades, water pollution seems to be a huge headache for living organisms. Water is polluted through several factors, among them one of the worst is the organic dye compound. The common well-known dyes include methylene blue, methyl orange, rhodamine B, and orange G, which are continuously damaging the water quality. So, wastewater treatment is of utmost importance. In this regard, the metal-organic compound is highly needed due to their structure-activity relationship.[106] The factors that affect the dye sorption phenomena are: (i) both the materials and the particular dye possess any kind of charge, (ii) presence of various types of functional groups, (iii) nature of porosity, (iv) effect of shape of the pore, (v) different types of interaction, (vi) Dye adsorption kinetics, (vii) time of contact and (viii) temperature of reaction.[107-110]

There is a possibility of more than one interaction that affects the dye sorption process. The types of interactions are as follows: electrostatic interaction, acid-base interaction, hydrogen-bonded interaction, π-π interaction, hydrophobic interaction, ion exchange, and so on.[111-113] There is an affinity of anionic framework towards the cationic dyes. Particularly in this section, many reports are there in the literature.[114-122]

Zheng and coworkers reported a highly porous nanotubular anionic compound, capable of cationic dye removal. The adsorption capacity for the MB, CV, and RhB are 455.6, 847.4, and 751.8 mg g^{-1} respectively. They have also shown the separation of selective dye from the mixture of dyes. The dye sorption mechanism lies in the ion exchange, H-bonding, and π-π interaction. An anionic indium-organic framework, synthesized by Huang *et al.*, possesses a honeycomb-type hexagonal and trapezoid type channel. They have investigated the MB dye removal phenomenon by ion exchange as well as π-π interaction. MB dye separation over the other dye, good recyclability and dye reversibility for adsorption-desorption cycles were shown by the researchers. Anionic dye sorption by cationic framework has also drawn some attention in the literature.[123-128] Zhang *et al.* synthesized a highly porous nanotubular cationic MOF which has the anionic dye removal ability. The framework is hydrolytically stable in a wide pH range. The framework has the ability to adsorb a variety of anionic dye namely, AO, MO, MeB, CR and RhB. The adsorption efficiencies are also very high. It has proven that the experimental data were best fitted in Langmuir adsorption isotherm and follows pseudo second order kinetics. Dye separation experiments were also done. In case of MO, the dye releasing experiment were done in aqueous sodium nitrate solution but it was failed in case of RhB. So, it proved that the dye sorption phenomenon was due to the strong host-guest interaction and ion exchange phenomenon. Shahid *et al.* investigated two cationic MOF, which were effective in dye removal processes for both cationic dye (MB) as well as anionic dye (MO). Since both the MOFs have π electron rich organic ligand, so there was a possibility of cation-anion π interaction. Adsorption of dye molecules through the neutral framework is possible due to the porous framework structure with the size and shape selective adsorption and host-guest interaction.[63, 129-137] Recently, Suresh and coworkers reported pillared-layered zinc-based neutral MOF for the investigation on dye removal ability towards MB, MV, MO and RhB. Through the column chromatographic method dye separation experiments were done. The framework has the recyclability up to six cycles and efficient dye removal in methanol solution. The sorption mechanism was explained through the electrostatic and π-π interaction between the framework host and dye guest molecules. A schematic representation of visual color change of liquid phase dye adsorption was shown in Figure 1.24.

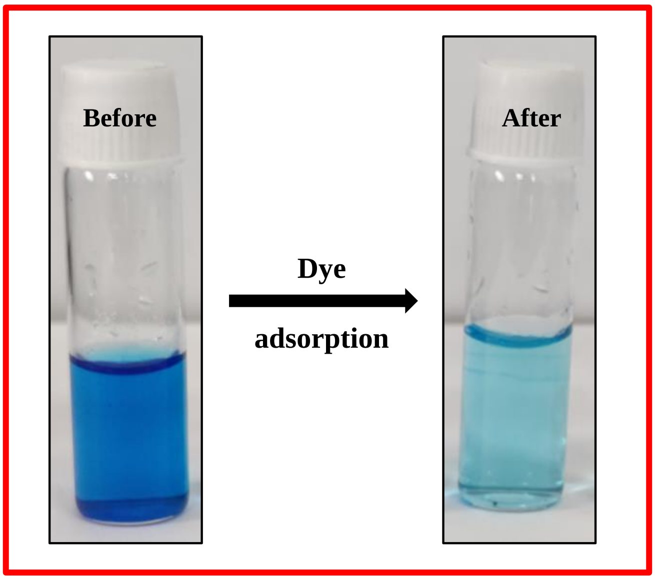

Fig. 1.24 visual color change in liquid phase after dye adsorption.

1.7.3 Fluorescence Imaging

Recently, cell imaging is an emerging field that helps us to detect and diagnose the diseases occurring in live cells. Nowadays it is an innovative idea for disease treatment. In living organisms, to investigate any biological processes, fluorescence imaging is a noninvasive imaging technique. Cell imaging is done in various manner but fluorescence-based cell imaging is a cutting-edge technology in recent times due to its high sensitivity. Live cell imaging through a metal-organic framework is due to their luminescence performance. In the past decades, various reports have been made on live cell imaging through fluorescence technique.[138-144] It is compulsory to ensure that the synthesized compound must be non-poisonous MOFs because every biological operation such as intracellular cell imaging must be successful.[145] In this regard, MOF formation by biologically active metal is very necessary.[146] Bioactive metal ions such as Zn^{2+}, Ca^{2+} or Fe^{2+}/ Fe^{3+} are the great choices of metal ions.[147] The stability of the framework with respect to the degradation are highly dependent on the choice of the ligands. Since MOFs can undergo modification like in situ or post-synthetic modification.[148] The broad inner pore size and flexible nature of MOFs made them successful in the field of cell imaging. In literature, non-toxic MOFs are preferred over the toxic ones. Different types of post-synthetic modification on metal-organic compounds also helps to high cellular activity. Cell imaging is a very useful method to study the spatial ordering in living cells. Live cell fluorescence microscopy is an important tool by which much additional information on the individual cells can be obtained. Bio-imaging can be done in various way like magnetic resonance imaging,[149-151] computed tomography[152], and fluorescence imaging.[153-155] Since fluorescence is a very sensitive, user-friendly operation, it is now widely employed. Zhang *et al.* derived a MOF from Zn^{2+} for fluorescence imaging. As observed the compound initially concentrated to the tumor site and then spread over the whole body.[153] In another report, Yang and coworkers reported a zirconium-based metal-organic framework with near-IR fluorescence properties. They observed the fluorescence imaging of liver tumors of mice by injecting the MOFs into the body. Up to 72 hours, the tumor area exhibited a high intensity of red. Here, the compound acted as a fluorescent material carrier.[154] Again, Yuan *et al.* reported a fluorescent probe formed from Gd, used to diagnose 4T1 cells. Using fluorescence imaging it has proved that the MOF was able to act as a fluorescent probe.[155] Verma *et al.* synthesized a naphthalene diimide-based compound for the cell imaging studies (see Figure 1.24). From the PXRD experiment, it was proved that the particle size was 40 nm and then they used it as imaging probes. Cytotoxicity studies explained it as a non-toxic framework. They used DAPI as a dye and it exclusively stains the nucleus. The experiment was performed in HCT-15 cells.[140]

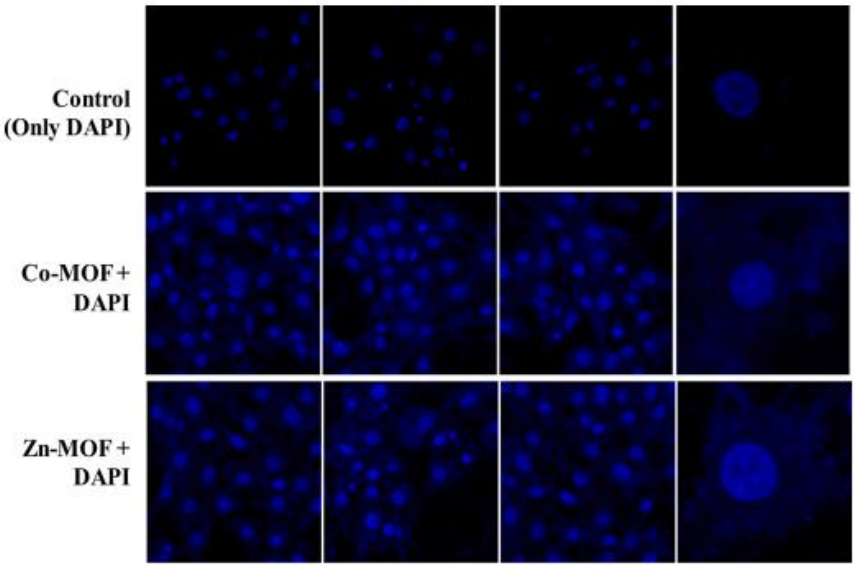

Fig. 1.24 Confocal imaging of HCT-15 cells. The upper lane (control) was stained with only DAPI. 2nd and 3rd lanes were stained with DAPI and also incubated with Co-MOF and Zn-MOF respectively.[140]

The main goal of the thesis is the investigation of the synthesis, structure, and properties of some metal-organic compounds. The purpose of the thesis is to synthesize various types of metal-organic compounds through different synthetic procedures by using varieties of organic ligands and different metal salts. Then through proper characterization techniques the synthesized compounds are thoroughly characterized. Further these compounds can be used in detection purpose for many analytes like anions and amino acid, pH. Moreover, these materials can be used in dye removal process as well as live cell imaging. The fields include smart sensing, dye adsorption and cell imaging (see Figure 1.25).

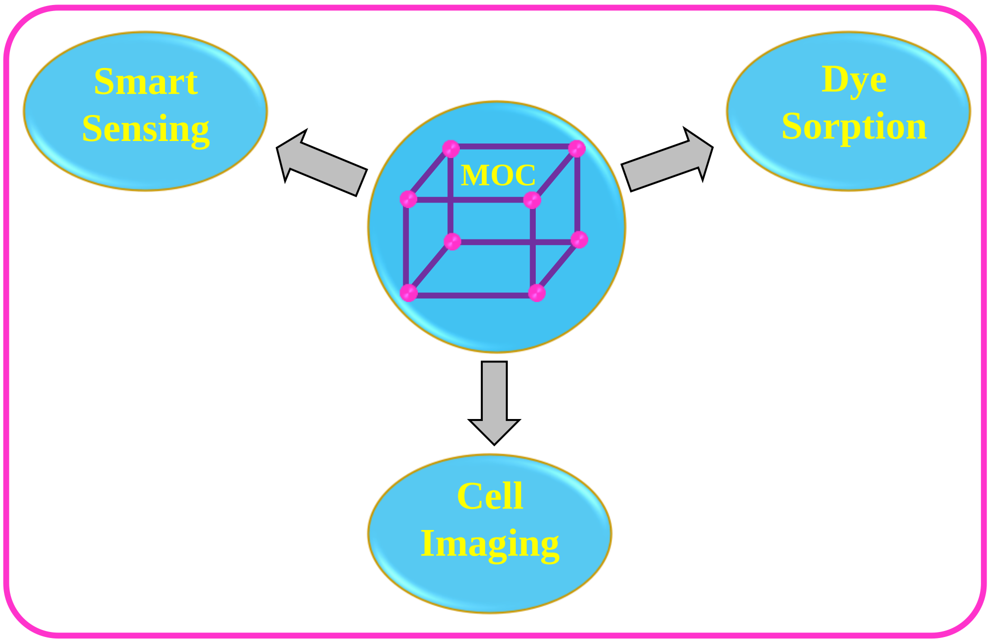

Fig. 1.25 Schematic diagram for application of Metal-organic Compound.

1.8 REFERENCES

1. Cook, T. R.; Zheng, Y.-R.; Stang, P. J., *Chem. Rev.* **2013,** *113* (1), 734-777.
2. Bowman-James, K., *Acc. Chem. Res.* **2005,** *38* (8), 671-678.
3. Robin, A. Y.; Fromm, K. M., *Coord. Chem. Rev.* **2006,** *250* (15), 2127-2157.
4. Iwamoto, T.; Nakano, T.; Morita, M.; Miyoshi, T.; Miyamoto, T.; Sasaki, Y., *Inorg. Chim. Acta* **1968,** *2*, 313-316.
5. Buser, H.; Schwarzenbach, D.; Petter, W.; Ludi, A. *Inorg. Chem.* **1977,** *16* (11), 2704-2710.
6. Tian, Y. Q.; Cai, C. X.; Ji, Y.; You, X. Z.; Peng, S. M.; Lee, G. H. *Angew. Chem.* **2002,** *114* (8), 1442-1444.
7. Kinoshita, Y.; Matsubara, I.; Higuchi, T.; Saito, Y., *Bull. Chem. Soc. Jpn.* **2006,** *32* (11), 1221-1226.
8. Hoskins, B. F.; Robson, R., *J. Am. Chem. Soc.* **1989,** *111* (15), 5962-5964.
9. Fujita, M.; Kwon, Y. J.; Washizu, S.; Ogura, K., *J. Am. Chem. Soc.* **1994,** *116* (3), 1151-1152.
10. Subramanian, S.; Zaworotko, M. J., *Angew. Chem., Int. Ed. Engl.* **1995,** *34* (19), 2127-2129.
11. Yaghi, O. M.; Richardson, D. A.; Li, G.; Davis, C. E.; Groy, T. L., *MRS Proc.* **1994,** *371*, 15.
12. Yaghi, O. M.; Li, G.; Li, H., *Nature* **1995,** *378* (6558), 703-706.
13. Li, H.; Eddaoudi, M.; Groy, T. L.; Yaghi, O. M., *J. Am. Chem. Soc.* **1998,** *120* (33), 8571-8572.
14. Braun, M. E. Ph.D., University of Michigan, United States -- Michigan, 2001.
15. Li, H.; Eddaoudi, M.; O'Keeffe, M.; Yaghi, O. M., *Nature* **1999,** *402* (6759), 276-279.
16. Kondo, M.; Yoshitomi, T.; Matsuzaka, H.; Kitagawa, S.; Seki, K., *Angew. Chem., Int. Ed. Engl.* **1997,** *36* (16), 1725-1727.
17. Hasegawa, S.; Horike, S.; Matsuda, R.; Furukawa, S.; Mochizuki, K.; Kinoshita, Y.; Kitagawa, S., *J. Am. Chem. Soc.* **2007,** *129* (9), 2607-2614.
18. Pedersen, C. J., *J. Am. Chem. Soc.* **1967,** *89* (26), 7017-7036.
19. Nath, K.; Wright, K. R.; Ahmed, A.; Siegel, D. J.; Matzger, A. J., *J. Am. Chem. Soc.* **2024,** *146* (15), 10517-10523.
20. Fan, W.; Zhang, X.; Kang, Z.; Liu, X.; Sun, D., *Coord. Chem. Rev.* **2021,** *443*, 213968-214024.
21. Altintas, C.; Altundal, O. F.; Keskin, S.; Yildirim, R., *J. Chem. Inf. Model.* **2021,** *61* (5), 2131-2146.

22. Connolly, B. M.; Madden, D. G.; Wheatley, A. E. H.; Fairen-Jimenez, D., *J. Am. Chem. Soc.* **2020,** *142* (19), 8541-8549.
23. Chen, Z.; Mian, M. R.; Lee, S.-J.; Chen, H.; Zhang, X.; Kirlikovali, K. O.; Shulda, S.; Melix, P.; Rosen, A. S.; Parilla, P. A.; Gennett, T.; Snurr, R. Q.; Islamoglu, T.; Yildirim, T.; Farha, O. K., *J. Am. Chem. Soc.* **2021,** *143* (45), 18838-18843.
24. Denning, S.; Majid, A. A. A.; Lucero, J. M.; Crawford, J. M.; Carreon, M. A.; Koh, C. A., *ACS Appl. Mater. Interfaces* **2020,** *12* (47), 53510-53518.
25. Gong, W.; Cui, H.; Xie, Y.; Li, Y.; Tang, X.; Liu, Y.; Cui, Y.; Chen, B., *J. Am. Chem. Soc.* **2021,** *143* (36), 14869-14876.
26. Saha, R.; Gupta, K.; Gómez García, C. J., *Cryst. Growth Des.* **2024,** *24* (5), 2235-2265.
27. Lu, Y.; Zhou, H.; Yang, H.; Zhou, Z.; Jiang, Z.; Pang, H., *J. Mater. Chem. A* **2024,** *12* (11), 6243-6260.
28. Thorarinsdottir, A. E.; Harris, T. D., Metal–Organic Framework Magnets. *Chem. Rev.* **2020,** *120* (16), 8716-8789.
29. Yadav, S.; Dixit, R.; Sharma, S.; Dutta, S.; Solanki, K.; Sharma, R. K., *Mater. Adv.* **2021,** *2* (7), 2153-2187.
30. Taghavi, R.; Rostamnia, S.; Farajzadeh, M.; Karimi-Maleh, H.; Wang, J.; Kim, D.; Jang, H. W.; Luque, R.; Varma, R. S.; Shokouhimehr, M., *Inorg. Chem.* **2022,** *61* (40), 15747-15783.
31. Yu, Q.; Wang, D., *J. Mater. Chem. A* **2023,** *11* (11), 5548-5558.
32. Tran, Y. B. N.; Nguyen, P. T. K.; Luong, Q. T.; Nguyen, K. D., *Inorg. Chem.* **2020,** *59* (22), 16747-16759.
33. Dhakshinamoorthy, A.; Li, Z.; Garcia, H., *Chem. Soc. Rev.* **2018,** *47* (22), 8134-8172.
34. Chen, X.; Song, J.-Y.; Zheng, J.; Wang, Y.-M.; Luo, J.; Weng, P.; Cai, B.-C.; Lin, X.-C.; Ning, G.-H.; Li, D., *J. Am. Chem. Soc.* **2024,** *146* (28), 19271-19278.
35. Xu, W.; Wu, Y.; Gu, W.; Du, D.; Lin, Y.; Zhu, C., *Chem. Soc. Rev.* **2024,** *53* (1), 137-162.
36. Ebrahimi, A.; Krivosudský, L.; Cherevan, A.; Eder, D., *Coord. Chem. Rev.* **2024,** *508*, 215764.
37. Misumi, Y.; Yamaguchi, A.; Zhang, Z.; Matsushita, T.; Wada, N.; Tsuchiizu, M.; Awaga, K., *J. Am. Chem. Soc.* **2020,** *142* (39), 16513-16517.
38. Hong, Y.-L.; Xu, Z.; Du, J.; Shi, Z.-Q.; Zuo, Y.-H.; Hu, H.-L.; Li, G., *Inorg. Chem.* **2024,** *63* (23), 10786-10797.
39. Hong, Y.-L.; Zuo, S.-W.; Du, H.-Y.; Shi, Z.-Q.; Hu, H.; Li, G., *ACS Appl. Mater. Interfaces* **2024,** *16* (11), 13745-13755.
40. Ye, Y.; Gong, L.; Xiang, S.; Zhang, Z.; Chen, B., *Adv. Mater.* **2020,** *32* (21), 1907090-1907118.

41. Peng, P.; Jiang, H. Z. H.; Collins, S.; Furukawa, H.; Long, J. R.; Breunig, H., Long *ACS Energy Lett.* **2024,** *9* (6), 2727-2735.
42. He, B.; Zhang, Q.; Pan, Z.; Li, L.; Li, C.; Ling, Y.; Wang, Z.; Chen, M.; Wang, Z.; Yao, Y.; Li, Q.; Sun, L.; Wang, J.; Wei, L., *Chem. Rev.* **2022,** *122* (11), 10087-10125.
43. Hussain, I.; Iqbal, S.; Lamiel, C.; Alfantazi, A.; Zhang, K., *J. Mater. Chem. A* **2022,** *10* (9), 4475-4488.
44. Lu, X. F.; Fang, Y.; Luan, D.; Lou, X. W. D., *Nano Lett.* **2021,** *21* (4), 1555-1565.
45. Li, D.-J.; Li, Q.-h.; Wang, Z.-R.; Ma, Z.-Z.; Gu, Z.-G.; Zhang, J., *J. Am. Chem. Soc.* **2021,** *143* (41), 17162-17169.
46. Wang, C.; Zhang, T.; Lin, W., *Chem. Rev.* **2012,** *112* (2), 1084-1104.
47. Abazari, R.; Yazdani, E.; Nadafan, M.; Kirillov, A. M.; Gao, J.; Slawin, A. M. Z.; Carpenter-Warren, C. L., *Inorg. Chem.* **2021,** *60* (13), 9700-9708.
48. Liu, X.; Liang, T.; Zhang, R.; Ding, Q.; Wu, S.; Li, C.; Lin, Y.; Ye, Y.; Zhong, Z.; Zhou, M., *ACS Appl. Mater. Interfaces* **2021,** *13* (8), 9643-9655.
49. Lawson, H. D.; Walton, S. P.; Chan, C., *ACS Appl. Mater. Interfaces* **2021,** *13* (6), 7004-7020.
50. Zhou, Z.; Vázquez-González, M.; Willner, I., *Chem. Soc. Rev.* **2021,** *50* (7), 4541-4563.
51. Linnane, E.; Haddad, S.; Melle, F.; Mei, Z.; Fairen-Jimenez, D., *Chem. Soc. Rev.* **2022,** *51* (14), 6065-6086.
52. Yan, J.; Liu, T.; Liu, X.; Yan, Y.; Huang, Y., *Coord. Chem. Rev.* **2022,** *452*, 214300.
53. Li, W.; Zhao, X.; Bi, Q.; Ma, Q.; Han, L.; Tao, K., *Dalton Transactions* **2021,** *50* (34), 11701-11710.
54. Ahmad, M. W.; Singh, J.; Syed, A.; Bahkali, A. H.; Subramaniam, M.; Yang, D.-J.; Choudhury, A., *Energy Fuels* **2024,** *38* (15), 14672-14684.
55. Hubber, A.; Hua, C., **2024,** *30* (32), e202400071.
56. Li, H.-Y.; Zhao, S.-N.; Zang, S.-Q.; Li, J., *Chem. Soc. Rev.* **2020,** *49* (17), 6364-6401.
57. Wang, J.-X.; Yin, J.; Shekhah, O.; Bakr, O. M.; Eddaoudi, M.; Mohammed, O. F., *ACS Appl. Mater. Interfaces* **2022,** *14* (8), 9970-9986.
58. Liu, C.-S.; Li, J.; Pang, H., *Coord. Chem. Rev.* **2020,** *410*, 213222-213261.
59. Hu, M.-L.; Razavi, S. A. A.; Piroozzadeh, M.; Morsali, A., *Inorg. Chem. Frontiers* **2020,** *7* (7), 1598-1632.
60. Yang, J.; Yang, Y.-W., **2020,** *16* (10), 1906846-1906869.
61. Liu, M.; Ren, X.; Meng, X.; Li, H., *Chin. J. Chem.* **2021,** *39* (2), 473-487.
62. Hui, S.; Saha, P. C.; Guha, S.; Mahata, P., *Inorg. Chem.* **2024,** *63* (29), 13439-13449.
63. Luo, C.-Y.; Ma, L.-J.; Liu, W.; Tan, Y.-C.; Wang, R.-N.; Hou, J.-L.; Zhu, Q.-Y., *Inorg. Chem.* **2024,** *63* (13), 5961-5971.
64. Shahnawaz Khan, M.; Khalid, M.; Shahid, M., *Mater. Adv.* **2020,** *1* (6), 1575-1601.

65. Parmar, B.; Bisht, K. K.; Rajput, G.; Suresh, E., *Dalton Trans.* **2021,** *50* (9), 3083-3108.
66. Cai, G.; Yan, P.; Zhang, L.; Zhou, H.-C.; Jiang, H.-L., *Chem. Rev.* **2021,** *121* (20), 12278-12326.
67. Singh, G.; Lee, J.; Karakoti, A.; Bahadur, R.; Yi, J.; Zhao, D.; AlBahily, K.; Vinu, A., *Chem. Soc. Rev.* **2020,** *49* (13), 4360-4404.
68. Yang, X.-Y.; Chen, L.-H.; Li, Y.; Rooke, J. C.; Sanchez, C.; Su, B.-L., *Chem. Soc. Rev.* **2017,** *46* (2), 481-558.
69. Healy, C.; Patil, K. M.; Wilson, B. H.; Hermanspahn, L.; Harvey-Reid, N. C.; Howard, B. I.; Kleinjan, C.; Kolien, J.; Payet, F.; Telfer, S. G.; Kruger, P. E.; Bennett, T. D., *Coord. Chem. Rev.* **2020,** *419*, 213388.
70. Abednatanzi, S.; Gohari Derakhshandeh, P.; Depauw, H.; Coudert, F.-X.; Vrielinck, H.; Van Der Voort, P.; Leus, K., *Chem. Soc. Rev.* **2019,** *48* (9), 2535-2565.
71. Mohsenpour Tehrani, M.; Chehrazi, E., *ACS Appl. Mater. Interfaces* **2024,** *16* (26), 32906-32929.
72. Gao, J.; Qian, X.; Lin, R.-B.; Krishna, R.; Wu, H.; Zhou, W.; Chen, B., *Angew. Chem.* **2020,** *59* (11), 4396-4400.
73. Mortensen, M. L.; Lewis, A. L.; McCandless, G.; Balkus, K. J., *crystals* **2021,** *11* (12), 1547-1557.
74. Boger, D. L.; Hong, J.; Hikota, M.; Ishida, M., *J. Am. Chem. Soc.* **1999,** *121* (11), 2471-2477.
75. Zhou, G.-W.; Guo, G.-C.; Liu, B.; Wang, M.-S.; Cai, L.-Z.; Huang, J.-S. J. *Bull. Korean Chem. Soc.* **2004,** *25* (5), 676-680.
76. Berl, V.; Huc, I.; Khoury, R. G.; Lehn, J. M. *Chem. Eur. J.* **2001,** *7* (13), 2798-2809.
77. Riegel, E. R.; Reinhard, M. C. *J. Am. Chem. Soc.* **1926,** *48* (5), 1334-1345.
78. Yang, L.; la Cour, A.; Anderson, O. P.; Crans, D. C., *Inorg. Chem.* **2002,** *41* (24), 6322-6331.
79. Fandos, R.; Hernández, C.; Otero, A.; Pacheco, J.; Rodríguez, A. M.; Ruiz, M. J.; Organero, J. Á., *Organometallics* **2018,** *37* (20), 3515-3523.
80. Du, M.; Li, C.-P.; Zhao, X.-J.; Yu, Q. *CrystEngComm* **2007,** *9* (11), 1011-1028.
81. Motieiyan, E.; Ghadermazi, M.; Nemati, A.; Ghasemi, N.; Silva, M. R.; Shokrollahi, A.; Karami Arokhloo, J., *Monatsh Chem* **2013,** *144* (8), 1141-1151.
82. Saha, D.; Maity, T.; Koner, S., *Dalton Trans.* **2014,** *43* (34), 13006-13017.
83. Ghosh, S. K.; Ribas, J.; El Fallah, M. S.; Bharadwaj, P. K., *Inorg. Chem.* **2005,** *44* (11), 3856-3862.
84. Ghosh, S. K.; Neogi, S.; Sañudo, E. C.; Bharadwaj, P. K., *Inorg. Chim. Acta* **2008,** *361* (1), 56-62.

85. Zou, J.-P.; Liu, X.-M.; Yan, L.-S.; Deng, A.-M.; Xing, Q.-J.; Chen, M.-H., *J. Coord. Chem.* **2010,** *63* (1), 56-66.
86. Lu, Y.-B.; Huang, J.; Yuan, X.-R.; Liu, S.-J.; Li, R.; Liu, H.; Liu, M.-P.; Wen, H.-R.; Zhu, S.-D.; Xie, Y.-R., *Cryst. Growth Des.* **2022,** *22* (2), 1045-1053.
87. Mani, P.; Ojha, A. A.; Reddy, V. S.; Mandal, S., *Inorg. Chem.* **2017,** *56* (12), 6772-6775.
88. Kaur, H.; Kumar, R.; Kumar, A.; Krishnan, V.; Koner, R. R. *Dalton Trans.* **2019,** *48* (3), 915-927.
89. Mirzaei, M.; Eshtiagh-Hosseini, H.; Lotfian, N.; Salimi, A.; Bauzá, A.; Van Deun, R.; Decadt, R.; Barceló-Oliver, M.; Frontera, A. *Dalton Trans.* **2014,** *43* (4), 1906-1916.
90. Zou, J.-P.; Chen, M.-H.; Zhang, L.-Z.; Xing, Q.-J.; Xiong, Z.-Q., *J. Chem. Crystallogr.* **2011,** *41* (12), 1820-1833.
91. Mani, P.; Ranjith, K. M.; Mandal, S.; Paul, A. K., *J. Chem. Sci.* **2018,** *130* (6), 60.
92. Bhat, Z. U. H.; Hanif, S.; Abbasi, A.; Ali, A.; Ahmad, M.; Shakir, M., *J. Mol. Struct.* **2024,** *1297*, 136955-136963.
93. Zhao, B.; Gao, H.-L.; Chen, X.-Y.; Cheng, P.; Shi, W.; Liao, D.-Z.; Yan, S.-P.; Jiang, Z.-H., *Chem. Eur. J.* **2006,** *12* (1), 149-158.
94. Zou, J.-P.; Zhou, G.-W.; Zhang, X.; Wang, M.-S.; Lu, Y.-B.; Zhou, W.-W.; Zhang, Z.-J.; Guo, G.-C.; Huang, J.-S. *CrystEngComm* **2009,** *11* (6), 972-974.
95. Qian, J.; Sun, M.-M.; Liu, M.; Gu, W., *ACS Omega* **2019,** *4* (7), 11949-11959.
96. Li, J.; Jin, Y.; Yang, Y.-Y.; Song, X.-Q., *Inorg. Chem.* **2024,** *63* (15), 6871-6882.
97. Gao, H.-L.; Zhao, B.; Zhao, X.-Q.; Song, Y.; Cheng, P.; Liao, D.-Z.; Yan, S.-P. *Inorg. Chem.* **2008,** *47* (23), 11057-11061.
98. Yang, W.; Dang, S.; Wang, H.; Tian, T.; Pan, Q.-J.; Sun, Z.-M. *Inorg. Chem.* **2013,** *52* (21), 12394-12402.
99. Li, Y.; Wen, G.; Li, J.; Li, Q.; Zhang, H.; Tao, B.; Zhang, J. *Chem. Commun.* **2022,** *58* (82), 11488-11506.
100. Madison, SMART (V 5.628), SAINT (V 6.45 a), XPREP, and SHELXTL. **2004**.
101. Krause, L.; Herbst-Irmer, R.; Sheldrick, G. M.; Stalke, D., *J Appl Crystallogr* **2015,** *48* (1), 3-10.
102. Altomare, A.; Cascarano, G. L.; Giacovazzo, C.; Guagliardi, A. *J. Appl. Crystallogr.* **1993,** *26*, 343-350.
103. Sheldrick, G., *Acta Crystallogr. C: Struct. Chem.* **2015,** *71* (1), 3-8.
104. Farrugia, L., *J. Appl. Crystallogr.* **1999,** *32* (4), 837-838.
105. Spek, A., *J. Appl. Crystallogr.* **2003,** *36* (1), 7-13.
106. Rojas, S.; Horcajada, P., *Chem. Rev.* **2020,** *120* (16), 8378-8415.

107. Yang, J.-M., *CrystEngComm* **2022,** *24* (3), 434-449.

108. Au, V. K.-M., *Front. Chem.* **2020,** *8*.

109. Beydaghdari, M.; Saboor, F. H.; Babapoor, A.; Asgari, M., ChemNanoMat **2022,** *8* (2), e202100400.

110. Jiang, D.; Chen, M.; Wang, H.; Zeng, G.; Huang, D.; Cheng, M.; Liu, Y.; Xue, W.; Wang, Z., *Coord. Chem. Rev.* **2019,** *380*, 471-483.

111. Li, Y.; Gao, C.; Jiao, J.; Cui, J.; Li, Z.; Song, Q., *ACS Omega* **2021,** *6* (49), 33961-33968.

112. Uddin, M. J.; Ampiaw, R. E.; Lee, W., *Chemosphere* **2021,** *284*, 131314-131331.

113. Yang, J.-M.; Ying, R.-J.; Han, C.-X.; Hu, Q.-T.; Xu, H.-M.; Li, J.-H.; Wang, Q.; Zhang, W., *Dalton Trans.* **2018,** *47* (11), 3913-3920.

114. Deng, S.-Q.; Miao, Y.-L.; Tan, Y.-L.; Fang, H.-N.; Li, Y.-T.; Mo, X.-J.; Cai, S.-L.; Fan, J.; Zhang, W.-G.; Zheng, S.-R., *Inorg. Chem.* **2019,** *58* (20), 13979-13987.

115. Gao, X.; Sun, G.; Ge, F.; Zheng, H., *Inorg. Chem.* **2019,** *58* (13), 8396-8407.

116. Gao, W.; Liu, F.; Pan, C.-W.; Zhang, X.-M.; Liu, J.-P.; Gao, Q.-Y. *CrystEngComm* **2019,** *21* (7), 1159-1167.

117. Zhang, X.; Liu, H.-L.; Zhang, D.-S.; Geng, L., *Inorg. Chem. Commun.* **2019,** *101*, 184-187.

118. Chiong, J. A.; Zhu, J.; Bailey, J. B.; Kalaj, M.; Subramanian, R. H.; Xu, W.; Cohen, S. M.; Tezcan, F. A., *J. Am. Chem. Soc.* **2020,** *142* (15), 6907-6912.

119. Li, Y.-Z.; Wang, G.-D.; Yang, H.-Y.; Hou, L.; Wang, Y.-Y.; Zhu, Z. *Inorg. Chem. Front.* **2020,** *7* (3), 746-755.

120. Zhang, N.; Xing, Y.-H.; Bai, F.-Y., *Cryst. Growth Des.* **2020,** *20* (3), 1838-1848.

121. Wan, S.; Li, L.; Liu, J.; Liu, B.; Li, G.; Zhang, L.; Liu, Y., *Cryst. Growth Des.* **2020,** *20* (5), 3199-3207.

122. Wang, C.; Yin, Z.; Cheng, Z.; Ma, W.-M.; Li, X.-Y.; Hu, X.-T.; Shi, R.; Chen, A.-W.; Ma, Y.-M. *CrystEngComm* **2020,** *22* (5), 878-887.

123. Deng, S.-Q.; Mo, X.-J.; Zheng, S.-R.; Jin, X.; Gao, Y.; Cai, S.-L.; Fan, J.; Zhang, W.-G., *Inorg. Chem.* **2019,** *58* (4), 2899-2909.

124. Wu, M. Z.; Shi, J. Y.; Chen, P. Y.; Tian, L.; Chen, J., *Inorg. Chem.* **2019,** *58* (5), 3130-3136.

125. Gaur, R. *Inorg. Chem. Front.* **2019,** *6* (1), 278-286.

126. Iman, K.; Shahid, M.; Khan, M. S.; Ahmad, M.; Sama, F. *CrystEngComm* **2019,** *21* (35), 5299-5309.

127. Mantasha, I.; Shahid, M.; Saleh, H. A.; Qasem, K. M.; Ahmad, M. *CrystEngComm* **2020,** *22* (22), 3891-3909.

128. Maity, K.; Biradha, K., *Cryst. Growth Des.* **2016,** *16* (5), 3002-3013.

129. Wang, Z.; Zhu, C.-Y.; Zhao, H.-S.; Yin, S.-Y.; Wang, S.-J.; Zhang, J.-H.; Jiang, J.-J.; Pan, M.; Su, C.-Y., *J. Mater. Chem. A* **2019,** *7* (9), 4751-4758.
130. Tang, Y.; Lu, X.-M.; Yang, G.; Wang, Y.-Y., *Inorg. Chem.* **2023,** *62* (4), 1735-1743.
131. Liu, J.; Wang, Z.; Bi, R.; Mao, F.; Wang, K.; Wu, H.; Wang, X. *Inorg. Chem. Front.* **2020,** *7* (3), 718-730.
132. Ai, J.; Tian, H.-R.; Min, X.; Wang, Z.-C.; Sun, Z.-M., *Dalton Trans.* **2020,** *49* (12), 3700-3705.
133. Yang, J.-M.; Zhang, W.; Zhang, R.-Z.; Tong, M.-X., *Dalton Trans.* **2020,** *49* (20), 6651-6660.
134. Patel, U.; Parmar, B.; Patel, P.; Dadhania, A.; Suresh, E., *Mater. Chem. Front.* **2021,** *5* (1), 304-314.
135. Ahamad, M. N.; Khan, M. S.; Shahid, M.; Ahmad, M., *Dalton Trans.* **2020,** *49* (41), 14690-14705.
136. Xie, X.; Huang, X.; Lin, W.; Chen, Y.; Lang, X.; Wang, Y.; Gao, L.; Zhu, H.; Chen, J., *ACS Omega* **2020,** *5* (23), 13595-13600.
137. Ukani, H.; Mehra, S.; Parmar, B.; Kumar, A.; Khan, I.; El Seoud, O. A.; Malek, N., *Ind. Eng. Chem. Res.* **2023,** *62* (12), 5002-5014.
138. Nguyen, N. T. T.; Nguyen, T. T. T.; Ge, S.; Liew, R. K.; Nguyen, D. T. C.; Tran, T. V., *Nanoscale Adv.* **2024,** *6* (7), 1800-1821.
139. Yang, P.; Men, Y.; Tian, Y.; Cao, Y.; Zhang, L.; Yao, X.; Yang, W., *ACS Appl. Mater. Interfaces* **2019,** *11* (12), 11209-11219.
140. Verma, T.; Singh, U. P.; Verma, P.; Butcher, R. J.; Ghosh, C.; Roy, P., *J. Mol. Struct.* **2024,** *1302*, 137467.
141. Li, S.; Tan, L.; Meng, X., *Adv. Funct. Mater.* **2020,** *30* (13), 1908924-1908949.
142. Zhang, Y.; Fu, H.; Chen, S.; Liu, B.; Sun, W.; Gao, H. *Chem. Commun.* **2020,** *56* (5), 762-765.
143. Demir Duman, F.; Forgan, R. S., *J. Mater. Chem. B* **2021,** *9* (16), 3423-3449.
144. Sava Gallis, D. F.; Rohwer, L. E. S.; Rodriguez, M. A.; Barnhart-Dailey, M. C.; Butler, K. S.; Luk, T. S.; Timlin, J. A.; Chapman, K. W., *ACS Appl. Mater. Interfaces* **2017,** *9* (27), 22268-22277.
145. Sun, Y.; Zheng, L.; Yang, Y.; Qian, X.; Fu, T.; Li, X.; Yang, Z.; Yan, H.; Cui, C.; Tan, W., *Nano-Micro Letters* **2020,** *12* (1), 103.
146. Safdar Ali, R.; Meng, H.; Li, Z., *Molecules* **2022,** *27* (1), 100.
147. Rojas, S.; Devic, T.; Horcajada, P., Metal organic frameworks based on bioactive components. *J. Mater. Chem. B* **2017,** *5* (14), 2560-2573.
148. Li, Z.; Fraile, J.; Viñas, C.; Teixidor, F.; Planas, J. G., *Chem. Commun.* **2021,** *57* (20), 2523-2526.

149. Jia, M.; Yang, X.; Chen, Y.; He, M.; Zhou, W.; Lin, J.; An, L.; Yang, S., *J. Mater. Chem. B* **2021,** *9* (41), 8631-8638.

150. Pandit, P.; Bhagat, S.; Rananaware, P.; Mohanta, Z.; Kumar, M.; Tiwari, V.; Singh, S.; Brahmkhatri, V. P., *Microporous Mesoporous Mater.* **2022,** *340*, 112008.

151. Zeng, X.; Chen, B.; Song, Y.; Lin, X.; Zhou, S.-F.; Zhan, G., *ACS Appl. Bio Mater.* **2021,** *4* (8), 6417-6429.

152. Bao, J.; Zu, X.; Wang, X.; Li, J.; Fan, D.; Shi, Y.; Xia, Q.; Cheng, J., *Int. J. Nanomed.* **2020,** 7687-7702.

153. Zhang, X.; Lu, Y.; Jia, D.; Qiu, W.; Ma, X.; Zhang, X.; Xu, Z.; Wen, F., *J. Nanobiotechnol.* **2021,** *19* (1), 455.

154. Wang, Y.-M.; Xu, Y.; Zhang, X.; Cui, Y.; Liang, Q.; Liu, C.; Wang, X.; Wu, S.; Yang, R., *Nanomater.* **2022,** *12* (2), 287.

155. Yuan, C.; Li, Y.; Xu, Z.; Wang, C.; Zhang, J.; Jin, Y.; Chen, Z.; Sun, H.; Wu, F.; Zhang, Q.; Tang, Y.; Wang, S., *ACS Appl. Nano Mater.* **2022,** *5* (10), 15318-15327.

Chapter: 2

pH Response of a Hydroxyl-Functionalized Luminescent Metal-Organic Framework based Phosphor

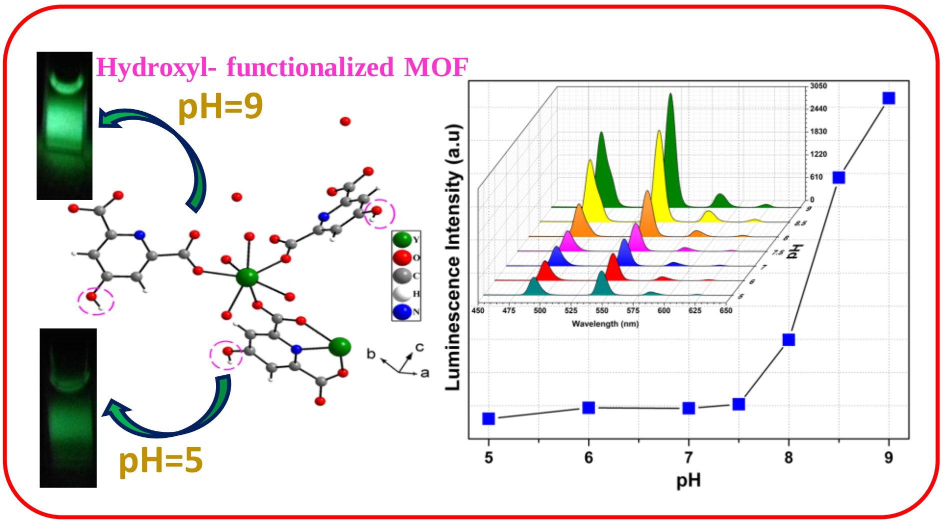

New J. Chem., 2021,45, 9394-9402.

2.1 Introduction

pH plays an invaluable role in the study of environmental protection, industrial production, biomedical research,[1-3] and water quality testing.[4-5] In the environment a minute change of pH can destroy many plants and animals as plants prefer basic or acidic soil, for example tea plantation.[3] In case of industrial product formulation there is a need of particular pH for each chemical reaction because instead of that a different product will come out.[3] Many physiological and pathological systems like cell cycle[6] and apoptosis,[7] receptor-mediated signal transduction,[8] ion transport,[9] muscle contraction,[10] inflammation,[11]tumor growth,[12] cystic fibrosis[13] can be controlled by the intracellular pH.[4] Generally the human blood pH is between 7.35 and 7.45, which is slightly basic and if the pH value is getting lowered than 7.30 then it may cause some severe diseases like diabetes, stroke, obesity, hypertension, cancer and Alzheimer's disease.[14-16] Therefore, for exploring the cellular function and monitoring the cell metabolism processes,[4,17] precise sensing of pH is very important. Several techniques have been exhibited for the measurement of pH such as pH test paper method, proton permeable microelectrode, electrochemical method (voltametric, amperometric, potentiometric), absorption spectroscopy, ^{31}P NMR spectroscopy, luminescence imaging.[18-31] Detection of pH using very small amount of sample is very tedious work, in that sense luminescence-based detection is important as it requires very minute amount of sample. Moreover, it is highly sensitive, cost effective, easily portable, having short response time, without any reference, high signal to noise ratio and also it can be used in both solid and liquid phase.[32-34] Now a days, in the field of analytical chemistry, bio-analytical chemistry, cellular biology (for measuring intracellular pH) and medicine, fluorescence pH sensors have extensive use.[35-38] Till now different kind of materials like quantum dots,[17,39,40] nano particles,[41-43] platinum nano clusters,[3] carbon dots,[44-46] conjugated polymer,[47] supramolecule,[48] ruthenium complex,[49] block co-polymers,[50,51] coordination compound[52] have been used for pH sensing. All these materials have very lengthy preparation procedure and poor photostability.

Metal-organic frameworks are a class of crystalline hybrid materials comprised of metal ions and polydentate bridging ligand with diverse structural properties and tunable size property.[53] In the last two decades due to their structural properties they are widely used in the many fields like gas storage and separation,[54] energy storage,[55] light harvesting,[56] non-linear optics,[57] drug delivery,[58] catalysis,[59] smart sensing,[60] magnetism,[61] proton conductivity,[62] and supercapacitor.[63] Recently, metal-organic frameworks, especially Zr based, have been developed as a new kind of material for the sensing of pH using ligand centered emission.[64] But ligand centered based luminescence detectors have small stokes shift, which prevent the naked eye detection of pH sensing as the color differences between the excitation and emission light are very low. For this purpose, few pure lanthanide-based MOFs have been reported for the pH sensing.[65] In the lanthanide-based metal-organic framework remarkable optical behaviour is observed through antenna effect, where the organic ligands serve as sensitizer. In this process, the ligands are excited to the singlet state, from which the energy is transferred to the metal center *via* inter system crossing and ultimately the lanthanide ions emit their characteristic luminescence. The pH sensing through the naked eye is still challenging due to the self-quenching of the pure lanthanide-based metal-organic framework.

For this purpose, we have successfully synthesized a 10% Tb doped Y based MOF, $[Y_{1.8}Tb_{0.2}(CAM)_3(H_2O)_4].2H_2O$, **1**, for the visible detection of pH in range of 7 to 9 where the self-quenching is minimized through the increase of distance between emitting centers. In this case, the compound **1** act as a phosphor material where the framework serves as host lattice whereas the organic ligand (CAM) and the Tb^{3+} ion contribute as sensitizer and activator, respectively. Structure elucidation of compound **1** is carried out by synthesizing the single crystals of isomorphous pure yttrium compound $[Y_2(CAM)_3(H_2O)_4].2H_2O$, **1a**, under similar experimental conditions. Systematic characterization of compound **1** was performed by TGA, IR and EDX, SEM-elemental mapping and BET analysis. The aqueous solution of compound **1** shows weak visible green emission upon excitation at 280 nm. It shows luminescence turn-on behaviour in higher pH range (7 to 9) in aqueous medium and it is closed to the physiological pH of human blood. As per literature survey, this is the first example where Tb doped Y based MOF used for the luminescence-based sensing of pH.

2.2 EXPERIMENTAL SECTION

2.2.1 Materials

The chemicals required for the synthesis of compound **1** and compound **1a**, $Y(NO_3)_3.6H_2O$ (Sigma-Aldrich, 99.9%), $Tb(NO_3)_3.5H_2O$ (Sigma-Aidrich, 99.9%), Chelidamic acid (Sigma-Aldrich, 99%), 1,2,4-triazole (Sigma-Aldrich, 99%), EtOH (Analytical Reagent, 99.9%) were used without further purification unless otherwise mentioned. The chemical used for the pH sensing experiment is HCl (Merck, 99%) and NaOH (Merck, 99%). The water used was double distilled.

2.2.2 Synthesis of Compound 1

Compound **1** was prepared by employing the hydrothermal method. $Y(NO_3)_3.6H_2O$ (0.0345 g, 0.09 mM), $Tb(NO_3)_3.5H_2O$(0.0043 g, 0.01 mM), 1,2,4- triazole (0.0070 g, 0.1 mM) and chelidamic acid (0.0603 g, 0.3 mM) were dispersed in a mixture of 5 mL water and 1 mL EtOH. Then the mixture was homogenized at room temperature for 30 min. The final reaction mixture was sealed in a 23 mL PTFE-lined stainless-steel autoclave and heated at 150 ºC for 72 hours. The starting pH value and the pH value after the reaction were 1 and 6, respectively. The final product, containing large quantities of yellow colored block-shaped crystals, was filtered, washed with deionized water and ethanol under vacuum, and dried at ambient conditions (Yield 75% based on Y).

2.2.3 Synthesis of Compound 1a

Compound **1a** was prepared by employing a similar experimental condition. For this purpose, $Y(NO_3)_3.6H_2O$ (0.0383 g, 0.1 mM), 1,2,4- triazole (0.0070 g, 0.1 mM), chelidamic acid (0.0603 g, 0.3 mM) were dispersed in a mixture of 5 mL water and 1 mL EtOH. Then the mixture was homogenized at room temperature for 30 min. The final reaction mixture was sealed in a 23 mL PTFE-lined stainless-steel autoclave and heated at 150 ºC for 72 hours. The final product, containing large quantities of yellow colored block-shaped crystals, was filtered, washed with deionized water and ethanol under vacuum, and dried at ambient conditions (Yield 70 % based on Y).

2.2.4 Instrumentation

Powder X-ray diffraction (XRD) patterns were recorded on well ground samples in the 2θ range 5-50º using Cu Kα radiation (Bruker D8 Discover instrument). Thermogravimetric analysis (TGA) using Perkin-Elmer instrument STA 6000 has been carried out in nitrogen atmosphere (flow rate = 20 ml min^{-1}) in the temperature range 40 – 900 ºC (heating rate = 20 ºC min^{-1}). The IR spectral studies were performed on Nicolet Magna IR 750 series-II FTIR- spectrophotometer in the solid state. The ratio of Tb and Y in compound **1** were determined using EDX analysis (EDAX, QUANTA 200). FE-SEM and elemental mapping analyses were carried out using a Zeiss Gemini SEM 45 field emission scanning electron microscope. Nitrogen gas adsorption - desorption of the sample (BET experiment) were carried out using Autosorb iQ2, Quantachrome Instruments, USA.

2.2.5 Single-Crystal Structure determination of compound 1a

A suitable single crystal was carefully selected under a polarising microscope and glued carefully to a thin glass fiber. The single crystal data were collected on a Burker AXS smart Apex CCD diffractometer at 293 (2) K. The X-ray generator was operated at 50 kV and 35 mA using Mo Kα (λ = 0.71073 Å) radiation. Data were collected with ω scan width of 0.3°. A total of 606 frames were collected in three different setting of φ (0, 90, 180°) keeping sample-to-detector distance fixed at 6.03 cm and the detector position (2θ) fixed at -25°. The final data sets were reduced by an APEX3 program, while a SAINTPLUS[66] program was utilized for the integration of diffraction profiles. The absorption correction (multiscan) was carried out by a SADABS program[67]. We initially solved the structure by SIR 92,[68] and the full matrix least-square method (SHELXL-2016[69]) was used further, which is present in the WinGx suit of programs (Version 1.63.04a).[70,71] We successfully located all the non-hydrogen atoms from Fourier maps and refined them with anisotropic displacement parameters at the final cycles. Finally, we fixed all the hydrogen atoms at calculated positions and included them in the refinement process using riding model associated with isotropic thermal parameters. Hydrogen atoms of water molecules in compound **1a** were not located. Details of the structure solution and final refinement is given in the Table 2.1. CCDC: 2057508 contain the crystallographic data for this paper. These data can be obtained free of charge from The Cambridge Crystallographic Data Center (CCDC) via www.ccdc.cam.ac.uk/data_request/cif.

Table 2.1: Crystal data and structure refinement parameters for $[Y_2(CAM)_3(H_2O)_4].2H_2O$, **1a.**

Empirical formula	$C_{21}H_9N_3O_{21}Y_2$
Formula weight	817.13
Crystal system	Monoclinic
Space group	$P2_1/n$ (no. 14)
a (Å)	8.9905(7)
b (Å)	14.5380(10)
c (Å)	21.7767(15)
α (deg)	90

β (deg)	90.917(2)
γ (deg)	90
Volume (Å^3)	2845.9(4)
Z	4
T (K)	273(2)
ρ_{calc} (g cm^{-3})	1.907
μ (mm^{-1})	4.159
θ range (deg)	1.871to 27.070
λ (Mo Kα) (Å)	0.71073
R indices [I>2σ(I)]	R_1 = 0.0359, wR_2 = 0.0979
R indices (all data)	R_1 = 0.0466, wR_2 = 0.1085

$R_1 = \Sigma ||F_0|-|F_c|| / \Sigma |F_0|$; $wR_2 = \{\Sigma[w(F_0^2 - F_c^2)^2] / \Sigma[w(F_0^2)^2]\}^{1/2}$. $w = 1/[\sigma^2(F_0)^2 + (aP)^2 + bP]$, $P = [\max.(F_0^2,0) + 2(F_c)^2]/3$, where a = 0.0567and b = 3.4107.

2.2.6 Photoluminescence measurements

The aqueous solution of compound **1** was prepared by introducing compound **1** (1.6 mg) into 4 ml water. The photoluminescence measurements were performed using 50 µl of the stock solution into 2 ml quartz cuvette. Photoluminescence properties of compound **1** were investigated at room temperature in water using a Hitachi F-7100 luminescence spectrofluorometer upon excited at 280 nm. The slit width was 5 nm for both excitation and emission. The photomultiplier voltage was 520 V. The cut off filter was set to 420 nm for excluding ligand center luminescence. UV-vis spectra were recorded using Shimadzu UV 3101PC spectrophotometer. The luminescence lifetime of Tb^{3+} center emission was measured using Hitachi F-7100 luminescence spectrofluorometer. The excitation wavelength was selected at 280 nm and emission decay curve was monitored at 545 nm.

2.3 RESULTS AND DISCUSSION

2.3.1 Structure of compound 1a

The asymmetric unit of compound **1a** consists of two crystallographically independent Y^{3+} ions, three chelidamates (CAM), four coordinated water molecules and two lattice water molecules (Figure 2.1). The $Y(1)^{3+}$ion is coordinated by the eight oxygen atoms and has a distorted square antiprism geometry through the carboxylate groups from CAM ligands and four coordinated water molecules (see Figure 2.2a). The Y(2)$^{3+}$ ion is coordinated by six oxygen atoms and three nitrogen atoms and has a distorted tricapped trigonal prism geometry through carboxylate groups and pyridine nitrogen from CAM ligands (see Figure 2.2b). The Y−O bonds have an average distance of 2.38 Å and the Y–N bonds have an average distance of 2.47 Å. The O/N-Y-O/N bond angles are in the range of 63.96(8)- 147.07(9) °. The selected bond distances and angles for compound **1a** are listed in Table 2.2 and 2.3.

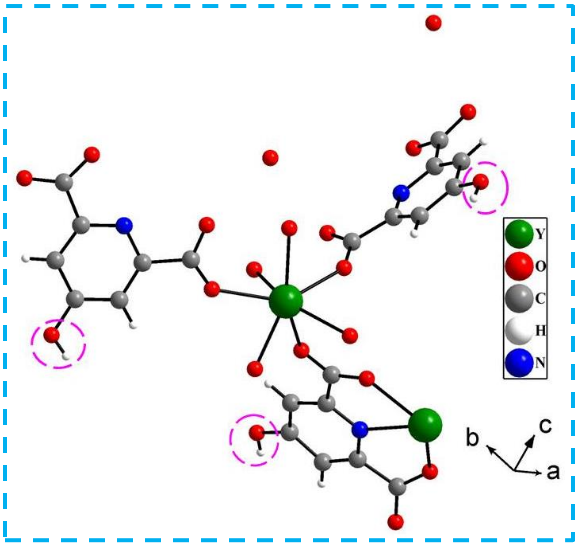

Fig. 2.1 The asymmetric unit of [$Y_2(CAM)_3(H_2O)_4$].$2H_2O$, **1a**. The free hydroxyl groups are encircled to show their position within the CAM ligands. Hydrogen atoms of water molecules are not shown.

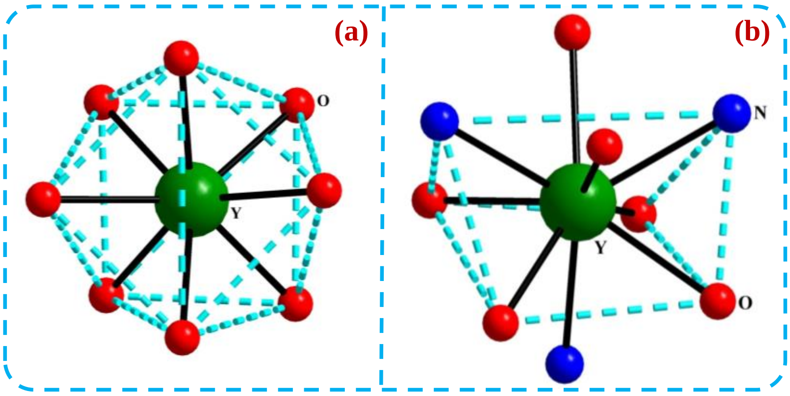

Fig. 2.2 (a) distorted square anti-prism geometry observed in Y(1) and (b) distorted tricapped trigonal prism geometry observed in Y(2) in [$Y_2(CAM)_3(H_2O)_4$].$2H_2O$, **1a**.

Table 2.2: Selected bond distances (Å) observed in [$Y_2(CAM)_3(H_2O)_4$].$2H_2O$, **1a.**

Bond	Distances, Å	Bond	Distances, Å
Y(1)-O(1)	2.380(2)	Y(2)-O(3)#2	2.381(2)
Y(1)-O(4)#1	2.343(2)	Y(2)-O(6)	2.402(2)
Y(1)-O(7)	2.369(2)	Y(2)-O(8)	2.397(2)
Y(1)-O(11)	2.336(3)	Y(2)-O(12)#3	2.437(2)
Y(1)-O(16)	2.373(3)	Y(2)-O(13)#3	2.420(3)
Y(1)-O(17)	2.405(3)	Y(2)-N(1)#2	2.460(3)
Y(1)-O(18)	2.382(3)	Y(2)-N(2)	2.478(3)
Y(1)-O(19)	2.376(2)	Y(2)-N(3)#3	2.467(3)
Y(2)-O(2)#2	2.368(2)		

Table 2.3: Selected bond angles observed in [$Y_2(CAM)_3(H_2O)_4$].$2H_2O$, **1a.**

Angle	Amplitude (°)	Angle	Amplitude (°)
O(11)-Y(1)-O(4)#1	117.15(9)	O(19)-Y(1)-O(1)	80.46(9)
O(11)-Y(1)-O(7)	78.00(9)	O(11)-Y(1)-O(18)	76.72(9)
O(4)#1-Y(1)-O(7)	139.73(9)	O(4)#1-Y(1)-O(18)	142.11(9)
O(11)-Y(1)-O(16)	144.09(9)	O(7)-Y(1)-O(18)	75.45(9)
O(4)#1-Y(1)-O(16)	77.78(8)	O(16)-Y(1)-O(18)	112.52(10)
O(7)-Y(1)-O(16)	71.62(9)	O(19)-Y(1)-O(18)	82.45(10)
O(11)-Y(1)-O(19)	71.35(9)	O(1)-Y(1)-O(18)	72.08(9)
O(4)#1-Y(1)-O(19)	70.86(9)	O(11)-Y(1)-O(17)	73.12(9)
O(7)-Y(1)-O(19)	145.54(9)	O(4)#1-Y(1)-O(17)	72.18(9)
O(16)-Y(1)-O(19)	142.34(8)	O(7)-Y(1)-O(17)	78.19(9)
O(11)-Y(1)-O(1)	140.16(9)	O(16)-Y(1)-O(17)	82.19(10)
O(4)#1-Y(1)-O(1)	77.24(9)	O(19)-Y(1)-O(17)	106.72(10)
O(7)-Y(1)-O(1)	116.20(9)	O(1)-Y(1)-O(17)	143.75(9)
O(16)-Y(1)-O(1)	72.60(9)	O(18)-Y(1)-O(17)	143.28(9)
O(2)#2-Y(2)-O(3)#2	129.30(8)	O(2)#2-Y(2)-O(8)	147.07(9)
O(3)#2-Y(2)-O(8)	76.49(9)	O(2)#2-Y(2)-O(6)	79.90(9)
O(3)#2-Y(2)-O(6)	84.85(9)	O(8)-Y(2)-O(6)	127.69(8)

O(2)#2-Y(2)-O(13)#3	79.41(9)	O(3)#2-Y(2)-O(13)#3	144.10(9)
O(8)-Y(2)-O(13)#3	87.92(9)	O(6)-Y(2)-O(13)#3	79.47(9)
O(2)#2-Y(2)-O(12)#3	83.79(9)	O(3)#2-Y(2)-O(12)#3	81.01(9)
O(8)-Y(2)-O(12)#3	80.68(9)	O(6)-Y(2)-O(12)#3	143.95(9)
O(13)#3-Y(2)-O(12)#3	128.61(8)	O(2)#2-Y(2)-N(1)#2	64.37(8)
O(3)#2-Y(2)-N(1)#2	64.97(8)	O(8)-Y(2)-N(1)#2	134.05(9)
O(6)-Y(2)-N(1)#2	74.14(9)	O(13)#3-Y(2)-N(1)#2	138.02(9)
O(12)#3-Y(2)-N(1)#2	69.82(9)	O(2)#2-Y(2)-N(3)#3	77.85(9)
O(3)#2-Y(2)-N(3)#3	134.06(9)	O(8)-Y(2)-N(3)#3	69.27(9)
O(6)-Y(2)-N(3)#3	140.63(9)	O(13)#3-Y(2)-N(3)#3	64.81(9)
O(12)#3-Y(2)-N(3)#3	64.28(9)	N(1)#2-Y(2)-N(3)#3	122.55(9)
O(2)#2-Y(2)-N(2)	136.32(9)	O(3)#2-Y(2)-N(2)	73.16(9)
O(8)-Y(2)-N(2)	63.93(8)	O(6)-Y(2)-N(2)	63.96(8)
O(13)#3-Y(2)-N(2)	70.94(9)	O(12)#3-Y(2)-N(2)	139.87(9)
N(1)#2-Y(2)-N(2)	122.28(9)	N(3)#3-Y(2)-N(2)	115.03(9)

Symmetry transformations used to generate equivalent atoms: #1 -x+y+1,-x+1,z #2 -y+1,x-y,z #3 -x+5/3,-y+4/3,-z+4/3

Out of the three CAM ligands, in CAM(1) both the carboxylate groups are bidentate through the connectivity with Y(1) and Y(2) (see Figure 2.3a). Whereas in CAM(2) and CAM(3) the connectivity of carboxylates are similar. In both cases, one carboxylate bidentate and connect Y(1) and Y(2) and other carboxylate monodentate through the connectivity with Y(2) (see Figure 2.3b and 2.3c).

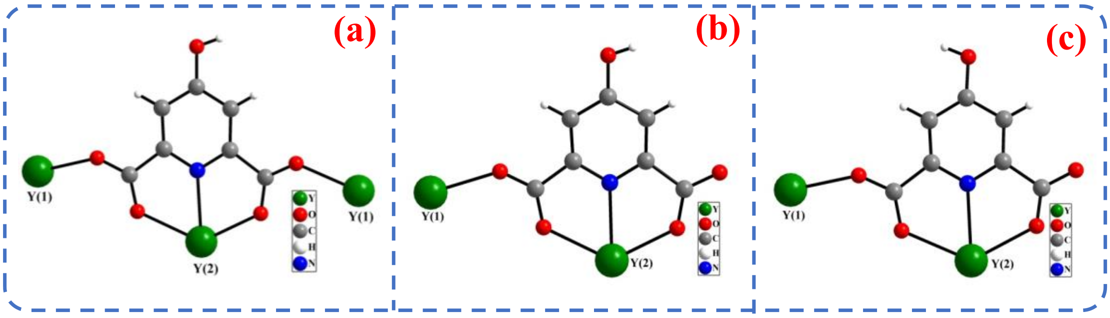

Fig. 2.3 The connectivity with the Y^{3+} ions- (a) CAM(1), (b) CAM(2), (c) CAM(3) in $[Y_2(CAM)_3(H_2O)_4].2H_2O$, **1a**.

In this structure, the Y^{3+} ions are connected by carboxylate groups and pyridine nitrogen atoms of CAM to generate a two-dimensional structure with water filled pore (Figure 2.4a). The two-dimensional structures are arranged in *AAA*… fashion to give rise over all three-dimensional arrangement (Figure 2.4b).

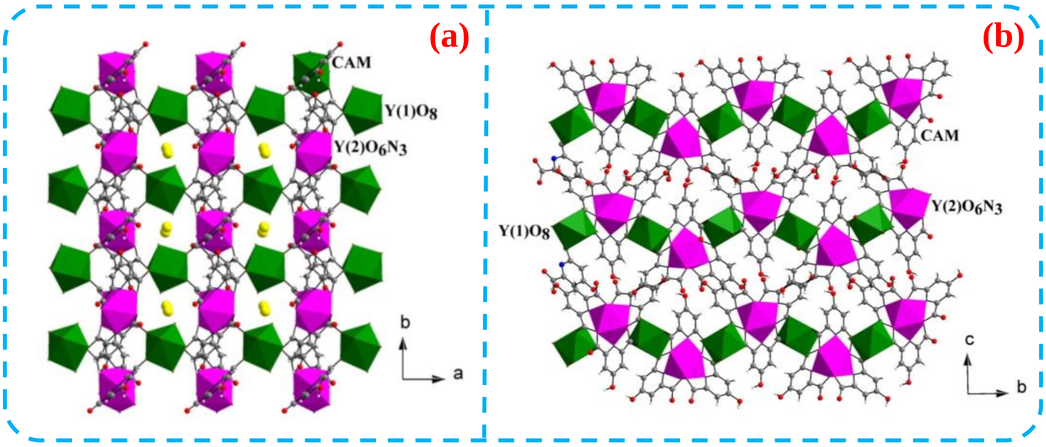

Fig. 2.4 (a) The two-dimensional structures $[Y_2(CAM)_3(H_2O)_4].2H_2O$, **1a**, in the *ab* plane formed by the connectivity of Y^{3+} ions and CAM. The oxygen atoms of lattice water molecules within the pores are shown in yellow color. (b) The three-dimensional arrangement of the two-dimensional structures in *AAA*… fashion.

2.3.2 Characterizations of Compound 1

Powder X-ray diffraction (XRD) patterns were recorded on well ground samples in the 2θ range 5-50° (Figure 2.5). The XRD patterns indicated that the product is a new material; the pattern is entirely consistent with the simulated XRD pattern generated based on the structure of pure Y compound, **1a**, determined using the single-crystal XRD.

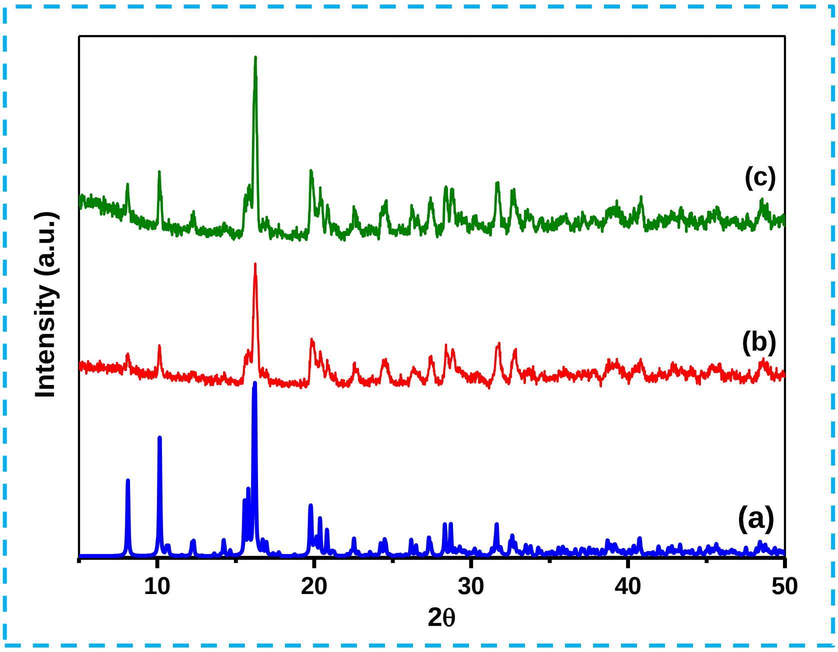

Fig. 2.5 Powder XRD (CuKα) patterns: (a) simulated from single crystal X-ray data of $[Y_2(CAM)_3(H_2O)_4].2H_2O$, **1a,** (b) hydrothermally synthesized $[Y_2(CAM)_3(H_2O)_4].2H_2O$, **1a,** and (c) hydrothermally synthesized $[Y_{1.8}Tb_{0.2}(CAM)_3(H_2O)_4].2H_2O$, **1.**

Thermogravimetric analysis (TGA) of compound **1** has been carried out in a nitrogen atmosphere (Figure 2.6a). The TGA experiment shows weight loss in three steps. The first weight loss of 4.40% (calculated 4.27%) up to 190°C is due to the removal of two lattice water molecules. The second weight loss of total 12.98% (calculated 12.81%) up to 340°C is due to the loss of four coordinated water molecules. The weight loss above 350°C is due to the decomposition of the framework. To understand about the porosity, nitrogen gas adsorption-desorption studies (BET experiment) of compound **1** were carried out. For that the powder sample were pretreated at 190 ºC for 60 min to ensure the removal of lattice water molecules. The BET experiment shows surface adsorption type behaviour with surface area of 32.4 m^2/g (Figure 2.6b). This is probably due to the contraction of the pore after the removal of lattice water molecules.

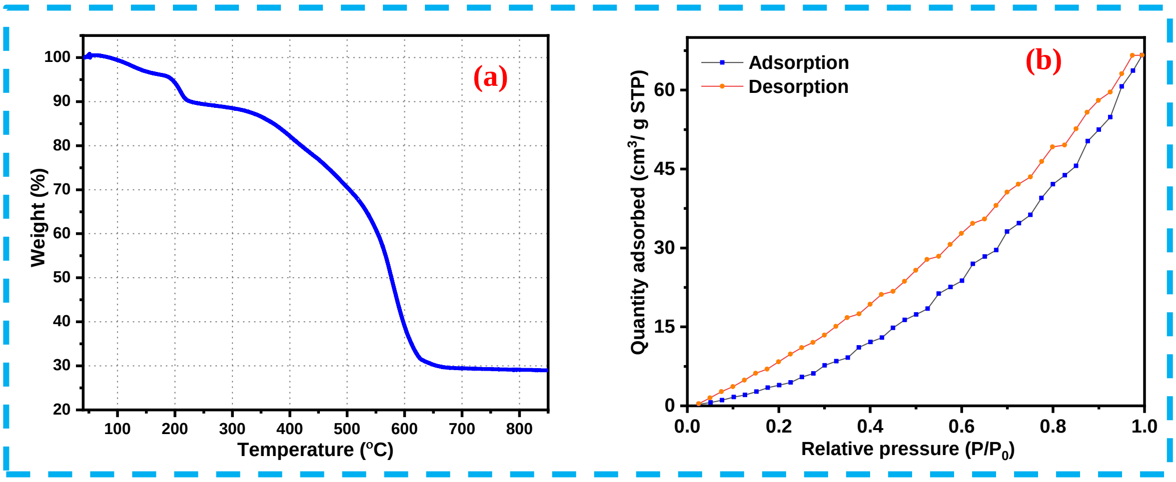

Fig. 2.6 (a) Thermogravimetric analysis (TGA) of compound **1** in nitrogen atmosphere and (b) N_2 sorption plot of compound **1**.

The IR spectra of the compounds were recorded in the spectral range 4000-500 cm^{-1}. All the characteristic peaks associated with the CAM ligands and water molecules have been observed. The prominent band around 3520 cm^{-1} is due to the presence of free hydroxyl group within the structure (Figure 2.7).

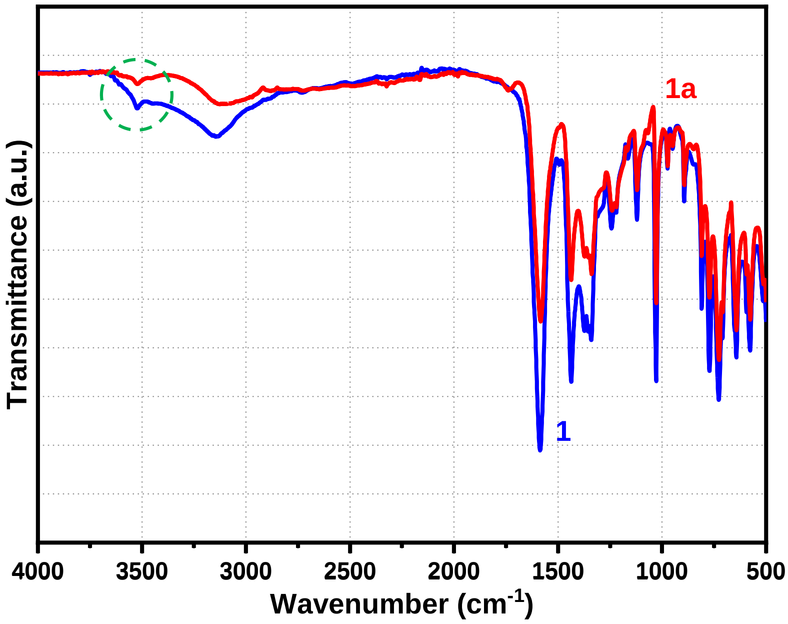

Fig. 2.7 IR spectra of compound **1** and **1a**. The peaks associated with free hydroxyl groups are encircled.

The EDX analysis was carried out on the well ground sample of compound **1** on several crystals which showed the presence of Tb and Y with a molar ratio of ~1:9 (Figure 2.8). Elemental mapping was also performed to confer the homogeneous presence of Tb and Y in compound **1** (Figure 2.9).

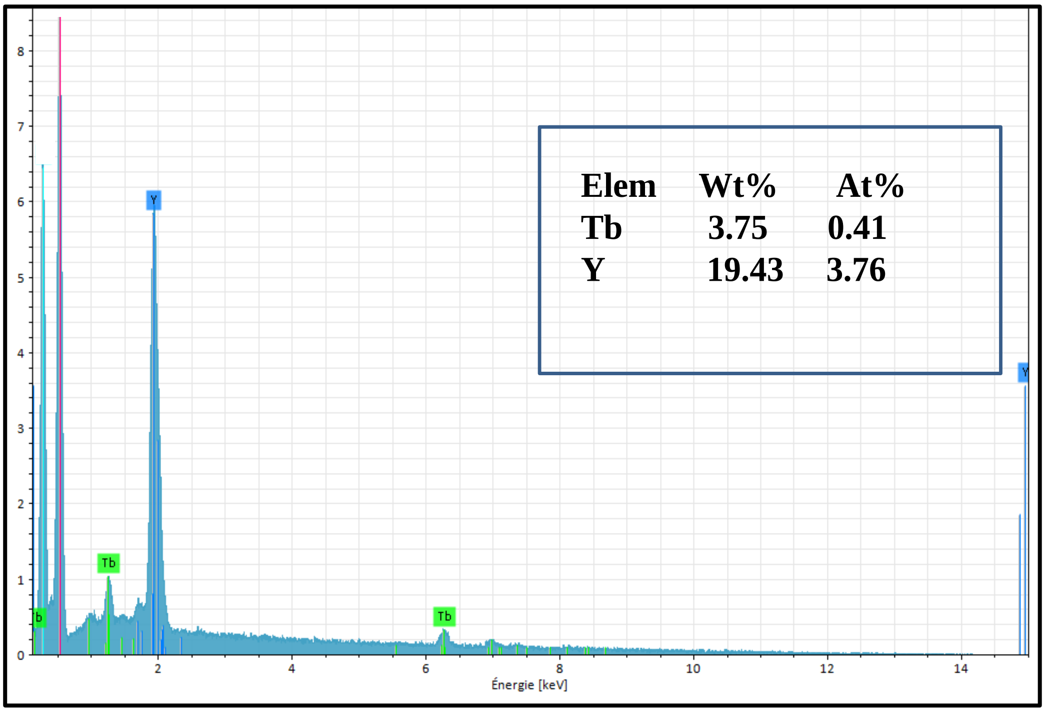

Elem	Wt%	At%
Tb	3.75	0.41
Y	19.43	3.76

Fig. 2.8 Representative EDX plot of compound **1.** Note the presence of Tb and Y are in molar ratio of ~ 1:9.

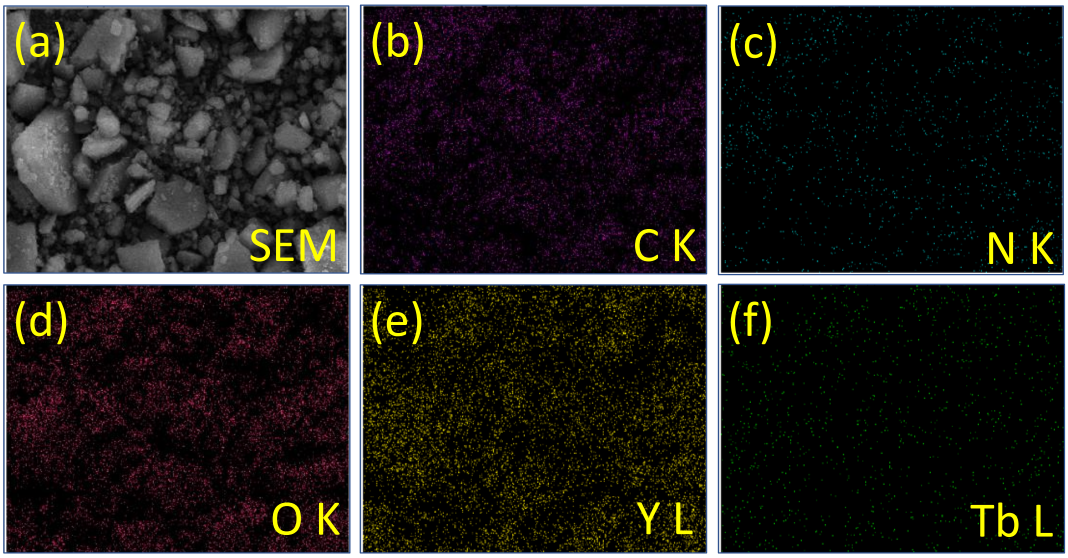

Fig. 2.9 SEM images of (a) compound **1**, corresponding to the elemental mapping images of compound **1** for (b) C K and (c) N K, (d) O K (e) Y L and (f) Tb L.

2.3.3 Photoluminescence behaviour

The photoluminescence property of compound **1** was investigated by using its aqueous solution upon excitation at 280 nm. The luminescence spectrum of **1** shows weak Tb^{3+} centered emission. The emission bands observed at 490, 545, 585 and 623 nm can be assigned to the $^5D_4 \rightarrow {}^7F_6$, $^5D_4 \rightarrow {}^7F_5$, $^5D_4 \rightarrow {}^7F_4$ and $^5D_4 \rightarrow {}^7F_3$ transitions, respectively, based on ligand sensitized Tb^{3+}centered emission (Figure 2.10). The emission at lower-wavelength regions observed for ligand center transitions of aromatic carboxylates were excluded by using appropriate cut-off filters.

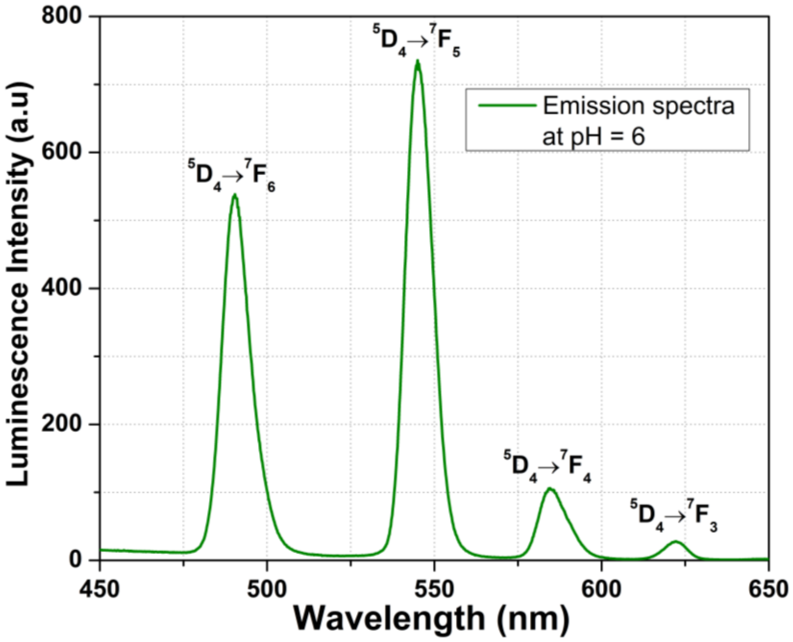

Fig. 2.10 Luminescence spectra of aqueous solution of compound **1** upon excitation at 280 nm at pH 6.

2.3.4 pH-Controlled Luminescence Behaviour

To see the pH response behaviour of **1**, the luminescence spectra of **1** were measured at different pH by adding NaOH/HCl solution. It can be seen from Figure 2.11; the luminescence intensity is significantly increased by 4.2 times (monitored at 545 nm) as pH is increased from 7.0 to 9.0. The changes in luminescence intensity in the basic medium indicate that compound **1** has a very high luminescence response behaviour that can be tuned by changing the pH of the medium. The change in luminescence intensity of **1** with the variation of pH of the solution is shown in Figure 2.12. There occurs a huge change in luminescence intensity when the pH value is increased from 7.5 which is also easily visible by the naked eye. The very high luminescence intensity enhancement in basic medium highlights that the sensitization process is highly pH dependent.

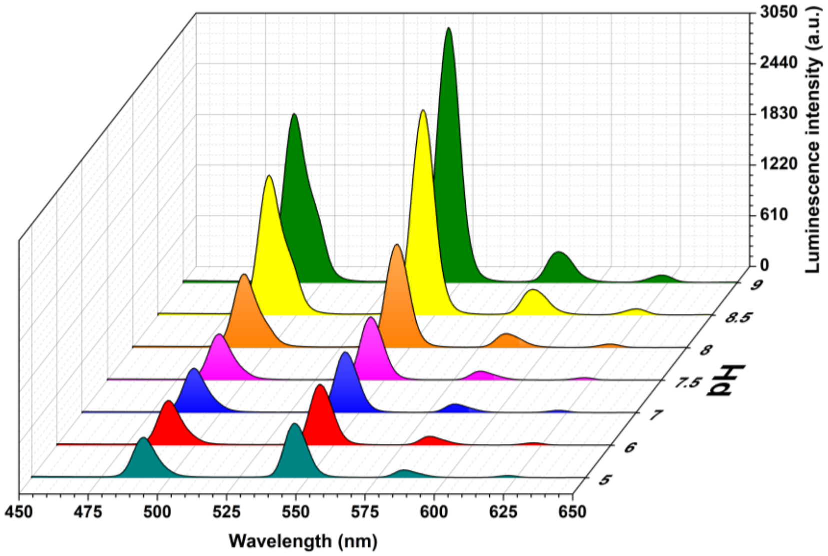

Fig. 2.11 Luminescence spectra of aqueous solution of compound **1** at different pH upon excitation at 280 nm.

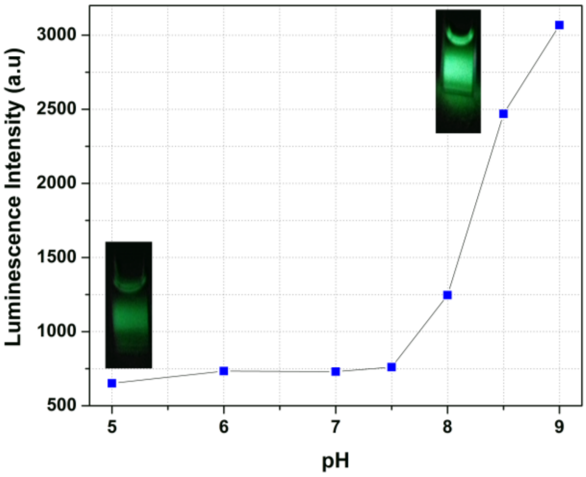

Fig. 2.12 Changes in luminescence intensity of **1** at different pH values, obtained by monitoring the luminescence intensity at λ_{em} = 545 nm. The insets show photographs of the sample solution at pH 5 (down) and pH 9 (top) under UV light (280 nm).

Luminescence spectra have also been measured in pH> 9 and pH< 5. In these regions, compound **1** shows negligible emission indicating the hampering of ligand-sensitized metal center emission (Figure 2.13a). The absorption spectra of compound **1** also show that it remains stable in the pH region 5-9 (Figure 2.13b). To check the stability of the compound in different pH, the powder samples (six sets) were immersed in water and controlled the pH by adding acid/base (HCl/NaOH) and kept for 2 hrs. After that, the powder samples have been collected by filtration. PXRD studies of the completely dried samples were carried out at room temperature. PXRD plots show that the compound is stable in the pH range of 5-9 (Figure 2.14). Small changes in PXRD have been observed at pH 4.

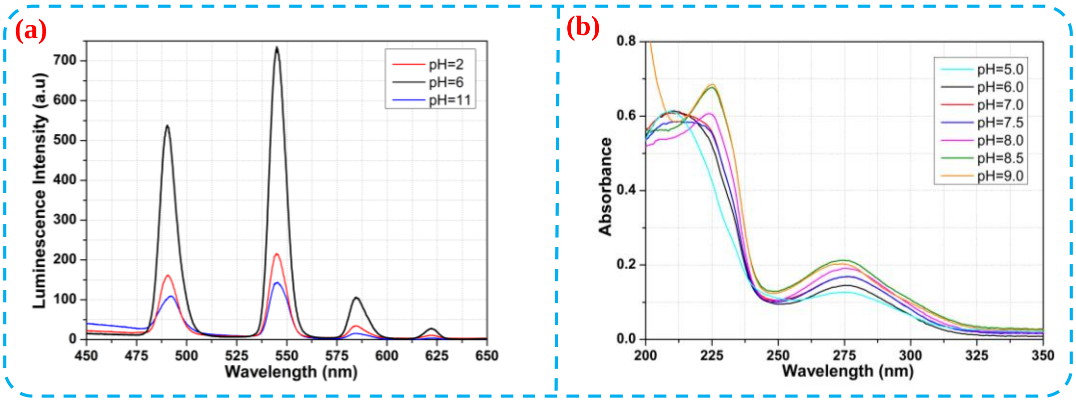

Fig. 2.13 (a) Luminescence spectra of aqueous solution of compound **1** at pH 2, pH 6, and pH 11 upon excitation at 280 nm and (b) Absorption spectra of compound **1** at different pH (5-9).

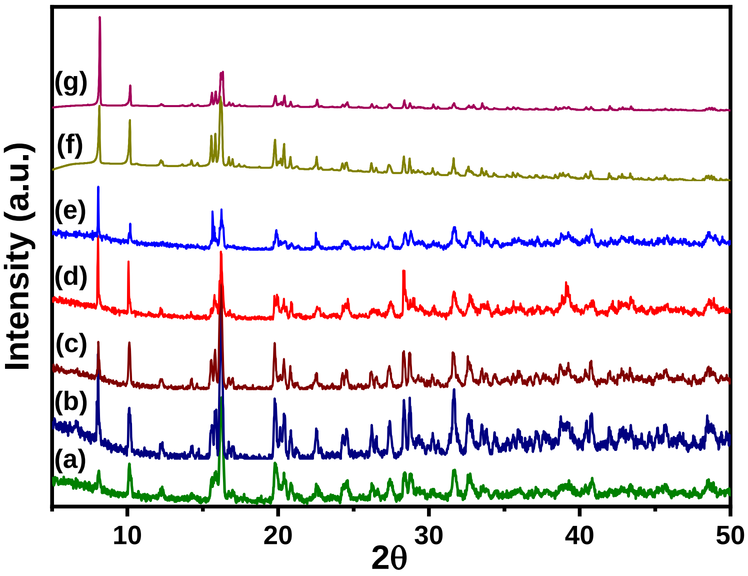

Fig. 2.14 Powder XRD (CuKα) patterns: (a) hydrothermally synthesized $[Y_{1.8}Tb_{0.2}(CAM)_3(H_2O)_4].2H_2O$, **1,** (b) pH= 4, (c) pH= 5, (d) pH=6, (e) pH=7, (f) pH= 8 and (g) pH= 9**.**

Luminescence lifetime measurements of **1** have been carried out at 545 nm (Tb^{3+}centered emission) upon excitation at 280 nm (Figure 2.15). The luminescence lifetime of **1** gradually increased from 0.74 ms to 0.99 ms when the pH value was changed from pH 5 to pH 9.

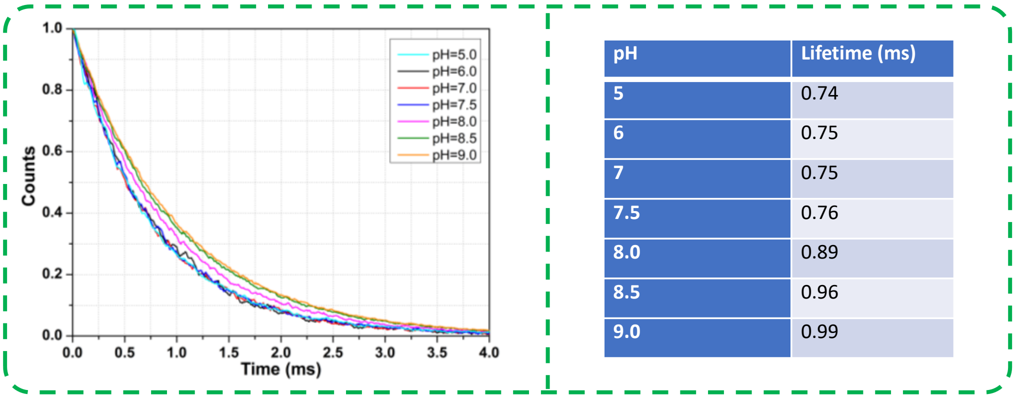

pH	Lifetime (ms)
5	0.74
6	0.75
7	0.75
7.5	0.76
8.0	0.89
8.5	0.96
9.0	0.99

Fig. 2.15 Time-resolved spectra of compound **1** at 545 nm upon excitation at 280 nm and the corresponding lifetime values at different pH.

The related luminescent MOF-based pH sensors are summarised in Table 2.4 to compare the range of sensing and output of luminescence response. The use of an f-electron (Tb) based activator supported by a non-f-based (Y) metal-organic host for the sensing of pH of the present compound is unique in comparison to other reported MOF materials. More importantly, the luminescence response of this compound in the biologically important pH range of 7-9 and a sharp increase in the physiological pH of human blood (~ 7.5) is noteworthy. For this purpose, we have also performed luminescence-based titration using the phosphate buffer in the pH range 6-8 (Figure 2.16a). Here also luminescence intensity of compound **1** increases with the increase of pH in the range of 7 to 8 (Figure 2.16b).

Table 2.4 A summary of luminescence-based detection of pH using the metal-organic framework.

Compound	pH sensing range	Nature of Output	Reference
$[Eu_3(C_{14}H_6N_2O_4)_4(OH)(H_2O)_4]\cdot 2H_2O$	5–7.5	turn on, the linear	65a
$Zr_6(\mu^3\text{-}O)_4(\mu^3\text{-}OH)_4(OH)_4(H_2O)_4(H_2TCPP)_2$	7-10	turn-on, linear	64a
F-UiO	5-7	turn-on,	64b
$Zr_6(\mu^3\text{-}OH)_8(OH)_8(CO_2)_8$, PCN-222	0-3	turn-off, turn-on	64c
MOF-253-Eu–TTA	5-7.2	turn on	65b
UiO-66-N=N-ind	9-12	turn on, the linear	64d
$[Eu_xTb_{1-x}(D\text{-}cam)(Himdc)_2(H_2O)_2]$	6.8-8	turn on, the linear	65c
$\{[Tb_4(\mu^3\text{–}OH)_4L_3\cdot(H_2O)_7]Cl_{0.63}\cdot(NO_3)_{4.37}\cdot 3H_2O\}_n$	2-7	turn on, the linear	65d
$[Tb(L_1)_{2/3}(L_2)_{1/2}(H_2O)_2].2H_2O$	4–10	4-7= turn on,	65e

		7-10=turn off	
$[H_3O][Eu_3(HBPTC)_2(BPTC)(H2O)_2]$. 4DMA	7.5-10	7.5-10=linear, turn off	65f
$\{[Cd_{1.5}(C_{18}H_{10}O_{10})]\cdot(H_3O)(H_2O)_3\}_n$	2.0-12.2	2-7=turn off, 9.5-11=turn on	70
Al-MIL-101-NH_2	4-7.7	turn on, the linear	35
$[Eu_2(pydcH)_6]\cdot 3H_2O$	2-6	turn on, the linear	65g
Eu_xTb_{1-x}Hdpda	3.90-7.50	Tb^{3+}= turn on, Eu^{3+}=not changed	65h
$Eu_{2x}Tb_{2-2x}(fum)_2(ox)(H_2O)_4$	3.00- 7.00	turn on	65i
DMF–Tb–Phen nanoparticles	2-10	turn off, linear	65j
RB-PCN	1.7-11.3	1.7-7 = turn on, 7.1-11.3= turn off	64e
$[Zn(cpon)]_n$	2-11.5	2-6.5= turn off, 8-11.5= turn on	71
CDs@UiO-$66(OH)_2$	3-7	turn off	64f
$Zr_6O_4(OH)_8(H_2O)_4(CTTB)_2$ $Zr_6O_4(OH)_8(H_2O)_4(CTNA)_2$	1-8	6-0=turn off, 6-9=remain same	64g
$Zr_6(\mu^3\text{-}O)_4(OH)_4(bpydc)_{12}$	1.06-10.99	1.06-8 =turn on, 8-12 =remain same	64h
$[Eu_2(NDC)_3(DMF)_2]\cdot DMF$	3-4	turn off	65k
$\{[Eu(PPTA)_{0.5}(NO_3)(DMF)_2]\cdot H_2O\}_n$	2-10.5	2-7=turn off, 7-10.5=turn on	65l
UiO-67-bpydc	1-9	4-6.5=linear, turn on	64i
$Zr_6(\mu^3\text{-}O)_4(\mu^3\text{-}OH)_4(ITTC)_4$	10.2-11.08	turn on, non-linear	64j
$CoLi(HL)\cdot 4DMA$ $CoLi_2(L)(DMF)_2\cdot DMF\cdot H_2O$	0.7-1.7	turn on	74
Eu- MOF composite	3-10	turn on, the linear	65m
$[(UO_2)(H_2DTATC)]$	9.4-11.5	turn on, the linear	65n
UiO-67-bpy-Eu-BTA	1.05-9.85	turn on, exponential	75
(1-OHP@Co/Tb-DPA MOF)	0.3-5	turn on, the linear	76
$[L_4Cd_3(H_2O)_2]_n$	2-3.12	turn on, the linear	77
$[Y_{1.8}Tb_{0.2}(CAM)_3(H_2O)_4].2H_2O$, **1**	7-9	linear, turn on	This work

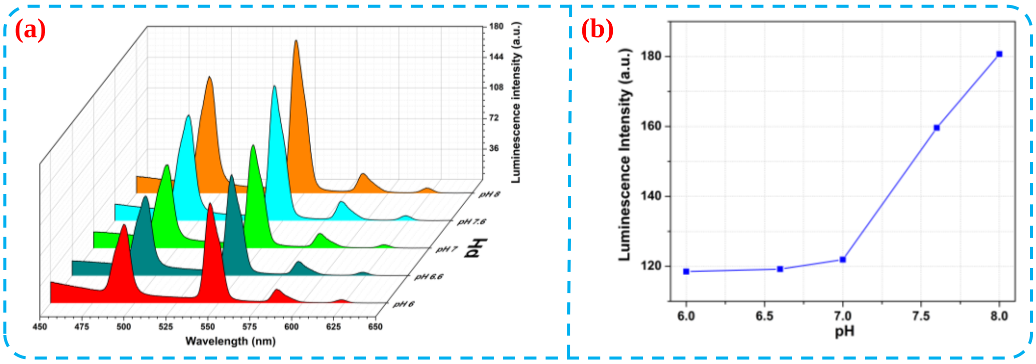

Fig. 2.16 (a) Luminescence spectra of compound **1** in phosphate buffer solution at different pH values upon excitation at 280 nm and (b) Changes in luminescence intensity of **1** at different pH values in phosphate buffer, obtained by monitoring the luminescence intensity at λ_{em} = 545 nm.

2.3.5 pH sensing mechanism

In the case of lanthanide-based metal-organic frameworks, the organic ligands are excited to the higher excited singlet state (S_2), from which non-radiative transition occurs to the excited state (S_1) of the ligand. A part of the energy is transferred from the excited state of ligands (S_1) to the terbium center, resulting in metal-centered luminescence. As the luminescence spectra of the terbium center arise due to the energy transfer from the excited state of the ligand to the terbium center, the characteristic spectral property of the ligand and the adeptness of energy transfer are important for the luminescence of the terbium center. So, it is easily perceived that the energy transfer process from the ligand to the Tb^{3+} ion may be tuned by the slight modification in the ligand through the changing of pH of the medium. Due to the deprotonation of the hydroxyl proton, the electron density within the aromatic ring of the ligand increases. This effect strengthens the bonding between ligands and Tb^{3+} metal ions. Eventually, due to the deprotonation of hydroxyl groups, the energy transfer from the ligand to the metal center increases which results in the gradual luminescence turn-on and steady increase of luminescence lifetime. The sharp change in luminescence intensity in pH ~ 7.5 which is close to the physiological pH of human blood is the important observation of this study.

2.4 CONCLUSIONS

A terbium-doped yttrium-based hydroxyl-functionalized metal-organic framework phosphor, compound **1** has been successfully synthesized using the hydrothermal technique. The structure of compound **1** was established by determining the single crystal structure of isomorphous pure yttrium-based compound,**1a**. Compound **1** was thoroughly characterized by PXRD, TGA, IR, EDX, SEM-elemental mapping, and BET analysis. The luminescence property of compound **1** was utilized for the sensing of pH and it has been observed that the emission intensity increased by 4.2 times from pH 7 to pH 9 along with a sudden jump at pH > 7.5. The luminescence lifetime decay studies also show a gradual increase in the lifetime of Tb^{3+}center emission from 0.75 ms to 0.99 ms (pH 7 to pH 9). The significance of the present work for pH sensing is noteworthy based on two important points.

(1) Present work, for the first time, demonstrates the potential of the use of an f-electron [Tb] based activator supported by a non-f-based [Y] metal-organic host for the

sensing of pH where the self-quenching, generally observed for pure Tb compounds, is minimized.

(2) The luminescence response of compound **1** in the biologically important pH range 7-9 based on the free hydroxyl groups suggests its usefulness for real-life applications and human health.

2.5 REFERENCES

1. Wencel, D.; Abel, T.; McDonagh, C., *Anal. Chem.*, **2014**, 86, 15-29.
2. Kwon, S. S.; Yi, J.; Lee, W. W.; Shin, J. H.; Kim, S. H.; Cho, S. H.; Nam, S.; Park, W., *ACS Appl. Mater. Interfaces*, **2016**, 8, 834-839.
3. Jin, L.; Shi, L.; Shi, W.; Meng, Z.; Shang, L.; Shen, Y., *Analyst*, **2019**, 144, 3533-3538.
4. Han, J.; Burgess, K., *Chem. Rev.*, **2010**, 110, 2709-2728.
5. Xia, T.; Cui, Y.; Yang, Y.; Qian, G., *ChemNanoMat,* **2017**,3, 51-58.
6. Martin, C.; Pedersen, S. F.; Schwab, A.; Stock, C., *Am. J. Physiol. Cell. Physiol.*, **2011**, 300, C490-C495.
7. Kennedy, R. T.; Huang, L.; Aspinwall, C. A., *J. Am. Chem. Soc.*, **1996**, 118, 1795-1796.
8. Matsuyama, S.; Reed, J. C., *Cell Death Differ.,* **2000**, 7, 1155-1165.
9. Casey, J. R.; Grinstein, S.; Orlowski, J., *Nat. Rev. Mol. Cell Biol.*, **2010**, 11, 50-61.
10. Hetzel, F. W.; Chopp, M., *Radiat. Res.*, **1990**, 122, 229-233.
11. Lyall, V.; Biber, T. U., *Am. J. Physiol. Renal. Physiol.*, **1994**, 266, F685-F696.
12. Zhang, X. M.; Lin, Y. X.; Gillies, R. J., *J. Nucl. Med.,* **2010**, 51,1167-1170.
13. Wang, J.; Li, Y.; Jiang, M.; Liu, Y.; Zhang, L.; Wu, P., *Chem. Eur. J.*, **2016**, 22, 13023-13028.
14. Feng, Y.; Liu, Y.; Su, C.; Ji, X.; He, Z., *Sens. Actuators, B,* **2014**, 203, 795-801.
15. Qu, F.; Li, N. B.; Luo, H. Q., *Langmuir*, **2013**, 29, 1199-1205.
16. Wu, Z. L.; Gao, M. X.; Wang, T. T.; Wan, X. Y.; Zheng, L. L.; Huang, C. Z., *Nanoscale*, **2014**, 6, 3868-3874.
17. Chen, X.; Sun, X.; Xu, W.; Pan, G.; Zhou, D.; Zhu, J.; Wang, H.; Bai, X.; Dong, B.; Song, H., *Nanoscale*, **2018**, 10, 1111-1118.
18. Zhang, X.; Jiang, K.; He, H.; Yue, D.; Zhao, D.; Cui, Y.; Yang, Y.; Qian, G., *Sens. Actuators, B*, **2018**,254, 1069-1077.

19. Galdino, F.E.; Smith, J.P.; Kwamou, S.I.; Kampouris, D.K.; Iniesta, J.; Smith, G.C.; Bonacin, J. A.; Banks, C. E., *Anal. Chem.*, **2015**,87, 11666-11672.
20. Santos, L.; Neto, J.P.; Crespo, A.; Nunes, D.; Costa, N.; Fonseca, I.M.; Barquinha, P.; Pereira, L.; Silva, J.; Martins, R.; Fortunato, E., *ACS Appl. Mat. Interfaces.,* **2014**,6, 12226-12234.
21. Qi, Z.; Chen, Y., *Biosens.Bioelectron.,* **2017**, 87, 236-241.
22. Wencel, D.; Abel, T.; McDonagh, C., *Anal. Chem.*, **2014**, 86, 15-29.
23. Kim, D.; Cho, S. J.; Cho, C.; Kim, K. B.; Kim M.; Shim, Y., *Biosens. Bioelectron.,***2016**, 79,165.
24. Dengler, A. K.; Wightman, R. M.; McCarty, G. S., *Anal. Chem.,* **2015**, 87,10556-10564.
25. Mori, S.; Eleff, S. M.; Pilatus, U.; Mori, N.; vanZijl, P. C. M., *Magn.Reson.Med.,***1998**, 40,36-42.
26. Yu, K. K.; Li, K.; Hou, J. T.; Yang, J.; Xie, Y. M.; Yu, X. Q., *Polym. Chem.*, **2014**, 5,5804-5812.
27. Chen, H.; Wang, J.; Shan, D.; Chen, J.; Zhang, S.; Lu, X., *Anal. Chem.*, **2018**, 90**,** 7056.
28. Spudich, J. L.; Koshland, D. E. J., *Nature,* **1976**, 262, 467.
29. Hesse, S. J. A.; Ruijter, G. J. G.; Dijkema, C.; Visser, J. J., *Biotechnol.*, **2000**, 77, 5.
30. Zhang, R. G.; Kelsen, S. G.; LaManna, J. C. J., *Appl. Physiol.*, **1990**, 68, 1101.
31. Xia, T.; Zhu, F.; Jiang, K.; Cui, Y.; Yang, Y.; Qian, G., *Dalton Trans.*, **2017**, 46, 7549.
32. Singha, D. K.; Majee, P.; Mondal, S. K.; Mahata, P., *RSC Adv.*, **2015**, 5, 102076.
33. Xiang, Z.; Fang, C.; Leng, S.; Cao, D., *J. Mater. Chem. A*, **2014**, 2, 7662.
34. Liu, S.; Xiang, Z.; Hu, Z.; Zheng, X.; Cao, D., *J. Mater. Chem.*, **2011**, 21, 6649.
35. Xu, X. Y.; Yan, B., *Dalton Trans.*, **2016**, 45, 7078.
36. Vicentini, L. M.; Villereal, M. L., *Life Sci.*, **1986**, 38, 2269.
37. Kubohara, Y.; Okamoto, K., *FASEB J.*, **1991**, 8, 869.
38. Ronnie, M. A.; Kjell, C.; Anders, L.; Hjalmar, B., *Anal. Biochem.*, **2000**, 283, 104.
39. Yan, P.; Li, X.; Dong, Y.; Li, B.; Wu, Y., *Analyst*, **2019**, 144, 2891-2897.
40. Jin, T.; Sasaki, A.; Kinjo, M.; Miyazaki, J., *Chem. Commun.*, **2010**, 46, 2408-2410.
41. Zhang, Z.; Bando, K.; Mochizuki, K.; Taguchi, A.; Fujita, K.; Kawata, S., *Anal. Chem.*, **2019**, 91, 3254-3261.
42. Robinson, K. J.; Huynh, G. T.; Kouskousis, B. P.; Fletcher, N. L.; Houston, Z. H.; Thurecht, K. J.; Corrie, S. R., *ACS Sens.,* **2018**, 3, 967-975.
43. Nsanzamahoro, S.; Li, L.; Mutuyimana, F. P.; Liu, J.; Ren, C.; Qin, H.; Chen, H., *New J. Chem.*, **2020**, 44, 19294-19299.
44. Shangguan, J.; He, D.; He, X.; Wang, K.; Xu, F.; Liu, J.; Tang, J.; Yang, X.; Huang, J., *Anal. Chem.*, **2016**, 88, 7837-7843.

45. Wang, L.; Li, M.; Li, W.; Han, Y.; Liu, Y.; Li, Z.; Zhangand, B.; Pan, D., *ACS Sustainable Chem. Eng.*, **2018**, 6, 12668.
46. Sun, Y.; Wang, X.; Wang, C.; Tong, D.; Wu, Q.; Jiang, K.; Jiang, Y.; Wang, C.; Yang, M., *Microchim Acta,* **2018**, 185, 83-90.
47. Ji, X.; Yao, Y.; Li, J.; Yan, X.; Huang, F., *J. Am. Chem. Soc.*, **2013**, 135, 74-77.
48. Mei, L.; He, S.; Zhang, L.; Xu, K.; Zhong, W., *Org. Biomol. Chem.*, **2019**, 17, 939-944.
49. Brown, R. T.; Fletcher, N. C.; Danosand, L. N.; Halcovitch, R., *Eur. J. Inorg. Chem.,***2019**, 110-117.
50. Hu, J.; Zhang, X.; Wang, D.; Hu, X.; Liu, T.; Zhang, G.; Liu, S., *J. Mater. Chem.*, **2011**, 21, 19030-19038.
51. Park, C. H.; Yang, H.; Lee, J. H.; Cho, H.; Kim, D.; Lee, D. C.; Kim, B. J., *Chem. Mater.,* **2015**, 27, 5288-5294.
52. Yang, Y.; Wang, K.Z.; Yan, D., *ACS Appl. Mater. Interfaces,* **2016**, 8, 15489-15496.
53. (a) Li, H.; Eddaoudi, M.; O'Keeffe, M.; Yaghi, O. M., *Nature*, **1999**, 402, 276-279.
    (b) Long, J. R.; Yaghi, O. M., *Chem. Soc. Rev.*, **2009**, 38, 1213-1214.
    (c) Kaye, S. S.; Dailly, A.; Yaghi, O. M.; Long, J. R., *J. Am. Chem. Soc.*, **2007**, 129, 14176-14177.
    (d) Mahata, P.; Natarajan, S., *Chem. Soc. Rev.*, **2009**, 38, 2304-2318.
54. (a) Li, Y.; Yang, R. T., *Langmuir*,**2007**, 23*,* 12937-12944.
    (b) Ma, S.; Zhou, H. C., *Chem. Commun.*, **2010**, 46, 44-53.
    (c) Li, J. R.; Kuppler, R. J.; Zhou, H. C., *Chem. Soc. Rev.*, **2009**, 38, 1477-1504.
    (d) Alezi, D.; Belmabkhout, Y.; Suyetin, M.; Bhatt, P. M.; Weseliński, L. J.; Solovyeva, V.; Adil, K.; Spanopoulos, I.; Trikalitis, P. N.; Emwas, A. H.; Eddaoudi, M., *J. Am. Chem. Soc.*, **2015**, 137, 13308-13318.
    (e) Dhainaut, J.; Bonneau, M.; Ueoka, R.; Kanamori, K.; Furukawa, S., *ACS Appl. Mater. Interfaces*, **2020**, 12, 10983-10992.
55. (a) Wu, H. B.; Lou, X. W., *Sci. Adv.*, **2017**, 3, eaap9252.
    (b) Xiao, P.; Bu, F.; Zhao, R.; Aly Aboud, M. F.; Shakir, I.; Xu, Y., *ACS Nano*, **2018**, 12, 3947-3953.
    (c) Liu, X. F.; Guo, X. Q.; Wang, R.; Liu, Q. C.; Li, Z. J.; Zang, S. Q.; Mak, T. C. W., *J. Mater. Chem. A*, **2019**, 7, 2838-2844.
    (d) Lee, C. S.; Moon, J.; Park, J. T.; Kim, J. H., *ACS Sustainable Chem. Eng.,* **2020**, 8, 3773-3785.
56. (a) Foster, M. E.; Azoulay, J. D.; Wong, B. M.; Allendorf, M. D. *Chem. Sci.*, **2014**, 5, 2081-2090.
    (b) Zhang, X.; Ballem, M. A.; Hu, Z. J.; Bergman, P.; Uvdal, K., *Angew. Chem.*, **2011**, 123, 5847-5851.

(c) Lee, C. Y.; Farha, O. K.; Hong, B. J.; Sarjeant, A. A.; Nguyen, S. B. T.; Hupp, J. T., *J. Am. Chem. Soc.*, **2011**, 133, 15858-15861.

(d) Ding, Z.; Wang, C.; Wang, S.; Wu, L.; Zhang, X., *Microchimica Acta*, **2019**, 186, 476-485.

57. (a) Wang, C.; Zhang, T.; Lin, W., *Chem. Rev.*, **2012**, 112, 1084-1104.

(b) Mingabudinova, L. R.; Vinogradov, V. V.; Milichko, V. A.; Hawkins, E. H.; Vinogradov, A. V., *Chem. Soc. Rev.,***2016**, 45, 5408-5431.

(c) Gu, C.; Zhang, H.; You, P.; Zhang, Q.; Luo, G.; Shen, Q.; Wang, Z.; Hu, J., *Nano Lett.*, **2019**, 19, 9095-9101.

(d) Ni, B.; Sun, W.; Kang, J.; Zhang, Y., *J. Phys. Chem. C*, **2020**, 124, 11595-11608.

58. (a) Horcajada, P.; Gref, R.; Baati, T.; Allan, P. K.; Maurin, G.; Couvreur, P.; Ferey, G.; Morris, R. E.; Serre, C., *Chem. Rev.*, **2012**, 112, 1232-1268.

(b) Chen, X.; Tong, R.; Shi, Z.; Yang, B.; Liu, H.; Ding, S.; Wang, X.; Lei, Q.; Wu, J.; Fang, W., *ACS Appl. Mater. Interfaces*, **2018**, 10, 2328-2337.

59. (a) Lee, J. Y.; Farha, O. K.; Roberts, J. K.; Scheidt, A.; Nguyen, S. T.; Hupp, J. T., *Chem. Soc. Rev.*, **2009**, 38, 1450-1459.

(b) Yoon, M.; Srirambalaji, R.; Kim, K., *Chem. Rev.*, **2012**, 112, 1196-1231.

(c) Wei, Y. S.; Zhang, M.; Zou, R.; Xu, Q., *Chem. Rev.*, **2020**, 120, 12089-12174.

(d) Huang, C.; Guo, Z.; Zheng, X.; Chen, X.; Xue, Z.; Zhang, S.; Li, X.; Guan, B.; Li, X.; Hu, G.; Wang, T., *J. Am. Chem. Soc.*, **2020**, 142, 9408-9414.

60. (a) Hu, Z.; Deibert, B. J.; Li, J., *Chem. Soc. Rev.*,**2014**, 43, 5815-5840.

(b) Samanta, P.; Let, S.; Mandal, W.; Dutta, S.; Ghosh, S. K., *Inorg. Chem. Front.*, **2020**, **7**, 1801-1821.

(c) Singha, D. K.; Majee, P.; Hui, S.; Mondal, S. K.; Mahata, P., *Dalton Trans.*, **2020**, 49, 829-840.

(d) Liu, X. Y.; Lustig, W. P.; Li, J., *ACS Energy Lett.*, **2020**, 5, 2671-2680.

(e) Goswami, R.; Mandal, S. C.; Pathak, B.; and Neogi, S., *ACS Appl. Mater. Interfaces*, **2019**, 11, 9042-9053.

(f) Wanga, X.; Chua, C.; Wua, Y.; Denga, Y.; Zhoua, J.; Yanga, M.; Zhanga, S.; Huoa, D.; Houa, C., *Sens. Actuators, B*, **2020**, 321, 128455-128463.

(g) Singha, D. K.; Bhattacharya, S.; Majee, P.; Mondal, S. K.; Kumar, M.; Mahata, P., *J. Mater. Chem. A*, **2014**, 2, 20908-20915.

61. (a) Mahata, P.; Natarajan, S.; Panissod, P.; and Drillon, M.; *J. Am. Chem. Soc.*, **2009**, 131, 10140-10150.

(b) Thorarinsdottir, A. E.; Harris, T. D., *Chem. Rev.*, **2020**, 120, 8716-8789.

(c) Mahata, P.; Sen, D.; Natarajan, S., *Chem. Commun.*, **2008**, 1278-1280.

(d) Dechambenoit, P.; Long, J. R., *Chem. Soc. Rev.*, **2011**, 40, 3249-3265.

62. (a) Li, A. L.; Gao, Q.; Xu, J.; Bu, X. H., *Coord. Chem. Rev.,* **2017**, 344, 54-82.
    (b) Sadakiyo, M.; Yamada, T.; Kitagawa, H., *J. Am. Chem. Soc.,* **2014**, 136, 13166-13169.
    (c) Yoon, M.; Suh, K.; Natarajan, S.; Kim, K., *Angew. Chem. Int. Ed.,* **2013**, 52, 2688-2700.
    (d) Agarwal, R. A.; Das, A.; Omar, S.; *J. Phys. Chem. C*, **2020**, 124, 18901-18910.
63. (a) Xu, B.; Zhang, H.; Mei, H.; D. Sun, *Coord. Chem. Rev.,* **2020**, 420, 213438-213459.
    (b) Miao, C.; Xiao, X.; Gong, Y.; Zhu, K.; Cheng, K.; Ye, K.; Yan, J.; Cao, D.; Wang, G.; Xu, P., *ACS Appl. Mater. Interfaces*, **2020**, 12, 9365-9375.
    (c) Rajak, R.; Saraf, M.; Mobin, S. M., *Inorg. Chem.*, **2020**, 59, 1642-1652.
    (d) Salunkhe, R. R.; Kaneti, Y. V.; Yamauchi, Y., *ACS Nano*, **2017**, 11, 5293-5308.
64. (a) Jiang, H. L.; Feng, D.; Wang, K.; Gu, Z. Y.; Wei, Z.; Chen, Y. P.; Zhou, H. C., *J. Am. Chem. Soc.,* **2013**, 135, 13934-13938.
    (b) He, C.; Lu, K.; Lin, W., *J. Am. Chem. Soc.*, **2014**, 136, 12253-12256.
    (c) Deibert, B. J.; Li, J., *Chem. Commun.,***2014**, 50, 9636-9639.
    (d) Sigalat, J. A.; Bradshaw, D., *Chem. Commun.*,**2014**,50, 4711-4713.
    (e) Chen, H.; Wang, J.; Shan, D.; Chen, J.; Zhang, S.; Lu, X., *Anal. Chem.*, **2018**, 90, 7056-7063.
    (f) Yao, C.; Xu, Y.; Xia, Z., *J. Mater. Chem. C*,**2018**, 6, 4396-4399.
    (g) Lv, X. L.; Xie, L. H.; Wang, B.; Zhao, M.; Cui, Y.; Li, J. R., *J. Mater. Chem. C*, **2018**, 6, 10628-10639.
    (h) Zhang, X.; Jiang, K.; He, H.; Yue, D.; Zhao, D.; Cui, Y.; Yang, Y.; Qian, G., *Sens. Actuators, B,* **2018**, 254, 1069-1077.
    (i) Wu, S. H.; Wang, S.; Fang, W. L.; Guo, X. F.; Wang, H., *Anal. Methods*, **2019**, 11, 36-43.
    (j) Guo, B.; Li, F.; Wang, C.; Zhang, L.; Sun, D., *J. Mater. Chem. A*, **2019**, 7, 13173-13179.
65. (a) Harbuzaru, B. V.; Corma, A.; Rey, F.; Jord, J. L.; Ananias, D.; Carlos, L. D.; Rocha, J., *Angew. Chem.*, **2009**, 121, 6598-6601.
    (b) Lu, Y.; Yan, B., *Chem. Commun.*,**2014**, 50, 13323-13326.
    (c) Han, Y. H.; Tian, C. B.; Li, Q. H.; Du, S. W., *J. Mater. Chem. C*, **2014**, 2, 8065-8070.
    (d) Li, H. Y.; Wei, Y. L.; Dong, X. Y.; Zang, S. Q.; Mak, T. C. W., *Chem. Mater.*, **2015**, 27, 1327-1331.
    (e) Wang, J.; Sun, W.; Chang, S.; Liu, H.; Zhang, G.; Wanga, Y.; Liu, Z., *RSC Adv.*, **2015**, 5, 48574-48579.
    (f) Meng, Q.; Xin, X.; Zhang, L.; Dai, F.; Wanga, R.; Sun, D., *J. Mater. Chem. A*, **2015**, 3, 24016-24021.

(g) Singha, D. K.; Majee, P.; Mondal, S. K.; Mahata, P., *Eur. J. Inorg. Chem.*,**2016**, 4631-4636.

(h) Xia, T.; Cui, Y.; Yang, Y.; Qian, G., *ChemNanoMat*, **2017**, 3, 51-57.

(i) Xia, T.; Zhu, F.; Jiang, K.; Cui, Y.; Yang, Y.; Qian, G., *Dalton Trans.*, **2017**, 46, 7549-7555.

(j) Qi, Z.; Chen, Y., *Biosens.Bioelectron*, **2017**, 87, 236-241.

(k) Zhao, Y.; Wan, M. Y.; Bai, J. P.; Zeng, H.; Lu, W.; Li, D., *J. Mater. Chem. A*, **2019**, **7**, 11127-11133.

(l) Hou, S. L.; Dong, J.; Tang, M. H.; Jiang, X. L.; Jiao, Z. H.; Zhao, B., *Anal. Chem.*, **2019**, 91, 5455-5460.

(m) Huang, S. Z.; Liu, S. S.; Zhang, H.; Han, Z.; Zhao, G.; Dong, X. Y.; Zang, S., *ACS Appl. Mater. Interfaces,* **2020**, 12, 28720-28726.

(n) Liu, T.; Yan, B., *Ind. Eng. Chem. Res.,* **2020**, 59, 1764-1771.

66. *Apex3 v2017.3-0*, *Saint V8.38A*, *SAINT V8.38A*; Bruker AXS Inc.: Madison, WI, **2018**.
67. Krause, L.; Herbst-Irmer, R.; Sheldrick, G. M.; Stalke, D. J., *Appl. Crystallogr.,* **2015**, 48, 3-10.
68. Altomare, A.; Cascarano, G.; Giacovazzo, C.; Guagliardi, A., *J. Appl. Crystallogr,.* **1993**, 26, 343-350.
69. Sheldrick, G. M., *Crystal Structure Refinement with SHELXL. Acta Crystallogr., Sect. C: Struct. Chem.,* **2015**, 71, 3-8.
70. Farrugia, L. J., *WinGX suite for Small-Molecule Single-Crystal Crystallography. J. Appl. Crystallogr.,* **1999**, 32**,** 837-838.
71. Spek, A. L., *Single-Crystal Structure Validation with the Program PLATON. J. Appl. Crystallogr,.* **2003**, 36, 7-13.
72. Wang, J.; Li, Y.; Jiang, M.; Liu, Y.; Zhang, L.; Wu, P., *Chem.-Eur. J.,* **2016**, 22, 13023-13027.
73. Xing, K.; Fan, R.; Wang, F.; Nie, H.; Du, X.; Gai, S.; Wang, P.; Yang, Y., *ACS Appl. Mater. Interfaces*, **2018**, 10, 22746-22756.
74. Lia, M.; Yanga, W.; Qiua, P.; Rena, G.; Lia, C.; Chena, Z.; Wang, Y.; Pan, Q., *J. Lumin.,* **2019**, 205, 380-384.
75. Gu, D.; Yang, W.; Ning, G.; Wang, F.; Wu, S.; Shi, X.; Wang, Y.; Pan, Q., *Inorg. Chem.,* **2020**, 59, 1778-1784.
76. Yu, L.; Zheng, Q.; Wu, D.; Xiao, Y., *Sens. Actuators, B,* **2019**, 294, 199-205.
77. Wu, K.; Hu, J.; Shi, S.; Li, J.; Cheng, X., *Dyes Pigm.,***2020**, 173, 107993-108001.

Chapter: 3

A Supramolecular Assembly of Anionic Metal-Organic Complex and Cationic Amine: Selective Recognition Behavior Towards Arginine and Histidine

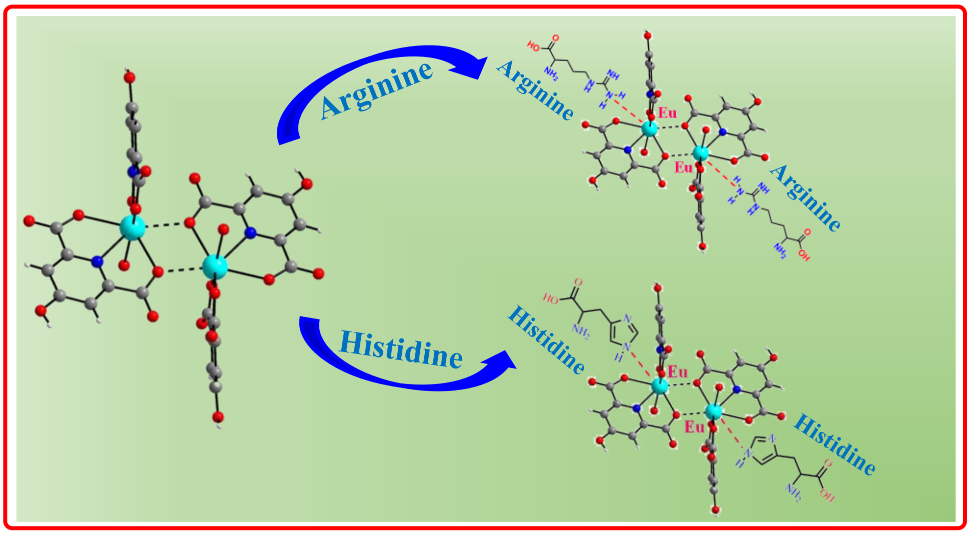

(Submitted for publication)

3.1 INTRODUCTION

Among the classes of coordination compounds, metal-organic materials (MOMs) consist of metal centers that undergo self-assembly with polydentate organic ligands.[1] The rational combination of supramolecular and coordination chemistry principles led to a fascinating variety of solids now known as metal-organic materials.[2] Versatility in their structure led to different important properties such as substantial surface area, precise structure and functionality.[3-6] Due to such attractive characteristics, MOMs are chosen by material chemists in the various fields of energy storage, gas adsorption and separation, biomedical research, catalytic application, single-molecule magnet, sensing, proton conductivity and many others.[7-17] Lanthanide complexes have drawn much attention due to their intriguing luminescence properties, which arise due to the deeply situated f orbitals and as a consequence of the high spin-orbit coupling constant. Besides these, lanthanide complexes have large stokes shift, color purity and high quantum yield. Since lanthanide ions have a low absorption cross-section area, they prefer to use an organic linker to excite through the energy transfer process.[18, 19] The organic ligand transfers the excitation energy to the lanthanide excited states through the inter-system crossing. Then, the characteristics luminescence emits from the metal ion via the non-radiative decay process.[20] In the last two decades, lanthanide metal-organic materials have been extensively used in the sensing field for their luminescence property.[21, 22] Amino acids, a fundamental protein unit in living organisms, play a huge role in the case of many life activities. Fluctuation in amino acid levels may lead to severe diseases like kidney damage, hepatic failure, neurological diseases and cardiovascular diseases.[23, 24] Among twenty naturally occurring amino acids, Arginine is the most basic amino acid having the guanidino group as a side chain.[25] With the help of the enzyme arginase, it degrades into urea and ornithine and again with the excess arginine urea reacts with ethanol and form urethane which is carcinogenic.[26] On the other hand, Histidine, as an essential amino acid plays an important role in the central nervous system in mammals.[27]

Various techniques like mass spectrometry, liquid chromatography, electrophoresis and colorimetry are used for amino acid detection.[28-31] But all these traditional methods suffer from device complications, long response times, low accuracy and tedious sample preparation methods. Amino acid sensing by using a few amounts of sample is a very difficult task, in that sense, luminescence-based detection is very important as it requires a minimum sample.[32] Furthermore, it is cost-effective, easy to handle, easily portable, quick response time and has a precise outcome. Nowadays, fluorescence amino acid sensors are widely used in chemistry, biology and medicine fields. To date, a variety of materials are used for the detection of amino acids such as carbon dots, conjugated polymers, metal nanoclusters, ruthenium complexes and coordination complexes.[33-37] Most of them have poor photostability and lengthy preparation time.

In the past few years, chemists have been working to develop luminescent metal-organic materials to detect amino acids. Few of them have reported Zn/Cd-based metal-organic materials but due to the small stokes shift it is not possible to detect pH via the naked eye.[32, 38-40] Zirconium-based metal-organic framework also showed some amino acid detection behavior.[26, 41] Very recently, Eu or Tb-based MOMs have been extensively used for the detection of amino acids since their large stokes shift and visual detection.[23, 27, 42-53]

Keeping all these things in mind, we have successfully synthesized a new Eu- based metal-organic material (MOM), $[Eu(CAM)_2(H_2O)]\cdot 0.5H_2Pip\cdot H_2O$, CAM= Chelidamate and H_2Pip= diprotonated piperazine, **2** via hydrothermal technique for the visible detection of amino acids. Standard characterization of compound **2** was performed by IR, TGA and UV- visible spectroscopy. The aqueous dispersion of compound **2** shows highly intense red emission upon excitation at 280 nm. It exhibits luminescence turn-on behavior in the basic pH region (11-13) in an aqueous medium. Moreover, Luminescence turn-off was observed in the presence of the two amino acids namely, arginine and histidine. To the best of our knowledge, this is the first observation that a simple supramolecular pure Eu-based coordination complex can detect pH in the highly basic medium through the naked eye as well as amino acids in an aqueous medium.

3.2 EXPERIMENTAL SECTION

3.2.1 Materials

The chemical substances used for the synthesis as well as the sensing experiment were all commercially available and used without further purification. For the synthesis purpose, we have used $Eu(NO_3)_3\cdot 6H_2O$ (Alfa Aesar, 99.9%), Chelidamic acid (Sigma Aldrich, >95%) and Piperazine (Sigma Aldrich, 99%). HCl (Merck, 99%) and NaOH (Merck, 99%) were used for the pH-sensing experiment. For the detection experiment regarding amino acids, we have used L-Arginine (Alfa Aesar, 98%), L- Histidine (Sigma Aldrich, >99%), L-Alanine (Sigma Aldrich, 98%), L-Cysteine (Sigma Aldrich, 97%), L- Cystine (Sigma Aldrich, 99%), L-Methionine (TCI, 99%), and L-Leucine (Sigma Aldrich, 98.5%). Throughout the whole experiment, doubly distilled water was used.

3.2.2 Synthesis of compound 2

A hydrothermal technique was used for the synthesis of the desired compound. $Eu(NO_3)_3 \cdot 6H_2O$ (0.1mM, 0.0446 g), Chelidamic acid (0.3mM, 0.0578 g) and Piperazine (0.3mM, 0.0260 g) were mixed with 5 mL distilled water and stirred well using a magnetic stirrer at room temperature for half an hour. The final homogenized reaction mixture was sealed in a 23 mL Teflon-based stainless-steel autoclave, heated at 170°C for 48h and kept under autogenous pressure. Then after 2 days, it was cooled to room temperature and white-coloured needle-shaped crystals were filtered and washed with distilled water under vacuum and dried under ambient conditions. The initial and final pH values measured were 5 and 6 respectively. Yield: 70% based on Eu.

3.2.3 Instrumentations

After synthesis of the compound, it is thoroughly characterized by Powder X-ray diffraction (PXRD), thermogravimetric analysis (TGA), and Infrared spectroscopic studies. By using Bruker D8 Discover instrument (Cu Kα radiation) PXRD patterns were measured in the 2θ range 5-50° at room temperature and a finely ground sample was used for this experiment. Perkin-Elmer instrument STA 6000 was utilized for the Thermogravimetric analysis and it was carried out in a Nitrogen atmosphere (flow rate = 20 ml min^{-1}) in the temperature range 40 – 800 ºC (heating rate = 20 ºC min^{-1}). The IR spectroscopic studies were carried out on Nicolet Magna IR 750 series-II FTIR-spectrophotometer in the solid state at room temperature. The UV-visible absorption studies were carried out in the SHIMADZU UV-1900i spectrophotometer. The photoluminescence spectra of aqueous dispersion compound **2** were measured at room temperature by using a Hitachi F-7100 spectrofluorometer using a xenon lamp as the excitation source. To exclude the ligand center emission, we set a cut-off filter at 420nm. The excitation and emission slit width was fixed to 5 nm.

3.2.4 Single-crystal structure determination of compound 2

A perfect single crystal was selected under a microscope and glued cautiously to a thin glass fiber. We have carried out the single crystal XRD experiment using Bruker D8 Quest machine at 293(2) K. The X-ray generator was operated at 1 mA and 50 kV using Mo Kα having λ=0.71073Å radiation. With ω scan width of 0.5º data were acquired. By keeping the sample-to-detector distance constant at 6.03 cm, a total of 408 frames were collected in three different settings of φ (0, 90, 180º) and the detector position (2θ) fixed at -25º. Using an APEX3 program the final data sets were reduced, while for the integration of diffraction profiles a SAINTPLUS[54] program was used. A SADABS program[55] was employed to carry out the absorption correction (multi-scan). The structure was initially solved by SIR 92.[56] Then we again used full matrix least-square method (SHELXL-2016)[57], which is present in the WinGx suit of programs (Version 1.63.04a).[58, 59] All the non-hydrogen atoms from Fourier maps are effectively located. At the final cycles, we have refined them with anisotropic displacement parameters. Finally, all the hydrogen atoms are fixed at premeditated positions and comprised them in the refinement procedure using riding model accompanied by isotropic thermal parameters. A detail of the structure solution and final refinement is given in Table 3.1. CCDC: 2391794 contains the crystallographic data for this paper. These data can be found free of charge from The Cambridge Crystallographic Data Center (CCDC) via www.ccdc.cam.ac.uk/data_request/cif.

Table 3.1: Crystal data and structure refinement parameters for [Eu(CAM)$_2$(H$_2$O)]·0.5H$_2$Pip·H$_2$O, CAM= Chelidamate and H$_2$Pip= diprotonated piperazine, **2.**

Empirical formula	$C_{16}H_{12}EuN_3O_{12}$
Formula weight	590.25
Crystal system	Triclinic
Space group	P-1
a (Å)	9.6179(13)
b (Å)	10.1078(14)
c (Å)	11.1194(15)
α (deg)	66.271(3)
β (deg)	73.830(3)
γ (deg)	78.243(3)

Volume (Å^3)	945.3(2)
Z	2
T (K)	273 (2)
ρ_{calc} (mg m^{-3})	2.074
μ (mm^{-1})	3.394
θ range (deg)	2.051 to 27.168
λ (Mo Kα) (Å)	0.71703
R indices [$I > 2\sigma(I)$]	R1 = 0.0213, wR2 = 0.0625
R indices (all data)	R1 = 0.0223, wR2 = 0.0720

$R_1 = \Sigma \,||F_0|-|F_c|| / \Sigma |F_0|$; $wR_2 = \{\Sigma[w(F_0^2 - F_c^2)^2] / \Sigma[w(F_0^2)^2]\}^{1/2}$. $w = 1/[\sigma^2(F_0)^2 + (aP)^2 + bP]$, $P = [\max.(F_0^2,0) + 2(F_c)^2]/3$, where a = 0.0383 and b = 0.9311.

3.2.5 Preparation of the sample solution for photoluminescence measurements

After drying the crystals, by the use of mortar and pestle, the crystals are ground to form powder of the sample. Then 2.5 mg of the sample is weighed and mixed in 5 mL distilled water and sonicated well for 2 min to get the dispersion and from this stock solution again 2 mL stock was taken out and mixed with 20 mL distilled water to get the final stock. We used 2 mL of the final stock in a quartz cuvette for the luminescence-based titration studies, performed at room temperature. For the amino acids' recognition behavior, we prepared all the solutions of concentration 5×10^{-3} M in an aqueous medium.

3.2.6 Time-Correlated Single Photon Counting Measurements

We have used the HORIBA Jobin Yvon instrument at room temperature in the nanosecond time domain for the luminescence lifetime decay measurements. For the ligand center emission, the excitation wavelength used is 280 nm and the emission decay curve was measured at 370 nm and 420 nm. In the case of metal center emission, the emission decay curve was measured at 616 nm. All the emission decay curves were fitted in a triexponential manner using Igor software.

3.3 RESULTS AND DISCUSSION

3.3.1 Structure of compound 2

The single crystal structure analysis revealed that compound **2** is crystalized in a triclinic crystal system with a P-1 space group. The asymmetric unit of compound **2** consists of one Eu^{3+} ion, two chelidamate, one coordinated water molecule, half diprotonated piperazine molecule and one lattice water molecule (Figure 3.1a). The Eu^{3+} ion is eight coordinated with six oxygen atoms and two nitrogen atoms and has a distorted bicapped trigonal prism geometry through five oxygen atoms from carboxylates and two nitrogen atoms from the pyridine ring of chelidamate ligands and one coordinated water molecule (Figure 3.1b).

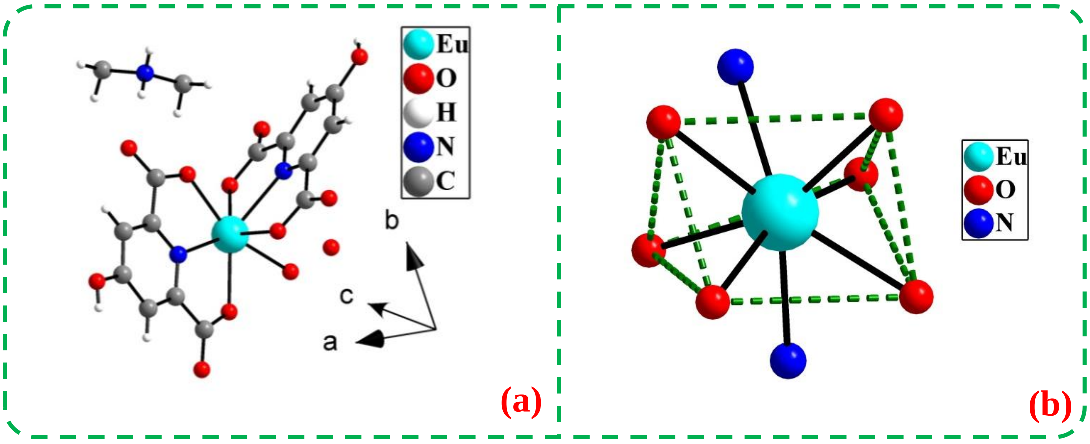

Fig. 3.1 (a) The asymmetric unit of $[Eu(CAM)_2(H_2O)] \cdot 0.5H_2Pip \cdot H_2O$, 2. Hydrogen atoms of water molecules are not shown. (b) The coordination geometry around Eu^{3+} ion.

The Eu- O bonds have an average bond length of 2.422 Å and the Eu–N bonds have an average length of 2.464 Å. The O/N-Eu-O/N bond angles range from 34.37(5)-162.65(5) °. The selected bond distances and angles for compound **2** are listed in Tables 3.2 and 3.3. The connectivity between Eu^{3+} and chelidamate ligands formed an anionic dimeric meta-organic structure containing two Eu^{3+} ions, four chelidamate ligands and two coordinated water molecules (Figure 3.2). Here the two polyhedral units are edge-shared and each dimeric unit contains four free hydroxyl groups.

Table 3.2: Selected bond distances (Å) observed in $[Eu(CAM)_2(H_2O)]\cdot 0.5H_2Pip\cdot H_2O$, CAM= Chelidamate and H_2Pip= diprotonated piperazine, **2.**

Bond	**Distances, Å**	**Bond**	**Distances, Å**
Eu(1)-O(4)	2.355(2)	Eu(1)-O(2)	2.474(2)
Eu(1)-O(3)	2.381(2)	Eu(1)-O(2)#1	2.486(2)
Eu(1)-O(1)	2.406(2)	Eu(1)-N(1)	2.490(3)
Eu(1)-O(5)	2.435(3)	Eu(1)-N(2)	2.437(3)

Symmetry transformations used to generate equivalent atoms: #1 -x+1,-y+1,-z+2

Table 3.3: Selected bond angles observed in $[Eu(CAM)_2(H_2O)]\cdot 0.5H_2Pip\cdot H_2O$, CAM= Chelidamate and H_2Pip= diprotonated piperazine, **2.**

Angle	**Amplitude (º)**	**Angle**	**Amplitude (º)**
O(4)-Eu(1)-O(3)	131.07(8)	O(5)-Eu(1)-O(2)#1	100.52(8)
O(4)-Eu(1)-O(1)	90.83(9)	N(2)-Eu(1)-O(2)#1	83.60(8)
O(3)-Eu(1)-O(1)	82.08(8)	O(2)-Eu(1)-O(2)#1	68.93(8)
O(4)-Eu(1)-O(5)	157.19(9)	O(4)-Eu(1)-N(1)	75.59(9)
O(3)-Eu(1)-O(5)	71.40(8)	O(3)-Eu(1)-N(1)	138.08(8)
O(1)-Eu(1)-O(5)	88.66(9)	O(1)-Eu(1)-N(1)	63.64(8)
O(4)-Eu(1)-N(2)	65.87(8)	O(5)-Eu(1)-N(1)	83.80(9)
O(3)-Eu(1)-N(2)	65.26(8)	N(2)-Eu(1)-N(1)	124.88(8)
O(1)-Eu(1)-N(2)	78.66(8)	O(2)-Eu(1)-N(1)	65.15(8)
O(5)-Eu(1)-N(2)	136.03(9)	O(2)#1-Eu(1)-N(1)	132.97(8)
O(4)-Eu(1)-O(2)	79.47(8)	O(1)-Eu(1)-O(2)#1	161.43(8)
O(3)-Eu(1)-O(2)	139.93(8)	O(3)-Eu(1)-O(2)#1	85.58(8)
O(1)-Eu(1)-O(2)	128.70(7)	O(4)-Eu(1)-O(2)#1	86.85(9)
O(5)-Eu(1)-O(2)	83.10(8)	N(2)-Eu(1)-O(2)	136.76(8)

Symmetry transformations used to generate equivalent atoms: #1 -x+1,-y+1,-z+2

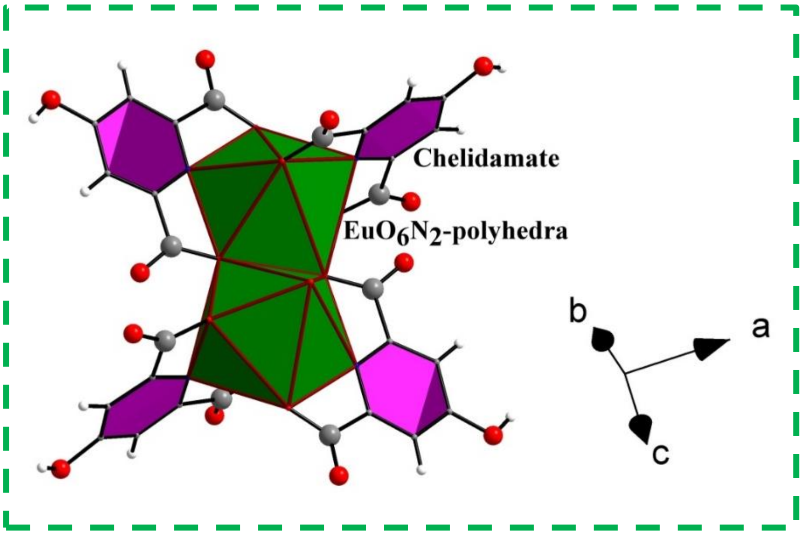

Fig. 3.2 The carboxylate connected dimeric unit of $[Eu(CAM)_2(H_2O)]\cdot 0.5H_2Pip\cdot H_2O$, **2**. Hydrogen atoms of water molecules are not shown.

The dimeric units formed inter-molecular hydrogen bond interactions involving the free hydroxyl groups and carboxylate oxygen atoms. The O–H···O hydrogen bonds connect each dimeric unit with four other dimeric units to form a supramolecular two-dimensional structure (Figure 3.3). The details of hydrogen bonds are summarised in Table 3.4. In this two-dimensional structure, each dimeric unit acts as four connected nodes and the connectivity among the nodes forms a rhombus grid network with $4^4.6^2$ Schläfli symbol and 4.4.4.4.*.* vertex symbol (Figure 3.4).

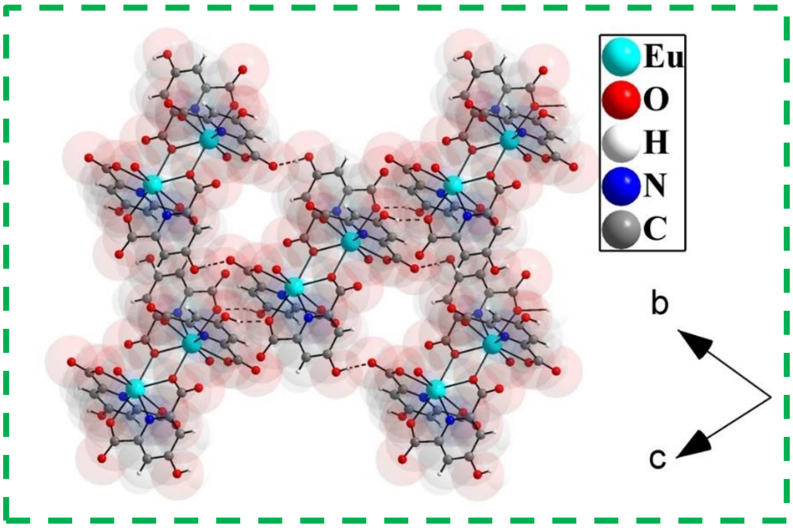

Fig. 3.3 The two-dimensional structure formed through O–H···O hydrogen bond interactions among dimeric units of $[Eu(CAM)_2(H_2O)]\cdot 0.5H_2Pip\cdot H_2O$, **2**. Dotted lines indicate hydrogen bonds.

Table 3.4: Summary of hydrogen-bond interaction observed in $[Eu(CAM)_2(H_2O)]\cdot 0.5H_2Pip\cdot H_2O$, **2**.

D–H···A[a]	D – H (Å)	H···A (Å)	D···A (Å)	D–H···A (°)
O(10) – H(10A)···O(8)$^{\#1}$	0.82	1.83	2.6294(4)	164
O(11) – H(11A)···O(1)$^{\#2}$	0.82	1.80	2.5726(4)	157
N(3) – H(3A)···O(9)	0.88	1.92	2.7851(4)	167
N(3) – H(3B)···O(3)$^{\#3}$	0.85	2.14	2.9004(4)	148

#1 = 1+x,-1+y,z; #2 = -x,1-y,1-z; #3 = x,-1+y,z

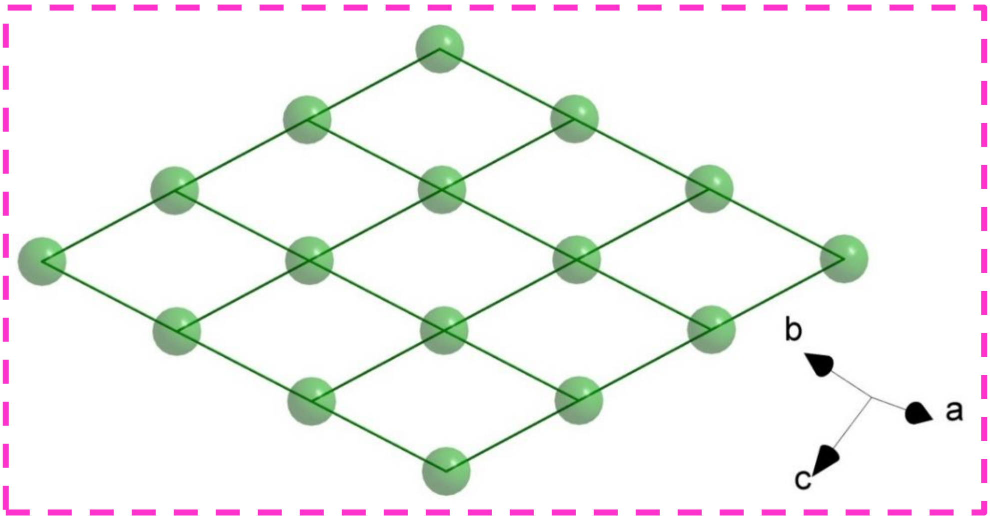

Fig. 3.4 Network topology of the supramolecular network. Green spheres are the centroid position of each dimeric unit.

The two-dimensional anionic hydrogen-bonded structures are further stabilized through N−H···O hydrogen bond interactions by involving piperazinediium ion to form an overall three-dimensional structure (Figure 3.5). Here protonated piperazine acts hydrogen bond donor and the carboxylate oxygen of chelidamate ions acts as a hydrogen bond acceptor. The details of hydrogen bonds are summarised in Table 3.4.

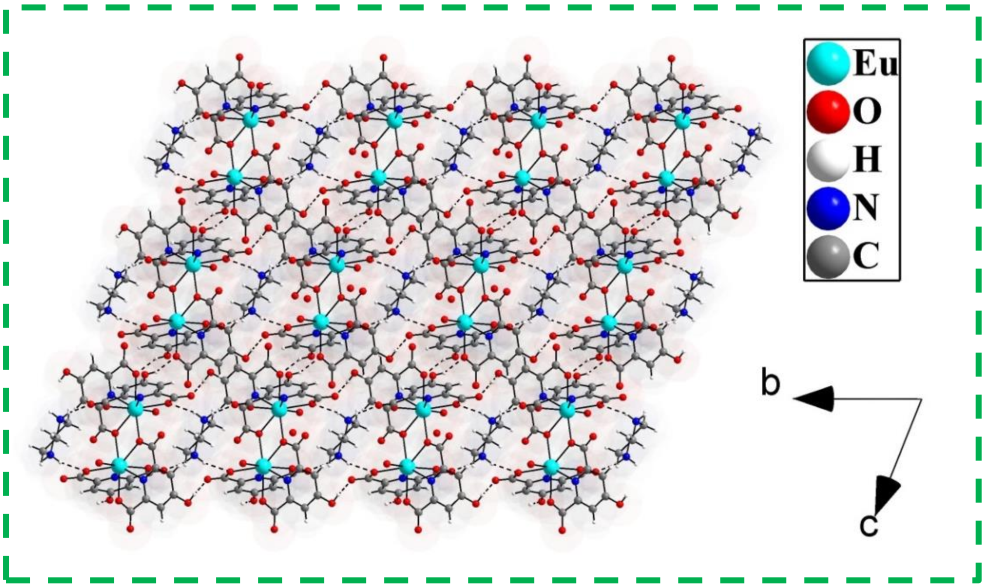

Fig. 3.5 The three-dimensional hydrogen bonded supramolecular structure of [Eu(CAM)$_2$(H$_2$O)] ·0.5H$_2$Pip·H$_2$O, **2**. Dotted lines indicate hydrogen bonds.

3.3.2 Characterization of compound 2

For the confirmation of the purity of the sample and configurational uniformity of compound **2**, the powder X-ray diffraction pattern was measured on a finely grounded sample within the 2θ range 5- 50° and compared with the simulated pattern, obtained from the single crystal X-ray instrument. Both these two PXRD patterns match well and we can conclude that the synthesized compound is in its pure phase (Figure 3.6).

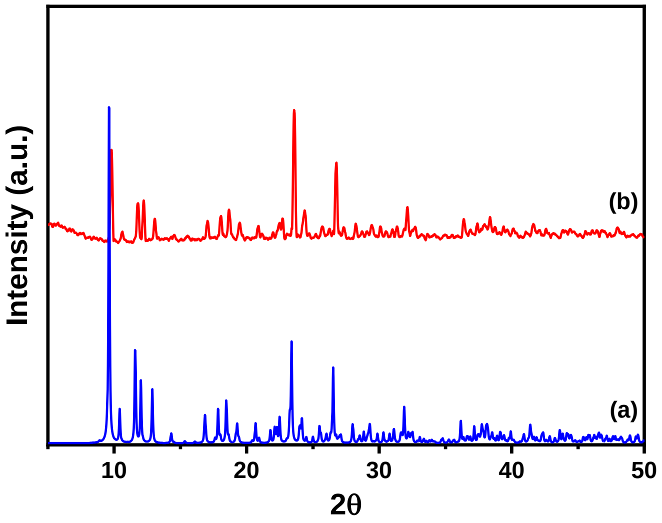

Fig. 3.6 Powder XRD (CuKα) patterns: (a) simulated from single crystal X-ray data of $[Eu(CAM)_2(H_2O)]\cdot 0.5H_2Pip\cdot H_2O$, **2** and (b) hydrothermally synthesized $[Eu(CAM)_2(H_2O)]\cdot 0.5H_2Pip\cdot H_2O$, **2.**

The IR spectrum of compound **2** was carried out in the spectral range between 4000-500 cm^{-1} at room temperature. All the remarkable peaks corresponding to chelidamate ligand and water have been observed (Figure 3.7a). The Thermogravimetric analysis (TGA) of compound **2** was recorded under a nitrogen atmosphere (Figure 3.7b). The weight loss of the compound occurred in multiple steps. The weight loss of 5.98% (calculated 6.06%) up to 215°C is due to the removal of one lattice water and one coordinated water molecule. The weight loss above 325 ºC is probably due to the decomposition of the framework.

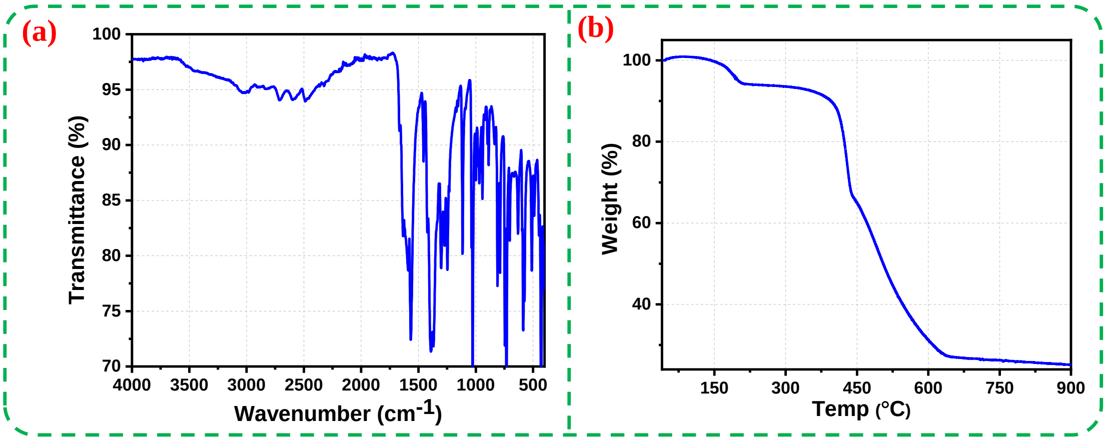

Fig. 3.7 (a) IR spectrum and **(b)** Thermogravimetric analysis (TGA) of compound **2** in nitrogen atmosphere.

The absorption spectrum of compound **2** was measured and the wavelength maxima was at 280 nm (Figure 3.8).

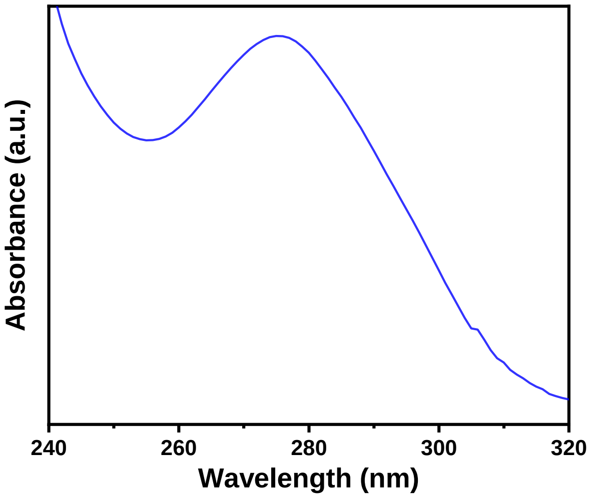

Fig. 3.8 UV- vis absorption spectrum of compound **2.**

3.3.3 Photoluminescence behavior

All the absorption and emission spectral studies were carried out in aqueous solution at room temperature. Compound **2** showed a bright red color emission which is visible through the naked eye when excited at 280 nm wavelength light. The emission bands with characteristics peak at 579, 593, 616, 653 and 694 nm should be ascribed to the $^5D_0 \rightarrow {}^7F_0$, $^5D_0 \rightarrow {}^7F_1$, $^5D_0 \rightarrow {}^7F_2$, $^5D_0 \rightarrow {}^7F_3$, and $^5D_0 \rightarrow {}^7F_4$ transitions of Eu^{3+} ions respectively. Compound **2** exhibits ligand-centered emission at 420 nm upon excitation at 280 nm. The ligand-centered emission spectra of **2** are shown in Figure 3.9a. By keeping the emission wavelength fixed at 616 nm the excitation spectra of compound **2** were taken and metal-centered emission spectra were taken upon excitation at 280 nm (Figure 3.9b). The metal-centered emission of compound **2** was used for the recognition behavior towards amino acids. In the case detection of amino acids, the excitation wavelength was fixed at 245 nm to avoid the changes in optical density at other possible excitation wavelengths.

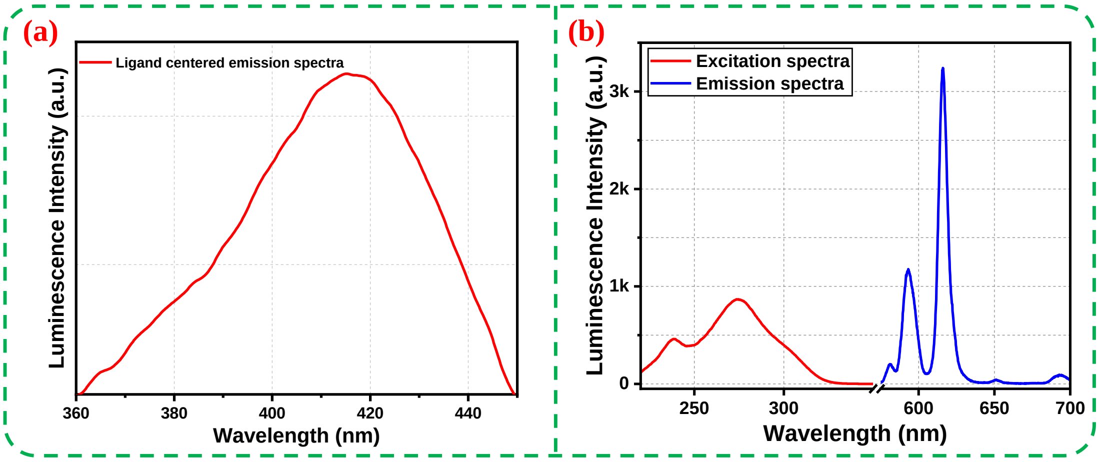

Fig. 3.9 (a) Ligand-centered emission spectra of compound **2** and **(b)** Excitation and emission spectra of **2.** The excitation wavelength was chosen at 280 nm for emission spectra and for the excitation spectra, emission was fixed at 616 nm.

3.3.4 pH response of compound 2

Our intension in this work is to establish the compound **2** as amino acids sensor. It is often found that with the addition of the amino acids in the medium the pH changes to some extent. Therefore, the compound **2** was systematically examined by the addition of HCl and NaOH solution to know whether it changes its luminescence intensity or peak position due to change in pH of the medium. From figure 3.10 and 3.11 we observed that compound **2** is not sensitive to the pH of the medium in the pH range 5 to 10. However, the luminescence intensity is significantly increased (monitored at 616 nm) as pH is increased from 11 to 13; in the pH range 2 to 5 there has been slight increase in luminescence intensity. The change in luminescence intensity of **2** with the variation of pH of the solution is shown in Figure 3.10.

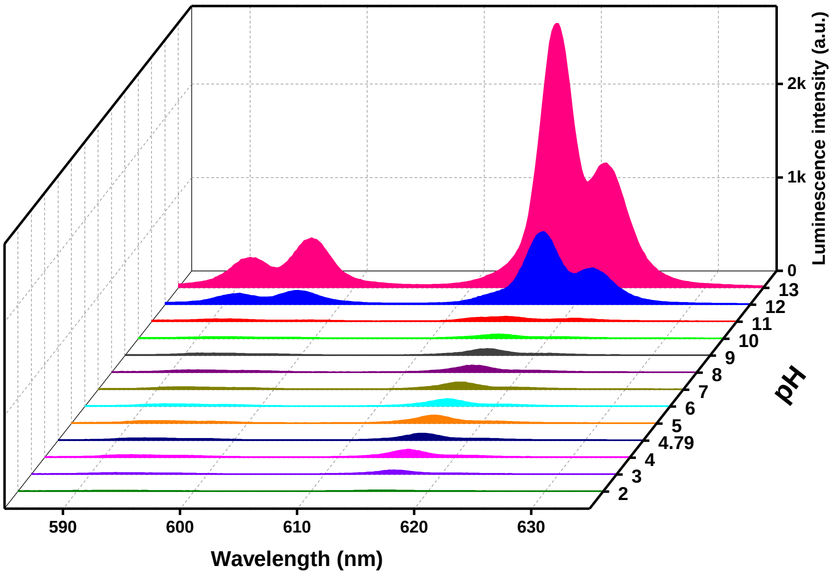

Fig. 3.10 Metal-centered luminescence spectra of compound **2** in an aqueous dispersion at different pH values (λ_{ex}= 280 nm).

A massive change in luminescence intensity was noticed between the pH region 11 to 13 (Figure 3.11a). By observing the very high luminescence intensity enhancement in the basic region, one can conclude that the sensitization process phenomenon is strongly pH-dependent only in the pH range 11 to 13. The absorption spectra showed that the compound is stable in the pH range of 11-13(Figure 3.11b).

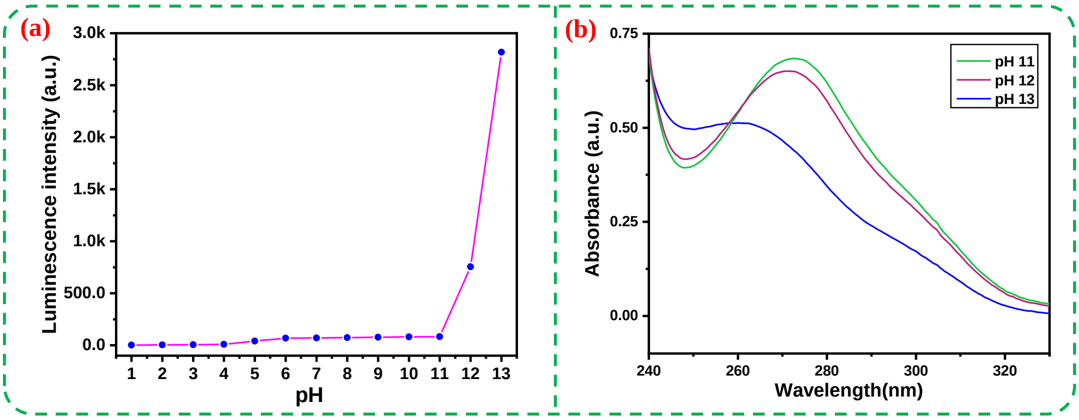

Fig. 3.11 (a) Changes in luminescence intensity of **2** at different pH values, obtained by monitoring the luminescence intensity at λ_{em} = 616 nm and **(b)** Absorption spectra of compound **2** at different pH (11-13).

We have also recorded the ligand-centered emission at different pH values. As we move from pH 2 to 11, the luminescence intensity remains almost constant. A blue shift of 50 nm in emission peak along with an increment in luminescence intensity was observed at pH 11, which arises due to the deprotonation of the free hydroxyl group present in the pyridine carboxylic acid. Again, at pH 12 and 13 a huge turn-on in the luminescence intensity was observed in the new emission center at 370 nm. The changes in the luminescence intensity in the case of ligand-centered emission at various pH was shown in Figure 3.12.

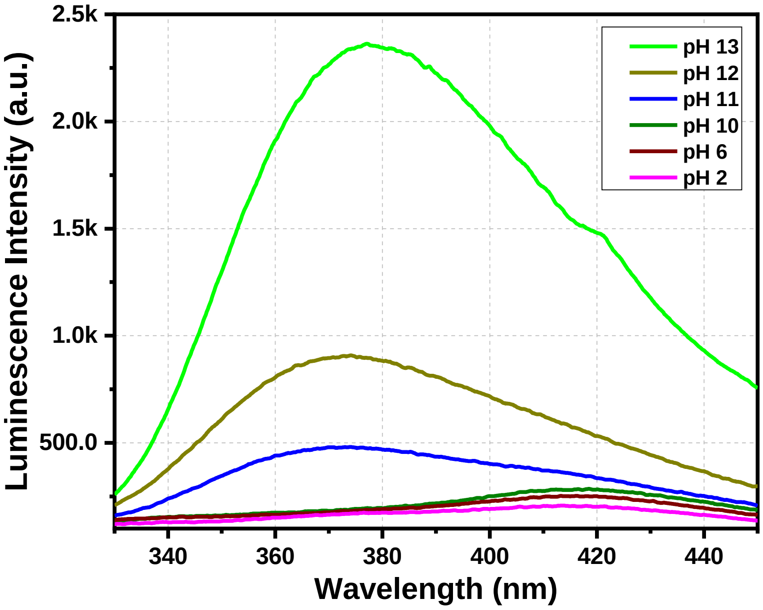

Fig. 3.12 Ligand-centered luminescence spectra of compound **2** in an aqueous dispersion at different pH values (λ_{ex}= 280 nm).

3.3.5 pH response mechanism

It is first necessary to check the stability of the compound at high pH values e.g. 11, 12, and 13 where drastic change in the luminescence intensity occurred. The compound was soaked in distilled water and by adding required amount of base (NaOH) the desired pH was reached and kept for 2 h. Afterward, the powdered compounds were collected by filtration and then dried up. Then at room temperature, the PXRD measurements were carried out. The resulting PXRD pattern at various pH values perfectly matched the simulated data obtained from a single crystal X-ray diffraction instrument. The PXRD patterns show that compound **2** is stable in the pH range between 11 to 13(Figure 3.13). The huge increase in luminescence in tensity is not due to the breakdown of the structure.

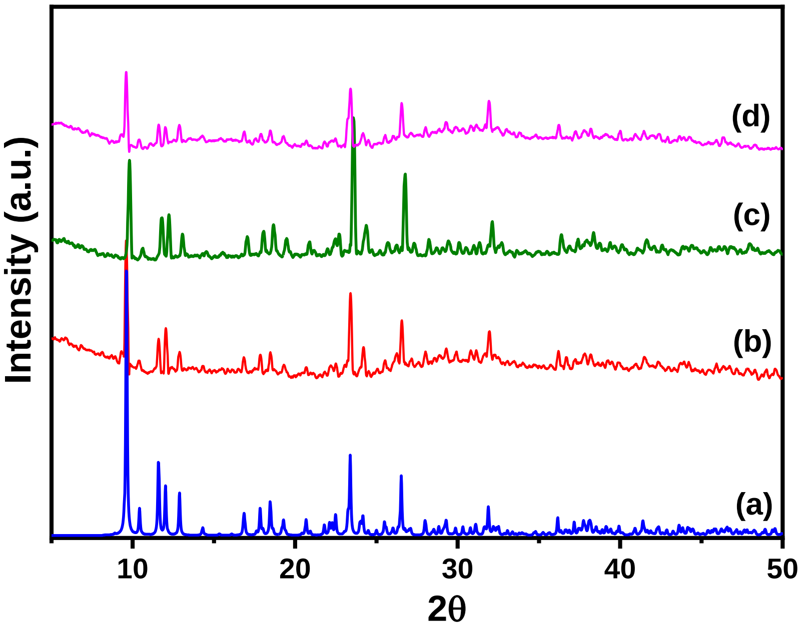

Fig. 3.13 Powder XRD (Cu Kα) patterns: (a) simulated from single crystal X-ray data of [Eu(CAM)$_2$(H$_2$O)] ·0.5H$_2$Pip·H$_2$O, (b) pH= 11, (c) pH= 12 and (d) pH= 13.

The characteristic metal-centered emission occurred due to the transference of a part of the energy from the excited state of the organic ligand to the Eu^{3+} center. The whole mechanism of pH sensing lies in the deprotonation effect of both the piperazine proton and the proton present on the free hydroxyl group present on the pyridine ring. At first, when the pH of the compound changes from 2 to 5, a slight turn-on in the luminescence intensity occurs due to the deprotonation of the piperazine proton that eventually breaks the H-bonding between piperazine and the chelidamate moieties. In the pH range 5 to 10 no significant change in luminescence intensity was observed because in this pH range no other deprotonation of the compound **2** occurs. Then as we move from the 10 to 13, there occurred a huge luminescence turn-on along with a 50 nm peak shift due to the hydroxyl group's deprotonation (Scheme 3.1). The electron density in the aromatic ring of the chelidamate ligand is increasing due to the deprotonation of hydrogen proton and as a result, the bonding between the organic ligand and europium center strengthened. Ultimately, the energy transfer process from the ligand to the europium center becomes easier and a huge enhancement of luminescence intensity happened.

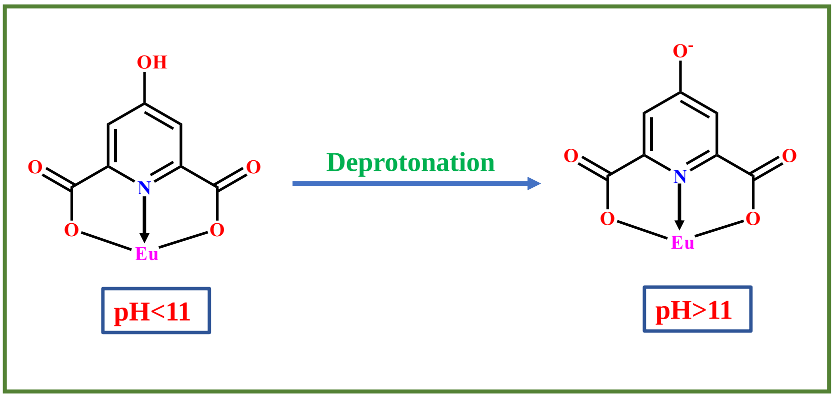

Scheme 3.1 Schematic representation of the pH response mechanism.

3.3.6 Photoluminescence behaviour of compound 2 towards amino acids

For the recognition behavior towards amino acids, we have performed photoluminescence- based titration of aqueous dispersion of compound **2** with the incremental addition of various amino acids. The titration was performed in the presence of different amino acids, namely, L- Arginine (Arg), L- Histidine (His), L-Cystine (Cti), L-Cysteine (Cys), L-Methionine (Met), L-Leucine (Leu) and L-Alanine (Ala). The intensity of the luminescence spectra was quenched upon incremental addition of Arg and His (up to 652 µM) to the compound as depicted in Figure 3.14.

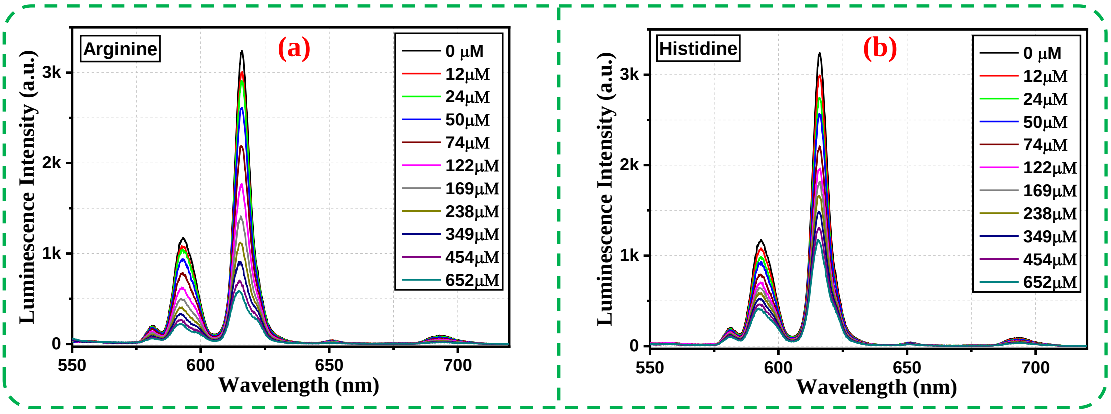

Fig. 3.14 Emission spectra of compound **2** dispersed in water upon the incremental addition of an aqueous solution of analytes (λ_{ex} = 245 nm): (a) Arginine and (b) Histidine. The final concentration of analytes in the medium is indicated in the legend.

Whereas for the other amino acids there have been no significant change in luminescence of the compound **2**. By monitoring the intensity at 616 nm, the quenching efficiency (η) was calculated by using the famous equation, $\eta = (1 - I/I_0) \times 100\%$, where I_0 is the initial luminescence intensity of the aqueous dispersion of compound **2** and I is the luminescence intensity after the addition of amino acid. The calculated values of quenching efficiencies were 80.52% and 61.56% for Arg and His respectively. For the rest of the amino acids, quenching efficiencies were not so significant (Figure 3.15).

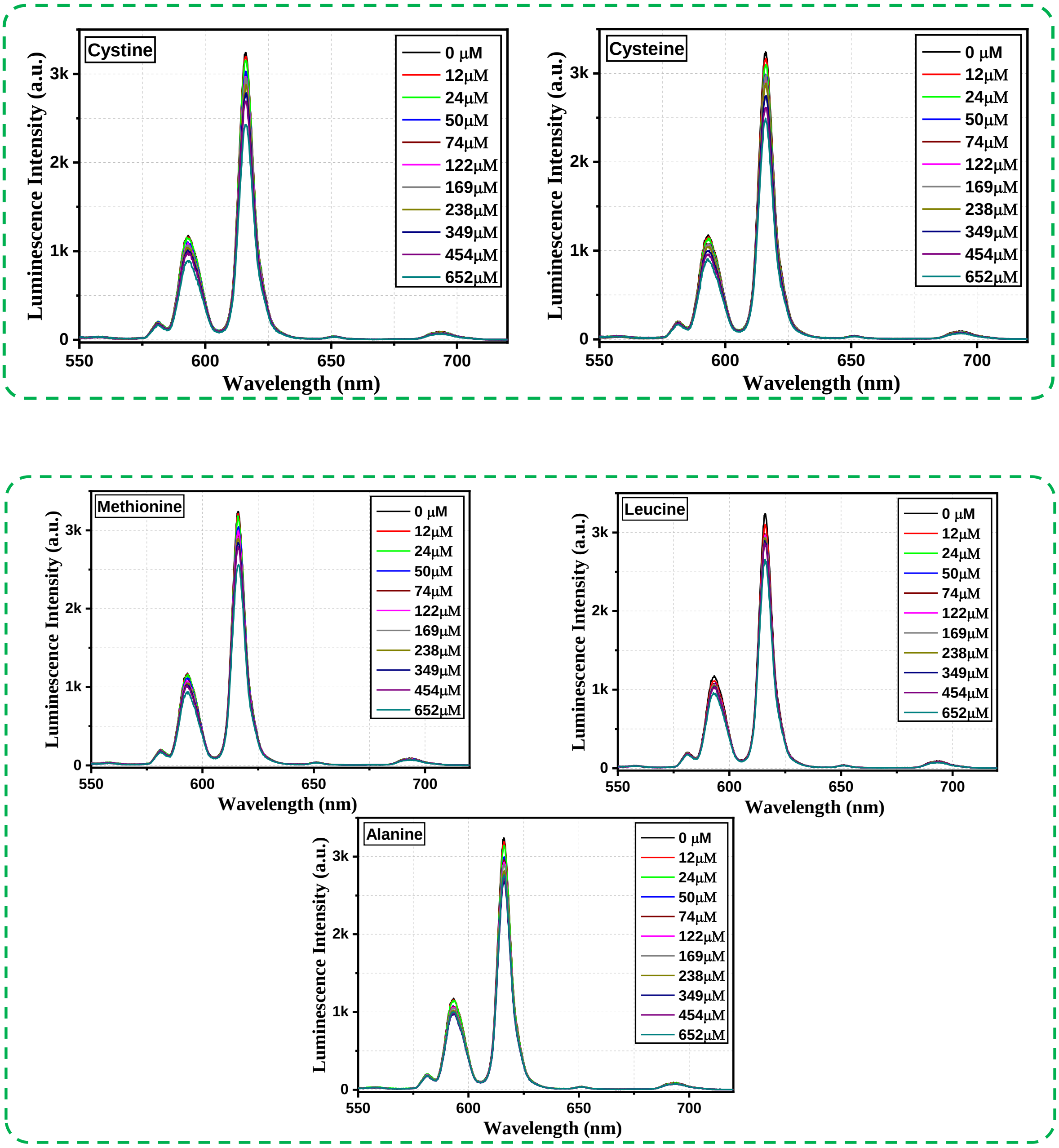

Fig. 3.15 Emission spectra of compound **2** dispersed in water upon the incremental addition of an aqueous solution of different analytes (λ_{ex} = 245 nm).

The quenching phenomena are represented as a bar diagram after the addition of 652 μM concentration of all the amino acids (Figure 3.16). We also obtained a 3D bar diagram (Figure 3.17) by plotting [(I_0/I)-1] vs the concentration of all amino acids, which proves the selective recognition behavior of compound **2** towards Arg and His.

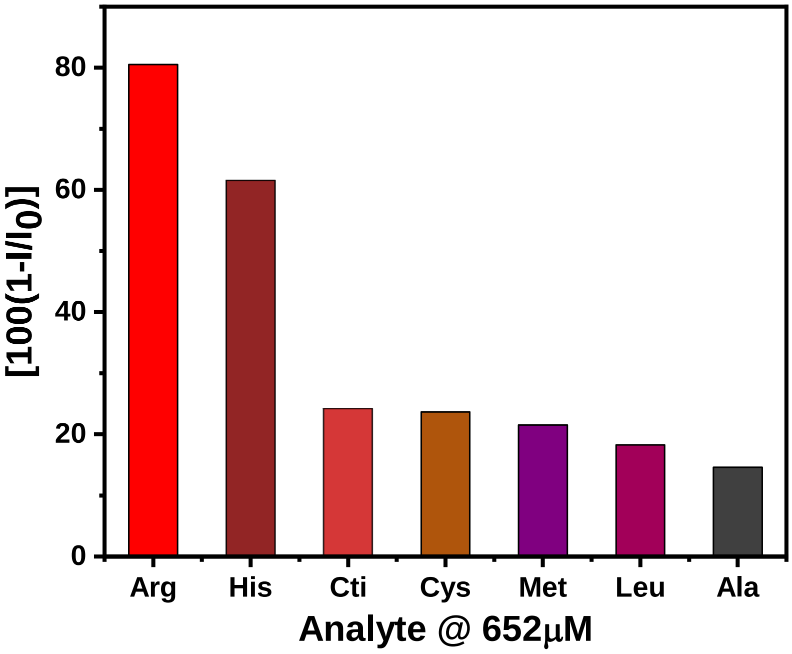

Fig. 3.16 Luminescence intensity changes of compound **2** towards different Amino acids after adding 652μM of these amino acids.

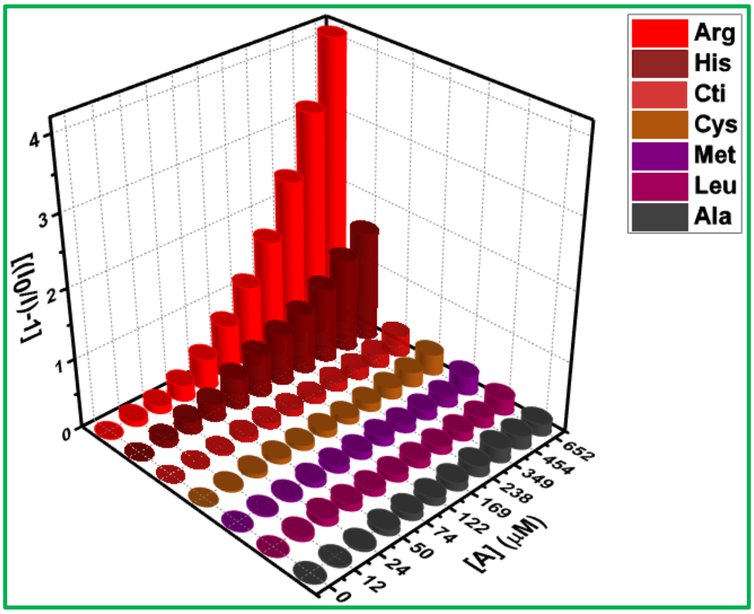

Fig. 3.17 The plot of [(I/I_0) - 1] of compound **2** against the concentration of analytes after adding 652 μM of analytes.

We calculated the limit of detection (LOD) by employing the equation, LOD= 3σ/m, where σ is the standard deviation of the blank titration and m is the slope of the straight line plotted at a minimum concentration for LOD calculation. The LOD values were calculated to be 0.29 and 0.37 μM for Arg and His respectively (Figure 3.18a and 3.18b).

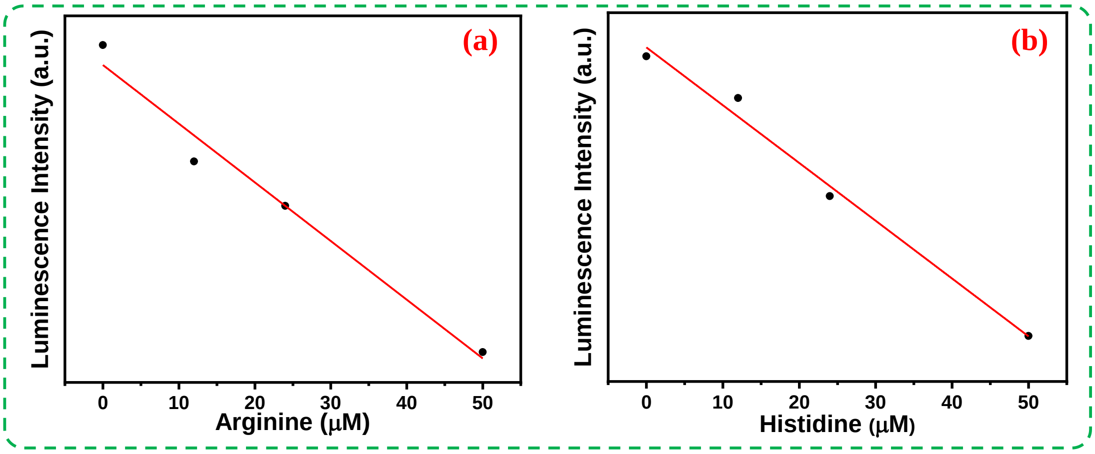

Fig. 3.18 Linear correlation between the luminescence intensity and concentration of **(a)** Arginine and **(b)** Histidine.

The quenching constant (K_{SV}) was obtained from the Stern-Volmer (SV) equation, $(I_0/I) = 1 + K_{SV}[M]$, where I_0 is the initial luminescence intensity, I is the luminescence intensity after the addition of the analyte and [M] is the molar concentration of the analyte. By plotting the luminescence intensity ratio (Io/I) against the analyte concentration (up to 50 μM) K_{SV} values were obtained from the linear fitting (Figure 3.19).

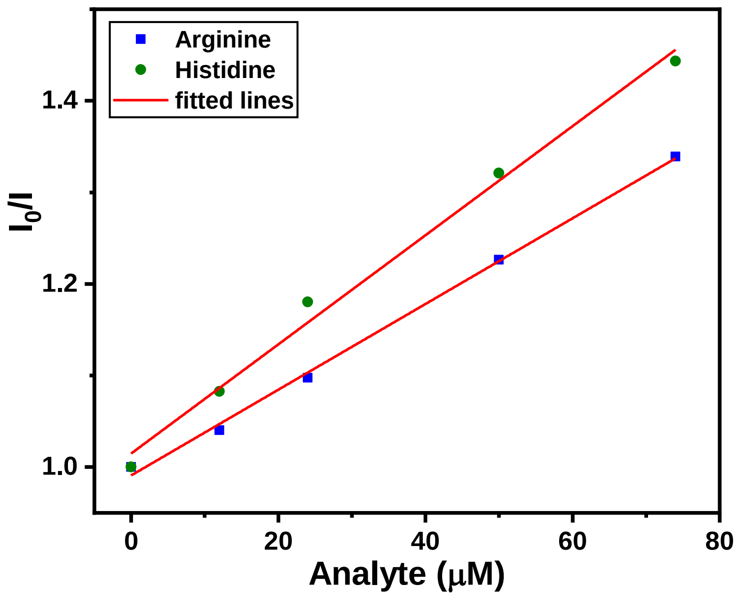

Fig. 3.19 K_{SV} curves of compound **2** in an aqueous solution in the presence of Arginine and Histidine.

The K_{SV} values were calculated to be 0.46×10^4 and 0.59×10^4 M^{-1} for Arg and His respectively. We have given a table related to the previous literature corresponding to some luminescence-based detection of amino acids by metal-organic material in Table 3.5 to compare our present work.[23, 27, 42-53]

Table 3.5 A brief of the previously reported metal-organic framework, used for the luminescence-based detection of amino acids.

Sl. No.	Compound	Amino Acid	LOD(μM)	K_{SV} (M^{-1})	Reference
1	$(UO_2)(nip)(2,2'\text{-bpy})$ and $(H_2bpp)\cdot[(UO_2)_2(nip)_3]\cdot H_2O$	Arg	1.06 and 6.42	-	23
2	anth-UiO-67 MOF	Arg	0.017	5.1×10^6	42
3	H_8L-Mn-MOF	Arg	41	-	43
4	ZnMOF@SA	Arg	20	-	44
5	BRSU-Al^{3+} complex	Arg	2.3	-	45
6	Zn(II)-terpyridine complex	Arg	2.05	1.78×10^4	46
7	La(TATB)	Arg	0.007	-	47
8	$[Nd(L)(DMF)_2]_n$	Arg	0.001	2.9×10^5	48
9	Eu/Bi-MOF	His	0.18	-	49
10	Cu^{2+}@UN	His	0.007	-	50
11	L-Cys/PCN-222	His	2.48	6.3×10^3	51
12	CuCP	His	0.30	3.89×10^5	52
13	$\{[Eu\text{-}(L)(H_2O)_2]\cdot DMF\}_n$	His	100	-	27
14	NH_2-MIL-101-Al	Arg and His	45.1 and 199	3.42×10^3 7.72×10^2	53
15	$[Eu(CAM)_2(H_2O)]\cdot 0.5H_2Pip\cdot H_2O$	Arg and His	0.29 and 0.37	0.46×10^4 0.59×10^4	This work

3.3.7 UV-visible absorption spectra

We have also measured the UV-visible absorption spectra of aqueous dispersion of compound **2** at different concentrations of Arg and His (Figure 3.20). The absorption spectra of compound **2** show dramatic changes with the appearance of a new peak at 225 nm and an isosbestic point at ~245 nm. The peak at 225 nm in the case of titration with Histidine was not observed because histidine itself has an absorption band in the region of 200-225 nm. These dramatic changes are clear indications of the strong interaction of the amino acids with compound **2** in the ground state. It should be remembered that in this wavelength range the said amino acids do not have any absorption (Figure 3.21), so whatever changes we observe in the absorption spectra is due to the interaction between the amino acids and the compound **2**. Here it should also be noted that the excitation wavelength for the luminescence titration experiments in the presence of amino acids was chosen to be 245 nm which is the isosbestic point in the absorption spectra and hence nullifies the possibility of the change in optical density effect that could contribute to the quenching effect. So, the quenching observed in the presence of Arginine and Histidine may be due to the static quenching.

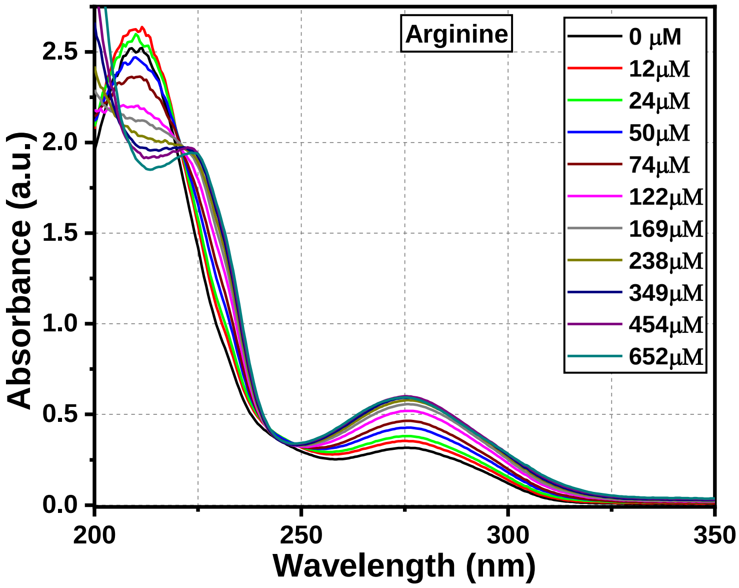

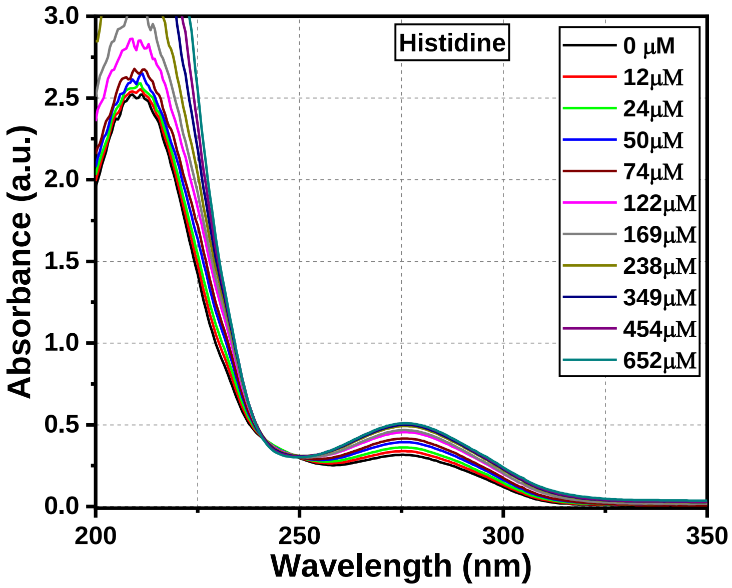

Fig. 3.20 Absorption spectra of compound **2** dispersed in water upon the incremental addition of an aqueous solution of Arginine and Histidine. The final concentration of Arginine and histidine in the medium is indicated in the legend.

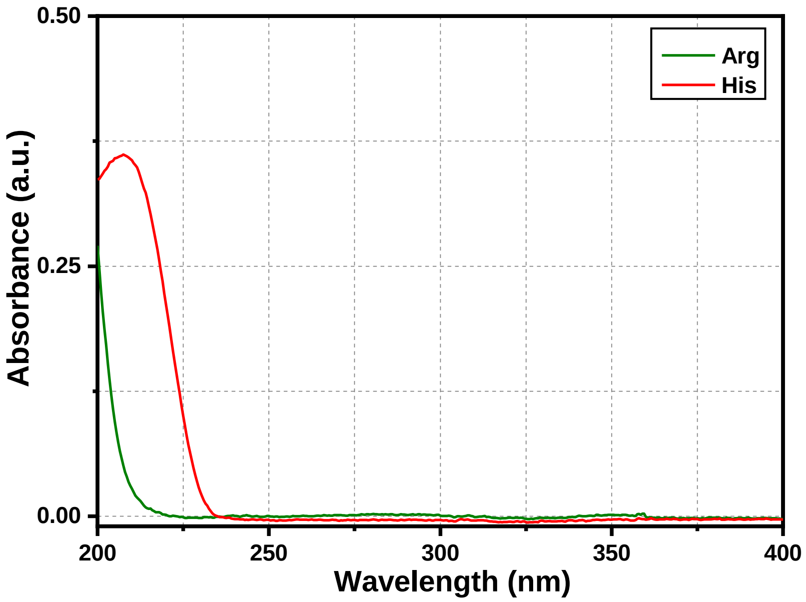

Fig. 3.21 Absorption spectra of Arg and His dispersed in water.

3.3.8 Luminescence lifetime measurements

We have carried out a detailed study of the time-dependent luminescence intensity decay profile of compound **2** and plotted in Figure 3.22 to investigate the amino acid sensing mechanism. The excitation wavelength was fixed at 310 nm and the ligand-centered emission i.e. 415 nm was fixed for the measurements of luminescence lifetime decay profiles. The decay curves were fitted employing the triexponential function and the results are compiled in Table 3.6. The luminescence lifetime of compound **2** was found to decrease from 1.1 ns to 0.30 ns with the addition of 652 μM Arginine. In the presence of histidine, there has been no change in lifetimes. The change in lifetimes in the presence of a quencher indicates the possibility of dynamic quenching. To calculate the dynamic quenching constant, we plotted the ratio of lifetimes vs the concentration of arginine (Figure 3.23). The calculated dynamic quenching constant was obtained to be 1.34×10^4 M^{-1}. So, the quenching in the presence of arginine was not only due to static quenching but also there is a significant dynamic quenching. No change in lifetime in the case of histidine indicates that the quenching was solely static quenching.

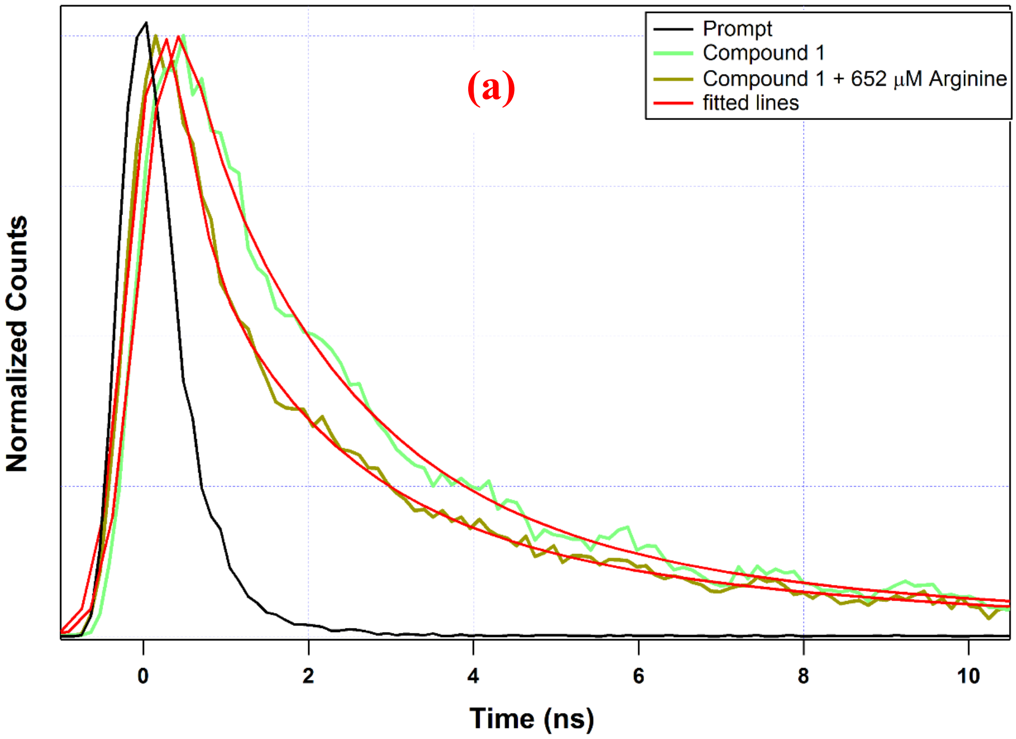

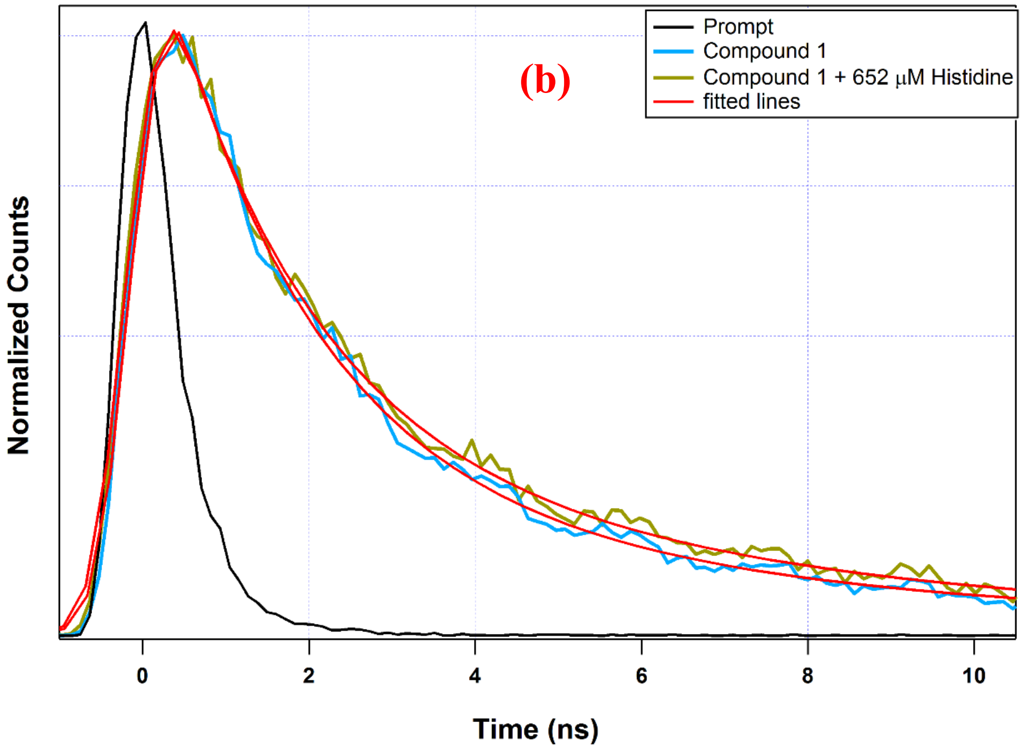

Fig. 3.22 Luminescence Intensity decay profile of compound **2** before and after the addition of (a) Arginine and (b)Histidine. The final concentrations of Arginine and Histidine in the medium are indicated in the legend. The instrument response function (prompt) is also shown. Here, λ_{ex} = 310 nm and λ_{em}= 415 were set during the experiment.

Table 3.6 Lifetime components of Compound **2** in presence of Arginine (λ_{ex} = 310 nm and λ_{em} = 415nm).

System	**a₁**	**τ₁ (ns)**	**a₂**	**τ₂ (ns)**	**a₃**	**τ₃ (ns)**	**<τ> (ns)**
Compound **2**	0.65	0.10	0.29	2.0	0.06	7.50	1.10
Compound **2**+24µM Arg	0.83	0.10	0.13	2.0	0.04	7.50	0.70
Compound **2**+74µM Arg	0.88	0.10	0.09	2.0	0.03	7.50	0.50
Compound **2**+122µM Arg	0.90	0.10	0.08	2.0	0.02	7.50	0.40
Compound **2**+238µM Arg	0.91	0.10	0.07	2.0	0.02	7.50	0.40
Compound **2**+652µM Arg	0.93	0.10	0.06	2.0	0.01	7.50	0.30

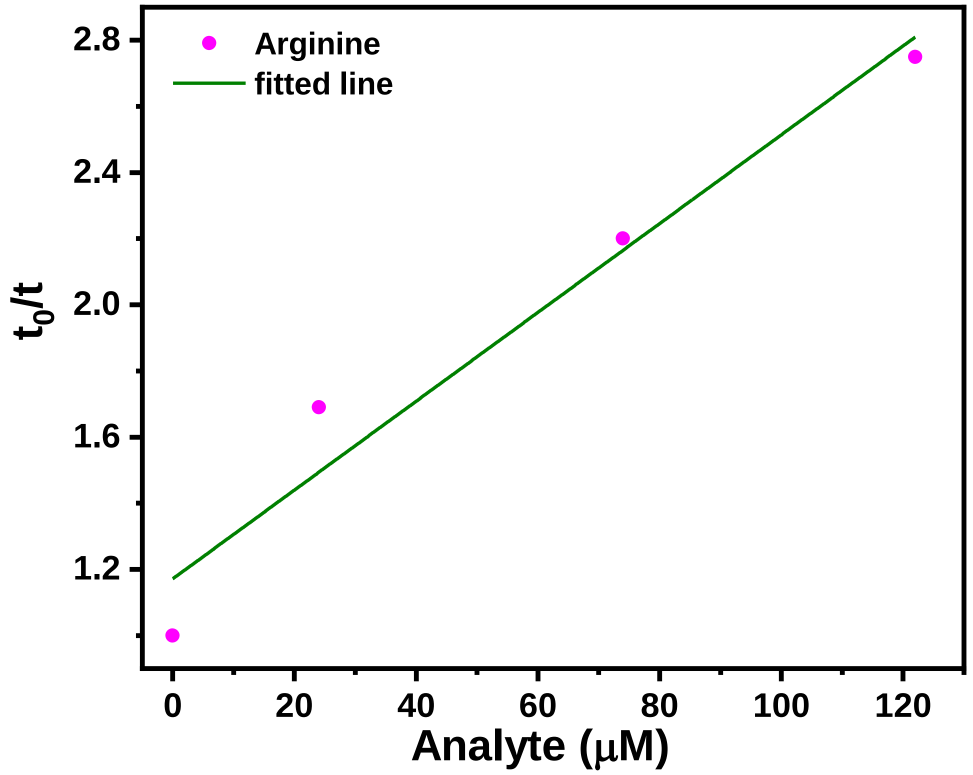

Fig. 3.23 t_0/t plot of compound **2** in the presence of Arginine.

3.3.9 Mechanism of Luminescence Quenching in the presence of Arginine and Histidine

To check the compound's stability in the presence of Arginine and Histidine, first, compound **2** was soaked in distilled water for 24 h. Then we checked its PXRD pattern and saw that it perfectly matched with the simulated pattern of compound **2**. So, it can be said that our compound remained stable. Then the powdered compound was immersed in the aqueous solution of Arginine and Histidine for the same. Again, the powdered pattern matched with the simulated one (Figure 3.24). Therefore, in conclusion, we can say that our compound remained stable after the incorporation of such analytes.

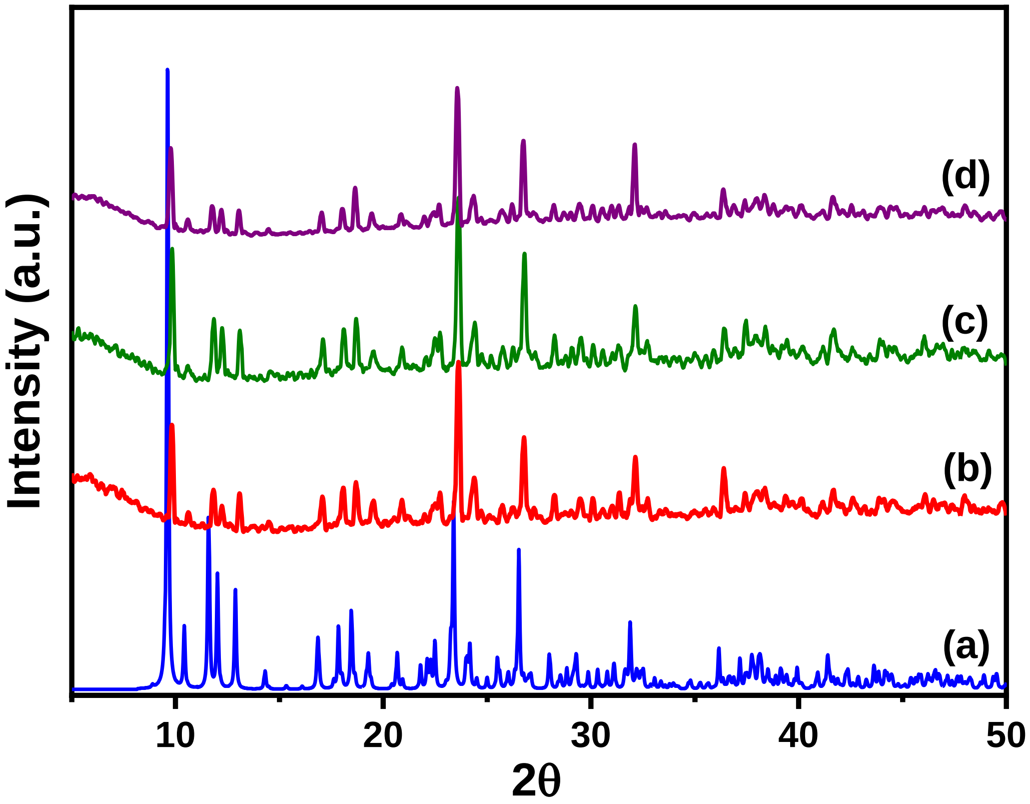

Fig. 3.24 Powder XRD (Cu Kα) patterns: (a) simulated from single crystal X-ray data of $[Eu(CAM)_2(H_2O)]\cdot0.5H_2Pip\cdot H_2O$, (b) compound **2** immersed in water, (c) compound **2** immersed in an aqueous solution of Arginine and (d) compound **2** immersed in an aqueous solution of Histidine for 24 h.

Now, it is important to note that the luminescence quenching effect has been observed in the case of arginine and histidine among the selected amino acids. These two amino acids are different from other amino acids due to the presence of a basic group (amine or imidazole) in the side chain. These basic groups, probably, interact with the Eu^{3+} center (Scheme 3.2) and make the Eu^{3+}-carboxylate bonds (chelidamate) weaker. As a result, the ligand-sensitized metal-centered luminescence is hampered through the competitive metal-ligand interaction. This can be observed from the absorption spectra during the titration of the compound in the presence of arginine and histidine, where an isosbestic point along with a new absorption peak was observed at 225 nm. The new peak is not very prominent in the case of histidine due to the presence of an absorption peak of histidine itself in the region 200- 225 nm. These dramatic changes in absorption spectra certify the molecular level interaction between the Eu^{3+} ion and the basic group of arginine and histidine in the ground electronic state. Therefore, the quenching can be categorized as static quenching in both cases. However, from Figure 10 it can be found that the plot of (I/I_0-1) at higher concentrations of arginine deviates from linearity and bends upward which is an indication of the involvement of more than one quenching process. The analysis of lifetime data reveals that in the case of arginine, there is a significant amount of dynamic quenching involved. Hence the quenching of luminescence of compound **2** by arginine is both due to static and dynamic quenching, but in the case of histidine, the quenching is purely static in nature.

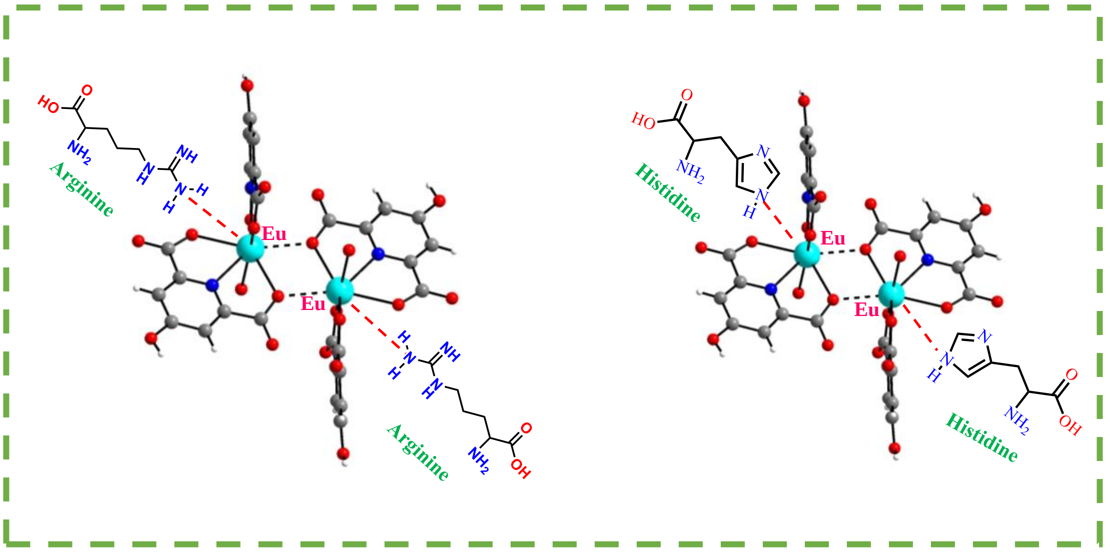

Scheme 3.2 Schematic representation of the amino acid sensing mechanism.

3.4 CONCLUSION

In conclusion, we have successfully synthesized a new Eu- based metal-organic material, $[Eu(CAM)_2(H_2O)]\cdot 0.5H_2Pip\cdot H_2O$, **2** by hydrothermal technique**.** By using a Single-crystal XRD instrument we got the crystal structure of compound **2.** The compound was systematically characterized by PXRD, IR, TGA and UV-visible spectroscopy. The compound exhibited excellent luminescence behavior. By utilizing its luminescence property, we have shown the pH-response behavior of our compound and also its selective recognition behavior towards Arg and His. The compound showed pH-responsive behavior in the basic region. A huge turn-on in the luminescence intensity with a 50 nm blue shift in the emission spectra was observed in the pH region 11 to 13. From the UV-visible spectroscopy experiment, it has confirmed that the compound was stable in this region. The TCSPC experiment also showed the same result as for the steady state. The mechanism of pH response behavior was attributed to the deprotonation effect of both the piperazine proton and the proton present in the free hydroxyl group. The compound also showed luminescence quenching in the case of Arg and His and the quenching efficiency was 80.52% and 61.56% for Arg and His respectively due to the molecular level interaction between the compound and amino acids. The corresponding LODs are excellent as compared to previous reports for the amino acid.

3.5 REFERENCES

1. Cook, T. R.; Zheng, Y.-R.; Stang, P. J., *Chem. Rev.* **2013,** *113* (1), 734-777.
2. Cai, G.; Yan, P.; Zhang, L.; Zhou, H.-C.; Jiang, H.-L., *Chem. Rev.* **2021,** *121* (20), 12278-12326.
3. Chakraborty, G.; Park, I.-H.; Medishetty, R.; Vittal, J. J., *Chem. Rev.* **2021,** *121* (7), 3751-3891.
4. Kreno, L. E.; Leong, K.; Farha, O. K.; Allendorf, M.; Van Duyne, R. P.; Hupp, J. T., *Chem. Rev.* **2012,** *112* (2), 1105-1125.
5. Bigdeli, F.; Fetzer, M. N. A.; Nis, B.; Morsali, A.; Janiak, C., *J. Mater. Chem. A* **2023,** *11* (41), 22105-22131.
6. Carné, A.; Carbonell, C.; Imaz, I.; Maspoch, D., *Chem. Soc. Rev.* **2011,** *40* (1), 291-305.
7. He, B.; Zhang, Q.; Pan, Z.; Li, L.; Li, C.; Ling, Y.; Wang, Z.; Chen, M.; Wang, Z.; Yao, Y.; Li, Q.; Sun, L.; Wang, J.; Wei, L., *Chem. Rev.* **2022,** *122* (11), 10087-10125.
8. Sanati, S.; Abazari, R.; Albero, J.; Morsali, A.; García, H.; Liang, Z.; Zou, R., Angew. Chem., Int. Ed. **2021,** *60* (20), 11048-11067.
9. Jiang, C.; Wang, X.; Ouyang, Y.; Lu, K.; Jiang, W.; Xu, H.; Wei, X.; Wang, Z.; Dai, F.; Sun, D., *Nanoscale Adv.* **2022,** *4* (9), 2077-2089.
10. Yang, J.; Yang, Y.-W., *Small* **2020,** *16* (10), 1906846-1906869.
11. Ye, G.; Chen, C.; Lin, J.; Peng, X.; Kumar, A.; Liu, D.; Liu, J., *Dalton Trans.* **2021,** *50* (47), 17438-17454.
12. Zhang, Y.; Liu, S.; Zhao, Z.-S.; Wang, Z.; Zhang, R.; Liu, L.; Han, Z.-B., *Inorg. Chem. Front.* **2021,** *8* (3), 590-619.
13. Bavykina, A.; Kolobov, N.; Khan, I. S.; Bau, J. A.; Ramirez, A.; Gascon, J., *Chem. Rev.* **2020,** *120* (16), 8468-8535.
14. Aulakh, D.; Pyser, J. B.; Zhang, X.; Yakovenko, A. A.; Dunbar, K. R.; Wriedt, M., *J. Am. Chem. Soc.* **2015,** *137* (29), 9254-9257.
15. Hui, S.; Daga, P.; Mahata, P., *Inorg. Chem.* **2023,** *62* (1), 591-600.
16. Hui, S.; Majee, P.; Singha, D. K.; Daga, P.; Mondal, S. K.; Mahata, P., *New J. Chem.* **2021,** *45* (21), 9394-9402.
17. Lim, D.-W.; Kitagawa, H., *Chem. Soc. Rev.* **2021,** *50* (11), 6349-6368.
18. Wang, X.; Jiang, Y.; Tissot, A.; Serre, C., *Coord. Chem. Rev.* **2023,** *497*, 215454-215478.
19. Zhao, Y.; Li, D., *J. Mater. Chem. C* **2020,** *8* (37), 12739-12754.
20. Cui, Y.; Yue, Y.; Qian, G.; Chen, B., *Chem. Rev.* **2012,** *112* (2), 1126-1162.
21. Luo, X.-Y.; Pan, M., *Coord. Chem. Rev.* **2022,** *468*, 214640-214664.

22. Sahoo, S.; Mondal, S.; Sarma, D., *Coord. Chem. Rev.* **2022,** *470*, 214707-214740.
23. Wang, L.; Tu, B.; Xu, W.; Fu, Y.; Zheng, Y., *Inorg. Chem.* **2020,** *59* (7), 5004-5017.
24. Pal, T. K., *Mater. Chem. Front.* **2023,** *7* (3), 405-441.
25. Khezri, S.; Bahram, M.; Samadi, N., *Anal. Methods* **2017,** *9* (46), 6513-6524.
26. Dong, J.; Zhang, X.-D.; Xie, X.-F.; Guo, F.; Sun, W.-Y., *RSC Adv.* **2020,** *10* (61), 37449-37455.
27. Yang, A.-F.; Hou, S.-L.; Shi, Y.; Yang, G.-L.; Qin, D.-B.; Zhao, B., *Inorg. Chem.* **2019,** *58* (9), 6356-6362.
28. Kilgore, M. B.; Platis, D.; Lim, T.; Isenberg, S.; Pickens, C. A.; Cuthbert, C.; Petritis, K., *Anal. Chem.* **2023,** *95* (6), 3187-3194.
29. Violi, J. P.; Bishop, D. P.; Padula, M. P.; Steele, J. R.; Rodgers, K. J., *TrAC, Trends Anal. Chem.* **2020,** *131*, 116018-116037.
30. Yin, X.; Adams, E.; Van Schepdael, A., J. Sep. Sci. **2023,** *46* (15), 2300213-2300245.
31. Bahadoran, A.; Khoshnoudi Jabarabadi, M.; Hameed Mahmood, Z.; Bokov, D.; Jushi Janani, B.; Fakhri, A., *Spectrochim. Acta, Part A* **2022,** *268*, 120636-120645.
32. Deng, Z.-P.; Ji, B.-T.; Chen, J.-H.; Zhao, B.; Li, J.-G.; Sun, Y.-X.; Sun, Y.,. *J. Mol. Struct.* **2024,** *1299*, 137132-137145.
33. Yang, Y. Z.; Xiao, N.; Liu, S. G.; Han, L.; Li, N. B.; Luo, H. Q., *Mater. Sci. Eng.,C* **2020,** *108*, 110401-110409.
34. He, G.; Yan, N.; Cui, H.; Liu, T.; Ding, L.; Fang, Y.,. *Macromolecules* **2011,** *44* (18), 7096-7099.
35. Paramanik, B.; Kundu, S.; De, G.; Patra, A., *J. Mater. Chem. C* **2016,** *4* (3), 486-496.
36. Chen, H.; Li, X.; Wu, Y.; Gao, W.; Bai, R., *Dalton Trans.* **2012,** *41* (43), 13292-13297.
37. Sarkar, S.; Daga, P.; Mondal, S. K.; Mahata, P., *Cryst. Growth Des.* **2024,** *24* (11), 4748-4757.
38. Lin, W.; Wang, Y.; Zhang, H.; Shan, K. H.; Si, P.; Yu, S.; Wang, Z.; Zhao, D.; Gao, J.; Wu, M.; Tang, B. Z., *Dalton Trans.* **2023,** *52* (41), 14967-14972.
39. Sun, Y. X.; Han, W.-Y.; Deng, Z.-P.; Sun, Y.-G.; Jia, Y.-H.; Sun, Y.; Zhang, S.-Z., *Inorg. Chim. Acta* **2023,** *556*, 121643-121652.
40. Zhao, Y.; Chai, Y.-H.; Wang, Y.-H.; Lu, Z.-M.; Cheng, X.-F.; Wang, S.; Ma, L.-F.; Zhao, B.-T., *J. Mol. Struct.* **2024,** *1296*, 136895-136903.
41. Sun, X.-y.; Zhang, H.-j.; Sun, Q.; Gao, E.-Q., *Cryst. Growth Des.* **2021,** *21* (12), 7218-7229.
42. Mohammadi, L.; Khavasi, H. R., *Inorg. Chem.* **2020,** *59* (18), 13091-13097.
43. Chakraborty, D.; Bej, S.; Chatterjee, R.; Banerjee, P.; Bhaumik, A., *Chem. Eng. J.* **2022,** *446*, 136916-136925.
44. Sha, H.; Yan, B., *J. Mater. Chem. C* **2022,** *10* (19), 7633-7640.

45. He, L.; So, V. L. L.; Xin, J. H., *Sens. Actuators, B* **2014,** *192*, 496-502.
46. Zhou, X.; Jin, X.; Li, D.; Wu, X., *Chem. Commun.* **2011,** *47* (13), 3921-3923.
47. Zeng, X.; Wei, S.; Hu, J.; Gou, L.; Wu, L.; Hou, X., *Anal. Chem.* **2022,** *94* (28), 10271-10277.
48. Wang, X. Z.; Wang, X. R.; Liu, Y. Y.; Huo, J. Z.; Li, Y.; Wang, Q.; Liu, K.; Ding, B., *Ultrason. Sonochem.* **2019,** *59*, 104734-104744.
49. Song, L.; Xiao, J.; Cui, R.; Wang, X.; Tian, F.; Liu, Z., *Sens. Actuators, B* **2021,** *336*, 129753-129761.
50. Farahmand Kateshali, A.; Moghzi, F.; Soleimannejad, J.; Janczak, J., *Inorg. Chem.* **2024,** *63* (7), 3560-3571.
51. Qin, S.; Meng, F.; Jin, F.; Xu, X.; Zhao, M.; Chu, H.; Gao, L.; Liu, S., *Anal. Methods* **2024,** *16* (15), 2386-2399.
52. Ghosh, R.; Nair, R. R.; Ghosh, S.; Debnath, S.; Chatterjee, P. B., *Inorg. Chem.* **2024,** *63* (18), 8320-8328.
53. Dong, J.; Dao, X.-Y.; Zhang, X.-Y.; Zhang, X.-D.; Sun, W.-Y., *Molecules* **2021,** *26* (17), 5336-5346.
54. Madison, W. J. B. A. I. U., SMART (V 5.628), SAINT (V 6.45 a), XPREP, and SHELXTL. **2004**.
55. Krause, L.; Herbst-Irmer, R.; Sheldrick, G. M.; Stalke, D., *J. Appl. Crystallogr.* **2015,** *48* (Pt 1), 3-10.
56. Altomare, A.; Cascarano, G. L.; Giacovazzo, C.; Guagliardi, A. J., *J. Appl. Crystallogr.* **1993,** *26*, 343-350.
57. Sheldrick, G., *Acta Crystallogr. Sect. C* **2015,** *71* (1), 3-8.
58. Farrugia, L., WinGX *J. Appl. Crystallogr.* **1999,** *32* (4), 837-838.
59. Spek, A., *J. Appl. Crystallogr.* **2003,** *36* (1), 7-13.

Chapter: 4

Highly Selective Luminescence Turn - On Based Sensing of Phosphate in Presence of Other Interfering Anions Using a Heterobimetallic (3d-4d) MOF with Acidic Pocket

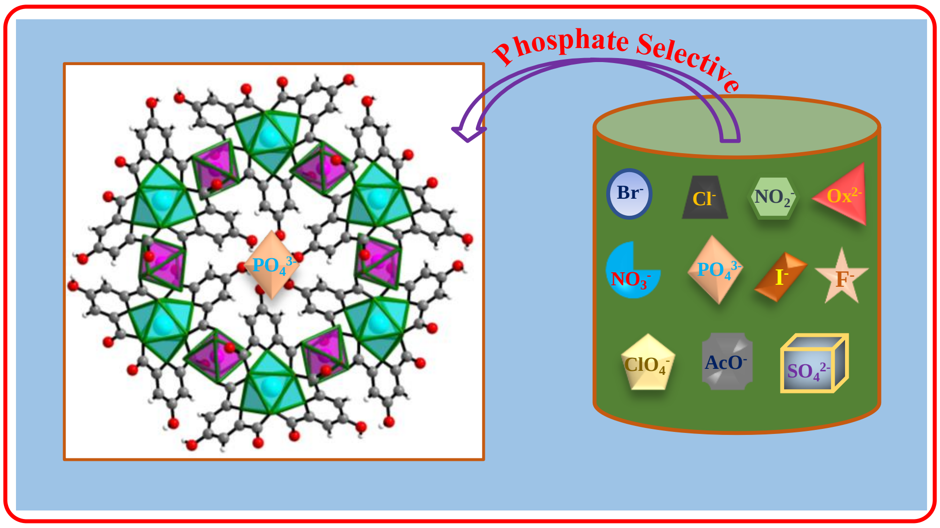

Inorg. Chem. **2023, 62, 591−600**

4.1 INTRODUCTION

It is due to some natural phenomena and human activities water gets polluted gradually. Many toxic chemical species pollute water. Phosphate (PO_4^{3-}), being a pollutant anion can cause water eutrophication when its concentration is getting increased and as a result serious problems in aquatic ecosystem occur like excessive algal growth accompanied by red tide, depletion of dissolved oxygen and reduction in water quality.[1-5] On the contrary, phosphate involves in many activities like it provides energy to cells in the form of ATP, activate proteins through phosphorylation, and restrict the growth of life when they are too abundant in an ecosystem.[6-7] In cells, phosphate acts as an important buffer which keeps the pH of a substance neutral. Having a high level of phosphate in blood is known as hyperphosphatemia causing severe kidney diseases and Osteoporosis whereas random use of medicine can cause phosphate shortage.[8-9] By determining the concentration of phosphate in body fluid can assist to recognize various diseases such as hyperparathyroidism and Fanconi syndrome.[10-12] Due to strong hydration effect of phosphate, it is very difficult task to detect phosphate ion in aqueous media.[13-14] Therefore, it is of great significance to detect phosphate ion in a reliable, sensitive, and quick manner in water medium and environmental samples for human safety and industrial environmental protection.[15]

Until now, numerous techniques such as single- layered graphene quantum dots strategy, spectrophotometry, colorimetry, chromatography, electrochemical methods, and enzymatic biosensors have been established for the selective detection of this anion in environmental samples.[16-21] But these methods have some limitations including time consuming, expensive apparatus and tedious sample pretreatment accompanied by skilled technicians. Luminescence based detections have attracted important attention owing to their quick response time, high sensitivity, ease of operation and portability.[22-24] Various kinds of materials such as organic dyes, quantum dots, metal nano clusters, conjugated polymer and supramolecules are reported for the detection of this anion.[25-29] However, these materials suffer from some disadvantages like poor water solubility, toxicity, laborious synthesis, and poor stability. Consequently, metal- organic framework consists of inorganic metal or metal oxide nodes and organic polydentate bridging ligand with excellent porosity, large surface area, high thermal stability and diverse structures are extensively used in many fields like smart sensing, gas storage and separation, drug delivery, non- linear optics, magnetism, proton conductivity, supercapacitor, catalysis and energy storage.[30-51] The luminescence properties of the MOFs have been extensively used for the sensing experiment of various types of analytes as the luminescence properties are very much dependent on their structural features and interaction with analytes through hydrogen bond, coordinate bond, π- π interaction, electron transfer and energy transfer.[52-54] Due to the different coordination environment, variable oxidation states and formal charges of metal ion, different binding sites of ligand, MOFs can be used in detection purpose even at the molecular level.[55-57]

There are few examples of heterometallic coordination polymers synthesized using chelidamate ligand to study magnetic behaviors.[58-59] Recently, metal- organic frameworks with special emphasis on Eu and Tb- based MOFs have been prepared to detect phosphate ion.[60-69] A very few examples of Zr- based MOFs have been found for the detection of these anions.[70-71] But there are no as such examples of heterobimetallic MOFs which can detect these anions as synthesis of MOFs containing 3d-4d hetero metal is a hard work for the synthetic chemist due to their similar mode of interactions with ligands. Besides that, many MOFs are already utilized for the detection of phosphate ion in presence of another analytes. But there are very few reports have been found for the selective and sensitive detection of phosphate anion. In maximum cases quenching of luminescence is used as a tool for the detection of phosphate anion by MOFs whereas the luminescence turn- on based detection of this anion are scarcely reported.[72-74]

Keeping all these things in mind, we have synthesized a 3d-4d heterobimetallic metal- organic framework, $[YMn_{1.5}(C_7N_1H_3O_5)_3(H_2O)_6]\cdot 11H_2O$, **3**, hydrothermally by using Y(III), Mn(II) and chelidamic acid for the luminescence turn- on based selective detection of this anion in water medium. This is the first observation to our knowledge, where a 3d- 4d heterobimetallic MOF is utilized for the selective detection of phosphate.

4.2 EXPERIMENTAL SECTION

4.2.1 Materials

All the chemicals were commercially available and used as received without further purification. $Y(NO_3)_3\cdot 6H_2O$ (Sigma Aldrich, 99.9%), Mn $(OAc)_2\cdot 4H_2O$ (Sigma Aldrich, 98%), Chelidamic acid (Sigma Aldrich, 99%) were used for synthesis. NaF (Merck, 97%), NaCl (Merck, 99%), NaBr (Merck, 99%), NaI (Merck, 99%), $NaNO_2$ (Merck, 99%), $NaNO_3$ (Merck, 99.5%), Na_2SO_4 (Merck, 99%), Na_3PO_4 (Sigma Aldrich, 99%), $CH_3COONa\cdot 3H_2O$ (Merck, 99%), $Na_2C_2O_4$ (Merck, 99%) and $ZnClO_4\cdot 6H_2O$

(Aldrich, 99%) were used for the sensing experiments. Doubly distilled water was used throughout the whole experiments.

4.2.2 Synthesis of compound 3

The compound **3** was synthesized by employing the hydrothermal method. $Y(NO_3)_3\cdot 6H_2O$ (0.05mM, 0.0191 g), $Mn(OAc)_2\cdot 4H_2O$ (0.075mM, 0.0185g) and chelidamic acid (0.15mM, 0.0301g) were dispersed in 5 mL water. Then the mixture was homogenized at room temperature for 30 min. Then the final reaction mixture was sealed in a 23 mL PTFE- lined stainless-steel autoclave, kept under autogenous pressure and heated at 120°C for 72 h and then cooled to room temperature. The starting pH and the pH value after the reaction were 1 and 3 respectively. The clear solution, obtained after completing the reaction was then kept at room temperature in a capped glass bottle and then after one day, light golden- yellow-colored hexagonal shaped crystals appear at the bottom of the bottle and were collected using filtration and washed with deionized water under vacuum and dried at ambient conditions. Elemental analysis calcd (%) for **3**: C 24.71, H 4.21, N 4.11; found: C 24.55, H 4.17, N 4.16 (Yield 70% based on Y and Mn).

4.2.3 Instrumentations

Powder X-ray diffraction (XRD) patterns were measured on well ground samples in the 2θ range 5-50° using Cu Kα radiation (Bruker D8 Discover instrument) at room temperature. To examine the stability of compound **3** in presence of phosphate ions, the powdered form of the compound was immersed in an aqueous solution of PO_4^{3-} ion (Na_3PO_4) for 24 h and 48 h respectively and dried. Then, the PXRD patterns were recorded for the compound **3** in the presence of phosphate ions. Thermogravimetric analysis (TGA) using Perkin-Elmer instrument STA 6000 has been carried out in nitrogen atmosphere (flow rate = 20 ml min^{-1}) in the temperature range 40 – 800 °C (heating rate = 20 °C min^{-1}). The IR spectral studies were performed on Nicolet Magna IR 750 series-II FTIR- spectrophotometer in the solid state. In case of IR spectroscopy measurement, for phosphate incorporated MOF, the powdered form of the compound was soaked into the aqueous solution of PO_4^{3-} ion (Na_3PO_4) for 24 h and dried, then we have performed IR spectroscopy experiment. Nitrogen gas adsorption - desorption of the sample (BET experiment) were carried out using Autosorb iQ2, Quantachrome Instruments, USA.

4.2.4 Single- crystal structure determination of compound 3

A suitable single crystal was carefully selected under a polarising microscope and glued carefully to a thin glass fibre. The single crystal data were collected using Bruker D8 Quest machine at 293(2) K. The X-ray generator was operated at 50 kV and 1 mA using Mo Kα (λ=0.71073Å) radiation. Data were collected with ω scan width of 0.5º. A total of 408 frames were collected in three different setting of φ (0, 90, 180º) keeping sample-to-detector distance fixed at 6.03 cm and the detector position (2θ) fixed at -25º. The final data sets were reduced by an APEX3 program, while a SAINTPLUS[75] program was utilized for the integration of diffraction profiles. The absorption correction (multi-scan) was carried out by a SADABS program.[76] We initially solved the structure by SIR 92,[77] and the full matrix least-square method (SHELXL-2016[78]) was used further, which is present in the WinGx suit of programs (Version 1.63.04a).[79-80] We successfully located all the non-hydrogen atoms from Fourier maps and refined them with anisotropic displacement parameters at the final cycles. Finally, we fixed all the hydrogen atoms at calculated positions and included them in the refinement process using riding model associated with isotropic thermal parameters. A detail of the structure solution and final refinement is given in the Table 4.1. CCDC: 2195093 contain the crystallographic data for this paper. These data can be obtained free of charge from The Cambridge Crystallographic Data Center (CCDC) via www.ccdc.cam.ac.uk/data_request/cif.

Table 4.1: Crystal data and structure refinement parameters for $[YMn_{1.5}(C_7N_1H_3O_5)_3(H_2O)_6] \cdot 11H_2O$ **(**$C_7N_1H_3O_5$ = chelidamate**), 3.**

Empirical formula	$C_7H_3Mn_{0.50}NO_{10.67}Y_{0.33}$
Formula weight	328.88
Crystal system	Trigonal
Space group	R-3 (No. 148)
a (Å)	14.4047 (13)
b (Å)	14.4047 (13)
c (Å)	33.900 (3)
α (deg)	90
β (deg)	90
γ (deg)	120
Volume (Å^3)	6091.6 (12)
Z	18

T (K)	273 (2)
ρ_{calc} (g cm^{-3})	1.614
μ (mm^{-1})	1.987
θ range (deg)	1.739 to 27.144
λ (Mo Kα) (Å)	0.71703
R indices [I>2σ(I)]	$R_1 = 0.0504$, $wR_2 = 0.1419$
R indices (all data)	$R_1 = 0.0685$, $wR_2 = 0.1549$

$R_1 = \Sigma ||F_0|-|F_c|| / \Sigma |F_0|$; $wR_2 = \{\Sigma[w(F_0^2 - F_c^2)^2] / \Sigma[w(F_0^2)^2]\}^{1/2}$. $w = 1/[\sigma^2(F_0)^2 + (aP)^2 + bP]$, $P = [\max.(F_0^2,0) + 2(F_c)^2]/3$, where a = 0.0792 and b = 29.9806.

4.2.5 Photoluminescence measurement

The aqueous solution of compound **3** was prepared by introducing compound **3** (1.6 mg) into 4 mL water and the mixture was then ultra-sonicated for 2 minutes. The photoluminescence measurements were performed using 150 µL of the stock solution into 2 mL of water in a quartz cuvette. Photoluminescence properties of compound **3** were investigated at room temperature in water using Horiba Fluoromax- 4 spectrofluorometer upon excited at 280 nm. The slit width was 5 nm for both excitation and emission. The UV- Vis spectra were recorded using SHIMADZU UV- 1900i spectrophotometer. The anion solutions of concentration 5 × 10^{-3} M were prepared from water. The whole experiment was done at room temperature. The analytes were added to the cuvette by using micropipette. Time- correlated single- photon counting (TCSPC) measurements were done at room temperature in water using HORIBA Jobin- Yvon instrument in the nano second time domain. For TCSPC measurement, the excitation wavelength was used at 280 nm and the emission decay curve was monitored at 388 nm.

4.3 RESULTS AND DISCUSSION

4.3.1 Structure of compound 3

Compound **3** crystallized in a trigonal crystal system with *R*-3 space group. The asymmetric unit of **3** consists of crystallographically independent one Y^{3+} ion with one-third occupancy, one Mn^{2+} ion with half occupancy, one chelidamate anion, two coordinated water molecules and five lattice water molecules (three with full occupancy and two with one-third occupancy) (Figure 4.1). The Y^{3+} ion is nine coordinated by the six oxygen atoms and three nitrogen atoms and has a tricapped trigonal prism geometry through the six oxygen atoms from six carboxylate groups and three nitrogen atoms of pyridine rings of three chelidamate ligands (Figure 4.2a). The Mn^{2+} ion is six coordinated by six oxygen atoms and has an octahedral geometry through the four oxygen atoms of four coordinated water molecules and two oxygen atoms of two chelidamate ligands (Figure 4.2b). The coordination mode of chelidamate ligand is shown in figure 4.2c. Out of the two carboxylate groups, one is bidentate with respect to one Y^{3+} ion and one Mn^{2+} ion and another one is monodentate with respect to one Mn^{2+} ion. The phenolic hydroxyl group remains free in the structure.

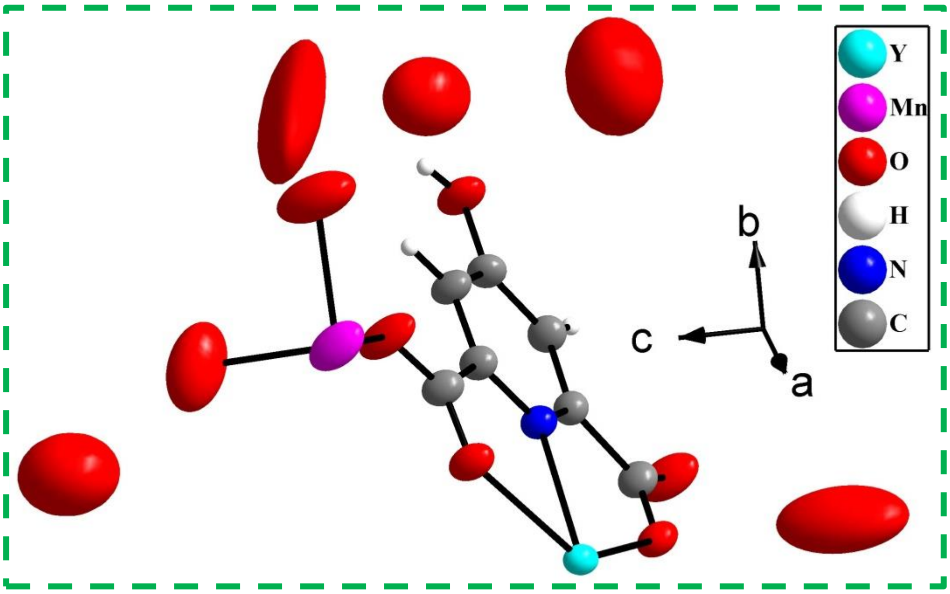

Fig. 4.1 Thermal ellipsoid model of the asymmetric unit of $[YMn_{1.5}(C_7N_1H_3O_5)_3(H_2O)_6]\cdot 11H_2O$ **(**$C_7N_1H_3O_5$ = chelidamate**), 3.**

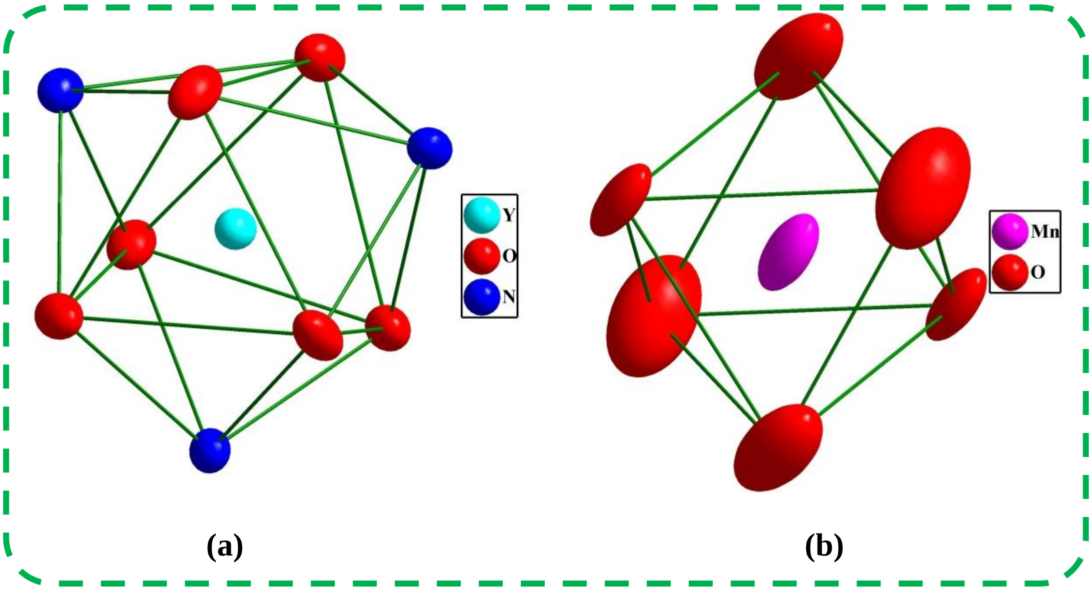

(a) (b)

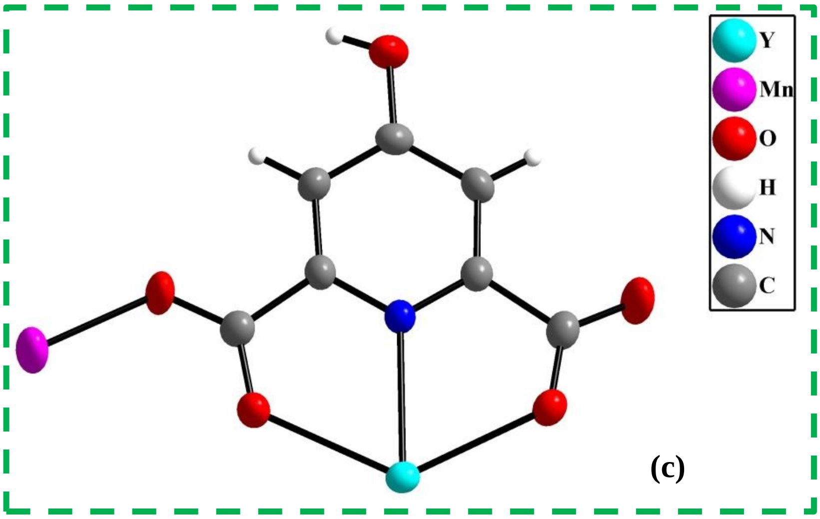

Fig. 4.2 Thermal ellipsoid model of tricapped trigonal prism geometry around Y^{3+} ion (a), octahedral geometry around Mn^{2+} ion (b), coordination modes of chelidamate ion (c) in $[YMn_{1.5}(C_7N_1H_3O_5)_3(H_2O)_6]\cdot 11H_2O$, **3.**

The Y−O bonds have an average distance of 2.39 Å, and Y-N bonds have an average distance of 2.47 Å. The Mn-O bonds have an average distance of 2.18 Å. The O/N-Y-N/O bond angles range is in the range of 63.84 (9) - 146.43 (10)° and the O-Mn-O bond angles is in the range of 87.75(18) – 180°. The selected bond distances are listed in Table 4.2 and the selected bond angles are listed in Table 4.3.

Table 4.2: Selected bond distances (Å) observed in $[YMn_{1.5}(C_7N_1H_3O_5)_3(H_2O)_6]\cdot 11H_2O$, **3**.

Bond	Distances, Å	Bond	Distances, Å
Y(1)- O(1)	2.388 (3)	Y(1)- O(3)#1	2.399 (3)
Y(1)- O(1)#1	2.388 (3)	Y(1)- N(1)#2	2.473 (3)
Y(1)- O(1)#2	2.388 (3)	Y(1)- N(1)#1	2.473 (3)
Y(1)- O(3)	2.399 (3)	Y(1)- N(1)	2.473 (3)
Y(1)- O(3)#2	2.399 (3)	Mn(1)-O(2)#3	2.144(3)
Mn(1)-O(2)	2.144(3)	Mn(1)-O(6)#3	2.197(6)
Mn(1)-O(6)	2.197(5)	Mn(1)-O(7)#3	2.205(4)
Mn(1)-O(7)	2.205(4)		

Symmetry transformations used to generate equivalent atoms: #1 -x+y+1,-x+1,z #2 -y+1,x-y,z #3 -x+5/3,-y+4/3,-z+4/3

Table 4.3: Selected bond angles observed in $[YMn_{1.5}(C_7N_1H_3O_5)_3(H_2O)_6]\cdot 11H_2O$, **3**.

Angle	Amplitude (°)	Angle	Amplitude (°)
O(1)- Y(1)- O(1)#1	77.50 (11)	O(3)#2- Y(1)- O(3)#1	79.39 (10)
O(1)- Y(1)- O(1)#2	77.50 (11)	O(1)- Y(1)- N(1)#2	134.24 (10)
O(1)#1- Y(1)- O(1)#2	77.50 (11)	O(1)#1- Y(1)- N(1)#2	70.54 (10)
O(1)- Y(1)- O(3)	128.23 (9)	O(1)#2- Y(1)- N(1)#2	64.41 (9)
O(1)#1- Y(1)- O(3)	146.43 (10)	O(3)- Y(1)- N(1)#2	75.92 (10)
O(1)#2- Y(1)- O(3)	87.04 (10)	O(3)#2- Y(1)- N(1)#2	63.84 (9)
O(1)- Y(1)- O(3)#2	146.42 (10)	O(3)#1- Y(1)- N(1)#2	138.61
O(1)#1- Y(1)- O(3)#2	87.04 (10)	O(1)- Y(1)- N(1)#1	70.54 (10)
O(1)#2- Y(1)- O(3)#2	128.23 (9)	O(1)#1- Y(1)- N(1)#1	64.41 (9)
O(3)- Y(1)- O(3)#2	79.39 (10)	O(1)#2- Y(1)- N(1)#1	134.24 (10)
O(3)- Y(1)- O(3)#1	87.03 (10)	O(3)- Y(1)- N(1)#1	138.61 (10)
O(1)#1- Y(1)- O(3)#1	128.23 (9)	O(3)#2- Y(1)- N(1)#1	75.92 (10)
O(1)#2- Y(1)- O(3)#1	146.42 (10)	O(3)#1- Y(1)- N(1)#1	63.84 (9)
O(3)- Y(1)- O(3)#1	79.39 (10)	N(1)#2- Y(1)- N(1)#1	119.895 (8)
O(1)-Y(1)-N(1)	64.41(9)	O(1)#1-Y(1)-N(1)	134.23(10)
O(1)#2-Y(1)-N(1)	70.53(10)	O(3)-Y(1)-N(1)	63.84(9)
O(3)#2-Y(1)-N(1)	138.61(10)	O(3)#1-Y(1)-N(1)	75.92(10)
N(1)#2-Y(1)-N(1)	119.895(9)	N(1)#1-Y(1)-N(1)	119.895(9)
O(2)#3-Mn(1)-O(2)	180.0	O(2)#3-Mn(1)-O(6)#3	92.25(18)
O(2)-Mn(1)-O(6)#3	87.75(18)	O(2)#3-Mn(1)-O(6)	87.75(18)
O(2)-Mn(1)-O(6)	92.25(18)	O(6)#3-Mn(1)-O(6)	180.0
O(2)#3-Mn(1)-O(7)#3	88.13(14)	O(2)-Mn(1)-O(7)#3	91.87(14)
O(6)#3-Mn(1)-O(7)#3	90.4(3)	O(6)-Mn(1)-O(7)#3	89.6(3)
O(2)#3-Mn(1)-O(7)	91.87(14)	O(2)-Mn(1)-O(7)	88.13(14)
O(6)#3-Mn(1)-O(7)	89.6(3)	O(6)-Mn(1)-O(7)	90.4(3)
O(7)#3-Mn(1)-O(7)	180.0(2)		

Symmetry transformations used to generate equivalent atoms: #1 -x+y+1,-x+1,z #2 -y+1,x-y,z #3 -x+5/3,-y+4/3,-z+4/3

The connectivity among Y^{3+} ions, Mn^{2+} ions and chelidamate ligands form a two-dimensional layer structure with acidic pockets decorated by the phenolic hydroxyl groups (Figure 4.3a). The distance between two opposite oxygen atoms of hydroxyl group is ≈ 8 Å. The layers are arranged along the *b* axis in ABAB…. fashion to give a three-dimensional packing arrangement stabilized by hydrogen bonds involving lattice water molecules and π…π interactions of pyridine rings (Figure 4.3b).

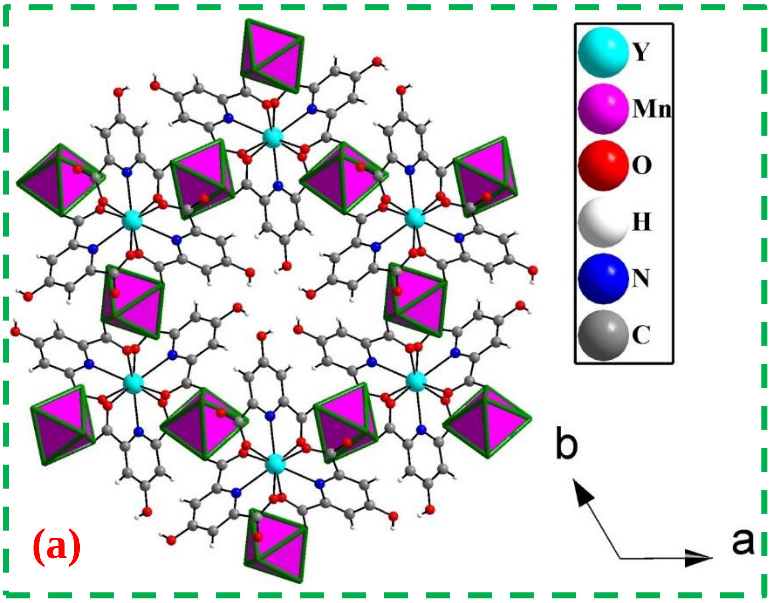

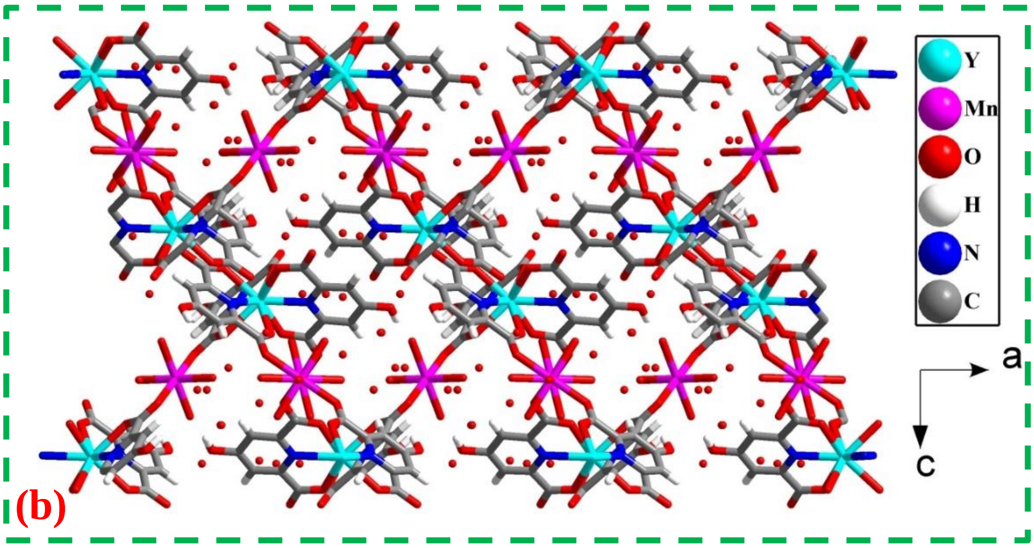

Fig. 4.3 (a) Figure shows connectivity between Y^{3+} ions and Mn^{2+} ions through chelidamate ligands. MnO_6 units are shown as octahedral polyhedra in $[YMn_{1.5}(C_7N_1H_3O_5)_3(H_2O)_6]\cdot 11H_2O$, **3**, (b) Arrangement of two layers to show three-dimensional packing arrangement (see text).

4.3.2 Characterization of compound 3

Powder X- ray diffraction (XRD) patterns were recorded on well- grounded samples in the 2θ range 5-50° (Figure 4.4). To confirm the phase purity, the powder X- ray patterns were compared with the simulated XRD pattern generated based on the structure determined using single crystal XRD. The experimental patterns were in good agreement with the simulated one.

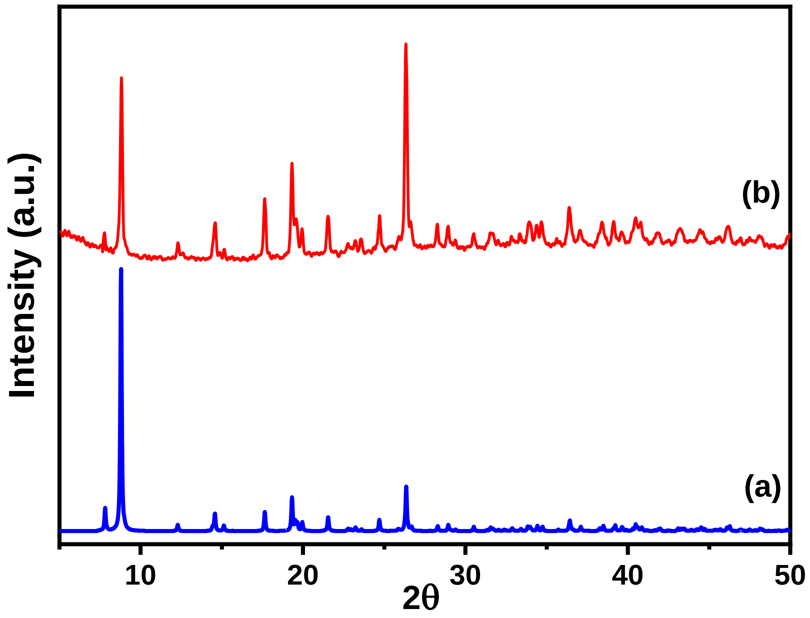

Fig. 4.4 Powder XRD (CuKα) patterns: (a) simulated from single crystal X-ray data of $[YMn_{1.5}(C_7N_1H_3O_5)_3(H_2O)_6]\cdot 11H_2O$, **3** and (b) hydrothermally synthesized $[YMn_{1.5}(C_7N_1H_3O_5)_3(H_2O)_6]\cdot 11H_2O$, **3.**

The thermogravimetric analysis (TGA) of compound **3** has been carried out in a nitrogen atmosphere (Figure 4.5a). The TGA experiment shows weight loss in three steps. The first weight loss of 18.5% (calculated 19.40%) up to 110°C is due to removal of eleven lattice water molecules. The second weight loss of 26.7% (calculated 29.98%) up to 270°C is due to removal of coordinated water molecules. The weight loss above 450°C is probably due to the decomposition of the framework. This result proved that the compound **3** is stable up to 450°C, suggesting its amazing thermal stability. The IR spectra of the compound were recorded in the spectral range 4000-500 cm^{-1}. All the characteristic peaks associated with the chelidamate ligand and water molecules have been observed. The prominent band around 3450 cm^{-1} is due to the presence of free hydroxyl group present within the structure (Figure 4.5b).

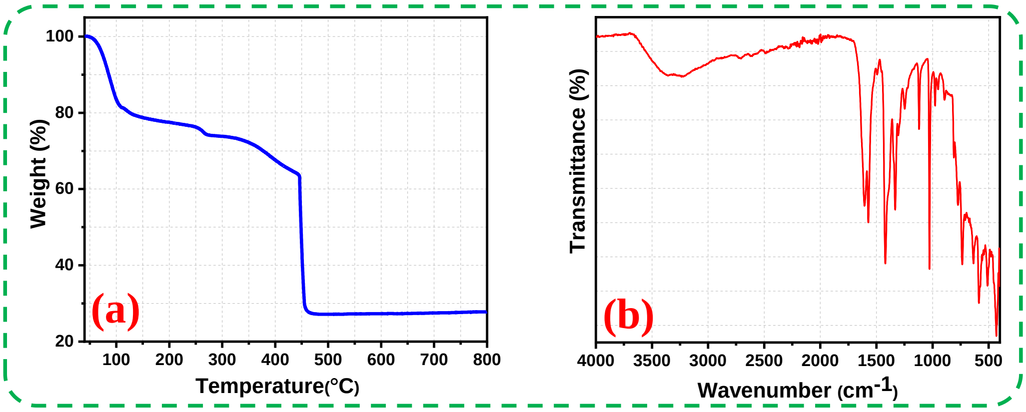

Fig. 4.5 (a) Thermogravimetric analysis (TGA) of compound **3** in nitrogen atmosphere and (b) IR spectrum of compound **3.**

To understand about the porosity, nitrogen gas adsorption-desorption studies (BET experiment) of compound **3** were carried out. For that the powder sample were pretreated at 150 °C for 60 min to ensure the removal of lattice water molecules. The BET experiment shows surface adsorption type behavior with surface area of 93.2 m^2/ g (Figure 4.6). This is probably due to the contraction of the pore after the removal of lattice water molecules.

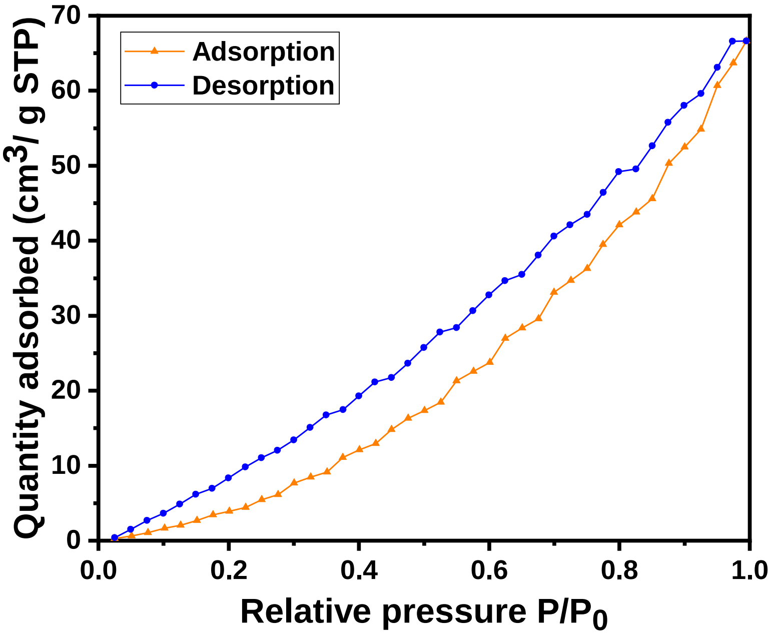

Fig. 4.6 N_2 sorption plot of compound **3**.

4.3.3 Photoluminescence behavior

All the absorption and luminescence spectra were measured in room temperature. The UV- Vis spectra of compound **3** and the ligand were recorded to observe the positions of electronic transitions (Figure 4.7). The photoluminescence property of compound **3** was investigated by using its aqueous dispersion upon excitation at 280 nm. The luminescence measurements were monitored at the emission wavelength ranging from 330 to 500 nm under an excitation wavelength (λ_{ex}) of 280 nm at room temperature. Upon excitation at 280 nm, **3** exhibits an intense emission peak centered at 388 nm. The observed emission arises from the intra- ligand transitions ($\pi^* \rightarrow \pi$ and $\pi^* \rightarrow n$) of the bonded organic ligands with the metal center. The excellent luminescence property of **3** encouraged us to explore its interaction with different anions in an aqueous medium based on the availability of free hydroxyl groups within the acidic pocket of compound **3**.

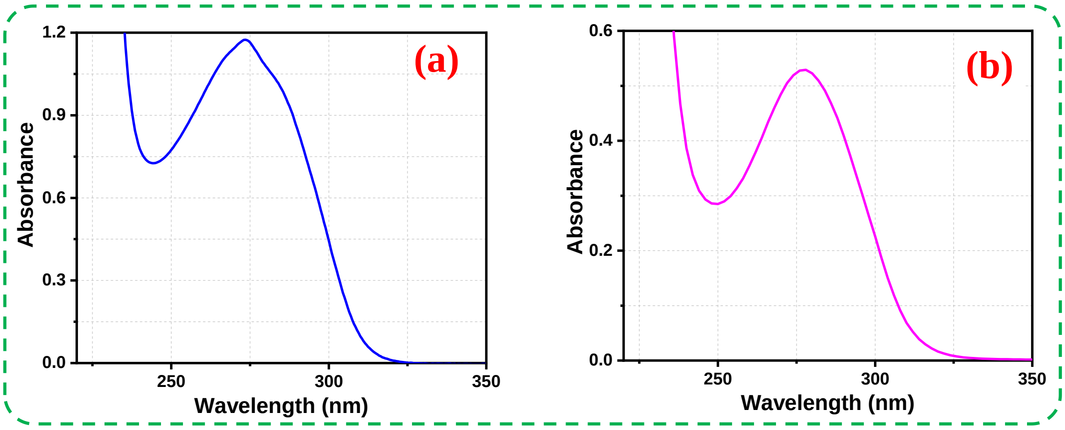

Fig. 4.7 The UV- Vis spectra of (a) the ligand (chelidamic acid) and (b) compound **3**.

4.3.4 Anions Sensing behaviors

To enquire about the efficiency of compound **3** towards the detection of a trace amount of anion, luminescence- based titration was performed with the incremental addition of different anions to the aqueous dispersion of **3**. The luminescence- based titration was performed in the presence of different anions, namely F^-, Cl^-, Br^-, I^-, NO_2^-, NO_3^-, SO_4^{2-}, $C_2O_4^{2-}$, CH_3COO^- and ClO_4^- (Figure 4.8- Figure 4.9).

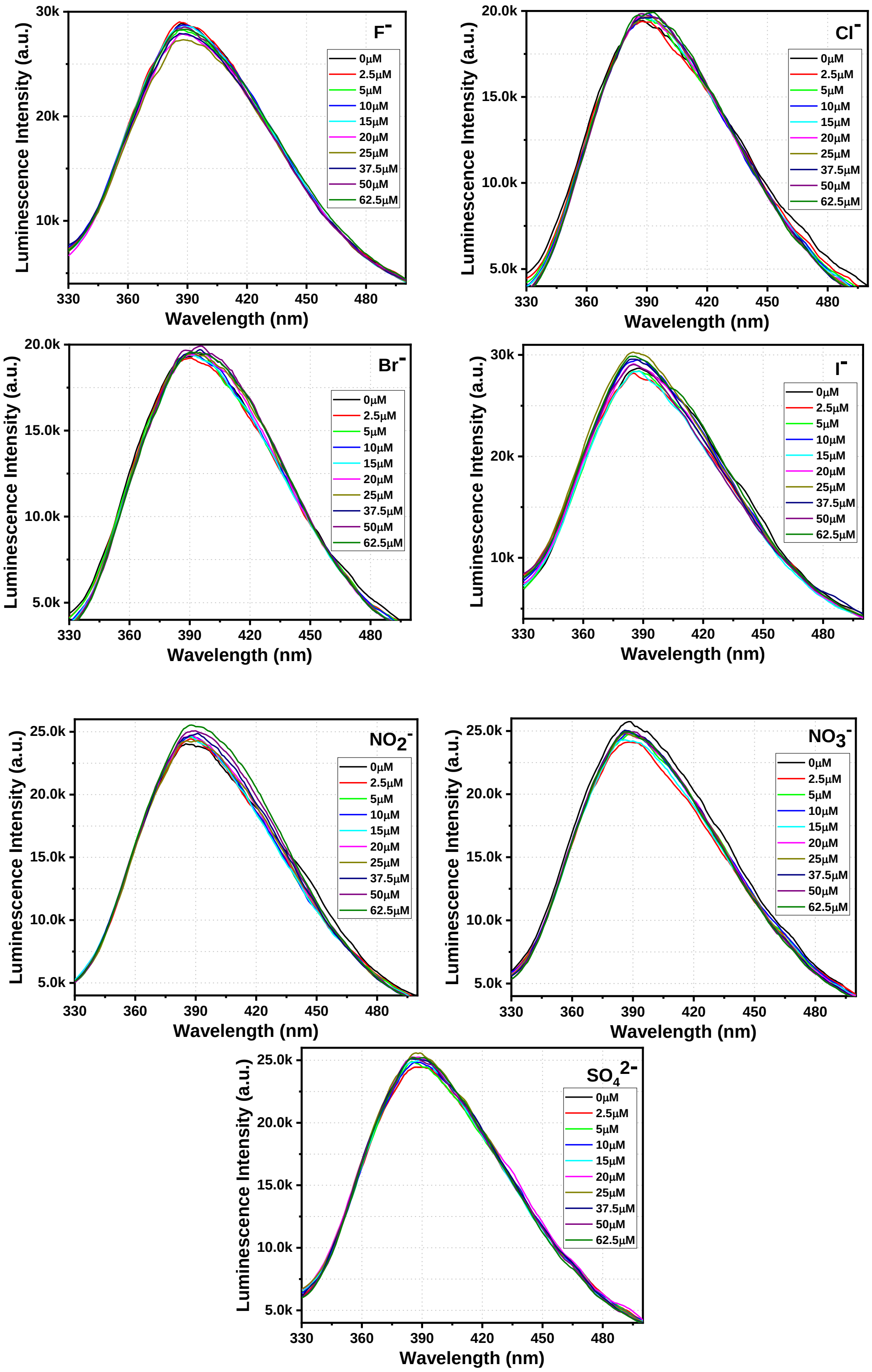

Fig. 4.8 Emission spectra of compound **3** in aqueous dispersion upon incremental addition of aqueous solution of different ions (λ_{ex}= 280 nm).

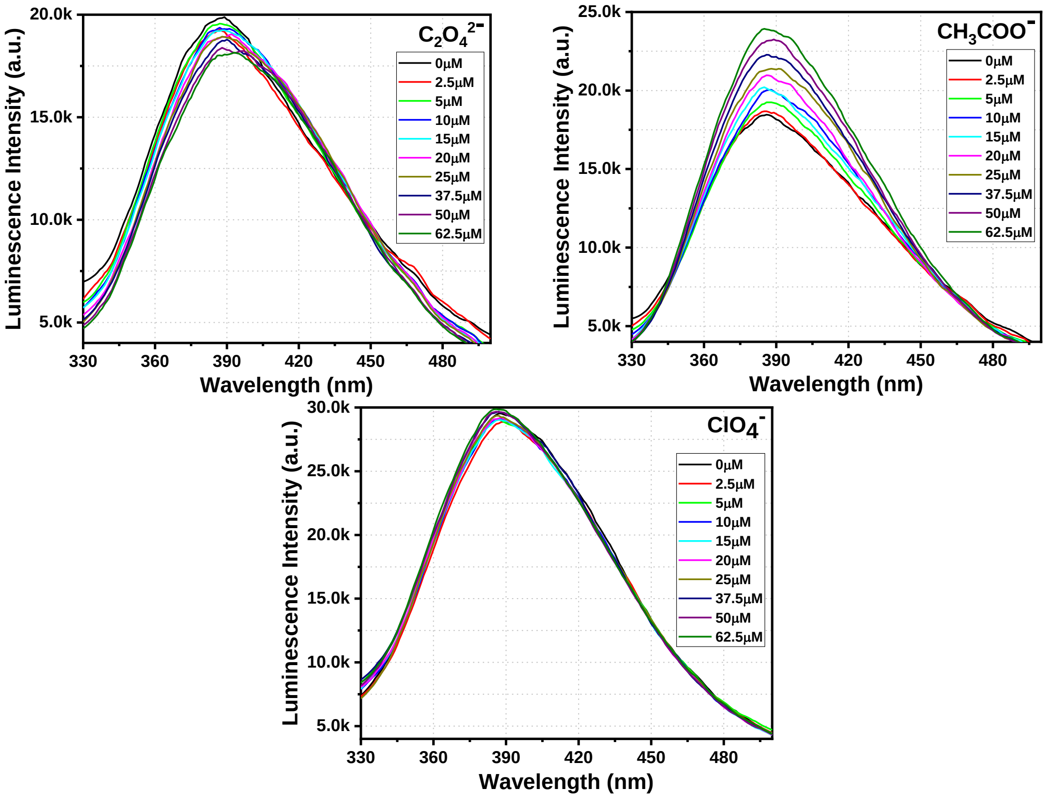

Fig. 4.9 Emission spectra of compound **3** in aqueous dispersion upon incremental addition of aqueous solution of different ions (λ_{ex}= 280 nm).

The luminescence intensity was changed upon incremental addition of phosphate ion (up to 62.5µM) in compound **3** is shown in Figure 4.10. In case of all the anions, after the addition of 62.5 µM, the changes in luminescence intensity based on the emission at 388 nm are shown in Figure 4.11 as a bar diagram with respect to turn- on percentage. Among all these anions the compound **3** showed significant changes in luminescence intensity in the case of only PO_4^{3-} anion. Upon exposure to UV light, the emission of compound **3** dispersed in water was increased with the addition of PO_4^{3-} (concentration up to 62.5 µM) and 4.09 times turn- on of the initial luminescence intensity was observed.

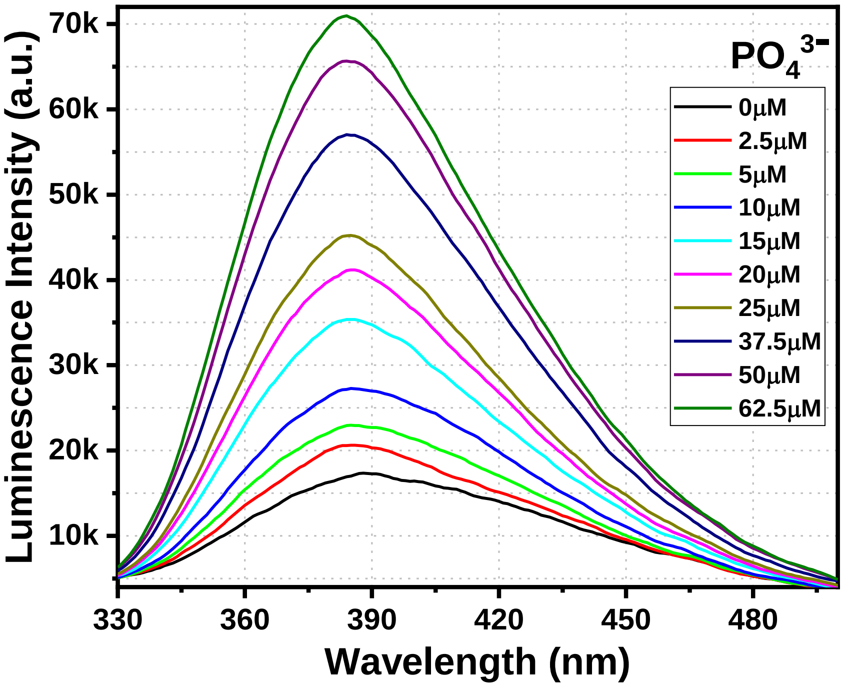

Fig. 4.10 Emission spectra of compound **3** in aqueous dispersion upon the incremental addition of aqueous solution of PO_4^{3-} ions. Final concentration of phosphate shown in legend.

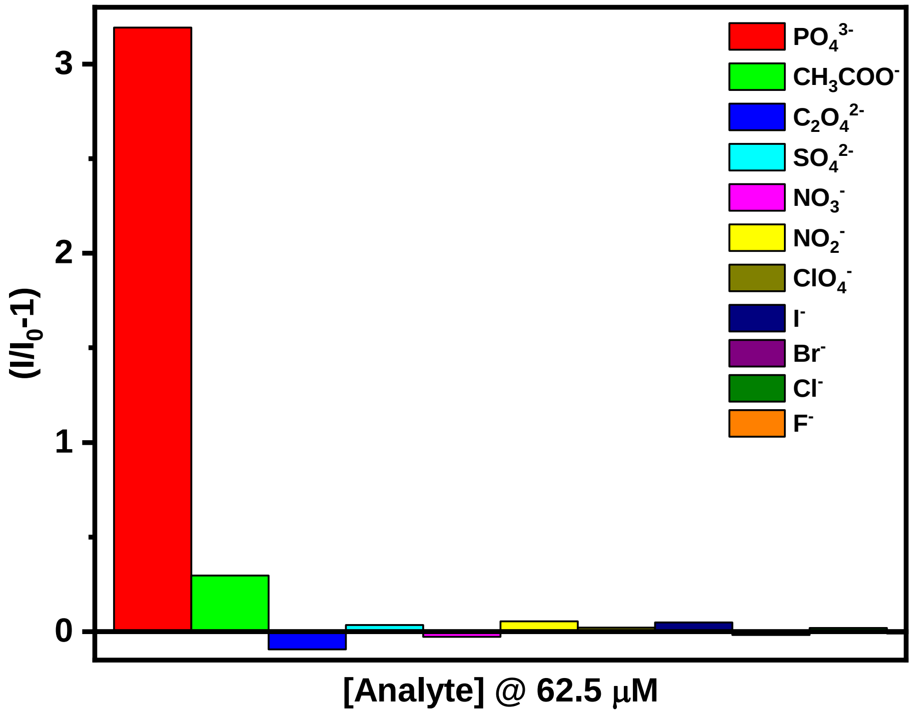

Fig. 4.11 Changes in luminescence intensity with respect to the emission of the compound **3** (at 388 nm) with 62.5 μM of different anions.

These results indicate that the luminescence behavior of compound **3** is significantly different in the presence of phosphate (PO_4^{3-}) ion. The limit of detection (LOD) for this anion was calculated using the equation, LOD= 3σ/m, where σ = standard deviation of blank determination and m = slope of the linear curve plotted at a lower concentration for LOD measurements. According to this equation, the LOD was found to be 0.20 µM (19.55 ppb) for PO_4^{3-} anion (Figure 4.12). The sensitivity could be further determined by calculating the luminescence enhancement coefficient, K_{SV} according to the equation: $I/I_0 = 1 + K_{SV}[A]$, where I_0 and I are the luminescence intensities before and after the addition of analytes, respectively, [A] is the molar concentration of the analyte and K_{SV} is the luminescence enhancement coefficient. A linear increase in (I/I_0) was observed for the above anions when the concentration was low (up to 10 µM; Figure 4.13). The SV plot diverged from linearity and turned upwards with the increase of concentration of the PO_4^{3-} anion (Figure 4.14).

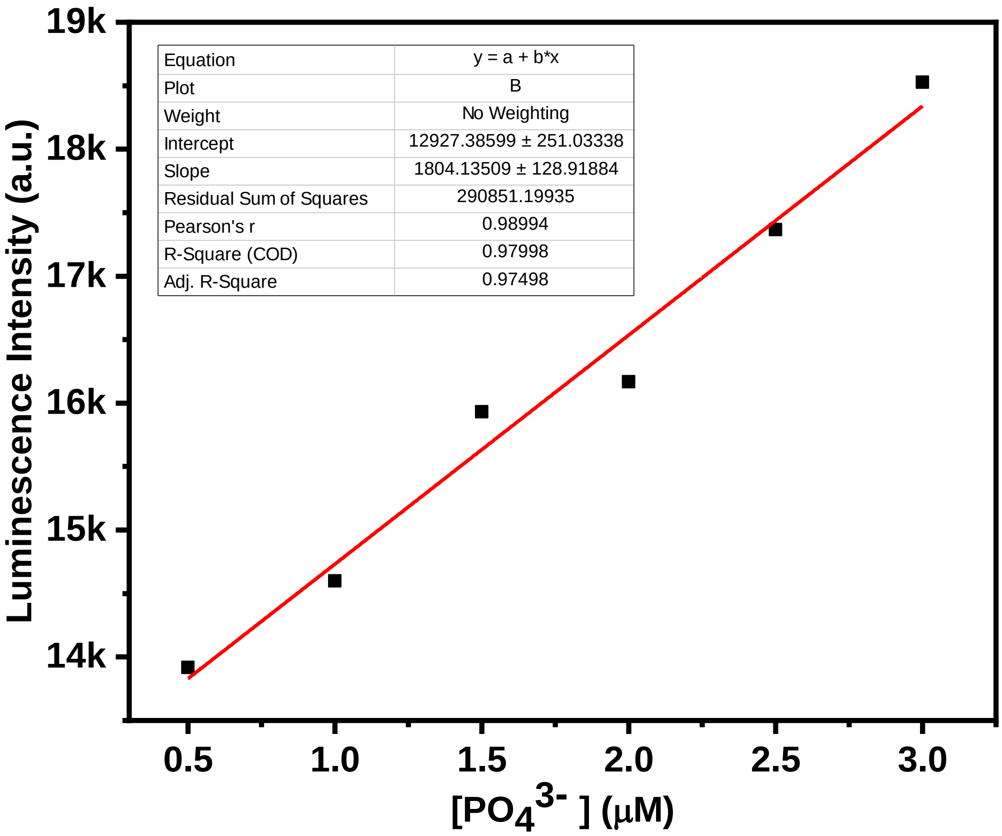

Equation	y = a + b*x
Plot	B
Weight	No Weighting
Intercept	12927.38599 ± 251.03338
Slope	1804.13509 ± 128.91884
Residual Sum of Squares	290851.19935
Pearson's r	0.98994
R-Square (COD)	0.97998
Adj. R-Square	0.97498

Fig. 4.12 Plot of luminescence intensity *vs* concentration of phosphate.

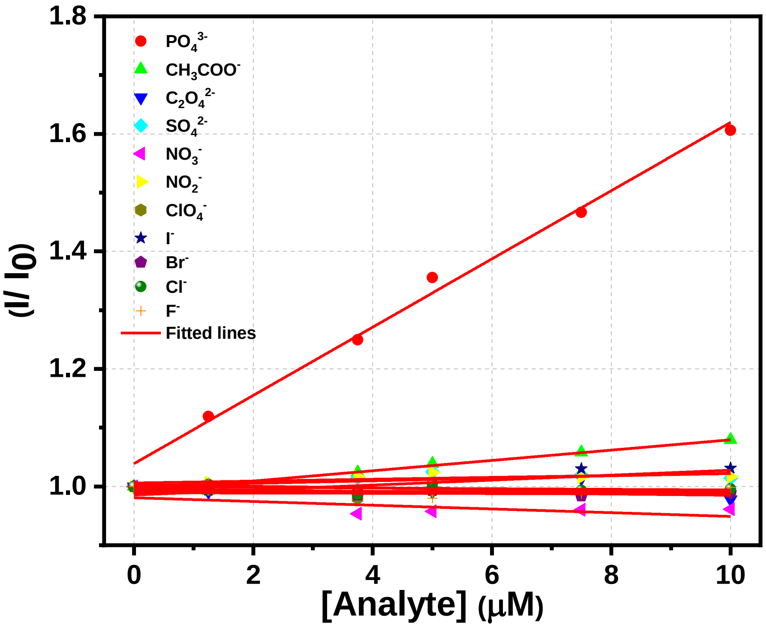

Fig. 4.13 Plot of I/I$_0$ of compound **3** (at 388 nm) *vs* concentration of analytes in the lower concentration range of analytes (up to 10 µM). I$_0$ and I are the luminescence intensity in absence and presence of the analyte, respectively.

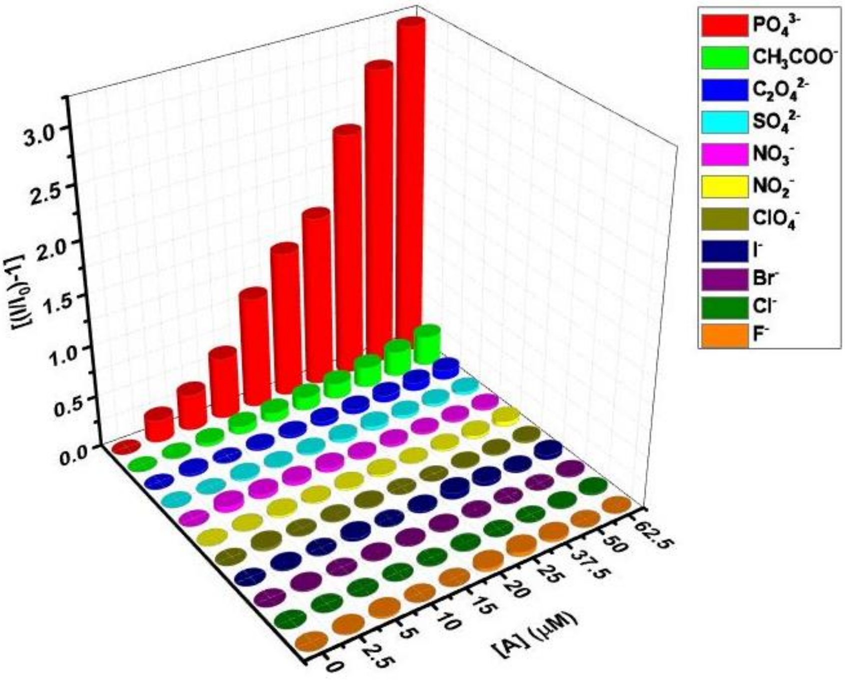

Fig. 4.14 Plot of [(I/ I$_0$)-1)] against the concentration of analytes for **3** after the addition of 62.5 µM of these analytes.

To obtain the luminescence enhancement coefficient (K_{SV}), we fitted the experimental data (up to 10 µM) in the S-V equation. The obtained K_{SV} value is 5.8×10^4 M^{-1} for PO_4^{3-}. The observed K_{SV} value for PO_4^{3-} is very high over other anions and which again proof the extreme sensitivity and high turn- on performance of the compound **3**, which make compound **3** amongst the most sensitive luminescence- based detector for this toxic anion. According to the previously reported literature survey and based on the comparison, the observed limit of detection and luminescence enhancement coefficient (K_{SV}) for compound **3** depicts it as one of the best luminescence- based metal- organic framework probe for the detection of this anion (Table 4.4).

Table 4.4: A summary of luminescence - based detection of PO_4^{3-} using metal- organic frameworks.

Name/ formula of MOF	Mechanism	Solvent	Limit of detection (LOD)	K_{SV} (M^{-1})	Ref.
$[Eu_2(ppda)_2(npdc)(H_2O)]\cdot H_2O$	Quenching	aqueous	14.2 µM	1.8×10^5	58
$[Eu(BDC)(NO_3)(DMF)_2]_n$	Quenching	aqueous	0.83 µM	2.79×10^4	59
$\{[Eu_{1.5}(BTB)_{1.5}(H_2O)]. 3DMF\}_n$	Quenching	aqueous	10 µM	7.97×10^3	60
$[Tb(H_2O)(BTB)]$	Quenching	aqueous	35 µM	Not given	61
$\{Eu_2L_3(DMF)\}\cdot 2DMF$	Quenching	HEPES buffer	6.62 µM	4×10^4	62
$[Pr(L)(NO_3)(H_2O)_2]_n$	Quenching	aqueous	1 µM	4.48×10^3	63
$\{[Eu(bcpt)(HCOO)]\cdot 0.5H_2O\}_n$	Quenching	aqueous	274 µM	1.27×10^4	64
$[\{Eu_5(OH)_6(TZI)_3(DMA)_{1.5}(H_2O)_{10.5}\}\cdot DMA\cdot 0.5H_2O]_n$	Quenching	aqueous	Not given	92,249	65
$[\{Tb_5(OH)_6(TZI)_3(DMA)_{1.5}(H_2O)_{10.5}\}\cdot DMA\cdot 0.5H_2O]_n$	Quenching	aqueous	Not given	90,485	65
Eu(O-cpia)(phen)	Quenching	aqueous	Not given	NA	66
$[Tb(cpboda)(DMF)_{1.863}(HCOOH)_{0.137}]_n$	Quenching	aqueous	453 µM	6.68×10^5	67
UiO-66-NH_2	Turn- on	HEPES buffer	1.25 µM	NA	68
$\{[Zn(btca)(py)_2]\}_n$	Turn- on	aqueous	0.473 µM	-3.52×10^2	69
$[(CH_3)_2NH_2]_6[Zn_6(OBA)_6(L_1)_3(SO_4)_2].SO_4.x$(solvent)	Quenching	aqueous	6.5 µM	6905	70
Zr-UiO-66-N_2H_3	Turn- on	Aqueous HEPES buffer	0.196 µM	NA	71
$\{[Zn_4(L^{3-})_2(O^{2-})(H_2O)_2]\cdot 4EtOH\}_n$	Quenching	aqueous Living cell buffer	0.010 µM	3.69×10^4	72

Besides, the observed limit of detection (LOD) is lower than the minimum contaminant limit (1 ppm)[81]. However, for practical field application, checking the selectivity of the detection of phosphate in the presence of another anion is utmost important because they may present with other anions. For this, we have performed the luminescence- based titration experiment by taking the dispersion of compound **3** in aqueous solution and added aqueous solution of 12.5 µM of other anions one after another to the compound **3** prior to the stepwise addition of phosphate solution until it reached to the total concentration of 25 µM. In case of phosphate, the luminescence spectral change remained unaltered even in presence of other interfering anions and also the enhancement coefficient (Figure 4.15).

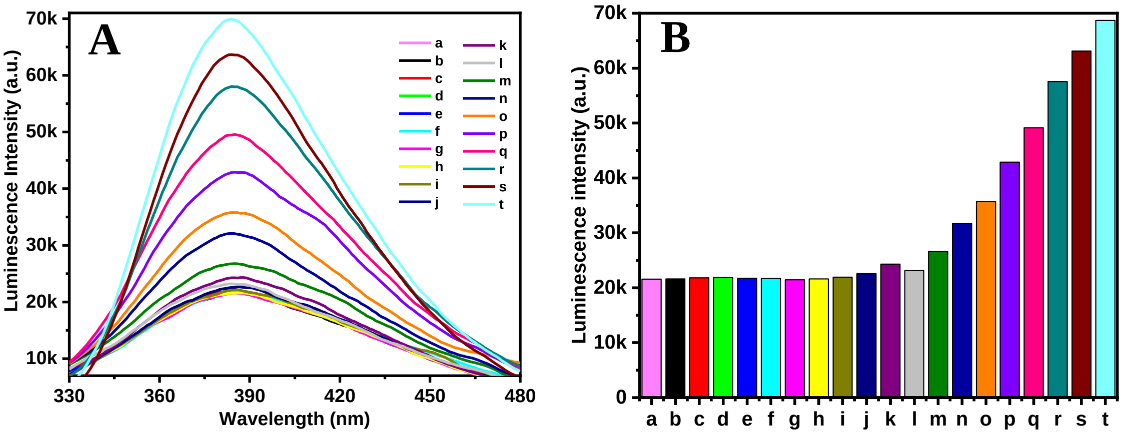

Fig. 4.15 (A) Emission spectra of **3** in an aqueous dispersion upon the incremental addition of PO_4^{3-} solution in the presence of 12.5 µM of different anion solution (λ_{ex} = 280 nm). (B) Corresponding bar diagram showing the luminescence intensity (monitored at 388 nm) after the sequential addition of the analytes. The composition and concentration of the system were as follows: (a) **3** in aqueous dispersion, (b) a + 12.5 µM F^-, (c) b + 12.5 µM Cl^-, (d) c + 12.5 µM Br^-, (e) d + 12.5 µM I^-, (f) e + 12.5 µM $C_2O_4^{2-}$, (g) f + 12.5 µM SO_4^{2-}, (h) g + 12.5 µM NO_3^-, (i) h + 12.5 µM NO_2^-, (j) i + 12.5 µM CH_3COO^-, (k) j + 12.5 µM ClO_4^-, (l) k + 2.5 µM PO_4^{3-}, (m) l + 5 µM PO_4^{3-}, (n) m + 10 µM PO_4^{3-}, (o) n + 15 µM PO_4^{3-}, (p) o + 20 µM PO_4^{3-}, (q) p + 25 µM PO_4^{3-}, (r) q + 37.5 µM PO_4^{3-}, (s) r + 50 µM PO_4^{3-}, and (t) s + 62.5 µM PO_4^{3-}.

These observations evidently exhibit that the compound **3** possessed tremendous selectivity and sensitivity towards phosphate anion in aqueous medium.

4.3.5 Chemical stability

It is very much important to check the stability of the compound in the presence of above anion in aqueous medium. At first, the powdered form of compound **3** was immersed in water for 24 h, then we have measured its PXRD patterns after drying and it remained well consistent with the simulated one. Then the powdered sample of **3** was immersed in an aqueous solution of PO_4^{3-} ion for 24 h and 48 h respectively and dried. The PXRD patterns were recorded for the compound **3** in the presence of this ion. Then, its PXRD pattern was compared with the simulated one obtained from single- crystal X-ray data (Figure 4.16). This result indicated that the compound remained stable in aqueous medium and also in the presence of phosphate ion even after the detection experiment.

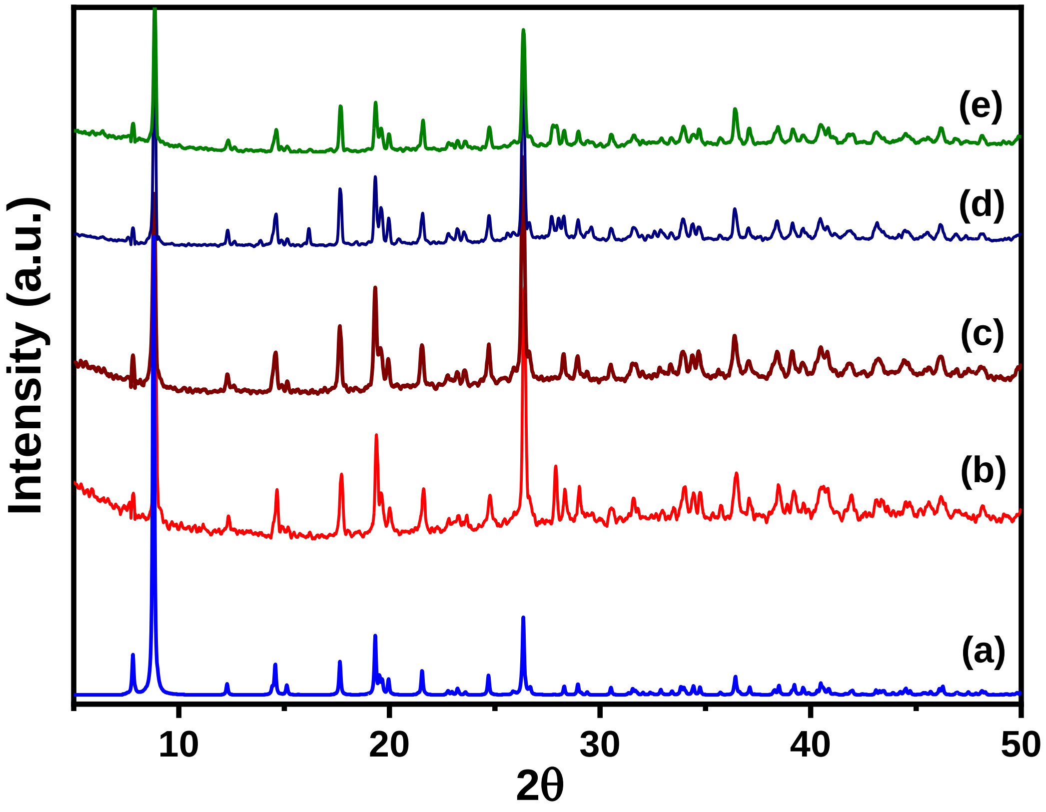

Fig. 4.16 Powder XRD (CuKα) patterns of (a) compound **3** simulated from single crystal X-ray data (b) as-synthesized **3**, (c) compound **3** after immersing in water for 24 h, (d) compound **3** after immersing in the aqueous solution of PO_4^{3-} for 24 h and (e) compound **3** after immersing in the aqueous solution of PO_4^{3-} for 48 h.

4.3.6 Lifetime decay analysis

Figure 4.17 illustrates the luminescence lifetime decay curves of the ligand- centered emission (λ_{em} = 388 nm) of compound **3** fitted in biexponential manner before and after addition of PO_4^{3-} anion. The average lifetime of compound **3** was found to be 1.21 ns in an aqueous dispersion. After the addition of 75 µM PO_4^{3-} anion, the average lifetime was increased to 3.25 ns (Table 4.5).

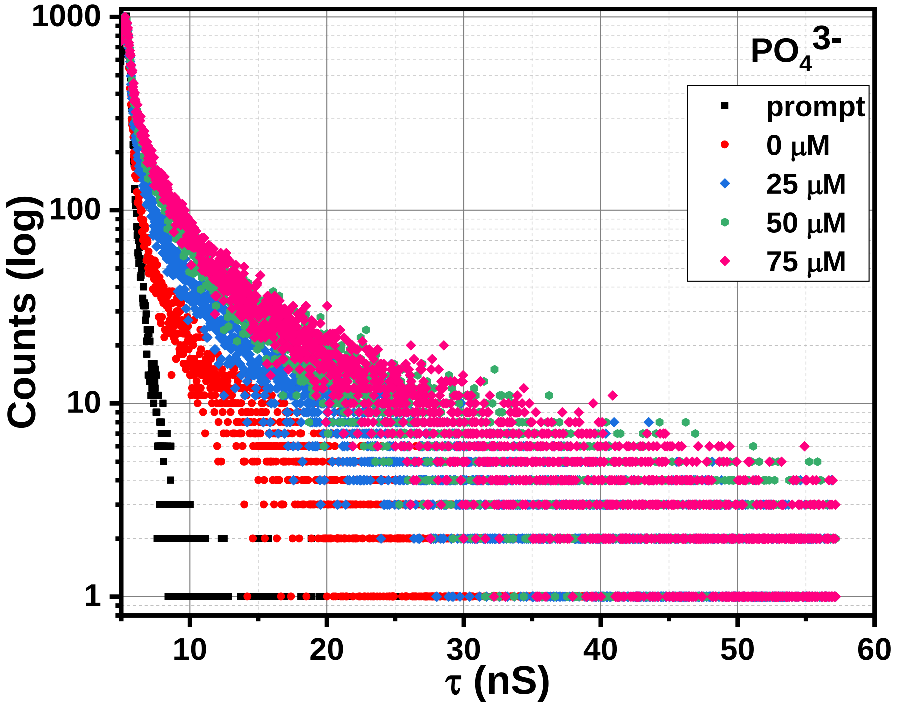

Fig. 4.17 Luminescence lifetime decay profile of compound **3** before and after the addition of PO_4^{3-} anion. The final concentration of PO_4^{3-} ion in the medium is indicated in the legend. The instrument response function (prompt) is also shown. Here, λ_{ex} = 280 nm and λ_{em} = 388 nm were set during the experiment.

Table 4.5: Average lifetime of compound **3** before and after the addition of PO_4^{3-} ((λ_{ex}= 280 nm; $\lambda_{em=}$ 388 nm).

Sl. No.	PO_4^{3-}	a_1	a_2	τ_1	τ_2	$a_1\tau_1 + a_2\tau_2$
1	0 µM	0.82	0.17	0.65	3.91	1.21 ns
2	25 µM	0.80	0.19	1.08	6.08	2.05 ns
3	50 µM	0.77	0.22	1.44	7.65	2.79 ns
4	75 µM	0.78	0.21	1.81	8.48	3.25 ns

4.3.7 Possible sensing mechanism of luminescence turn-on

Highly selective and turn-on luminescence behavior of **3** in presence of PO_4^{3-} ions can be explained from its preferential interactions with the compound **3** (Figure 4.18). The hydroxyl groups decorated acidic pocket is the important part of the compound for molecular level interactions with the anions. These interactions mainly depend on the two factors: size of the anions and the basicity of the anions. Probably, the sizes of the F^-, Cl^-, Br^-, I^-, NO_2^-, NO_3^- are too small for efficient molecular level interactions whereas $C_2O_4^{2-}$ and CH_3COO^- are too big for entering into the acidic pocket. Now it is important to differentiate among the three tetrahedral anions PO_4^{3-}, SO_4^{2-} and ClO_4^-. The conjugate acids of these anions are namely H_3PO_4, H_2SO_4 and $HClO_4$, respectively. According to the Bronsted- Lowry acid- base theory, the concept of conjugate acid and base arises. Now, the conjugate acids of SO_4^{2-} and ClO_4^- i.e., H_2SO_4 and $HClO_4$ are very strong in nature and consequently the conjugate bases are weak whereas the conjugate acid of the anion, PO_4^{3-} i.e., H_3PO_4 is a weak one and as a result the anion, PO_4^{3-} is strong in nature. So, the interaction between strong base with the inner hydroxyl group of chelidamate ligand is stronger than the weak base. As a result, the interaction of free hydroxyl group of chelidamate ligand with the PO_4^{3-} anion is higher than other two namely, SO_4^{2-} and ClO_4^-.

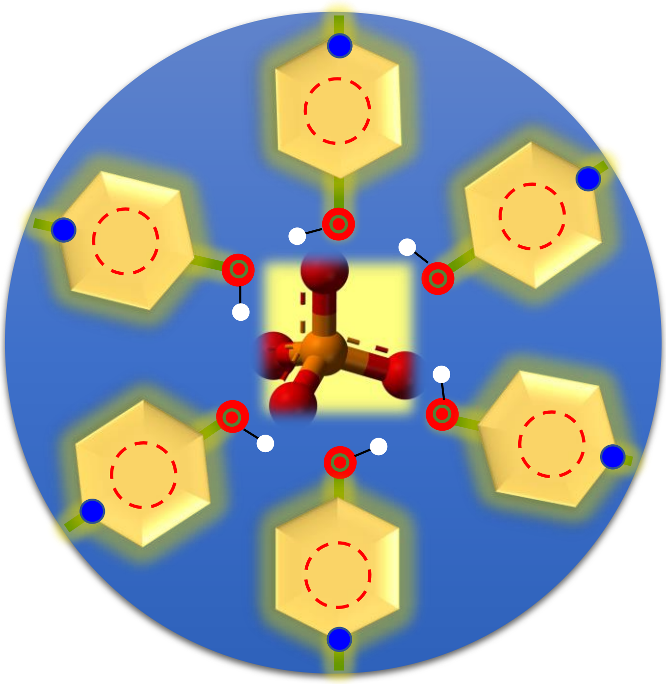

Fig. 4. 18 Schematic representations to show the position of phosphate anion inside the hydroxyl- functionalized pocket.

In case of luminescence decay of compound **3** in presence of PO_4^{3-} (Table 4), it was observed that the luminescence lifetime gradually increased from 1.21 ns to 3.25 ns with the addition of 0 to 75 µM of PO_4^{3-}. These observations support flexibility of the chelidamate ligands in **3** gets decreased through molecular level interactions which eventually reduced the chance of non-radiative energy decay of electronic excited state of **3** and consequently, the luminescence turn-on occurred.

Again, to investigate about the probable sensing mechanism of our synthesized compound **3** towards the analyte, PO_4^{3-}, we have done FTIR experiment to gather more knowledge about the molecular level interaction between the framework of the compound **3** and the phosphate moiety (Figure 4.19). For that the powdered form of the compound was soaked into the aqueous solution of PO_4^{3-} ion for 24 h and dried, then we have performed IR spectroscopy experiment. The prominent band around 3450 cm^{-1}, which is due to the free hydroxyl group of the MOF is shifted to the lower wavenumber region due to the interaction between the free – OH group and the phosphate moiety, which again proof the interaction between the phosphate moiety with the framework. The intense doublet at 1604 and 1570 cm^{-1} can be assigned to the stretching modes of the carboxylic acids. After immersion in an aqueous solution of phosphate, the broad P- O stretching vibration bands between 900 and 1200 cm^{-1} appear confirming the insertion of phosphate molecules into the cavity of the compound **3.**

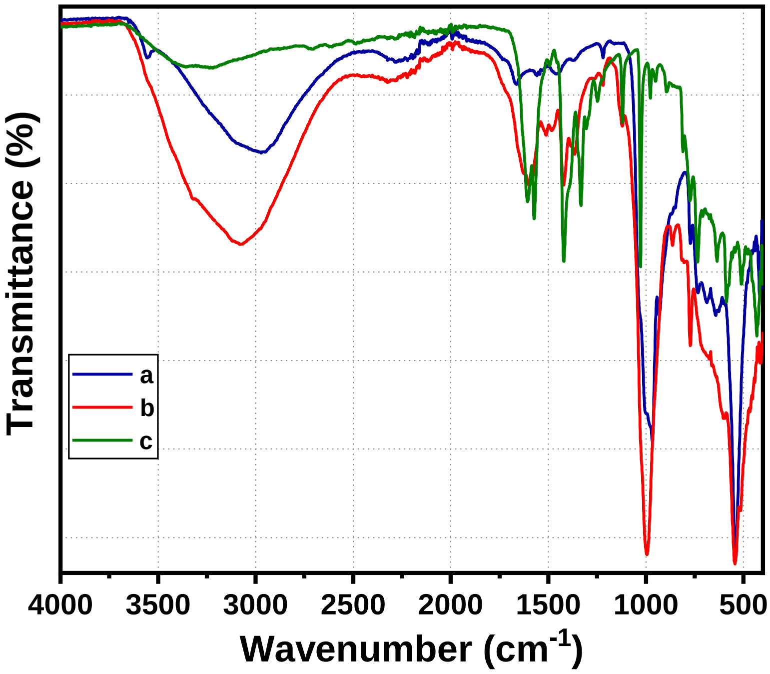

Fig. 4.19 IR spectra of (a) Na_3PO_4, (b) compound **3** in presence of PO_4^{3-} and (c) compound **3**.

4.4 CONCLUSIONS

In summary, we have successfully synthesized a 3d- 4d heterobimetallic metal- organic framework, $[YMn_{1.5}(C_7N_1H_3O_5)_3(H_2O)_6]\cdot11H_2O$, **3,** by hydrothermal technique**.** By employing single- crystal structure determination strategy, we have determined the structure of the compound **3.** Compound **3** was carefully characterized by PXRD, TGA, IR, UV- Vis spectroscopy, BET analysis, steady state and time resolved photoluminescence studies. For the detection of anions in aqueous solution, we have utilized the luminescence property of compound **3**. The present work, for the first time, demonstrates the selective detection of phosphate anion by a 3d- 4d heterobimetallic metal- organic framework *via* luminescence turn- on mechanism. The observed LOD value is very low and much lower than the recommended permissible level of phosphate in water towards human health. Time resolved luminescence studies confirm the turn-on behavior in presence of phosphate anions through preferential molecular level interactions by reducing non-radiative decay pathways. Additionally, the compound **3** is demonstrated to be a promising material for the detection and estimation of PO_4^{3-} ions in the real-life applications due to its high selectivity and sensitivity.

4.5 REFERENCES

1. Zhao, P.; Liu, Y.; He, C.; Duan, C., *Inorg. Chem.* **2022**, 61, 3132−3140.
2. Zhao, H. X.; Liu, L. Q.; Liu, Z. D.; Wang, Y.; Zhao, X. J.; Huang, C. Z., *Chem. Commun.* **2011**, 47, 2604- 2606.
3. Warwick, C.; Guerreiro, A.; Soares, A., *Biosens. Bioelectron.* **2013**, 41, 1- 11.
4. Mak, W. C.; Chan, C.; Barford, J.; Renneberg, R., *Biosens. Bioelectron.* **2003**, 19, 233-237.
5. Lawal, A. T.; Adeloju, S. B., *Talanta,* **2013**, 114, 191-203.
6. Xu, Y.; Ma, B.; Nussinov, R., *J. Phys. Chem. B.* **2012**, 116, 4801−4811.
7. Cohen, P. *Proc. R. Soc. Lond*. **1988**, 234, 115-144.
8. Fan, C.; Lv, X.; Tian, M.; Yu, Q.; Mao, Y.; Wang, H.; Liu, G., *Microchim. Acta.* **2020**, *187,* 84.
9. Dhingra, R.; Sullivan, L.M.; Fox, C.S.; Wang, T.J.; D’Agostino, R.B.; Gaziano, J.M., *Arch. Intern. Med.* **2007**,167, 879–885.
10. Yang, J.; Dai, Y.; Zhu, X.; Wang, Z.; Li, Y.; Zhuang, Q.; Shi, J.; Gu, J., *J. Mater. Chem. A.* **2015**, 3, 7445- 7452.
11. Wygladacz, K.; Qin, Y.; Wroblewski, W.; Bakker, E., *Anal. Chim. Acta,* **2008**, 614, 77-84.
12. Cheng,W.-L.; Sue, J.-W.; Chen, W.-C.; Chang, J.-L.; Zen, J.-M., *Anal. Chem.* **2010**, 82, 1157- 1161.
13. Asha, K. S.; Bhattacharjee, R.; Mandal, S., *Angew. Chem., Int. Ed.* **2016**, 55, 11528−11532.
14. Beer, P. D.; Gale, P. A., *Angew. Chem., Int. Ed*. **2001**, 40, 486−516.
15. Song, X.; Ma, Y.; Ge, X.; Zhou, H.; Wang, G.; Zhang, H.; Tang, X.; Zhang, Y., *RSC Adv.* **2017**, 7, 8661- 8669.
16. Chen, B.B.; Li, R.S.; Liu, M.L.; Zou, H.Y.; Liu, H.; Huang, C.Z., *Talanta*, **2018**, 178, 172–177.
17. Singha, D. K.; Majee, P.; Hui, S.; Mondal, S. K.; Mahata, P., *Dalton Trans.* **2020**, 49, 829-840.
18. McNaughton, A. D.; Fares, M.; Picci, G.; Gale, Philip A.; Caltagirone, C., *Coord. Chem. Rev.* **2021**, 427, 213573- 213615.
19. Colina, M.; Gardiner, P. H. E, *J. Chromatogr. A.* **1999**, 847, 285–290.
20. Cheng, W. L.; Sue, J. W.; Chen, W. C.; Chang, J. L.; Zen, J. M., *Anal. Chem.* **2010**, 82, 1157–1161.
21. Gilbert, L.; Jenkins, A. T. A.; Browning, S.; Hart, J. P., Sens. Actuators B Chem. **2011**, 160, 1322–1327.

22. Singha, D. K.; Majee, P.; Mondal S. K.; Mahata, P., *RSC Adv.* **2015**, 5, 102076- 102084.
23. Lakowicz, J. R. Principles of Fluorescence Spectroscopy. Springer, US, **2013**.
24. Xiang, Z.; Fang, C.; Leng, S.; Cao, D., *J. Mater. Chem. A.* **2014**, 2, 7662- 7665.
25. Martínez-Peragón, A.; Miguel, D.; Orte, A.; Mota, A.; Ruedas-Rama, M. J.; Justicia, J.; Alvarez-Pez, J. M.; Cuerva, J. M.; Crovetto, L., *Org. Biomol. Chem.* **2014**, 12, 6432-6439.
26. Borse, V.; Jain, P.; Sadawana M.; Srivastava, R., *Sens. Actuators, B.* **2016**, 225, 340–347.
27. Dai, C.; Yang C. X.; Yan, X. P., *Anal. Chem.* **2015**, 87, 11455–11459.
28. Zhao, Q.; Zhang, Z.; Tang, Y., *Chem. Commun.* **2017**, 53, 9414- 9417.
29. Liu, Y.; Bonizzoni, Marco., *J. Am. Chem. Soc.* **2014**, 136, 14223−14229.
30. Li, H.; Eddaoudi, M.; O'Keeffe, M.; Yaghi, O. M., *Nature,* **1999**, 402, 276-279.
31. Mahata, P.; Natarajan, S., *Chem. Soc. Rev.* **2009**, 38, 2304- 2318.
32. Hui, S.; Majee, P.; Singha, D. K.; Daga, P.; Mondal, S. K.; Mahata, P., *New J. Chem.* **2021**, 45, 9394- 9402.
33. Daga, P.; Manna, P.; Majee, P.; Singha, D. K.; Hui, S.; Ghosh, A. K.; Mahata, P.; Mondal, S. K., *Dalton Trans.* **2021**, 50, 7388- 7399.
34. Majee, P.; Singha, D. K.; Daga, P.; Hui, S.; Mahata, P.; Mondal, S. K., *CrystEngComm.* **2021**, 23, 4160- 4168.
35. Daga, P.; Sarkar, S.; Majee, P.; Singha, D. K.; Hui, S.; Mahata, P.; Mondal, S. K., *Mater. Adv.* **2021,** 2, 985- 995.
36. Li, Y.; Yang, R. T., *Langmuir.* **2007**, 23, 12937- 12944.
37. Dhainaut, J.; Bonneau, M.; Ueoka, R.; Kanamori, K.; Furukawa, S., *ACS Appl. Mater. Interfaces.* **2020**, 12, 10983- 10992.
38. Horcajada, P. Gref, R.; Baati, T.; Allan, P. K.; Maurin, G.; Couvreur, P.; Ferey, G.; Morris, R. E.; Serre, C., *Chem. Rev.* **2012**, 112, 1232- 1268.
39. Chen, X.; Tong, R.; Shi, Z.; Yang, B.; Liu, H.; Ding, S.; Wang, X.; Lei, Q.; Wu, J.; Fang, W., *ACS Appl. Mater. Interfaces.* **2018**, 10, 2328- 2337.
40. Wang, C.; Zhang, T.; Lin, W., *Chem. Rev.*, **2012**, 112, 1084.
41. Ni, B.; Sun, W.; Kang, J.; Zhang, Y., *J. Phys. Chem. C*, **2020**, 124, 11595- 11608.
42. Mahata, P.; Natarajan, S.; Panissod, P.; Drillon, M., *J. Am. Chem. Soc.* **2009**, 131, 10140- 10150.
43. Thorarinsdottir, A. E.; Harris, T. D., *Chem. Rev.* **2020**, 120, 8716- 8789.
44. Li, A. L.; Gao, Q.; Xu, J.; Bu, X. H., *Coord. Chem. Rev.* **2017**, 344, 54- 82.
45. Agarwal, R. A.; Das, A.; Omar, S., *J. Phys. Chem. C.* **2020**, 124, 18901- 18910.
46. Xu, B.; Zhang, H.; Mei, H.; Sun, D., *Coord. Chem. Rev.*, **2020**, 420, 213438- 213460.

47. Miao, C.; Xiao, X.; Gong,Y.; Zhu, K.; Cheng, K.; Ye, K.; Yan, J.; Cao, D.; Wang, G.; Xu, P., *ACS Appl. Mater. Interfaces*, **2020**, **12**, 9365- 9375.
48. Lee, J. Y.; Farha, O. K.; Roberts, J. K.; Scheidt, A.; Nguyen, S. T.; Hupp, J. T., *Chem. Soc. Rev.* **2009**, 38, 1450- 1459.
49. Wei, Y. S.; Zhang, M.; Zou, R.; Xu, Q., *Chem. Rev.* **2020**, 120, 12089- 12174.
50. Liu, X. F.; Guo, X. Q.; Wang, R.; Liu, Q. C.; Li, Z. J.; Zang, S. Q.; Mak, T. C. W., *J. Mater. Chem. A.* **2019**, 7, 2838- 2844.
51. Lee, C. S.; Moon, J.; Park, J. T.; Kim, J. H., *ACS Sustainable Chem. Eng.* **2020**, 8, 3773-3785.
52. Lin, Z.-J.; Lu, J.; Hong, M.; Cao, R., *Chem. Soc. Rev.* **2014**, 43, 5867–5895.
53. Li, B.; Chrzanowski, M.; Zhang, Y.; Ma, S., *Coord. Chem. Rev.* **2016**, 307, 106–129.
54. Yin, Z.; Zhou, Y.-L.; Zeng, M.-H.; Kurmoo, M., *Dalton Trans.* **2015**, 44, 5258–5275.
55. Cheng, J.; Zhou, X.; Xiang, H., *Analyst*. **2015**, 140, 7082–7115.
56. Singha, D. K.; Majee, P.; Mondal, S. K.; Mahata, P., *ChemistrySelect*. **2017**, 2, 5760-5768.
57. Singha, D. K.; Majee, P.; Mondal, S. K.; Mahata, P., *Inorg. Chem.* **2018**, 57, 12155-12165.
58. Gao, H. -L.; Zhao, B.; Zhao, X. -Q.; Song, Y.; Cheng, P.; Liao, D. -Z.; Yan, S. -P., *Inorg. Chem.* **2008**, 47, 11057-11061.
59. Zhao, B.; Gao, H. -L.; Chen, X. -Y.; Cheng, P.; Shi, W.; Liao, D. -Z.; Yan, S. -P.; Jiang, Z. -H., *Chem. Eur. J.* **2006**, 12, 149 – 158
60. Zhan, Z.; Liang, X.; Zhang, X.; Jia, Y.; Hu, Ming., *Dalton Trans.* **2019**, 48, 1786- 1794.
61. Song, X.; Ma, Y.; Ge, X.; Zhou, H.; Wang, G.; Zhang, H.; Tang, X.; Zhang, Y., *RSC Adv.* **2017**, 7, 8661- 8669.
62. Xu, H.; Cao, C-S.; Zhao, B., *Chem. Commun.* **2015**, 51, 10280- 10283.
63. Asha, K. S.; Bhattacharjee, R.; Mandal, S., *Angew. Chem.* **2016**, 128, 11700 –11704
64. Rao, P. C.; Mandal, S., *Inorg. Chem.* **2018**, 57, 11855−11858.
65. Gao, E.; Sun, N.; Zhan, Y.; Qiu, X.; Ding, Y.; Zhanga, S.; Zhu, M., *RSC Adv.* **2016**, 6, 85704- 85709.
66. Li, L.; Zou, J.-Y.; You, S.-Y.; Liu, Y.-W.; Cui, H.-M.; Zhang, S.-W., *Dyes and Pigments*. **2020**, 173, 108004- 108009.
67. Liu, F.; Gao, W.; Li, P.; Zhang, X.-M.; Liu, J.-P., *J. Solid State Chem.* **2017**, 253, 202–210.
68. Wang, Q.-S.; Li, J.-J.; Zhang, M.-N.; Li, X., *Sens. Actuators, B.* **2018**, 258, 358–364.
69. Yanga, D.-D.; Lu, L.-P.; Zhu, M.-L., *Inorg. Chim. Acta.* **2021**, 515, 120030- 120036.
70. Yang, J.; Dai, Y.; Zhu, X.; Wang, Z.; Li, Y.; Zhuang, Q.; Shi, J.; Gu, J., *J. Mater. Chem. A.* **2015**, 3, 7445- 7452.

71. Xie, Y.; Ning, S.; Zhang, Y.; Tang, Z.; Zhang, S.; Tang, R., *Dyes Pigm.* **2018**, 150, 36–43.
72. Qin, B.; Zhang, X.; Zhang, J., *Cryst. Growth Des.* **2020**, 20, 5120−5128.
73. Das, A.; Das, S.; Trivedi, V.; Biswas, S., *Dalton Trans.* **2019**, 48, 1332- 1343.
74. Ji, G.; Gao, X.; Zheng, T.; Guan, W.; Liu, H.; Liu, Z. *Inorg. Chem.* **2018**, 57, 10525−10532.
75. Apex3 v2017.3-0, Saint V8.38A, SAINT V8.38A; Bruker AXS Inc.: Madison, WI, **2018**.
76. Krause, L.; Herbst-Irmer, R.; Sheldrick, G. M.; Stalke, D., *J. Appl. Crystallogr.* **2015**, *48*, 3- 10.
77. Altomare, A.; Cascarano, G.; Giacovazzo, C.; Guagliardi, A. Completion and Refinement of Crystal Structures with SIR92. *J. Appl. Crystallogr.* **1993**, *26*, 343- 350.
78. Sheldrick, G. M. Crystal Structure Refinement with SHELXL. *Acta Crystallogr. C: Struct. Chem.* **2015**, *71*, 3- 8.
79. Farrugia, L. J. WinGX suite for Small-Molecule Single-Crystal Crystallography. *J. Appl. Crystallogr.* **1999**, *32***,** 837- 838.
80. Spek, A. L. Single-Crystal Structure Validation with the Program PLATON. *J. Appl. Crystallogr.* **2003**, *36*, 7- 13.
81. Vervloet, M. G.; Sezer, S.; Massy, Z. A.; Johansson, L.; Cozzolino, M.; Fouque, D., China. *Nat. Rev. Nephrol.* **2017**, 13, 27−38.

Chapter: 5

A Two-Dimensional Cu-Based MOF for Selective Staining of Cellular Nucleus through Fluorescence Imaging and Selective Sorption of Dye Molecules in Aqueous Medium

---

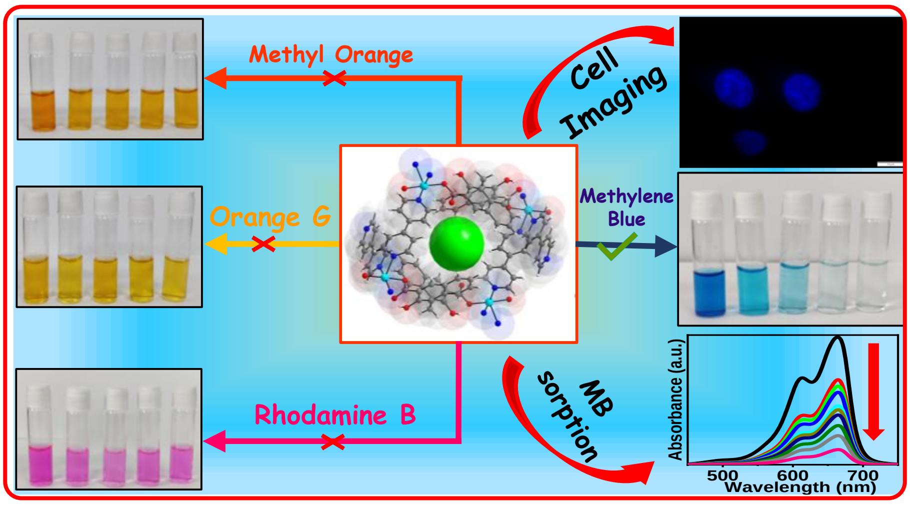

Inorg. Chem. **2024, 63, 13439−13449**

5.1 INTRODUCTION

Water, an indispensable natural resource, gets polluted daily by a variety of pollutants. One of the main reasons behind water pollution is the wastewater released from leather, plastic and textile industries including both inorganic and organic moiety.[1-4] Among the organic contaminants the most frequently used are fertilizers, pesticides, antibiotics, plasticizers and organic dyes.[5-8] These organic dyes are composed of aromatic rings and have stable conjugated structures and as a result, these are chemically inert with respect to sunlight, heat and oxidizing agents.[9, 10] Moreover, dyes possess some harmful properties like non-biodegradable, carcinogenic, poisonous and mutagenic.[11-13] Thus, it is necessary to take some drastic steps for the removal of these dangerous organic dyes from the stream of water for environmental safety issues. Among various synthetic commercially available organic dyes, methylene blue is a blue-colored cationic thiazine dye.[14] Administration of methylene blue for both children and adults can cause severe adverse effects like hyperbilirubinemia, hemolytic anemia and respiratory depression when it is used in high concentration.[15, 16] Therefore, it is of great significance to use such kinds of dyes in a very careful manner. In this regard, various techniques are being applied for the removal of these hazardous organic dyes from wastewater, including ion exchange, ultrafiltration, coagulation, photocatalytic degradation, membrane technology and advanced oxidation processes (AOPs).[17-22] But each of these methods has some individual drawbacks like being expensive, less efficient and sometimes producing secondary toxic substances. As a result, sorption is a progressing approach to elute such pollutants due to its simplicity, high efficiency, reliability and cost effectiveness.[23-25] For the successful sorption process, the selection of a sorbent is very vital. In that sense, to function well as a sorbent, it must have a highly exposed surface area and distinct pore structure so that the transfer of particles would be faster.[26-28] Hence, for the sorption, decontamination or differentiation of pollutants in wastewater, highly porous materials are significantly used.[29] Subsequently, metal-organic frameworks are considered as a class of porous crystalline coordination polymer, consisting of inorganic clusters and organic polydentate bridging linkers with multi-dimensional assembly.[30-32] The sorption phenomenon has wide application especially in the field of gas sorption.[33, 34] Recently, there have been a significant number of MOFs based on both transitions as well as rare-earth metal ions reported for dye removal through sorption.[35-46] But the synthesis of MOFs with good sorption capacity is still a challenging issue.

On the other hand, cell imaging is a relatively new but reliable medical advancement that gives an overview of cellular level details to detect and diagnose the diseases. Nowadays, to discover many analytes and diagnose many diseases live cell imaging has been emerged as an innovative technology. In case of living organisms, to anticipate many biological processes fluorescence imaging is a non-intrusive imaging technique.[47, 48] Moreover, in the field of biomedical application, porous substances have drawn much attention due to their large tunable pore size, high surface area, and controllable chemical properties. There are numerous kinds of cell imaging techniques are available but fluorescence imaging has proved to be more trustworthy due to its sensitivity towards live- cells.[49, 50] Till now, various kinds of luminescent materials like quantum dots, nanosheets, metal nano clusters have been used for cell imaging.[51-54] But nowadays, MOFs are used as unique probes in cell imaging due to their luminescence performance and quenching and turn-on properties.[55] Over the past few years, several research works on bio-imaging studies of MOF-based materials have been reported.[47, 56-60]

Keeping all these things in mind, we have successfully prepared a porous Cu-based metal-organic framework, $[Cu(C_{23}H_{14}O_6)(C_{10}H_8N_2)_2]\cdot H_2O\cdot DMSO$, **4** by layer diffusion technique by using Cu(II), pamoic acid and 4, 4’- bipyridine for selective staining of the cellular nucleus through fluorescence imaging and selective sorption of methylene blue dye.

5.2 EXPERIMENTAL SECTION

5.2.1 Materials

All the reagents, used for this work are easily available in the market and we used them without additional purification. For the synthesis of the compound, we have used $Cu(NO_3)_2\cdot 3H_2O$ (Merck, 99%), Pamoic acid (PAM) (Aldrich, 97%), 4, 4’- bipyridine (Aldrich, 98%), DMSO (Merck, 99.5%) and Methanol (Finar, 99%). For the Biocompatibility experiment, we used NaCl (Merck, 99%), KCl (Merck, 99%), $MgCl_2$ ($\geq$ 96%), $CaCl_2$ ($\geq$ 99%), NaF (Merck, 97%), Cysteine (Sigma Aldrich, $\geq$ 97%) and H_2O_2 (Merck, 29-32%). For the sorption experiment, we used Methylene blue (MB) (Sigma Aldrich), Methyl Orange (MO) (Sigma Aldrich), Orange G (OG) (Sigma) and

Rhodamine B (RhB) (Sigma). We have used distilled water throughout the whole experiment.

5.2.2 Synthesis of compound 4

Layer diffusion technique was used for the synthesis of the compound **4** at room temperature. At first, in beaker 1 we took 0.5 mM Pamoic acid (0.2 g) in 20 mL DMSO and then stirred well to get the homogeneous mixture. Then, in beaker 2, 0.5 mM 4,4'-bipyridine (0.08 g) in 20 mL MeOH was taken and stirred till mixed well. After that, in a narrow glass tube, we took 0.1 mM $Cu(NO_3)_2 \cdot 3H_2O$ (0.0244 g). Then from the beaker 1, 2 mL pamoic acid solution was taken out and poured into the glass tube containing metal ion and then firmly shaken for the dissolution. To this metal-acid solution, 2mL methanolic solution of beaker 2 was successfully layered with the help of a glass syringe. Then, after 2 weeks blue- colored block-shaped crystals suitable for the single crystal X- ray diffraction, were obtained from the wall of the test tube. Then, the crystals were collected from the test tube and washed with DMSO- MeOH mixed solvent and dried up in the air. Elemental analysis calc (%) for **4**: C 62.96, H 3.49, N 6.52; found: C 62.79, H 3.52, N 6.55. (Yield 70% based on Cu)

5.2.3 Single- crystal structure determination of compound 4

A perfect single crystal was selected under a microscope and glued cautiously to a thin glass fibre. We have carried out the single crystal XRD experiment using Bruker D8 Quest machine at 293(2) K. The X-ray generator was operated at 1 mA and 50 kV using Mo Kα having λ=0.71073Å radiation. With ω scan width of 0.5° data were acquired. By keeping sample-to-detector distance constant at 6.03 cm, a total of 408 frames were collected in three different setting of φ (0, 90, 180°) and the detector position (2θ) fixed at -25°. Using an APEX3 program the final data sets were reduced, while for the integration of diffraction profiles a SAINTPLUS[61] program was used. A SADABS program[62] was employed to carry out the absorption correction (multi-scan). The structure was initially solved by SIR 92,[63] and then we have again used full matrix least-square method (SHELXL-2016[64]), which is present in the WinGx suit of programs (Version 1.63.04a).[65, 66] All the non-hydrogen atoms from Fourier maps are effectively located and at the final cycles we have refined them with anisotropic displacement parameters. Finally, all the hydrogen atoms are fixed at premeditated positions and comprised them in the refinement procedure using riding model accompanying with isotropic thermal parameters. A detail of the structure solution and final refinement is given in the Table 5.1. CCDC: 2345066 contain the crystallographic data for this paper. These data can be found free of charge from The Cambridge Crystallographic Data Center (CCDC) via www.ccdc.cam.ac.uk/data_request/cif.

Table 5.1: Crystal data and structure refinement parameters for $[Cu(C_{23}H_{14}O_6)(C_{10}H_8N_2)_2] \cdot H_2O \cdot DMSO$, **4.**

Empirical formula	$C_{45}H_{30}CuN_4O_8S$
Formula weight	850.33
Crystal system	Monoclinic
Space group	$P2_1/c$
a (Å)	13.3282(12)
b (Å)	16.4897(14)
c (Å)	19.7376(17)
α (deg)	90
β (deg)	107.543(2)
γ (deg)	90
Volume (Å^3)	4136.1(6)
Z	4
T (K)	273 (2)
ρ_{calc} (g cm^{-3})	1.366
μ (mm^{-1})	0.637
θ range (deg)	1.642 to 27.165
λ (Mo Kα) (Å)	0.71703
R indices [I>2σ(I)]	$R_1 = 0.0784$, $wR_2 = 0.1516$
R indices (all data)	$R_1 = 0.1229$, $wR_2 = 0.1733$

$R_1 = \Sigma ||F_0|-|F_c|| / \Sigma |F_0|$; $wR_2 = \{\Sigma[w(F_0^2 - F_c^2)^2] / \Sigma[w(F_0^2)^2]\}^{1/2}$. $w = 1/[\sigma^2(F_0)^2 + (aP)^2 + bP]$, $P = [\max.(F_0^2,0) + 2(F_c)^2]/3$, where a = 0.0435 and b = 9.3893.

5.2.4 Biocompatibility studies

To study the biocompatibility, we have carried out UV- visible absorption spectroscopy of the compound in the presence of different metal cations (Na^+, K^+, Mg^{2+} and Ca^{2+}), anions (F^- and Cl^-), sulphur containing amino acid (Cysteine) and H_2O_2. For this study, we have prepared the stock solution of compound **4** by adding 1.2 mg sample in 4 ml water and sonicate for 2 minutes. For the UV measurements, we have taken 100 µL of the stock solution in 2 ml water in a quartz cuvette. UV- visible absorption spectroscopy of the compound in presence of different analytes was carried out at room temperature by using SHIMADZU UV-1900i spectrophotometer. The analytes were prepared in water.

5.2.5 Dye sorption experiments

Two types of dyes were selected for the purpose of the sorption studies such as cationic and anionic dyes and the whole process was carried out at room temperature by using aqueous solution of dyes. In our experiment, we have chosen MB and RhB as a positive or cationic dye and OG and MO as negative or anionic dye. The protocols, used for this experiment were carried out by some previously realized methods.[35, 40, 67, 68] At first, we prepared four different dye solutions with concentration of 5×10^{-5} M at room temperature. To prepare these dye solutions, we have used distilled water and four different volumetric flasks. The volume of each prepared dye solution was 50 mL. Then we took 20 mg of compound **4** into a 30 mL glass bottle containing 20 mL organic dye solution. Then, firstly we sonicated the mixture for 1 min and then by hand shaking we generated a homogeneous mixture of the dye solution and the compound **4**. UV- Visible spectroscopy was carried out to investigate about the sorption phenomenon. At different time intervals, we took out about 3 mL of the solution from the bulk and then centrifuged by centrifuge machine. Then the supernatant liquid was used for the UV- Visible measurement. Similarly, the MB dye solutions of 0.625×10^{-5} M, 1.25×10^{-5} M, 2.5×10^{-5} M and 10×10^{-5} M concentrations were prepared and measured the absorption spectra. Furthermore, for the separation of dye mixtures (MB and MO), we used the same process. The two organic dyes were mixed 1:1 volume ratio of same concentration of 5×10^{-5} M. Then 20 mg of compound **4** was added to the mixture of dyes (MB‖MO) of volume 20 mL.

5.2.6 Instrumentations

We have measured the Powder X-ray diffraction pattern on the finely crushed sample in the 2ϴ region 5-50° by using Cu kα radiation (Bruker D8 discover instrument) at room temperature. Thermogravimetric analysis was carried out by using Perkin- Elmer Diamond instrument (STA 6000) in a nitrogen atmosphere in the temperature range 30-800°C (flow rate= 20 ml min^{-1}) with heating rate of 20°C min^{-1}. The FTIR spectrum of the sample was noted by using Nicolet Magna IR 750 series II FTIR spectrophotometer on the solid sample at room temperature. The UV- Visible absorption studies were carried out in SHIMADZU UV-1900i spectrophotometer. Fluorescence microscopic images were captured using an Olympus IX71 inverted fluorescence microscope. Nitrogen gas adsorption - desorption of the sample (BET experiment) were carried out using Autosorb iQ2, Quantachrome Instruments, USA.

5.2.7 Photoluminescence measurement

To study the photoluminescence properties, we have prepared the stock solution of compound **4** by weighing 1.2 mg of sample in 4 ml water and sonicating it for 2 minutes. We have taken 100µL of the stock solution in 2 ml water in a quartz cuvette for the photoluminescence measurements. Photoluminescence spectra of compound **4** were carried out at room temperature by using Horiba Fluoromax- 4 spectrofluorometer in an aqueous dispersion upon excited at 370 nm. During the experiment the slit width was set to 5 nm for both the excitation and emission. By using HORIBA Jobin- Yvon instrument, Time-correlated single- photon counting (TCSPC) measurements were recorded at room temperature in the nano second time domain. For the TCSPC study, the excitation and emission wavelength were used at 370 nm and 525 nm respectively.

5.3 RESULTS AND DISCUSSION

5.3.1 Structure of compound 4

Compound **4** crystallized in a monoclinic crystal system with $P2_1/c$ space group. The asymmetric unit of compound **4** consists of one Cu^{2+} ion, one pamoate anion, two 4,4’-bipyridine unit, one lattice water molecule and one lattice DMSO molecule (Figure 5.1). The Cu^{2+} ion is five coordinated with three nitrogen atoms and two oxygen atoms and has a distorted square pyramid geometry through three nitrogen atoms from pyridine ring of 4,4’- bipyridine and two oxygen atoms from carboxylate groups of pamoate ligand (Figure 5.2a). Two long Cu-O oxygen interactions have also been observed from the carboxylate oxygen atoms [O(1) and O(4)] with distances 2.81 and 2.96 Å, respectively. The coordination mode of pamoate ligand is shown in Figure 5.2b. Out of the two bipyridines (bpy), one connects only one Cu^{2+} ion and acts as terminal ligand (bpy1) and other one connects two Cu^{2+} ions (bpy2) (Figure 5.3).

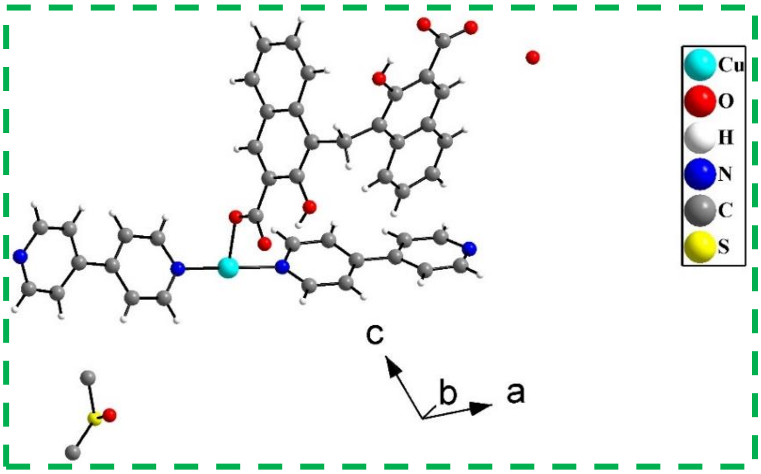

Fig. 5.1 Figure shows the asymmetric unit of $[Cu(C_{23}H_{14}O_6)(C_{10}H_8N_2)_2]·H_2O·DMSO$, **4** (hydrogen atoms of water and DMSO molecules not included).

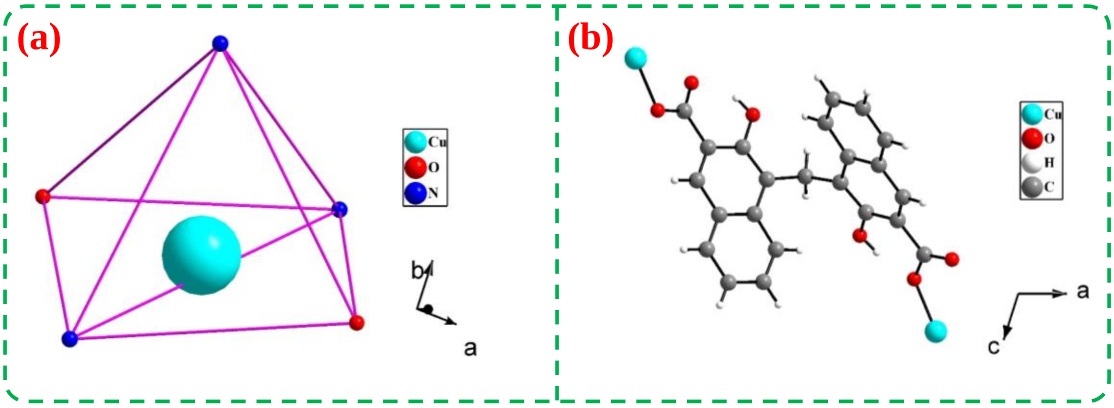

Fig. 5.2 Square pyramidal geometry around Cu^{2+} ion (a) and coordination modes of pamoate anion (b) in $[Cu(C_{23}H_{14}O_6)(C_{10}H_8N_2)_2]·H_2O·DMSO$, **4**.

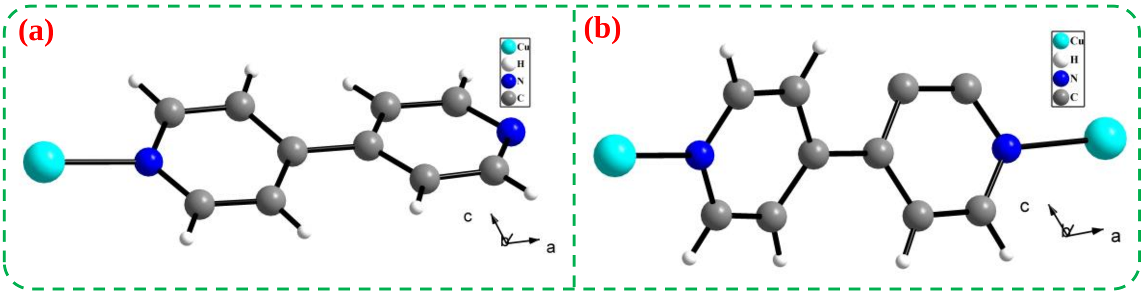

Fig. 5.3 Figure shows the coordination modes of 4,4'-bipyridines in $[Cu(C_{23}H_{14}O_6)(C_{10}H_8N_2)_2] \cdot H_2O \cdot DMSO$, **4**: (a) bpy1, (b) bpy2.

The Cu- O bonds have an average distance of 1.96 Å, and Cu- N bonds have an average distance of 2.16 Å. The O/N-Cu-O/N bond angles are in the range of 87.22(13) to 177.25(14)°. The selected bond distances and bond angles are listed in Table 5.2 and Table 5.3, respectively. To confirm the actual coordination geometry around Cu^{2+} ion, Addison parameter (τ_5) was calculated.[69] The calculated value of $\tau_5 \approx 0.13$ indicate the formation of distorted square pyramidal geometry around the Cu^{2+} ion.

Table 5.2: Selected bond distances (Å) found in $Cu(C_{23}H_{14}O_6)(C_{10}H_8N_2)_2] \cdot H_2O \cdot DMSO$, **4**.

Bond	Distances, Å	Bond	Distances, Å
Cu(1)- O(2)	1.959 (3)	Cu(1)-N(3)	2.069 (4)
Cu(1)-O(3)#1	1.964 (3)	Cu(1)-N(4)#2	2.348(4)
Cu(1)-N(1)	2.051 (4)		

Symmetry transformations used to generate equivalent atoms: #1 x-1, -y+1/2, z-1/2 #2 -x, y+1/2, -z+1/2

Table 5.3: Selected bond angles observed in $[Cu(C_{23}H_{14}O_6)(C_{10}H_8N_2)_2] \cdot H_2O \cdot DMSO$,**4**.

Angle	Amplitude (°)	Angle	Amplitude (°)
O(2)-Cu(1)-O(3)#1	177.25(14)	O(2)-Cu(1)-N(3)	89.30(14)
O(2)-Cu(1)-N(1)	87.22(13)	O(3)#1-Cu(1)-N(3)	89.26(13)
O(3)#1-Cu(1)-N(1)	93.78(13)	N(1)-Cu(1)-N(3)	169.29(15)
O(2)-Cu(1)-N(4)#2	88.99(13)	O(3)#1-Cu(1)-N(4)#2	93.45(13)
N(1)-Cu(1)-N(4)#2	95.65(14)	N(3)-Cu(1)-N(4)#2	94.42(14)

Symmetry transformations used to generate equivalent atoms: #1 x-1, -y+1/2, z-1/2 #2 -x, y+1/2, -z+1/2

The connectivity among Cu^{2+} ions, pamoate ions and 4,4’- bipyridine ligands generate a two- dimensional structure with the formation of solvent molecules (DMSO and H_2O) filled cages (Figure 5.4). The two- dimensional structures packed in such a manner to form a three- dimensional arrangement of the framework along with the formation of one– dimensional solvent filled channels (Figure 5.5). Note the presence of free hydroxyl groups of pamoate ligands.

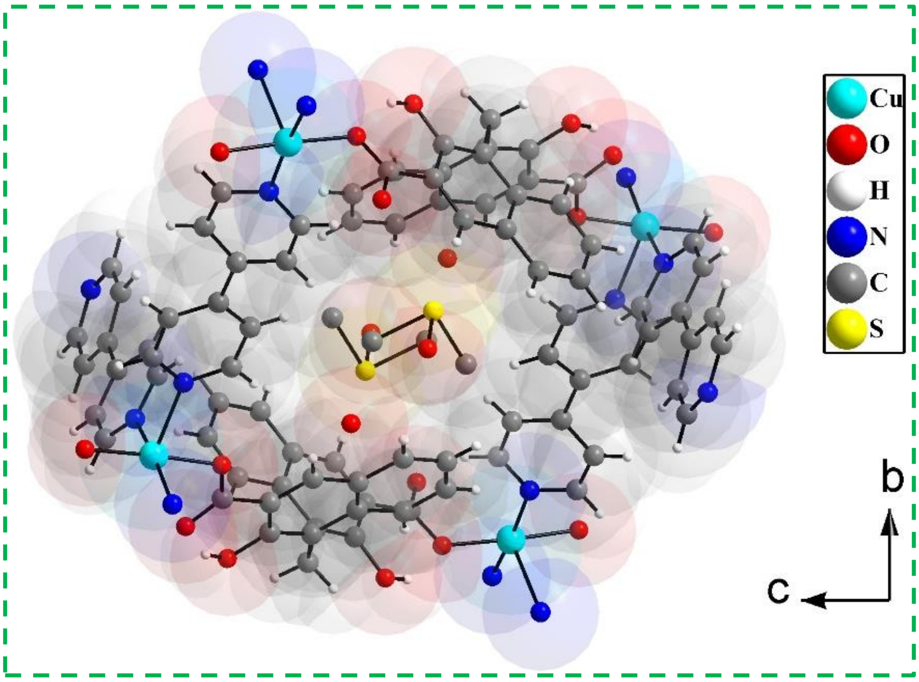

Fig. 5.4 Figure shows connectivity among Cu^{2+} ions, pamoate ligand and 4,4’-bipyridine moiety in $[Cu(C_{23}H_{14}O_6)(C_{10}H_8N_2)_2]\cdot H_2O\cdot DMSO$, **4** (hydrogen atoms of solvent molecules not included)

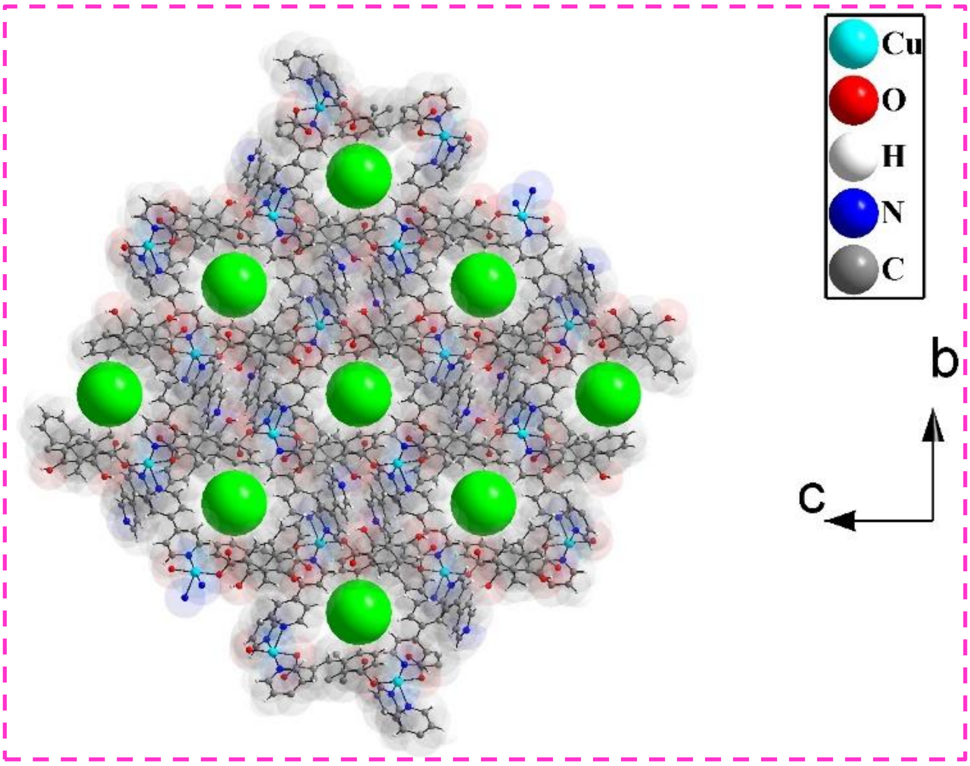

Fig. 5.5 Packing arrangement of two-dimensional structures (see text). The green balls represent solvent molecules inside the one-dimensional channels.

5.3.2 Characterization of compound 4

Details of the instrumentation of characterization of the compound **4** have been described in ESI. The Powder X-ray diffraction patterns were recorded in the 2Θ region of 5-50° (Figure 5.6) on the finely ground samples. When we compared both the experimental data and the simulated data obtained from the single crystal X- ray instrument, they showed a good agreement with each other. So, we can say that the formation of compound **4** occurred in pure form.

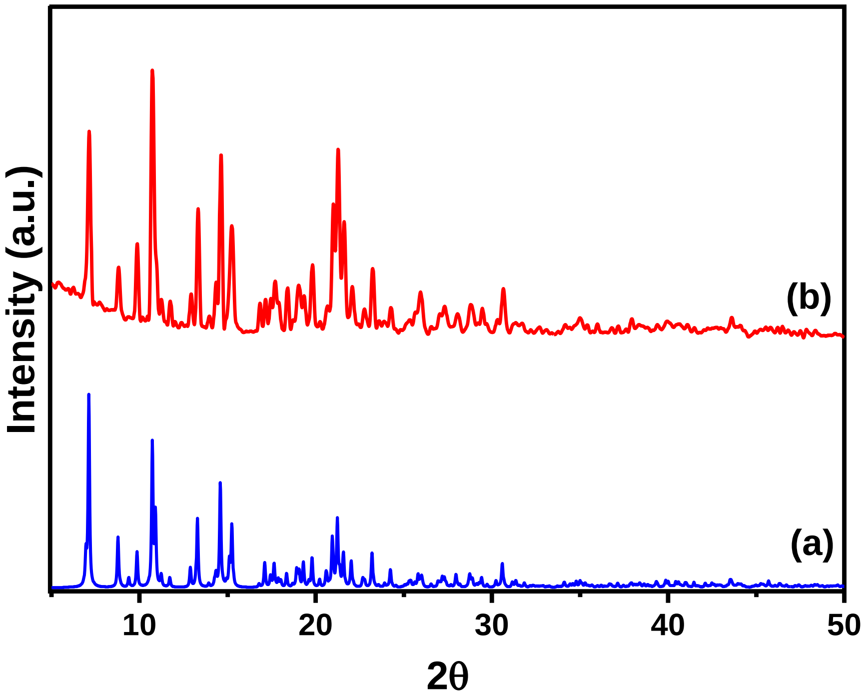

Fig. 5.6 Powder XRD (CuKα) patterns: (a) simulated from single crystal X-ray data of $[Cu(C_{23}H_{14}O_6)(C_{10}H_8N_2)_2] \cdot H_2O \cdot DMSO$, **4**. and (b) as synthesized $[Cu(C_{23}H_{14}O_6)(C_{10}H_8N_2)_2] \cdot H_2O \cdot DMSO$, **4**.

The thermogravimetric analysis (TGA) was carried out under a nitrogen atmosphere (Figure 5.7a). The weight loss follows some steps throughout the experiment. The first weight loss of 11.20% (calculated 11.46%) up to 220°C is due to the removal of water and DMSO molecules. The second weight loss of 47.59% (calculated 47.54%) up to 260°C is due to the removal of bipyridine molecule. The weight loss above 450°C is probably due to the decomposition of the pamoate connected framework. The IR spectrum of the compound was carried out in the spectral region between 4000 and 500 cm^{-1} at room temperature (Figure 5.7b). All the peaks corresponding to the pamoate ligand and 4,4'- bipyridine have been observed. The prominent band around 3450 cm^{-1} is due to the presence of free hydroxyl group in the framework from pamoate ligands.

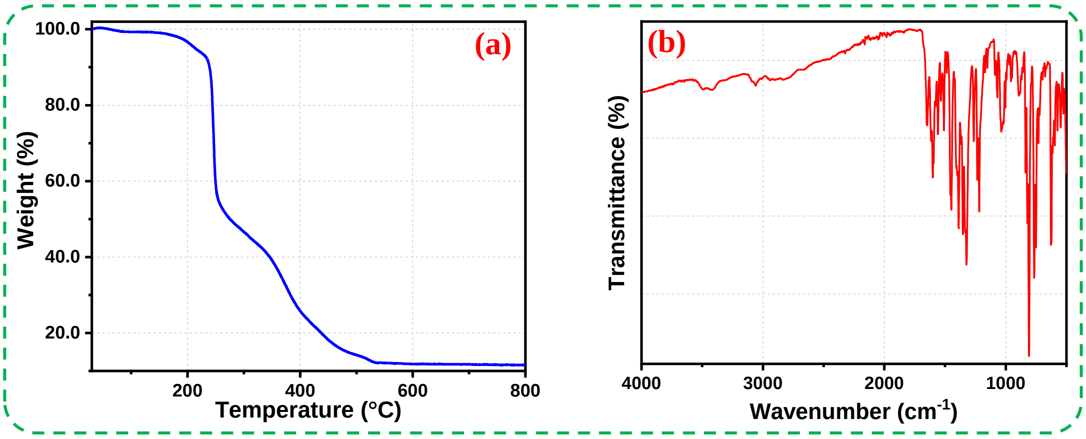

Fig. 5.7 (a) Thermogravimetric analysis (TGA) of compound **4** in nitrogen atmosphere and **(b)** IR spectrum of compound **4**.

We have carried out nitrogen gas adsorption-desorption studies (BET experiment) to know about the porosity of compound **4**. To do the experiment, the powder samples were pretreated at 220 ºC for 60 min to confirm the removal of solvent molecules. Powder X-ray diffractions were used to check the stability of the compound after de-solvation (Figure 5.8).

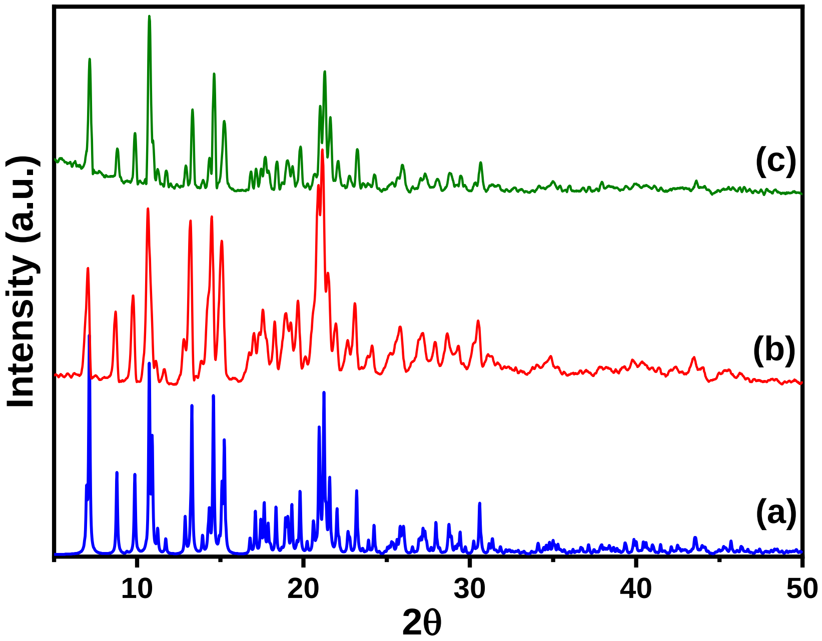

Fig. 5.8 Powder XRD (CuKα) patterns: (a) simulated from single crystal X-ray data of $[Cu(C_{23}H_{14}O_6)(C_{10}H_8N_2)_2] \cdot H_2O \cdot DMSO$, **4**, (b) as-synthesized compound **4** and (c) after treating the compound at 220° C.

The BET experiment shows surface sorption type behavior with surface area of 170 m^2/g (Figure 5.9). The observed lower surface area value, probably, is due to the contraction of the pore/channel after the removal of solvent molecules.

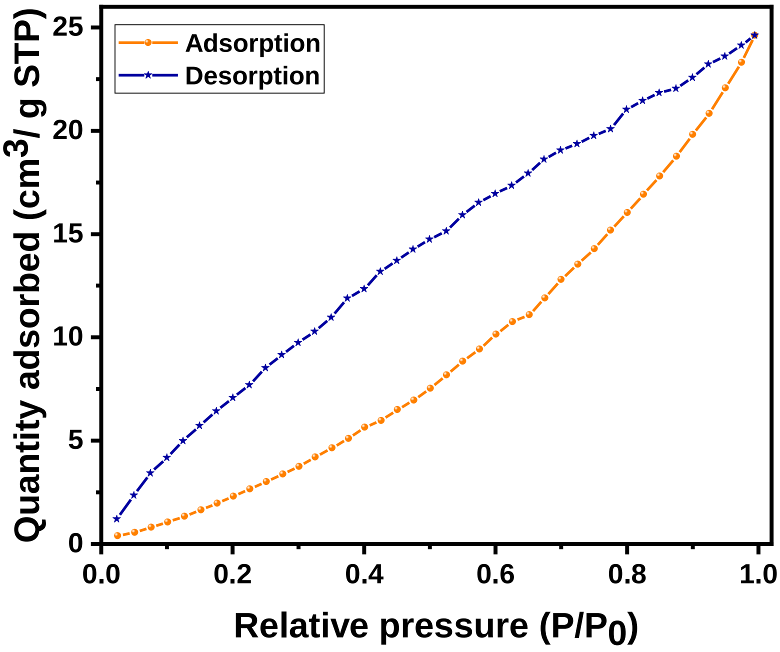

Fig. 5.9 N_2 sorption plot of compound **4.**

The absorption spectrum of compound **4** was also investigated and the observed wavelength maximum is at 370 nm (Figure 5.10).

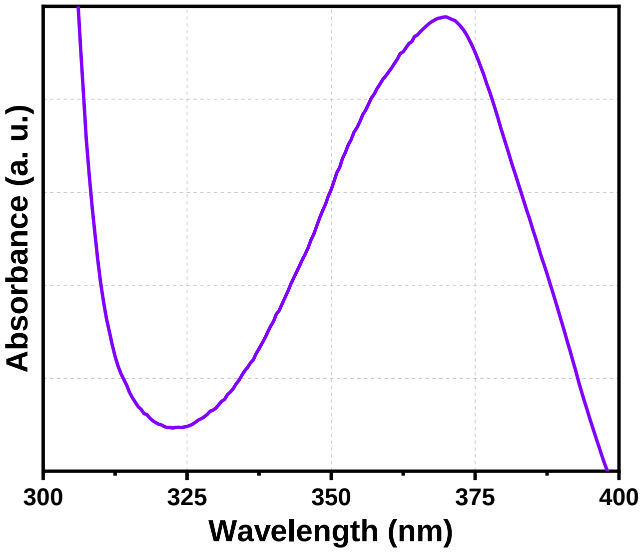

Fig. 5.10 UV- Vis absorption spectrum of compound **4.**

5.3.3 Photoluminescence behavior

All the absorption and emission spectra were measured at room temperature. Details of the photoluminescence experiment were given in the ESI. The photoluminescence property of both compound **4** and the pamoate ligand was carried out by using its aqueous dispersion upon excitation at 370 nm (Figure 5.11). The luminescence measurements were recorded at the emission wavelength ranging from 450 to 650 nm. Upon excitation at 370 nm, the compound **4** exhibits a broad peak centered at 525 nm. The observed emission comes out due to the intra- ligand transitions (π* → π and π* → n) of the bonded organic ligands with the metal center.[70, 71 72] The excitation spectra of aqueous dispersion of compound **4** and pamoate ligand were carried using emission wavelength value of 525 nm (Figure 5.12).

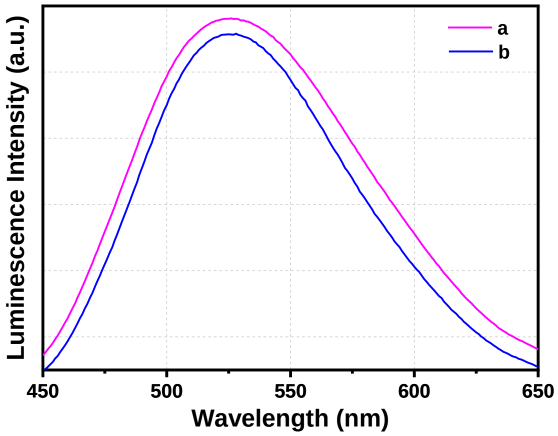

Fig. 5.11 Emission spectra of (a) compound **4** and (b) the ligand in aqueous solution upon excitation at 370 nm at room temperature.

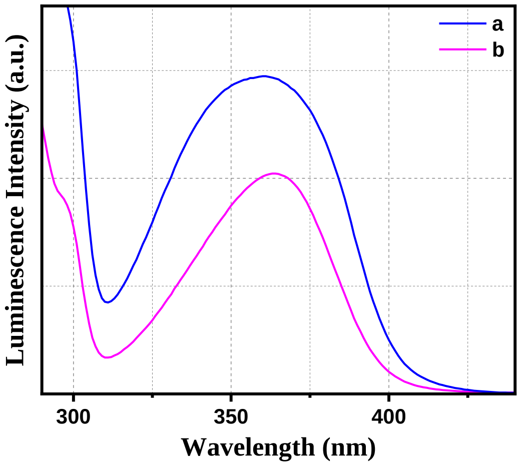

Fig. 5.12 Excitation spectra of (a) the ligand and (b) compound **4** in aqueous dispersion upon fixing the wavelength at 525 nm at room temperature.

5.3.4 Luminescence lifetime decay analysis

Figure 5.13 demonstrates the luminescence lifetime decay curve of the ligand centered emission (λ_{em} =525 nm) of compound **4** fitted in a biexponential manner. The calculated average lifetime of the excited state of the compound **4** was found to be 1.08 ns in an aqueous solution. The brilliant emission property of compound **4** inspired us to utilize the compound **4** for fluorescence microscopy imaging studies.

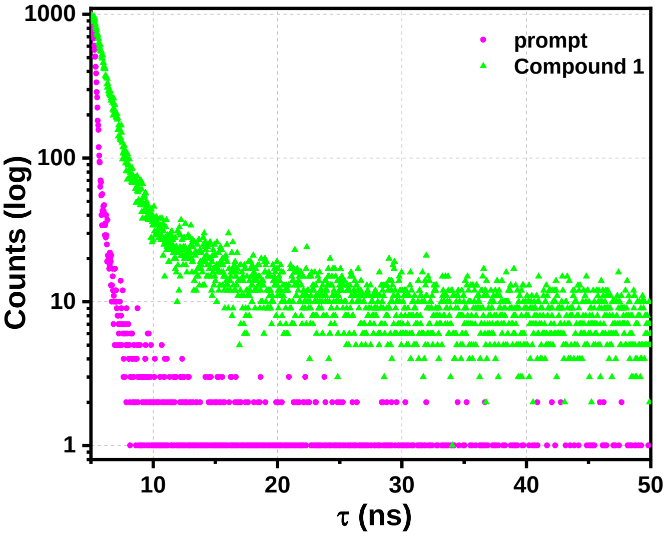

Fig. 5.13 Luminescence lifetime decay curve of compound **4** in aqueous dispersion at room temperature**.** The instrument response function (prompt) is also shown. Here, λ_{ex} = 370 nm and λ_{em} = 525 nm were set during the experiment.

5.3.5 Cell culture and fluorescence microscopic studies

HeLa cells were cultured in DMEM at pH 7.4 with 10% fetal bovine serum (FBS) and antibiotic-antimycotic solution 100× [comprising penicillin (10000 units), streptomycin (10 mg), and amphotericin B (25 µg) per mL in 0.9% normal saline). HeLa cell line was grown at 37°C in a 5% CO_2 incubator and routinely passaged. Fluorescence microscopic images (Figure 5.14) were captured using fluorescence microscope equipped with a 60× and 100× oil plan apochromatic objective. HeLa cells were seeded on a cover slip and developed in DMEM. Cells were fixed with 4% paraformaldehyde for 30 min and subjected to fluorescence microscopy. Fixed cells were incubated with 5 µM concentration of compound **4** for 10 min at 37 °C in darkness and then washed twice with 1x PBS. Cells were mounted with antiq6uench agent n-propyl gallate for microscopic slide preparation and imaged by fluorescence microscope[73-75].

From fluorescence microscopic experiments using human epithelioid cervix carcinoma HeLa cell line it is clear that the compound **4** selectively stains the cellular nucleus. For the compound **4** laser excitation wavelength was 370 nm, emission wavelength = 525 nm, emission range or bandpass = 485-535 nm. The selective staining of the nucleus are, prabably, due to the intercation of MOF within the DNA base pair in the nucleus.

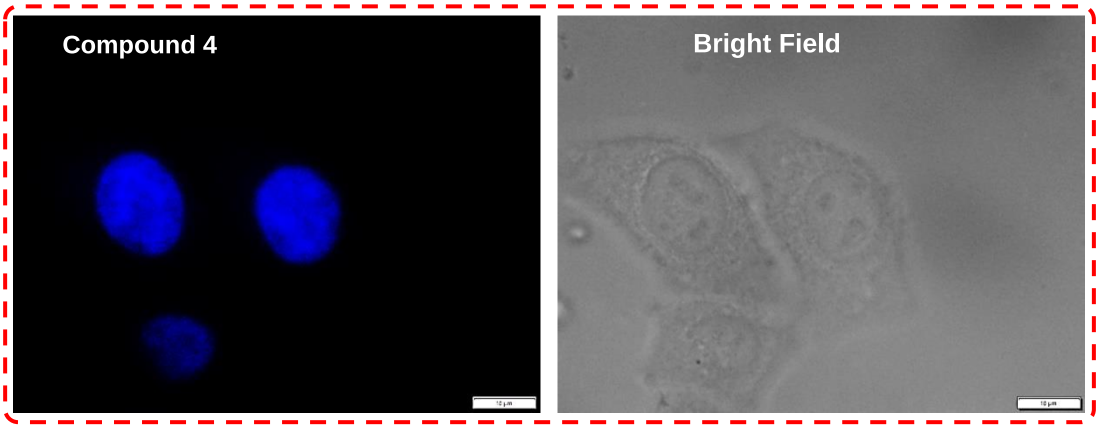

Fig. 5.14 Fluorescence microscopic images of compound **4** in fixed human epithelioid cervix carcinoma HeLa cells. Blue channel clearly indicates the selectivity of our synthesized probe to carcinoma cell nucleus. Compound **4**: laser excitation wavelength: 370 nm, emission wavelength: 525nm, emission range or bandpass: 485-535 nm.

5.3.6 Cell Viability

MTT study was utilized to determine the cell viability of HeLa and A549 cells against MOF (Figure 5.15). Freshly harvested HeLa and A549 cells were separately seeded in a 96-well plate at a population of nearly 10^4 cells in DMEM and cultured at 37°C for 24 h. After 24 h incubation, different concentrations of MOF (0, 1, 2, 5, and 10 μM per well) were treated for 24 h at 37°C. Following the HeLa and A549 cells were separately incubated with MTT (10 μL) material (5 mg mL^{-1} in PBS) at 37°C for 4 h in dark. Afterward 4 h incubation, DMSO was added to each well and the absorption (*A*) at 570 nm was measured. The values (performed the assay in triplicates) were determined through the following equation:

Viable cells (%) = (*A* of treated cells / *A* of untreated cells) × 100.

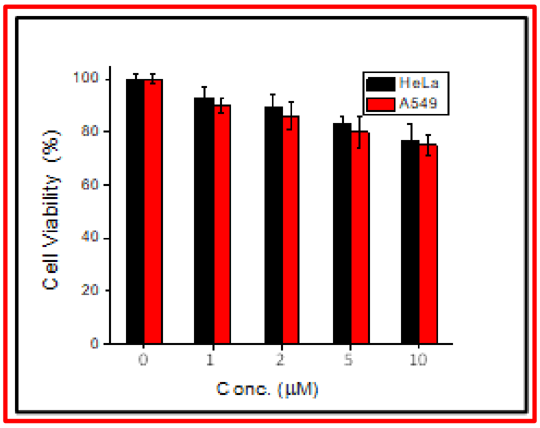

Fig. 5.15 Cell viability study for HeLa, and A549 cells over 24 h at different concentration of MOF.

5.3.7 Biocompatibility

To check the biocompatibility of our synthesized compound, we have carried out UV-Visible absorption spectroscopy of compound **4** in aqueous dispersion in the presence of different metal cations (Na^+, K^+, Mg^{2+} and Ca^{2+}), anions (F^- and Cl^-), sulphur containing amino acid (Cysteine) and H_2O_2 by varying their concentration (Figure 5.16 to Figure 5.19). In every case, the absorbance value of the compound remains almost unchanged with the incremental addition of that particular species. So, we can conclude that our compound has excellent biocompatibility.

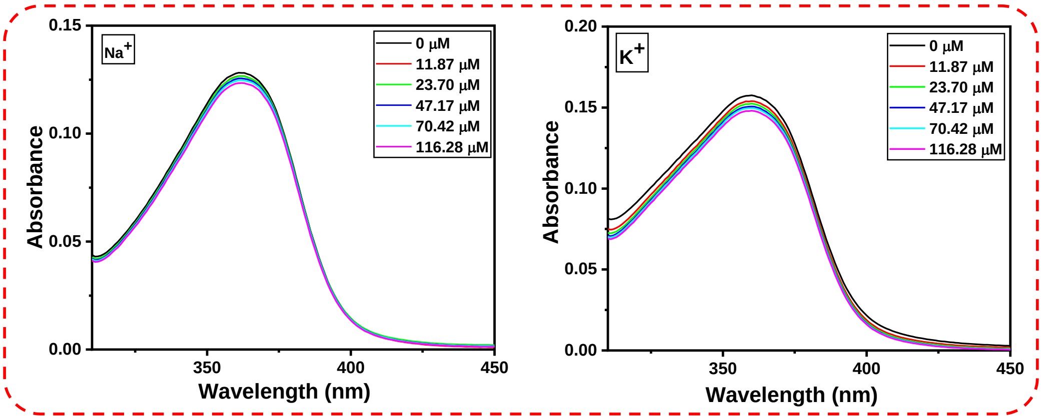

Fig. 5.16 The UV- Vis spectra of compound **4** in aqueous dispersion upon incremental addition of aqueous solution of alkali metal ions. Final concentration of different ions in the medium is indicated in the legend.

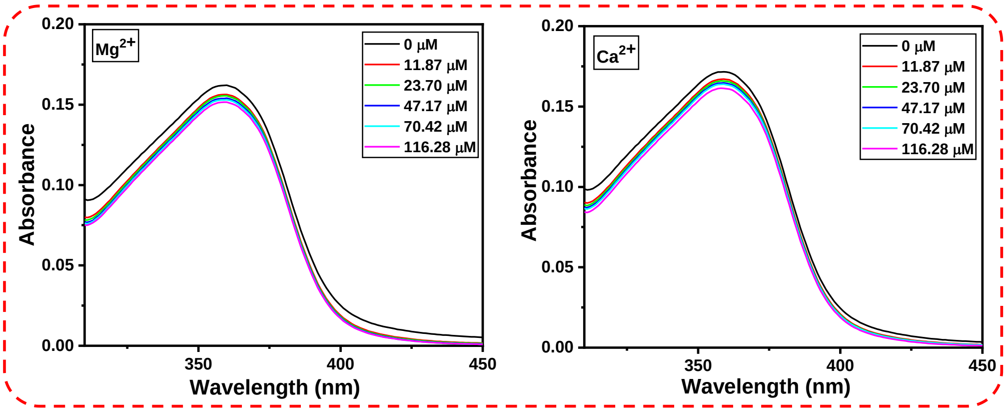

Fig. 5.17 The UV- Vis spectra of compound **4** in aqueous dispersion upon incremental addition of aqueous solution of alkaline earth metal ions. Final concentration of different ions in the medium is indicated in the legend.

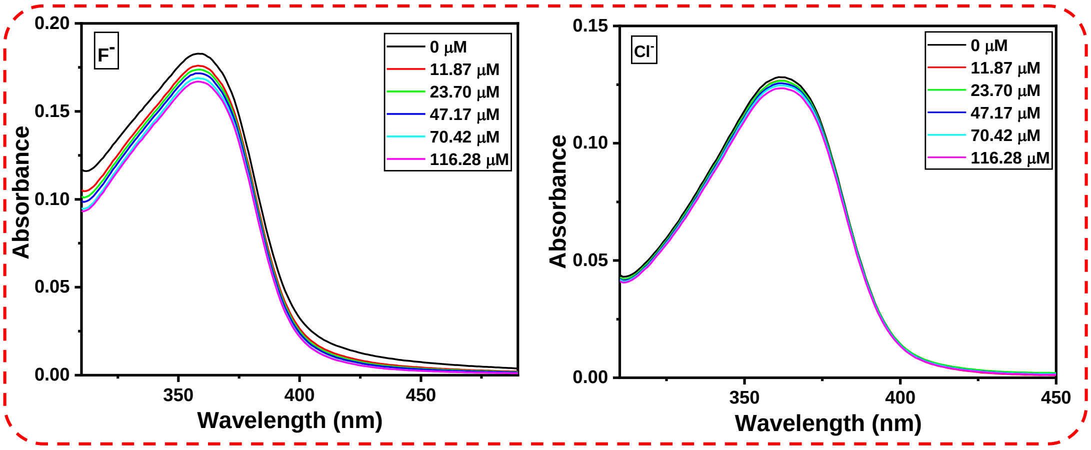

Fig. 5.18 The UV- Vis spectra of compound **4** in aqueous dispersion upon incremental addition of aqueous solution of alkaline earth metal ions. Final concentration of different ions in the medium is indicated in the legend.

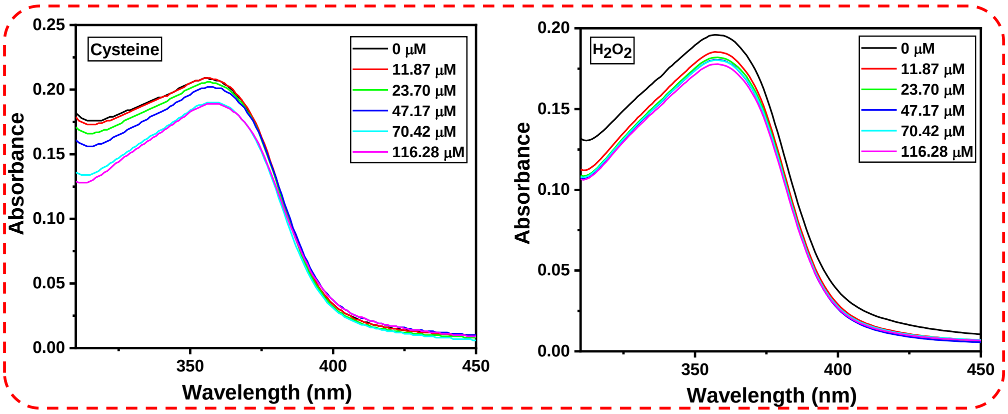

Fig. 5.19 The UV- Vis spectra of compound **4** in aqueous dispersion upon incremental addition of aqueous solution of alkaline earth metal ions. Final concentration of different ions in the medium is indicated in the legend.

5.3.8 Sorption studies of dyes using compound 4

To investigate about the efficiency of the compound **4** towards the dye sorption studies, we have performed absorption spectroscopy after a definite time interval with the centrifuged sample. The sorption studies were performed with the four different dyes such as MB, MO, OG and RhB. The sorption process was monitored by the variation in intensity of the maximum absorption peaks of MB, MO, OG and RhB in aqueous solution (663, 464, 475 and 553 nm, respectively). The sorption efficiency was calculated using the following equation:

$$\frac{\mathbf{I_0\text{-}I}}{\mathbf{I_0}} \times \mathbf{100\%}$$

where I_0 is the initial intensity and I is the final intensity. Among these dyes, MB shows highest sorption capacity. After experimenting, it has been noticed that the compound **4** can sorb maximum extent of MB (88%) within 2 h (Figure 5.20) although at first 5 minute, the sorption was quite significant i.e.34%. Whereas the sorption efficiency of MO, OG and RhB are only 18%, 19.65%, and 20%, respectively (Figure 5.21). These results suggested that the sorption behavior of the compound **4** is different towards MB dye. Due to the presence of free hydroxyl group, which are electron rich in nature, have strong electrostatic interaction with the cationic dye and it probably satisfy the reason of highest sorption capacity. Besides, the size factor plays a major role for determining the dye sorption. Only the perfect dimension of dye can enter into the cavity of compound **4**. If the dimension of dye perfectly matches with the dimension of the cavity of the compound, then selectivity arises. Methylene blue, being a small dimensional dye, can easily go into the vacant space of the compound **4** whereas in case of comparatively large dimensional dye, penetration is not possible into the MOF pores and they try to reorientate them. On the contrary, in case of anionic dye, such as MO and OG, having negative charge feels strong electrostatic repulsion from the electron rich hydroxyl groups present at the periphery of the compound **4** and results in very low sorption efficiency (18% and 19.65% respectively). The real images of the dye solutions captured by digital camera during the sorption studies were shown in Figure 5.22.

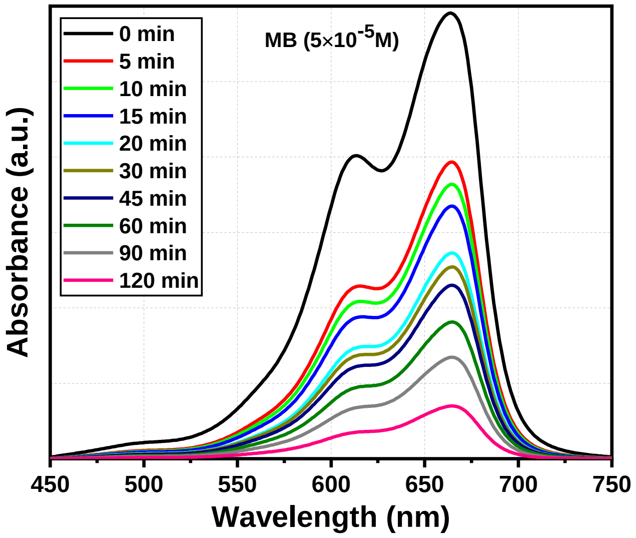

Fig. 5.20 UV- Visible absorption spectra of cationic MB dye in aqueous solution with compound **4** during the sorption process.

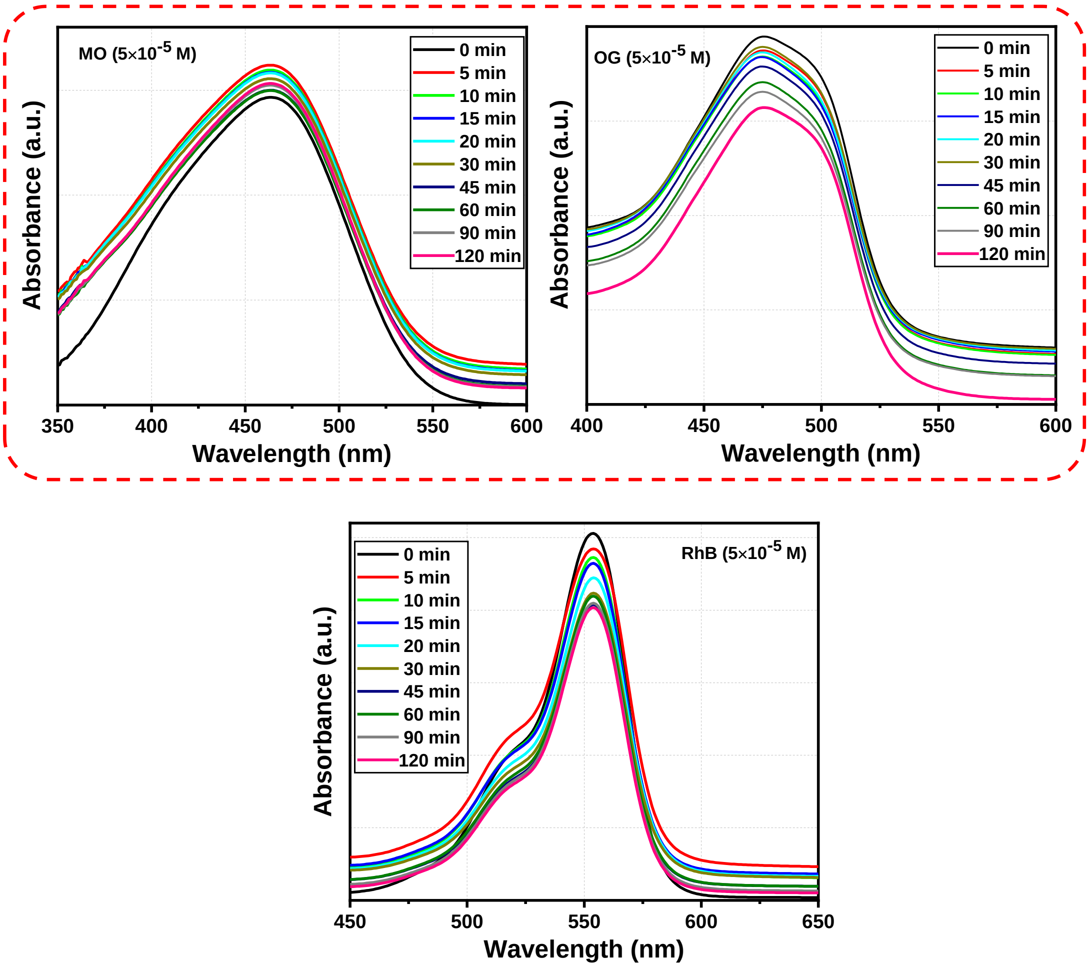

Fig. 5.21 UV- Visible absorption spectra of different dyes in aqueous solution with compound **4** during the sorption process.

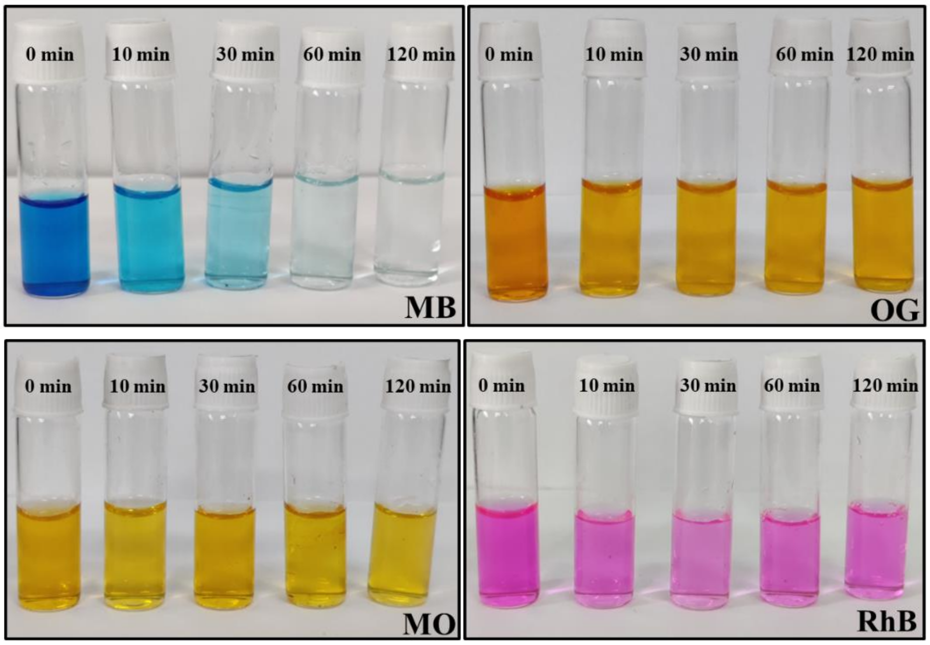

Fig. 5.22 The change in color of the dye solutions after the sorption process by using compound **4** (photographs captured by digital camera).

The sorption capacity[76] (q_t) was calculated by the following equation:

$$\mathbf{q_t\ (mg\ g^{-1}) = \frac{v(c_o\text{-}c_t)}{m}}$$

where V= volume of the dye solution, C_0 and C_t= dye concentration in mg L^{-1} at time t= 0 and t respectively and m = mass of the compound **4**. For the determination of q_t, we used five different concentrations of MB dye and studied their sorption characteristics. From the experimental data, it was found that the compound **4** sorbed 88% of MB with an initial concentration of 32 mg L^{-1}, exhibiting a sorption capacity of 29.79 mg g^{-1} within 2h (Figure 5.23), which is comparable to the previous literature (Table 5.4).

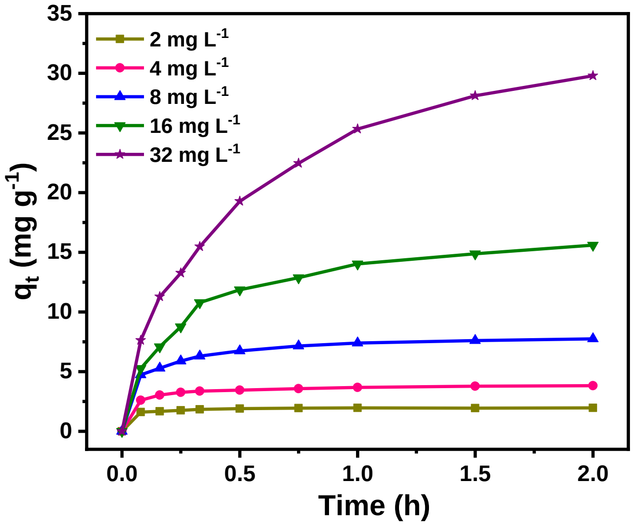

Fig. 5.23 Sorption capacities of compound **4** using five different concentrations of MB dye with variation in time.

Table 5.4. Previous literature on the sorption capacity of MB dye using different materials.

Sl. No.	Material	MOF Surface area (m^2 g^{-1})	% sorption or Sorption capacity	Time	Reference
1	$\{[Cd(PA)(4,4'\text{-}bpy)_2](H_2O)\}_n$	342.14	29.60 mg g^{-1}	2 h	51
2	$[Mn_4(L)_2(H_2O)_4]_n\cdot 4DMF\cdot H_2O$	-	17.62 mg g-1	2 h	52
3	$[(C_2H_5)_2NH_2]_2[Mn_6(L)(OH)_2(H_2O)_6]\cdot 4DEF$	-	67.5%	96 h	53
4	$[Cd_6(L)_2(bib)_2(DMA)_4]$	38	30 mg g^{-1}	72 h	54
5	$\{[Cd_2(BPTC)(DMA)_2(DMPU)_{0.5}(H_2O)_{0.5}]\ (DMPU)_{0.5}\}_n$	-	73.4%	24 h	55
6	$[Cd_3(tib)_2(BTB)_2]\cdot 3DEF\cdot 4.5H_2O$ $[Cd_3(tib)_2(BTB)_2(DMA)_2(H_2O)_2]\cdot 2\ DMA\cdot 8H_2O$	517 358	69% 55%	24 h	56
7	$[Co_3(tib)_2(BPT)_2(H_2O)_2]\cdot DMA\cdot 2.5H_2O$ $[Co_3(tib)_2(BTB)_2]\cdot 2DMF\cdot 6H_2O$	187.65 358.02	0.6×10^{-3} mg g^{-1} 6.4×10^{-3} mg g^{-1}	24 h	57

8	$[Cu_{24}(5\text{-hip})_{24}(bpy)_6(H_2O)_{12}]$	-	0.546 mmol g^{-1}	48 h	58
9	$[(CH_3)_2NH_2]_2[ZnNa_2(\mu\text{-}H_2O)_2(H_2O)_2(TATAT)]\cdot 2DMF$	-	0.75 mg g^{-1}	-	59
10	Acetic acid-promoted UiO-66	892-1090	13.2 mg g^{-1}	2 h	60
11	Cu- BTC	45.16	30- 40 mg g^{-1}	24 h	61
12	Fe_3O_4@ZIF-8	1068	20.2	15 h	62
13	$[Cu(C_{23}H_{14}O_6)(C_{10}H_8N_2)_2]\cdot H_2O\cdot DMSO$	170	29.79 mg g^{-1}	2 h	present work

We have also explored the dye desorption phenomenon to affirm that whether the dye molecules are sorbed only on the surface of the sorbent or it insert into the pore of the MOF. To understand the desorption phenomenon, we did a small experiment, the dye incorporated compound was soaked in simple deionized water for 48h and there is hardly any release of dye into the water and as a result no significant color change was observed. So, by observing this result we can conclude that the dye molecule was strongly bind with the pore of the compound by electrostatic force of interaction and for this the release of methylene blue dye molecule is negligible. This type of sorption process cannot be called physisorption.

5.3.9 Sorption kinetics

There are several kinetic models to explain the sorption behavior of compound **4** towards the methylene blue dye. Comparing all, the pseudo second order kinetics model results better fitting. The high correlation coefficient (R^2= 0.999) data proves it again (Table 5.5).

The pseudo second order kinetic equation is as follows[77]:

$$\frac{t}{q_t} = \frac{1}{k_2 q_e^2} + \frac{t}{q_e}$$

Where, q_t= sorption capacity at time t (h), K_2= rate constant of second order sorption (h g mg^{-1}) and q_e= equilibrium sorption capacity. If we plot t/q_t versus t, we get a straight line and from the slope we get the value of q_e and from the intercept we get the value of K_2 (Figure 5.24).

Table 5.5. Pseudo-second-order kinetic parameters for MB dye sorption into compound **4**.

Adsorbent	**q_e (mg g^{-1})**	**K_2 (h g mg^{-1})**	**R^2**
Compound **4**	37.34	0.0542	0.95062
	16.58	0.3573	0.99495
	7.95	1.88	0.99911
	3.87	6.32	0.99962
	1.99	24.25	0.99988

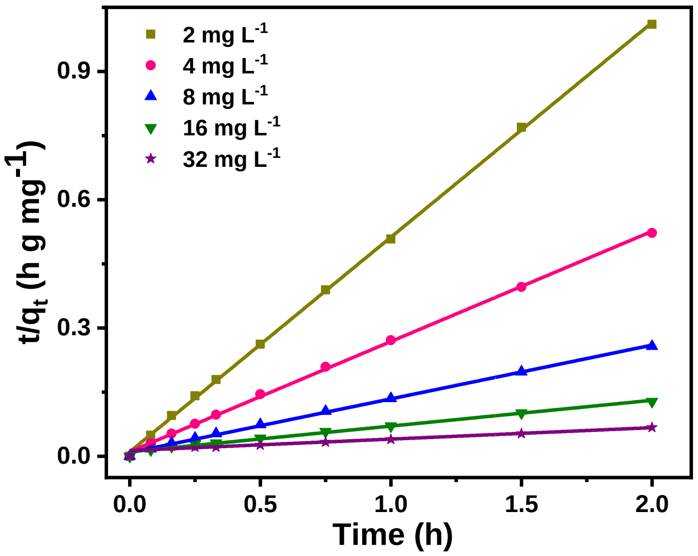

Fig. 5.25 Simulation of pseudo second order kinetic model for the sorption studies of MB dye using compound **4**.

5.3.10 Sorption Isotherm

The relationship between sorbate and sorbent can be better represented by sorption isotherm. To determine the sorption capacity, there are various methods to utilize but the experimental data obtained is fitted well with the Langmuir isotherm. To know the mechanism of the sorption, we have employed the Langmuir sorption isotherm,[78, 79] which can be written as following:

$$\frac{c_e}{q_e} = \frac{c_e}{q_m} + \frac{1}{q_m k_L}$$

Where, C_e= The concentration of the sorbed dye in equilibrium in mg L^{-1}, q_m= Maximum sorption capacity of the sorbent in mg g^{-1} and K_L= Langmuir sorption constant in L mg^{-1}. The values of q_m and K_L can be obtained from the slope and intercept (Figure 5.26) of a straight line respectively when we plot between C_e/q_e and C_e. The Langmuir model is fitted perfectly and is confirmed by the high correlation coefficient (R^2= 0.99624) value (Table 5.6).

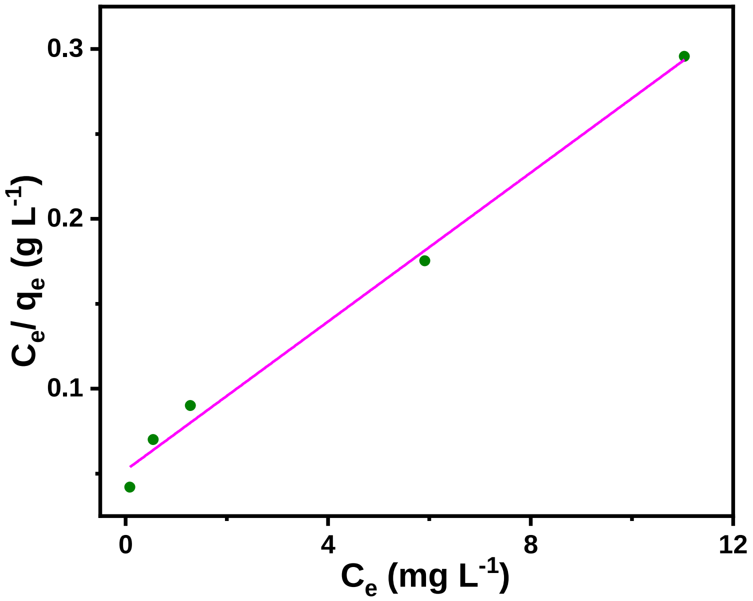

Fig. 5.26 Langmuir model for MB dye sorbed into the compound **4**.

Table 5.6: Parameters of Langmuir model for MB dye sorption into compound **4**.

Adsorbent	**Dye**	**K_L (L mg^{-1})**	**q_m (mg g^{-1})**	**R^2**
Compound 4	MB	0.42	45.66	0.99624

5.3.11 Chemical stability

It is necessary to check the stability of the compound after incorporation of dye molecule. Firstly, the compound **4** was soaked in distilled water and kept it for 1 day and then checked its PXRD and it was found that both the PXRD patterns matched well. Then the powdered compound was dissolved into the aqueous solution of methylene blue for 1 day and 2 days and then dried up and PXRD experiment was done using the sample (Figure 5.27). The resulting PXRD pattern was perfectly matches with the simulated data obtained from the single crystal XRD. So, it can be concluded that the compound stayed stable even after the dye sorption.

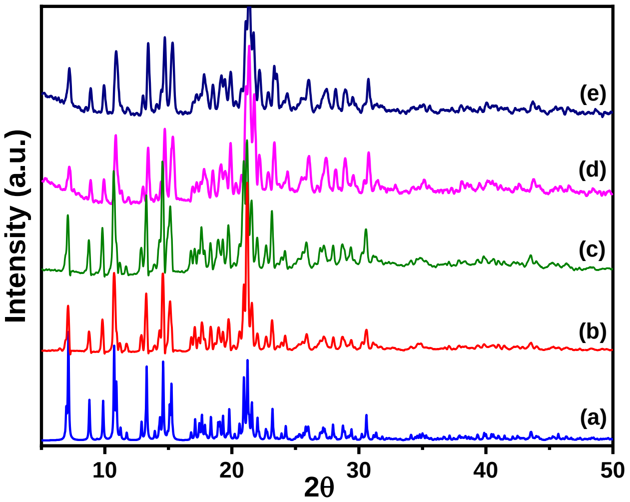

Fig. 5.27 Powder XRD (CuKα) patterns: (a) compound **4** simulated from single crystal X-ray data, (b) as-synthesized **4**, (c) compound **4** after immersing in water for 24 h, (d) compound **4** after immersing in the aqueous solution of MB dye for 24 h and dried and (e) compound **4** after immersing in the aqueous solution of MB dye for 48 h and dried.

5.3.12 Separation of mixtures of dyes

It is very much important to observe whether our compound can separate the selective dye from a solution of mixture of dyes. To see the result, we have chosen mixture equimolar mixture of MB and MO (MB‖MO). In case of mixture of dyes also the selectivity of MB dye towards the compound **4** is highly noticeable. This selectivity was observed through visual color change and absorption spectroscopic measurement. In case of MB‖MO mixtures (Figure 5.28), it has found that in case of MB dye, at the wavelength 664 nm there is a sharp decrease (86%) in the absorbance intensity whereas in case of MO, in the wavelength 464 nm, there is no as such decrease in intensity was observed. The change in color of the mixture of dye solutions before and after the sorption process by using compound **4** was captured by digital camera (Figure 5.29). So, from this result, we can again conclude that our compound can selectively sorb only MB dye molecule.

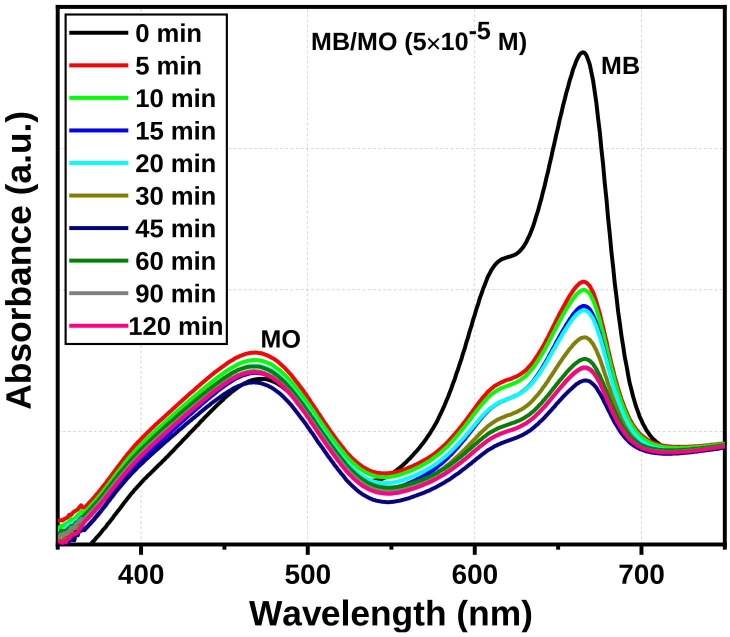

Fig. 5.28 UV- visible absorption spectra of mixtures of dye MB/MO in aqueous solution with compound **4** for separation experiments during the sorption process.

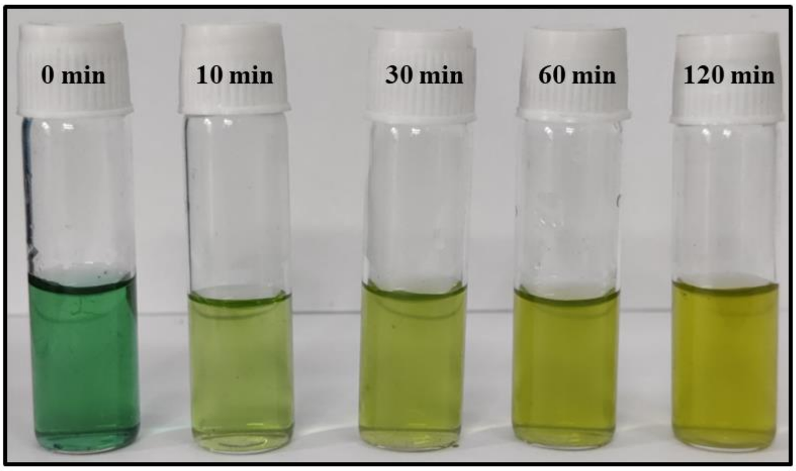

Fig. 5.29 The change in color of the mixture of dye solutions (MB+ MO) after the sorption process by using compound **4** (photographs captured by digital camera).

5.3.13 Dye sorption mechanism

There are various mechanism lies for the dye sorption phenomenon such as electrostatic interaction, H- bonding interaction, π- π stacking, acid- base interaction, hydrophobic interaction and so on. In case of our compound, the mechanism for the dye sorption phenomenon is mainly attributed to the electrostatic interactions and π- π interactions between the wall of the framework and the aromatic benzene ring of organic dye molecules (Figure 5.30). Now, there may be two factors are important for the possible dye sorption mechanism: (i) molecular size and (ii) charge of the dye molecule. The compound **4** is highly electron-rich due to the presence of enough aromatic rings and also the hydroxyl group. So, there may be some interaction between the electron rich framework and the cationic dye molecule, MB. On the contrary, RhB, being a cationic dye cannot sorb into the pore of the framework. In this case, probably, the size of the dye molecule plays the role. The molecular size of RhB (14.1× 9.8× 5.4 Å^3) is larger than MB dye (13.4× 5.00× 4.2 Å^3). MB molecule, with a proper size that perfectly matches the pore size of compound **4** is probably forming some supramolecular interaction with the framework of compound **4** and as a result the fast sorption may occur. Due to the well- ordered structure and crystalline porous framework, they have one unique characteristic to adapt the pore size keeping the framework intact. Correspondingly, the size selective sorption of the organic dye molecules occurs. On the other hand, the electrostatic repulsions between the electron-rich framework and anionic dyes (MO and OG) are the key factor for negligible sorption behavior of MO and OG.

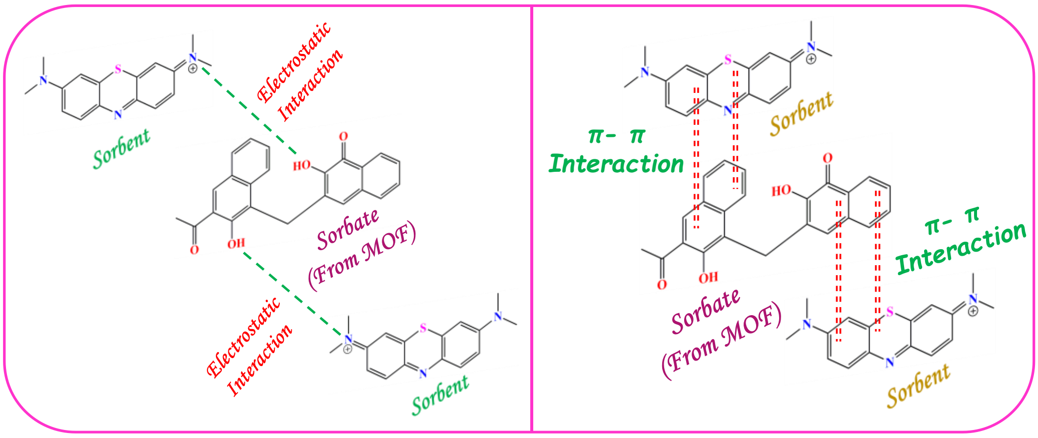

Fig. 5.30 Schematic representation of the dye sorption mechanism.

5.4 CONCLUSIONS

In conclusion, a two- dimensional copper-based metal-organic framework has been synthesized by layer diffusion technique. The crystal structure of the synthesized MOF was determined by using single crystal X-ray diffraction. The compound was comprehensively characterized by PXRD, IR, TGA, UV- vis spectroscopy, BET analysis, steady state and time-resolved photoluminescence studies. Fluorescence microscopic experiments using the MOF compound were utilized for selective staining of the cellular nucleus of the human epithelioid cervix carcinoma HeLa cell line. Dye sorption behavior of the compound in an aqueous solution was carried out and it showed high affinity for methylene blue (MB) dye. The synthesized compound exhibited 88% MB dye sorption with an initial concentration of 32 mg L^{-1} and the sorption capacity of MB was 29.79 mg g^{-1}. The calculated sorption capacity is also comparable with the previous literature value. Time-dependent sorption data fitted well using Langmuir sorption isotherm and it was also simulated by pseudo-second-order kinetics. The compound is also useful for the separation of MB (cationic dye) and MO (anionic dye). The importance of the molecular level interactions between the framework and the dye molecules has also been described to explain the selective dye sorption behavior. Overall, the present compound is useful for selective staining of the cellular nucleus through fluorescence imaging and for the successful removal of organic dye molecules in the context of wastewater treatment and environmental protection.

5.5 REFERENCES

1. Hassaan, M. A.; Nemr, A. E., *Am. J. Environ. Sci.* **2017,** *1*, 4, 64-67.
2. Dixit, S.; Yadav, A.; Dwivedi, P. D.; Das, M., *J. Cleaner Prod.* **2015,** *87*, 39-49.
3. Bhatia, D.; Sharma, N. R.; Singh, J.; Kanwar, R. S., *Crit. Rev. Environ. Sci. Technol.* **2017,** *47* (19), 1836-1876.
4. Rochman, C. M.; Browne, M. A.; Halpern, B. S.; Hentschel, B. T.; Hoh, E.; Karapanagioti, H. K.; Rios-Mendoza, L. M.; Takada, H.; Teh, S.; Thompson, R. C., *Nature* **2013,** *494* (7436), 169-171.
5. Dias, E. M.; Petit, C., *J. Mater. Chem. A.* **2015,** *3* (45), 22484-22506.
6. Wang, C.-C.; Li, J.-R.; Lv, X.-L.; Zhang, Y.-Q.; Guo, G., *Energy Environ. Sci.* **2014,** *7* (9), 2831-2867.
7. Mo, C.-H.; Cai, Q.-Y.; Li, Y.-H.; Zeng, Q.-Y., China. *J. Hazard. Mater.* **2008,** *152* (3), 1208-1213.
8. Rojas, S.; Rodríguez-Diéguez, A.; Horcajada, P., *ACS Appl. Mater. Interfaces.* **2022,** *14* (15), 16983-17007.
9. Yu, C.; Sun, Y.; Fang, X.; Li, J.; Wu, Q.; Bu, W.; Guo, X.; Wang, H.; Jiao, L.; Hao, E., *Inorg. Chem.* **2022,** *61* (42), 16718-16729.
10. Rojas, S.; Horcajada, P., *Chem. Rev.* **2020,** *120* (16), 8378-8415.
11. Adeyemo, A. A.; Adeoye, I. O.; Bello, O. S., *Toxicol. Environ. Chem.* **2012,** *94* (10), 1846-1863.
12. Shahnawaz Khan, M.; Khalid, M.; Shahid, M., *Mater. Adv.* **2020,** *1* (6), 1575-1601.
13. Parmar, B.; Bisht, K. K.; Rajput, G.; Suresh, E., *Dalton Trans.* **2021,** *50* (9), 3083-3108.
14. Haluzík, M.; Nedvídková, J.; Schreiber, V., *Sb. Lek.* **1995,** *96* (4), 319-322.
15. Cragan, J. D., *Teratology* **1999,** *60* (1), 42-48.
16. Crooks, J., *Arch. Dis. Child.* **1982,** *57* (11), 872-873.
17. Kumari, P.; Disha; Nayak, M. K.; Dhruwe, D.; Patel, M. K.; Mishra, S., *Ind. Eng. Chem. Res.* **2023,** *62* (3), 1245-1256.
18. Gholami Derami, H.; Gupta, P.; Gupta, R.; Rathi, P.; Morrissey, J. J.; Singamaneni, S., *ACS Appl. Nano Mater.* **2020,** *3* (6), 5437-5448.
19. Abujazar, M. S. S.; Karaağaç, S. U.; Abu Amr, S. S.; Alazaiza, M. Y. D.; Bashir, M. J. K., *J. Cleaner Prod.* **2022,** *345*, 131133-131145.
20. Rauf, M. A.; Ashraf, S. S., *Chem. Eng. J.* **2009,** *151* (1), 10-18.
21. Moradihamedani, P., *Polym. Bull.* **2022,** *79* (4), 2603-2631.
22. Nidheesh, P. V.; Zhou, M.; Oturan, M. A., *Chemosphere* **2018,** *197*, 210-227.

23. Yagub, M. T.; Sen, T. K.; Afroze, S.; Ang, H. M., *Adv. Colloid Interface Sci.* **2014,** *209*, 172-184.
24. Deng, F.; Qin, X.; Chai, K.; Wei, Z.; Wang, K.; Liao, B.; Wu, J.; Pang, Z.; Shen, F., *ACS Appl. Nano Mater.* **2023,** *6* (10), 8675-8684.
25. Yang, J.-M., *CrystEngComm* **2022,** *24* (3), 434-449.
26. Chae, H. K.; Siberio-Pérez, D. Y.; Kim, J.; Go, Y.; Eddaoudi, M.; Matzger, A. J.; O'Keeffe, M.; Yaghi, O. M.; Materials, D.; Discovery, G., *Nature* **2004,** *427* (6974), 523-527.
27. Gong, J.; Lin, H.; Antonietti, M.; Yuan, J., *J. Mater. Chem. A.* **2016,** *4* (19), 7313-7321.
28. Liu, F.; Guo, Z.; Ling, H.; Huang, Z.; Tang, D., *Microporous Mesoporous Mater.* **2016,** *227*, 104-111.
29. Stefa, S.; Griniezaki, M.; Dimitropoulos, M.; Paterakis, G.; Galiotis, C.; Kiriakidis, G.; Klontzas, E.; Konsolakis, M.; Binas, V., *ACS Appl. Nano Mater.* **2023,** *6* (3), 1732-1743.
30. Boukayouht, K.; Bazzi, L.; El Hankari, S., *Coord. Chem. Rev.* **2023,** *478*, 214986-215008.
31. Furukawa, H.; Cordova, K. E.; O’Keeffe, M.; Yaghi, O. M., *Science* **2013,** *341* (6149), 1230444-1230457.
32. Zhu, Q.-L.; Xu, Q., *Chem. Soc. Rev.* **2014,** *43* (16), 5468-5512.
33. Xiang, F.; Zhang, H.; Yang, Y.; Li, L.; Que, Z.; Chen, L.; Yuan, Z.; Chen, S.; Yao, Z.; Fu, J.; Xiang, S.; Chen, B.; Zhang, Z., *Angew. Chem.* **2023,** *62* (13), e202300638.
34. Sillar, K.; Kundu, A.; Sauer, J., *J. Phys. Chem. C* **2023,** *127* (27), 13317-13326.
35. Kaur, H.; Kumar, R.; Kumar, A.; Krishnan, V.; Koner, R. R., *Dalton Trans.* **2019,** *48* (3), 915-927.
36. Cheng, S.; Wu, Y.; Jin, J.; Liu, J.; Wu, D.; Yang, G.; Wang, Y.-Y., *Dalton Trans.* **2019,** *48* (22), 7612-7618.
37. He, Y.-C.; Yang, J.; Kan, W.-Q.; Zhang, H.-M.; Liu, Y.-Y.; Ma, J.-F., *J. Mater. Chem. A.* **2015,** *3* (4), 1675-1681.
38. Yi, F.-Y.; Li, J.-P.; Wu, D.; Sun, Z.-M., *Chem. Eur. J.* **2015,** *21* (32), 11475-11482.
39. Ji, W.-J.; Hao, R.-Q.; Pei, W.-W.; Feng, L.; Zhai, Q.-G., *Dalton Trans.* **2018,** *47* (3), 700-707.
40. Li, Y.-L.; Zhao, Y.; Wang, P.; Kang, Y.-S.; Liu, Q.; Zhang, X.-D.; Sun, W.-Y., *Inorg. Chem.* **2016,** *55* (22), 11821-11830.
41. Li, Y.-L.; Zhao, Y.; Kang, Y.-S.; Liu, X.-H.; Sun, W.-Y., Cryst. Growth Des. **2016,** *16* (12), 7112-7123.

42. Wang, H.-N.; Liu, F.-H.; Wang, X.-L.; Shao, K.-Z.; Su, Z.-M., *J. Mater. Chem. A.* **2013,** *1* (42), 13060-13063.
43. Sun, C.-Y.; Wang, X.-L.; Qin, C.; Jin, J.-L.; Su, Z.-M.; Huang, P.; Shao, K.-Z., *Chem. Eur. J.* **2013,** *19* (11), 3639-3645.
44. Qiu, J.; Feng, Y.; Zhang, X.; Jia, M.; Yao, J., *J. Colloid Interface Sci.* **2017,** *499*, 151-158.
45. Li, Y.; Gao, C.; Jiao, J.; Cui, J.; Li, Z.; Song, Q., *ACS Omega* **2021,** *6* (49), 33961-33968.
46. Zheng, J.; Cheng, C.; Fang, W.-J.; Chen, C.; Yan, R.-W.; Huai, H.-X.; Wang, C.-C., *CrystEngComm* **2014,** *16* (19), 3960-3964.
47. Nguyen, N. T. T.; Nguyen, T. T. T.; Ge, S.; Liew, R. K.; Nguyen, D. T. C.; Tran, T. V., *Nanoscale Adv.* **2024,** *6* (7), 1800-1821.
48. Wang, Y.-M.; Xu, Y.; Zhang, X.; Cui, Y.; Liang, Q.; Liu, C.; Wang, X.; Wu, S.; Yang, R., *Nanomaterials* **2022,** *12* (2), 287-298.
49. Tian, C.; Zhu, L.; Lin, F.; Boyes, S. G., *ACS Appl. Mater. Interfaces.* **2015,** *7* (32), 17765-17775.
50. Yang, J.; Wang, T.; Zhao, L.; Rajasekhar, V. K.; Joshi, S.; Andreou, C.; Pal, S.; Hsu, H. T.; Zhang, H.; Cohen, I. J.; Huang, R.; Hendrickson, R. C.; Miele, M. M.; Pei, W.; Brendel, M. B.; Healey, J. H.; Chiosis, G.; Kircher, M. F., *Nat Biomed Eng* **2020,** *4* (7), 686-703.
51. Jensen, E. C., *Anat Rec* **2013,** *296* (1), 1-8.
52. Deng, J.; Wang, K.; Wang, M.; Yu, P.; Mao, L., *J. Am. Chem. Soc.* **2017,** *139* (16), 5877-5882.
53. Qu, F.; Ding, Y.; Lv, X.; Xia, L.; You, J.; Han, W., *Anal Bioanal Chem* **2019,** *411* (17), 3979-3988.
54. Liu, M.; Ren, X.; Meng, X.; Li, H., *Chin. J. Chem.* **2021,** *39* (2), 473-487.
55. Yang, P.; Men, Y.; Tian, Y.; Cao, Y.; Zhang, L.; Yao, X.; Yang, W., *ACS Appl. Mater. Interfaces.* **2019,** *11* (12), 11209-11219.
56. Verma, T.; Singh, U. P.; Verma, P.; Butcher, R. J.; Ghosh, C.; Roy, P., *J. Mol. Struct.* **2024,** *1302*, 137467-137477.
57. Li, S.; Tan, L.; Meng, X., *Adv. Funct. Mater.* **2020,** *30* (13), 1908924-1908949.
58. Zhang, Y.; Fu, H.; Chen, S.; Liu, B.; Sun, W.; Gao, H., *Chem. Commun.* **2020,** *56* (5), 762-765.
59. Demir Duman, F.; Forgan, R. S., *J. Mater. Chem. B* **2021,** *9* (16), 3423-3449.
60. Sava Gallis, D. F.; Rohwer, L. E. S.; Rodriguez, M. A.; Barnhart-Dailey, M. C.; Butler, K. S.; Luk, T. S.; Timlin, J. A.; Chapman, K. W., *ACS Appl. Mater. Interfaces.* **2017,** *9* (27), 22268-22277.

61. Madison, W. J. B. A. I. U., SMART (V 5.628), SAINT (V 6.45 a), XPREP, and SHELXTL. **2004**.
62. Krause, L.; Herbst-Irmer, R.; Sheldrick, G. M.; Stalke, D., *J. Appl. Crystallogr.* **2015,** *48* (Pt 1), 3-10.
63. Altomare, A.; Cascarano, G. L.; Giacovazzo, C.; Guagliardi, A. J., *J. Appl. Crystallogr.* **1993,** *26*, 343-350.
64. Sheldrick, G., Crystal structure refinement with SHELXL. *Acta Crystallogr., Sect. C* **2015,** *71* (1), 3-8.
65. Farrugia, L., WinGX suite for small-molecule single-crystal crystallography. *J. Appl. Crystallogr.* **1999,** *32* (4), 837-838.
66. Spek, A., Single-crystal structure validation with the program PLATON. *J. Appl. Crystallogr.* **2003,** *36* (1), 7-13.
67. Deng, S.-Q.; Mo, X.-J.; Zheng, S.-R.; Jin, X.; Gao, Y.; Cai, S.-L.; Fan, J.; Zhang, W.-G., *Inorg. Chem.* **2019,** *58* (4), 2899-2909.
68. Tang, Y.; Lu, X.-M.; Yang, G.; Wang, Y.-Y., *Inorg. Chem.* **2023,** *62* (4), 1735-1743.
69. Addison, A. W.; Rao, T. N.; Reedijk, J.; van Rijn, J.; Verschoor, G. C., *J. Chem. Soc., Dalton Trans.* **1984,** (7), 1349-1356.
70. Kavak, E.; Şevik, M.; Değirmenci, G.; Alp Arici, T.; Özdemir, R.; Arici, M., Cryst. Growth Des. **2024,** *24* (6), 2415-2424.
71. Rani, P.; Husain, A.; Bhasin, K. K.; Kumar, G., *Inorg. Chem.* **2024,** *63* (7), 3486-3498.
72. Dinda, S.; Mahato, B.; Maiti, A.; Ghoshal, D., *Inorg. Chem.* **2024,** *63* (13), 5996-6004.
73. Das, R. S.; Maiti, D.; Kar, S.; Bera, T.; Mukherjee, A.; Saha, P. C.; Mondal, A.; Guha, S., *J. Am. Chem. Soc.* **2023,** *145* (37), 20451-20461.
74. Chandra Saha, P.; Das, R. S.; Chatterjee, T.; Bhattacharyya, M.; Guha, S., *Bioconjugate Chem.* **2020,** *31* (5), 1301-1306.
75. Saha, P. C.; Bera, T.; Chatterjee, T.; Samanta, J.; Sengupta, A.; Bhattacharyya, M.; Guha, S., *Bioconjugate Chem.* **2021,** *32* (4), 833-841.
76. Vadivelan, V.; Kumar, K. V., *J. Colloid Interface Sci.* **2005,** *286* (1), 90-100.
77. Ho, Y. S.; McKay, G., *Process Biochem.* **1999,** *34* (5), 451-465.
78. Hall, K. R.; Eagleton, L. C.; Acrivos, A.; Vermeulen, T., *Ind. Eng. Chem. Fundam.* **1966,** *5* (2), 212-223.
79. Hameed, B. H.; Rahman, A. A., *J. Hazard. Mater.* **2008,** *160* (2), 576-581.

List of Publications

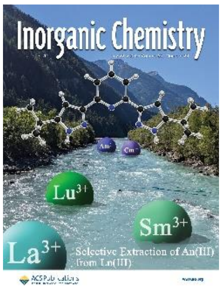

1. **Hui, S**.; Saha, P. C.; Guha, S.; Mahata, P.* Two-Dimensional Cu-Based MOF for Selective Staining of the Cellular Nucleus through Fluorescence Imaging and Selective Sorption of Dye Molecules in Aqueous Medium. *Inorg. Chem.,* **2024**, 63, 13439-13449.

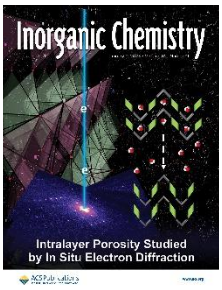

2. **Hui, S**.; Daga, P.; Mahata, P.* Selective Luminescence Turn-On-Based Sensing of Phosphate in the Presence of Other Interfering Anions Using a Heterobimetallic (3d–4d) MOF with an Acidic Pocket. *Inorg. Chem.,* **2023**, 62, 591-600.

3. **Hui, S**.; Majee, P.; Singha, D. K.; Daga, P.; Mondal, S. K.; Mahata, P.* pH response of a hydroxyl-functionalized luminescent metal–organic framework based phosphor. *New J. Chem*., **2021**, 45, 9394–9402.

4. **Hui, S**.; Azam, S.; Dutta, S.; Mondal, S. K.; Mahata, P.* A Supramolecular Assembly of Anionic Metal-Organic Complex and cationic Amine: Selective Recognition Behavior Towards Arginine and Histidine (Manuscript submitted).

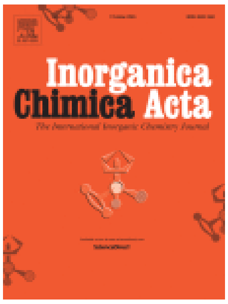

5. Azam, S.; Dutta, S; **Hui, S**.; Jana, N. C.; Bagh, B; Mahata, P.; Mondal, S. K. Highly Selective Recognition of L-Tyrosine by Perceiving Huge Luminescence Turn-On of a Cobalt (II) Based Metal-Organic Compound at Physiological pH. (Manuscript accepted)

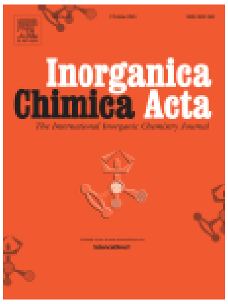

6. Saha, D.; Majee, P.; Singha, D. K.; Dutta, S.; Azam, S.; **Hui, S**.; Mahata, P.*; Mondal, S. K. Resonance energy transfer aided detection of nitroaromatics in aqueous medium by a luminescent Mn based metal-organic framework. *Inorganica. Chim. Acta,* **2024**, 571, 122244-13449

7. Daga, P.; **Hui, S**.; Sarkar, S.; Majee, P.; Singha, D. K.; Mahata, P.*; Mondal, S. K. pH dependent sensitization of europium in a hydrogen bonded three-dimensional metal–organic compound with $(4^9 6^6)_2(4^4 6^2)_3$ topology: luminescence titration and time-resolved studies. *Mater. Adv*., **2022**, 3, 1182–1190.

8. Daga, P.; Manna, P.; Majee, P.; Singha, D. K.; **Hui, S**.; Ghosh, A. K.; Mahata, P.* Mondal, S. K. Response of a Zn(II)-based metal–organic coordination polymer towards trivalent metal ions (Al^{3+}, Fe^{3+} and Cr^{3+}) probed by spectroscopic methods. *Dalton Trans.,* **2021**, 50, 7388–7399.

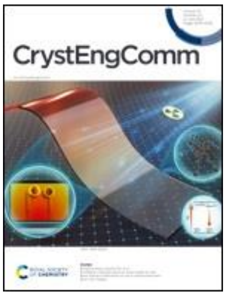

9. Majee, P.; Singha, D. K.; Daga, P.; **Hui, S**.; Mahata, P.*; Mondal, S. K. Photophysical studies of a room temperature phosphorescent Cd(II) based MOF and its application towards ratiometric detection of Hg^{2+} ions in water. *CrystEngComm*, **2021**, 23, 4160–4168.

10. Daga, P.; Sarkar, S.; Majee, P.; Singha, D. K.; **Hui, S**.; Mahata, P.*; Mondal, S. K. A selective detection of nanomolar-range noxious anions in water by a luminescent metal−organic framework. *Mater. Adv.* **2021**, 2, 985–995.

11. Daga, P.; Majee, P.; Singha, D. K.; Manna, P.; **Hui, S**.; Ghosh, A. K.; Mahata, P.*; Mondal, S. K. Dramatic luminescence signal from a Co(II)-based metal–organic compound due to the construction of charge-transfer bands with Al^{3+} and Fe^{3+} ions in water: steady-state and time-resolved spectroscopic studies. *New J. Chem.*, **2020**, 44, 4376-4385.

12. Singha, D. K.; Majee, P.; **Hui, S**.; Mondal, S. K.; Mahata, P.* Luminescent metal−organic framework-based phosphor for the detection of toxic oxoanions in an aqueous medium. *Dalton Trans*., **2020**, 49, 829−840.

List of scientific conference attended and poster presentation

- National Seminar on Chemical Sciences: Today and Tomorrow (CSTT-2019), Department of Chemistry, Jadavpur University, Kolkata-700032, India, 14th March, **2019**.

- National Seminar on Celebration of the International Year of the Periodic Table (CIYPT), Department of Chemistry Jadavpur University, Kolkata-700032, India, 13 & 14th August, **2019**.

- National Seminar on Emerging Trends in Chemical Sciences, Department of Chemistry, Jadavpur University, Kolkata-700032, India, 7th January, **2020**.

- National Seminar on RECENT TRENDS IN INORGANIC CHEMISTRY, Inorganic chemistry section, Department of Chemistry, Jadavpur University, Kolkata-700032, India, 6th March, **2020**.

- International Seminar on Recent Advances in Chemistry and Material Science (RACMS-2022), Indian Chemical Society in association with the Bangladesh Chemical Society, Bangladesh and Department of Chemistry, Jadavpur University, Kolkata, July 30-31 & August 02-03, **2022**.

- International Conference on "AGGREGATION-INDUCED EMISSION FROM FUNDAMENTALS TO APPLICATIONS (ICAIEFA2022), Department of Chemistry, BITS Pilani @ K.K. Birla Goa Campus, 16th-18th December, **2022**.

- National Seminar on Recent trends in Chemistry and related disciplines, Department of Chemistry, The University of Burdwan, 11th January, **2024**.